Univerzita Karlova

1. lékařská fakulta

Studijní program: Doktorské studijní programy v biomedicíně
Studijní obor: Vývojová a buněčná biologie

Mgr. Tomáš Chum

Studium trojrozměrné organizace signálních molekul na T buňkách pomocí kvantitativních metod fluorescenční mikroskopie

Quantitative fluorescence microscopy techniques to study three-dimensional organisation of T-cell signalling molecules

Dizertační práce

Školitel: Mgr. Marek Cebecauer, Ph.D.

Praha, 2020

Prohlášení:

Prohlašuji, že jsem závěrečnou práci zpracoval samostatně a že jsem řádně uvedl a citoval všechny použité prameny a literaturu. Současně prohlašuji, že práce nebyla využita k získání jiného nebo stejného titulu.

Souhlasím s trvalým uložením elektronické verze mé práce v databázi systému meziuniverzitního projektu Theses.cz za účelem soustavné kontroly podobnosti kvalifikačních prací.

V Praze, 12. 08. 2020

Tomáš Chum

Identifikační záznam:

CHUM, Tomáš. *Studium trojrozměrné organizace signálních molekul na T buňkách pomocí kvantitativních metod fluorescenční mikroskopie. [Quantitative fluorescence microscopy techniques to study three-dimensional organisation of T-cell signalling molecules]*. Praha, 2020. 233 stran, 7 příloh. Dizertační práce (Ph.D.). Univerzita Karlova, 1. Lékařská fakulta. Vedoucí práce Cebecauer, Marek.

Acknowledgements

I would like to thank to all the people who made this thesis possible. Firstly, I would like to express my gratitude to my supervisor Marek Cebecauer for the possibility to work in his team. I am sincerely grateful for his human approach combined with never ending optimism, for his support, guidance and insightful advices and critical discussions.

My big thanks also belongs to all my colleagues from our lab and department of Biophysical Chemistry of the J. Heyrovsky Institute of Physical Chemistry for teaching me all new things, for helpful discussions and willingness to answer all my stupid questions. Also, many thanks for creating the friendly atmosphere! My thanks also go to the Laboratory of Leukocyte Signalling at the Institute of Molecular Biology for fruitful cooperation. I would like to express my special thanks to Peter Kapusta, for everything he taught me about microscopy. Many thanks also to him and Petra Riegerová for their critical comments on this work.

My greatest gratitude goes to my whole family. I would like to dedicate this thesis to my wife Zuzi for her unfailing support, help and endless patience during the demanding years of the entire doctoral study. I promise that everything will be fine from now on ☺.

Foreword

Dear reader, thank you in particular for your interest in this work. Due to the fact that huge part of the work is technically focused, some details concerning the information in the main text are further explained for the sake of clarity as inserted notes in order not to disrupt the flow of the main text.

TABLE OF CONTENTS

SUMMARY

Proteins represent one of the basic building blocks of all organisms. To understand their function at the molecular level is one the critical goals of current biological, biochemical and biophysical research. It is important to characterise all aspects that affect the localisation of proteins into different compartments with specific functions, the dynamic structure of proteins and their role in multiprotein assemblies, because altering these properties can lead to various diseases.

Most of the proteomic studies are nowadays performed using biochemical approaches that allow us to study multicellular organism or tissue at once. The disadvantage of these methods is complex preparation of sample and the need for a large number of cells, which leads to the loss of information at the molecular level and in individual cells.

On the contrary, microscopy can provide rather detailed information about proteins of interest and at the level of a single cell. A variety of fluorescence microscopy methods in combination with recombinant DNA techniques were applied to elucidate subcellular localisation of transmembrane adaptor proteins (TRAPs) in human lymphocytes and their nanoscopic organisation at the plasma membrane. Linker of activation of T lymphocytes (LAT), phosphoprotein associated with glycosphingolipid-enriched membrane microdomains (PAG) and non-T-cell activation linker (NTAL) were selected for our studies. These are single spanning proteins that lack significant extracellular domain, are palmitoylated and share comparable hydrophobicity and length of their transmembrane domain (TMD).

The necessity of palmitoylation for plasma membrane sorting of LAT, but not for other studied TRAPs, was demonstrated using transient expression of fluorescent fusion proteins. This different behaviour could be caused by the presence of helix-breaking residues introducing a dynamic kink in the centre of the structure of LAT TMD. The positive charge inside-rule was confirmed using model TRAP-like proteins carrying artificial TMD with different symmetry at the ends of the transmembrane segments. Also the presence of the DxE/ YxxØ amino acid sequence motifs responsible for release of proteins from endoplasmic reticulum was confirmed in the C-terminal part of LAT and PAG.

New sample preparation procedure for super-resolution microscopy was developed. This procedure radically improved the quality of acquired single molecule fluorescence data and, in addition, preserved the surface morphology of lymphocytes immobilised on the optical surface. The origin of previously described microclusters of CD4 was discovered by combination of our new protocol and improved and simplified version of the quantitative 3D analysis of single molecule localisation microscopy data. These accumulation patterns of CD4 at the tips of microvilli are palmitoylation dependent. In comparison, CD45 molecule was shown to be randomly distributed over the shaft and the base of microvilli. Indeed, its segregation from the tips of microvilli suggests the mechanism how surface morphology can regulate signalling in T cells.

In summary, the presented data indicate the importance of quantitative fluorescence microscopy for characterisation of proteins in their physiological environment, in individual cells and, in some cases, at the single molecule level.

Key words: LAT, PAG, NTAL, TRAP, CD4, CD45, fluorescence microscopy, super-resolution microscopy, T cell, transmembrane protein sorting, cell surface morphology

SOUHRN

Proteiny patří mezi základní stavební jednotky všech organismů. Proto je pochopení jejich funkce na molekulární úrovni jedním z klíčových cílů současného biologického, biochemického a biofyzikálního výzkumu. Je důležité charakterizovat aspekty ovlivňující lokalizaci bílkovin do vnitrobuněčných částí se specifickými funkcemi a jejich samotnou dynamickou strukturu, včetně multiproteinových komplexů. Jakékoliv narušení těchto proteinových vlastností může vést ke vzniku různých onemocnění.

Většina proteomických studií je dnes prováděna pomocí biochemických přístupů, které nám umožňují studovat mnohobuněčný organismus nebo tkáň najednou. Nevýhodou těchto metod je složitá příprava vzorku a potřeba velkého počtu buněk. Tato kombinace vede ke ztrátě informací z jednotlivých buněk na molekulární úrovni.

Oproti tomu mikroskopické techniky mohou poskytnout poměrně podrobné informace o sledovaných bílkovinách, navíc z jednotlivých buněk. Pro studium lokalizace proteinů v různých částech lidských lymfocytů jsme vybrali trans-membránové adaptorové proteiny (TRAPy). Kombinací metod DNA manipulace a fluorescenční mikroskopie jsme sledovali i jejich nanoskopickou organizaci na plazmatické membráně. Jako zástupci byly vybrány tyto proteiny: „linker of activation of T lymphocytes” (LAT), “phosphoprotein associated with glycosphingolipid-enriched membrane microdomains” (PAG) a “non-T-cell activation linker” (NTAL). Jedná se o bílkoviny s jednou trans-membránovou doménou (TMD), která je palmitoylovaná a u všech má podobnou hydrofobicitu a délku. Navíc tito zástupci postrádají extracelulární doménu, která by měla vliv na jejich vlastnosti.

Pomocí transientní transfekce buněk fluorescenčně označenými proteiny jsme prokázali efekt palmitoylace na cílení LATu na plazmatickou membránu. Podobné působení nebylo u ostatních zástupců pozorováno. Takto odlišné chování může být způsobené přítomností aminokyselinových zbytků, které narušují spirální strukturu TMD. Jejich přítomnost vede ke vzniku dynamického zlomu uprostřed α-šroubovice. Transfekcí umělých proteinů s vysoce hydrofobní TMD jsme potvrdili pravidlo „pozitivního náboje na vnitrobuněčné straně“ tohoto segmentu. Účinnost jejich transportu na membránu byla snížena, pokud byl elektrostatický náboj symetrický na obou stranách. Dále jsme potvrdili funkci DxE / YxxØ aminokyselinových sekvenčních motivů, které jsou kódovány v sekvenci C-terminální části LATu a PAGu. Tyto motivy slouží proteinům k uvolnění z endoplasmatického retikula.

Byl vyvinut nový postup zpracování vzorku pro mikroskopii s vysokým rozlišením. Naše metoda radikálně zlepšila kvalitu získaných jedno-molekulárních dat a navíc zachovala morfologii povrchu lymfocytů přichycených k mikroskopickému sklu. Díky nové přípravě vzorku a vylepšené a zjednodušené trojrozměrné kvantitativní analýze dat jsme zjistili, že dříve popsané mikrostruktury CD4 jsou ve skutečnosti akumulací tohoto koreceptoru na vrcholcích mikrovilů. Tato organizace je závislá na palmitoylaci CD4. Oproti tomu CD45 molekula byla distribuována náhodně na těle a bázi mikrovilů. Segregace těchto dvou molekul naznačuje mechanismus regulace signalizace T buněk pomocí uspořádání jejich plasmatické membrány.

V souhrnu všechny prezentované výsledky ukazují důležitost metod fluorescenční mikroskopie při charakterizaci proteinů v jejich přirozeném prostředí. Jak v jednotlivých buňkách, tak na úrovni individuálních studovaných molekul.

Klíčová slova: LAT, PAG, NTAL, TRAP, CD4, CD45, fluorescenční mikroskopie, mikroskopie s vysokým rozlišením, T buňka, sorting trans-membránových proteinů, morfologie buněčného povrchu

LIST OF ABBREVIATIONS

2D	two-dimensional
3D	three-dimensional
7 AAD	7-Amino-Actinomycine D
APT	acyl protein thioesterases
BCR	B-cell receptor
BP	biplane imaging
bSOFI	balanced super-resolution optical fluctuation imaging
CALM	complementation-activated light microscopy
Cbp	Csk-binding protein
CCD	charge coupled devices
CCR5	C-C chemokine receptor type 5
CD4	cluster of differentiation 4
CD45	cluster of differentiation 45
CMOS	complementary metal oxide semiconductor
CoA	Coenzym A
Cryo-EM	cryo-electron microscopy
DIC	differential interference contrast
dSTRORM	direct stochastic optical reconstruction microcopy
dTRABI	direct temporal, radial-aperture-based intensity estimation
ECM	extracellular matrix
eGFP	enhanced green fluorescent protein
EM	electron microscopy
EMCCD	electron multiplying charge coupled devices
ER	endoplasmic reticulum
ERM	ezrin, radixin, moesin
FCS	fluorescence correlation spectroscopy
FLIM	fluorescence lifetime imaging microscopy
FLIM-FRET	fluorescence lifetime imaging microscopy – Förster resonance energy transfer
FRET	Förster resonance energy transfer
FWHM	full width at half maximum
GFP	green fluorescent protein
GPI	glycosylphosphatidylinositol
HDR	high density regions
HILO	highly inclined and laminated optical sheet illumination
iPALM	interferometric photoactivated localisation microscopy
LAT	linker of activation of T lymphocytes
LED	light emitting diodes
LLS-SIM	lattice light sheet structured illumination microscopy
LSFM	Light sheet fluorescence microscopy
MD	molecular dynamic
MHCII	major histocompatibility complex class II
NA	numerical aperture
NK	natural killer

NMR	nuclear magnetic resonance
NSOM	near-field scanning optical microscope
NTAL	non-T-cell activation linker
PAG	phosphoprotein associated with glycosphingolipid-enriched membrane microdomains
PAINT	point accumulation for imaging in nanoscale topography
PAT	palmitoyl acyltransferases
PALM	photoactivated localisation microscopy
PDL	poly-D-lysine
PLL	poly-L-lysine
PMT	photomultiplier tubes
PSF	point-spread functions
PTPRC	protein tyrosine phosphatase receptor type C
Q-dots	quantum-dots
QE	quantum efficiency
ROI	region of interest
sCMOS	scientific complementary metal oxide semiconductors
SEM	scaning electron microscope
SIM	structured illumination microscopy
SPAD	single photon avalanche photodiodes
SMLM	single molecule localisation microscopy
SNR	signal-to-noise ratio
SOFI	super-resolution optical fluctuation imaging
SPB	supported planar bilayers
SR	super-resolution
SR-CLEM	super-resolution correlative light electron microscopy
STED	Stimulated emission depletion
STORM	stochastic optical reconstruction microscopy
SUMO	small ubiquitin-like modifier
TCR	T-cell receptor
TEM	transmission electron microscope
TIRF	total internal reflection fluorescence
TMD	transmembrane domains
TRABI	temporal, radial-aperture-based intensity estimation
TRAP	transmembrane adaptor proteins
VA-TIRF	varying angle total internal reflection fluorescence
VAEM	variable angle epifluorescence microscopy

1 GENERAL INTRODUCTION

Approximately 20% of human body is composed of proteins (Snyder *et al.*, 1972). This is reflected by the fact that our DNA carries ~22.300 putative protein-coding genes as defined by the Human Genome Project (Pertea and Salzberg, 2010). Obtained genetic data opened the path for 'protein-fishing' and understanding of their function in a subsequent Human Proteome Project, which, to date, discovered ~20.350 protein entries based on transcriptional and translational levels encoded in human genome. The studies focused on the characterisation of new proteins are more complex since proteins may have cell-specific expression. Therefore we still lack the evidence for about 20% of putative proteins encoded in our genome up today ("Nextprot database," 2020). Even more, we are far from understanding the detailed function of majority of already discovered proteins.

Many proteins serve as one of the basic building blocks in our bodies (the others are lipids, sugars and nucleic acids). But proteins function also as enzymes, signal transducers, transporters, mechano-sensors, or have any adaptor-like functions. All proteins can be formally divided into the main three categories derived from their tertiary structure: globular proteins, fibrous proteins and membrane proteins (Andreeva *et al.*, 2014).

The extracellular fibrous proteins build scaffolds and the physical support of the multicellular organisms in the form of the dynamic, three-dimensional extracellular matrix (ECM) mostly composed of collagens, proteoglycans, elastins, fibronectins and various other glycoproteins. The ECM is directly associated with plasma membrane proteins and can regulate diverse cellular functions such as survival, growth, migration and differentiation. Moreover, close contact with proteins of the ECM is essential for maintaining regular cell homeostasis (Theocharis *et al.*, 2016).

The intracellular fibrous proteins involved in shaping of the cells are mainly connected to the cytoskeleton structures: microtubules, actin network and intermediate filaments mash. Again, in addition to the structural role, they are often directly involved in many essential cellular processes.

In addition, the overall vitality of multi-/single-cellular organisms depends on the activity of soluble globular proteins and membrane proteins, which will be described in more details in the following sections. Soluble proteins are primarily responsible for the fundamental cellular processes, such as metabolism, DNA replication, RNA transcription and protein translation, transfer of signals, degradative processes and many others. Some of these proteins are responsible for the recognition and transport of small-molecule metabolites and nutrients. Others bind secondary messengers carrying information to the specific parts of the cell or between the tissues in the body that can be quite distant from each other (Lodish *et al.*, 2016; Voet and Voet, 2011).

Transport of molecules and information across the membranes is ensured by membrane proteins with different structure and geometry. This structural diversity is caused by a large variety of nutrients and signals, which are required for a normal function of cells and organisms. The final geometry of these functional units is often accomplished by the assembly of proteins into multimolecular complexes with lipids, sugars and nucleic acids. Such complexity has high demands on adaptability of all components and needs a precise control. Unfortunately, it is prone to abnormalities, which may in higher vertebrates cause diseases (Dobson, 1999; Knowles *et al.*, 2014).

The onset of diseases is usually triggered by injuries, infections, genetic predispositions (congenital mutations) and/or unhealthy lifestyle. The latter case is to date the least understood, even though it plays an increasing role in the global causes of human deaths ("WHO statistics," 2018). Although the genetic predispositions can accelerate the non-communicable diseases, the environment and lifestyle remain the critical and often decisive factors for these cases.

Next-Generation Sequencing nowadays provides a rapid method to link genetic changes with specific diseases. On the other hand, our options to track the effect of the environment and lifestyle remain inadequate, partially due to the limitations of applied technologies which are capable to monitor physiological changes in living organisms (including humans). Additionally, these factors affect the human being at various levels: clinical, psychological, biochemical etc, but the impact is not understood properly yet. Among the recently described abnormalities connected to the unhealthy environment and lifestyle at the cellular level are most pronounced the reduced protective capacity of mitochondria, oxidative stress or altered proteostasis (Aon *et al.*, 2015; Labbadia and Morimoto, 2015; Morimoto and Cuervo, 2014; Radak *et al.*, 2005; Videla *et al.*, 2004). All these appointed abnormalities are probably caused by altered protein structure (misfolding or a higher-order disorganisation) or inappropriate protein localisation. They can be also a consequence of such a phenomena because the evidence for genetic mutations is usually unconvincing or, in many cases, non-existent.

Since protein localisation connected to the structure was at the centre of my work, these topics will be described in more detail in the following chapters, with a special focus on membrane proteins.

1.1 Protein structure and organisation

Protein structure is defined by the combination of its primary amino acid sequence and interactions with small molecule co-factors and interacting partners. Proteins are often forming hetero-/homo-dimmers, oligomers or even larger supramolecular complexes. Such bigger complexes are essential for the cell life. As example microtubule organising centre is responsible for the shape and polarity, mitochondrial electron transport chain produces energy, molecular transport works thanks selective pores and chromatin protects and maintain the genetic information. A common property of these extremely multipart structures is the participation of diverse proteins on their formation/stabilisation and achievement of a desired geometry. Moreover, these assemblies have often a dynamic character. Ions, organic co-factors and other biomolecules like nucleic acids or lipids frequently help to provide the optimal functionality of such complexes.

Membrane proteins are an extraordinary case because they cannot fold into their proper ternary (or quaternary) structures in the absence of a lipid bilayer. Indeed, a specific lipid composition of a membrane can be required for the appropriate protein function (Bernardino de la Serna *et al.*, 2016). In general, proteins can accommodate diverse positions with respect to the membrane lipid bilayer, which led to their arrangement into several different categories. The three mostly accepted membrane protein classifications are listed below.

1.2 Basic classification of membrane proteins

Firstly, membrane proteins can be distinguished based on their association with cellular membranes: i) **integral membrane proteins** containing polypeptide structure(s) anchoring the protein directly into the membrane lipid bilayer and ii) **peripheral membrane proteins** which associate with the surface of cell membranes even though they lack a protein segment passing through the membrane.

1.2.1 Transmembrane proteins

Integral membrane proteins are also often called transmembrane proteins. It is probably the largest group of proteins present in cells as they comprise almost 30% of all proteins encoded by human genome (Almén *et al.*, 2009). This group can be subdivided either by the structure of their transmembrane segments called transmembrane domains (TMD) or by their topology. TMDs of integral proteins can accommodate either an α-helical or a β-sheet structure. Membrane proteins forming a transmembrane β-barrel configuration are a separate group (Khoury *et al.*, 2011; Lodish *et al.*, 2016; von Heijne, 2007). The prevalent group in vertebrates represent proteins anchored in a membrane via α-helical structures. For topological classifications of integral membrane proteins, see section **Two topological classifications of membrane proteins**.

1.2.2 Peripheral membrane proteins

Peripheral proteins lack polypeptide structure which passes through the phospholipid bilayer. Mostly, they have a higher content of α-helix bundles in their structure (von Heijne, 2007). Frequently, due to the missing TMD, peripheral proteins interact with the membrane temporarily. These interactions are driven by ionic (electrostatic) and/or amphipathic interactions with the lipid headgroups and carbonyls, respectively. Another way of interactions is based on direct contact with integral membrane proteins. Proteins can also carry a hydrophobic lipid moiety such as glycosylphosphatidylinositol (GPI) anchor, covalently attached to their structure (Chou and Cai, 2005; Chou and Shen, 2009, 2007; Jung and Jensen, 2006; Spiess, 1995). If there is a need of protein dissociation from the membrane, lipid-anchored proteins require additional enzymatic activity for their removal. On the contrary, a simple change in the ion environment can alter the association of peripheral membrane protein without modifications.

1.2.3 Two topological classifications of membrane proteins

Transmembrane proteins containing α-helical TMD can be classified according to their orientation in the membrane. Because there exist various opinions how to divide membrane proteins into groups, it can be a bit confusing. I've selected the two main approaches of the classification, which are described in more details below.

1.2.3.1 Membrane protein classification based on the pure amphipathic characteric of the protein TMD

Based on the amphipathic character of their TMDs, integral membrane proteins can be subdivided into three different types (see **Figure 1**). **Type I** are single-passing proteins with their N-termini facing into the lumen of intracellular membrane compartments and therefore the outside of a cell at the surface. **Type II** are single-passing proteins with their C-termini facing the outside of the cell and **Type III** are all multi-passing (polytopic) membrane proteins, which usually own several TMDs. Other types group together all peripheral proteins without direct peptide-membrane interactions (Chou and Cai, 2005; Chou and Elrod, 1999).

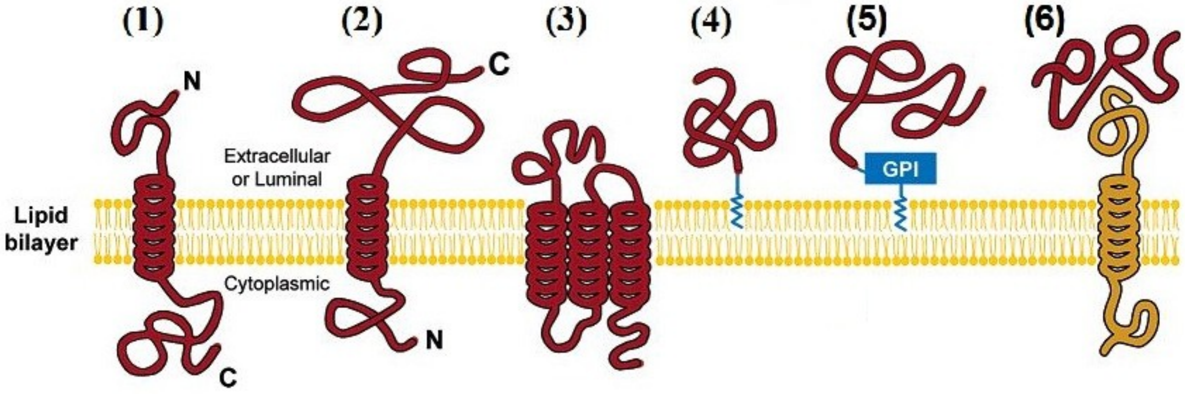

FIGURE 1: Classification of the membrane protein based on amphipathic effect

(1) Type I transmembrane protein with N-terminus facing the outside of a cell; (2) type II transmembrane protein with C-terminus facing the outside of a cell; (3) type III transmembrane protein with two and more transmembrane domains – multispanner; (4, 5, 6) different types of peripheral proteins with no transmembrane domain to anchor the protein to the membrane – alternative membrane-anchoring is used such as lipid anchoring or membrane association via an adaptor protein (adapted from Chou and Cai, 2005).

1.2.3.2 Membrane protein classification according to von Heijne and Gavel (modified)

The second classification system considers the properties of TMD in combination with the features of the surrounding segments (see **Figure 2**). These can additionally influence the insertion of a protein into the membrane. This classification system is nowadays the most accepted in the field of membrane biology. Its current version is an adaptation of the original classification defined by von Heijne and Gravel (Heijne and Gavel, 1988). It distinguishes five groups of integral membrane proteins. **Type I** group are single-passing transmembrane proteins with their N-termini facing out of the cell (or a lumen of intracellular membrane compartments). But their co-translational incorporation is guided by a leader peptide that is cleaved off after successful insertion. **Type II** group are single-passing proteins with their C-termini facing the outside of a cell. **Type III** group are proteins topologically overlapping with the **Type I** proteins, but lacking the leader peptide. Therefore, they are also often called as leaderless. These proteins are inserted according to the unique structure and sequence of the TMD. In addition, their incorporation is not mechanically connected with translation. **Type IV** group are single-passing proteins anchored to the membrane by the α-helical TMD structure at the C-terminus, which is followed by only a very short exterior sequence. Together with **Type II** proteins they do not have any signal peptides. They have so called signal anchor sequence at the beginning of the alpha helical TMD structure and are more or less fully translated before their insertion into the membrane. **Type V** are multi-passing (polytopic) proteins which can be also classified as sub-Type I, II, or III according to the orientation of their first translocated TMD and the other types group together all peripheral proteins without direct peptide-membrane interactions (Chou and Shen, 2009, 2007; Spiess, 1995).

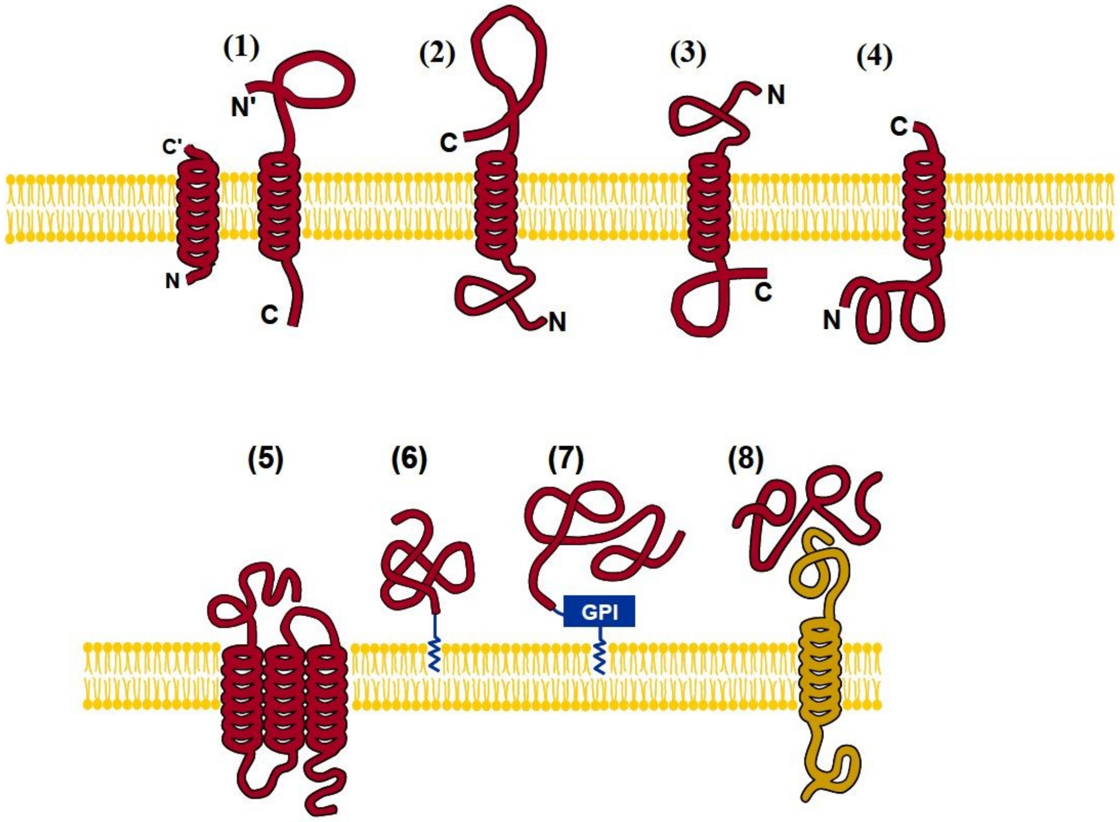

FIGURE 2: Classification of the membrane proteins based on von Heine and Gavel system

(1) Type I transmembrane proteins with signal peptide carrying N-terminus facing out of the cell. The peptide (on the left of the protein) is cleaved off upon the protein insertion into the membrane. The cleavage site is indicated with the endings N' and C'. (2) Type II proteins with C-terminus facing out of the cell. (3) Type III transmembrane proteins with N-terminus facing out of the cell but lacking the signal peptide sequence. These proteins are also called leaderless. (4) Type IV proteins with a very short C-terminus facing out of the cell. (5) Type V multi-spanning transmembrane proteins that can be divided into subtypes according to the orientation of their first TMD. (6, 7, 8) Different types of peripheral proteins lacking any transmembrane domain (see **Figure 1**) (adapted from Chou and Shen 2007).

1.3 Post-translational modifications of membrane proteins

Proteins are synthesized by ribosomes translating diverse mRNAs encoded in chromosomes into polypeptide chains. For the proper folding into fully functional units, several proteins require adaptation of their polypeptide chain by various post-translational modifications. Such modifications can occur either at the side chains of the polypeptide amino acids or at the C- and/or N-terminus. The adjustments dramatically extend the chemical repertoire of the 20 standard amino acids. The novel gained properties open up new avenues for the folding of proteins into three-dimensional (3D) structures or modulate a panel of protein interacting partners, including the involvement of membranes (Khoury *et al.*, 2011; Wold, 1981). There are more than 400 post-translational protein modifications described. Only some of them were identified in membrane proteins, which I will focus on.

Phosphorylation is the most common post-translational modification and, according to the experimental data, the abundance of protein phosphorylation events dominates other modifications by a number of magnitude (Khoury *et al.*, 2011). The best described is phosphorylation of tyrosine, serine and threonine residues (Wold, 1981). Phosphorylation is a reversible modification that often serves as a docking site for specific interacting partners or as a regulatory mechanism for the function of proteins, including membrane proteins (Cohen, 2002; Vlastaridis *et al.*, 2017).

The second most abundant protein post-translational modification is glycosylation that occurs almost exclusively in membrane and secreted proteins. Glycosylation is a covalent binding of a sugar structure to the amino acid side chain of asparagine and serine/threonine residues via N- and O-glycosidic bond, respectively. The prevalent one is N-linked glycosylation which is the most variable protein modification of all post-translational modifications. Protein glycosylation is a stepwise process in which the core structure of N-glycosylation is coupled to a protein during several enzymatic events in the endoplasmic reticulum (ER), while subsequent extensive adaptations take place in the Golgi apparatus. The process of O-glycosylation takes place exclusively in the Golgi apparatus. Both types of glycosylation can be understood as quality checkpoints during protein maturation. Proper glycosylation is important for the folding and secretion (see below) of many eukaryotic glycoproteins and for the formation of the cell-to-cell and cell-to-extracellular matrix connections (Khoury *et al.*, 2011; Maverakis *et al.*, 2015; Wold, 1981). Only the required number of correctly folded and post-translationally modified proteins are delivered to the plasma membrane.

Poly-ubiquitination is also a very common form of reversible protein post-translational modification. Even though it is best known for its function in the protein quality control, it acts also as a factor regulating membrane protein trafficking, sorting, signal transduction or controlling the function of ion channels (Foot *et al.*, 2017). Ubiquitin is a very small protein formed by 76 amino acids with approximately 8 kDa. Its attachment involves glycine residue on ubiquitin and lysine with its ε-amino group on the target protein. Such modification of a plasma membrane protein usually induces its rapid removal from the surface followed by degradation in lysosomes. Similar effects were described for covalent bound of small ubiquitin-like modifier (SUMOylation) and other small-protein modifications of membrane proteins (Czuba *et al.*, 2018).

Another reversible post-translational modification of lysine ε-amino group in membrane proteins can be its acetylation (Lundby *et al.*, 2012). This modification regulates function of several transporters but its general function in membrane proteins still awaits more experimental results (Czuba *et al.*, 2018).

Finally, proteins can be post-translationally modified with binding of hydrophobic lipid groups. Covalent bond of myristoyl, palmitic, prenyl acid residues or addition of the GPI anchor (Jung and Jensen, 2006) modulate local physical protein properties, which can facilitate the localisation of the protein to the membrane. These modifications are all rather common, especially in the peripheral membrane proteins. I will especially focus on S-palmitoylation, effect of which was investigated on several transmembrane proteins during my PhD studies.

1.3.1 Palmitoylation

Covalent S-bond of fully saturated palmitic acid residue ($C_{15}H_{31}COOH$) is quite common post-translational acylation of cystein amino acid residues. Using bioinformatics, over 3 000 human genes was found to encode putative palmitoylated proteins. The search was obstructed by the fact that no consensus palmitoylation motif has been found yet (Zeidman *et al.*, 2009). Nowadays it is generally accepted that the enzymatic transfer of highly hydrophobic palmitate onto cysteine occurs by the DHHC protein family palmitoyl acyl transferases (PAT) (Blaskovic *et al.*, 2013; Roth *et al.*, 2002) (see **Figure 3**). The active site of the enzyme resides at the membrane-cytosol interface, so that cystein residues within CxxC or CxC proximal motifs are candidates for palmitoylation (Lobo, 2013). However, spontaneous palmitoylation of membrane-anchored cysteines was observed in synthetic membranes containing palmitoyl-Coenzym A (CoA) (Quesnel and Silvius, 1994).

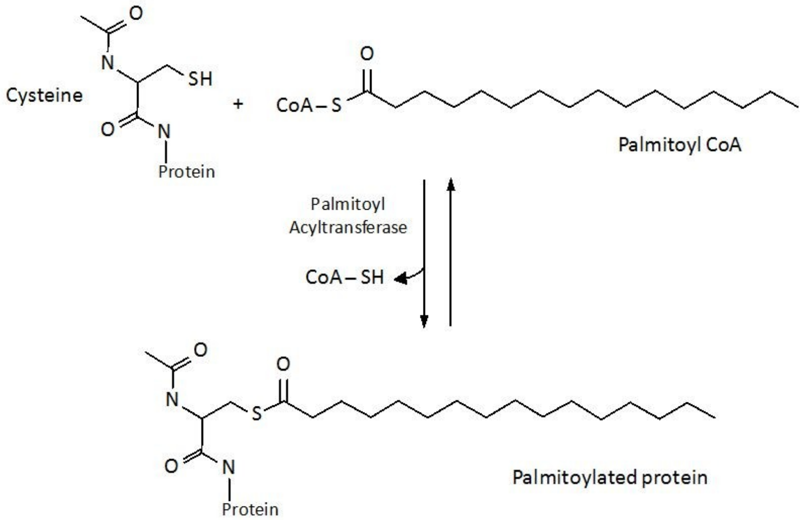

FIGURE 3: Cartoon of the palmitoylation process

Palmitoylation is a two-step process. During the first step, the biologically active palmitoyl-CoA transfers palmitate in the autoacylation reaction to the active site of the DHHC palmitoyl acyltransferase and is released. In the second step the palmitic acid residue is transferred from the active site to the sidechain thiol of a cystein in the proximal sequence of the protein (adopted from Lobo, 2013).

Palmitoylation is the only known reversible post-translational lipid protein modifications. The reverse reaction is carried out by acyl protein thioesterases (APT) (Bijlmakers, 2003, 2009; Blaskovic *et al.*, 2013).

The primary role of palmitoylation described to date is regulation of protein trafficking and localisation (Bijlmakers, 2003; Blaskovic *et al.*, 2014). For example, palmitoylation stabilizes the plasma membrane localisation of many myristoylated or farnesylated proteins which would remain soluble in the absence of additional lipid modification (Rocks *et al.*, 2010). However, palmitoylation can also modify the protein conformation, formation of multimolecular complexes, or it can regulate the efficiency of other post-translational modifications like phosphorylation and ubiquitination (Blaskovic *et al.*, 2013) (see **Figure 4**).

Finally, addition of palmitates to juxtamembrane cysteine residues is also believed to target some proteins to putative sphingolipid- and cholesterol-enriched membrane microdomains, frequently called lipid rafts (Hořejší, 2005, 2004; Hořejší *et al.*, 2010, 2004; Hořejší and Hrdinka, 2014; Levental *et al.*, 2010; Štěpánek *et al.*, 2014). It was further shown that palmitoylation can regulate the plasma membrane localisation of linker of activation of T lymphocytes (LAT), which is an integral membrane protein involved in activation of T cells (Chum *et al.*, 2016; Hundt *et al.*, 2009). This findings were combined into the theory that the ability of a protein to associate with lipid rafts is also a determinant of plasma membrane protein localisation (Diaz-Rohrer *et al.*, 2014; Lorent *et al.*, 2017).

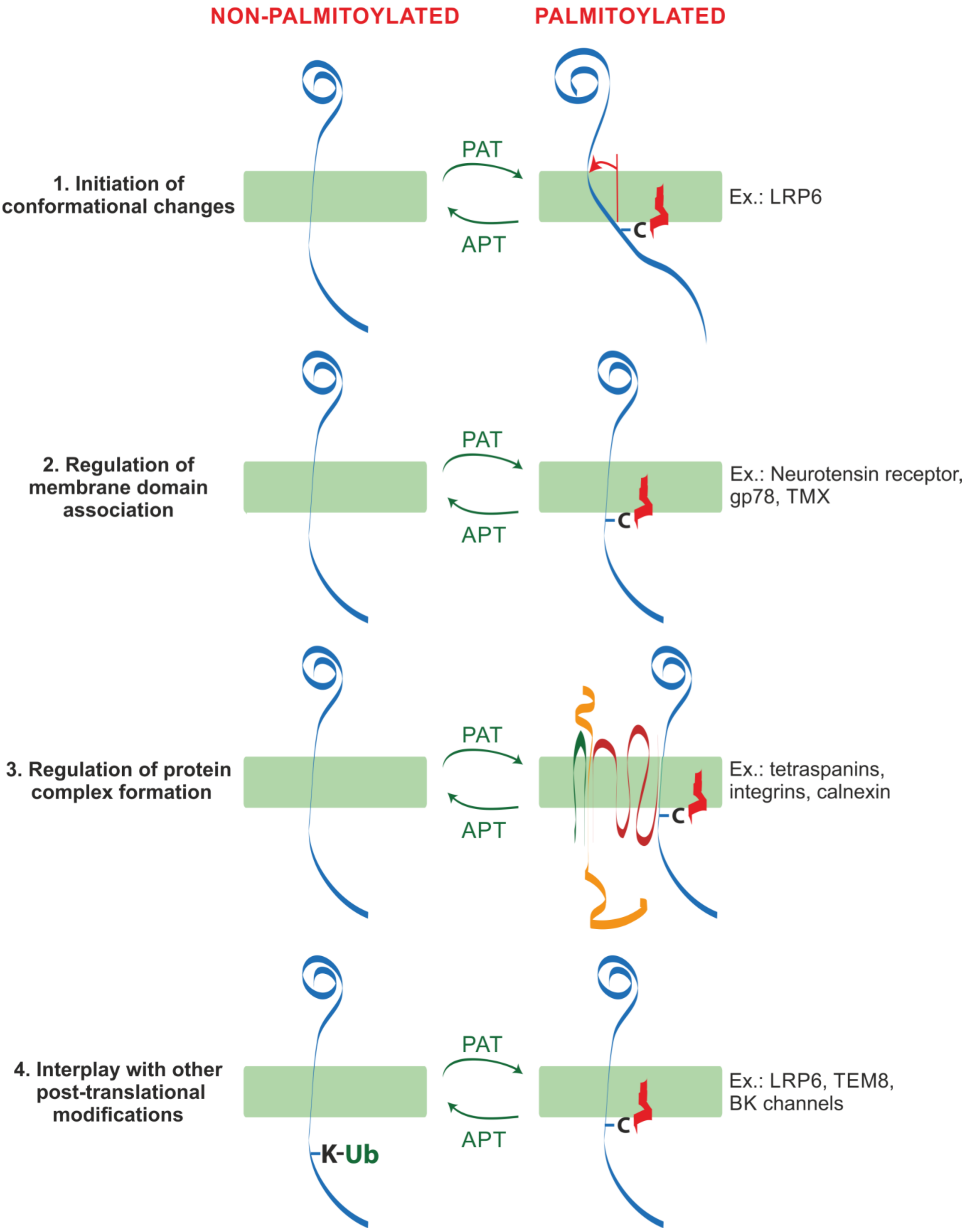

FIGURE 4: Reported functions of palmitoylation of membrane proteins

Palmitoylation of proteins in the proximity of their transmembrane domain (red zig-zag) has been proposed (1) to affect the conformation of their transmembrane domain such as tilting angle; (2) to regulate in a positive, but potentially also in a negative manner their association with lipid rafts; (3) to promote the formation of protein complexes; and (4) to prevent or regulate ubiquitination of lysines in the proximity to the palmitoylation site(s). Examples of each effect are given. These effects do not have to be mutually exclusive and might actually support one another, e.g. tilting of the transmembrane domain could promote its association with another domain, which can reduce its accessibility for an E3 ubiquitin ligase and/or promote its association with other proteins. PAT states for DHHC palmitoyltransferases and APT for acyl-protein thioesterases (adapted from Blaskovic *et al.*, 2013).

1.4 Protein localisation

As mentioned above, besides the chemical structure, topology and function, proteins are regulated by their localisation. For example, some soluble proteins can shuttle between cytosol and the cell nucleus and perform diverse functions in the both compartments. Src-family kinases can relocalise to the plasma membrane after palmitoylation (Rocks *et al.*, 2005; Zlatkine *et al.*, 1997). This way or by other lipid post-translational modifications, they are delivered to the places of their action.

In fact, intracellular membrane compartments show high diversity and specialisation, so they require very precise control of membrane composition. Although the mobility of membrane proteins is strongly restricted by the properties of the lipid bilayer, they have to use an efficient mechanism for targeting into compartments associated with their function (see below). Additionally, proteins have to localise to their appropriate functional sites within a multicellular organism. This can be achieved by a specific gene expression but often proteins are delivered to these places after secretion and directed (or not) diffusion through an organism. Mislocalisation of proteins can lead to their malfunction or loss of function. Such phenomena often cause diseases. And reversely, some phenotypes associated with diseases can influence the localisation of some proteins (Hung and Link, 2011; Lee *et al.*, 2013; Wang and Li, 2014).

During my PhD I was focused on study of the impact of the TMD structure on trafficking and final localisation of plasma membrane proteins. The following text summarises the available literature on these events.

1.5 Membrane protein sorting

Transmembrane proteins are synthesised at the rough endoplasmic reticulum. Preferentially, such proteins are inserted into the phospholipid bilayer during translation. When post-translationally modified and properly folded, they have to get to the place of their action (Khoury *et al.*, 2011; Lodish *et al.*, 2016; Maverakis *et al.*, 2015; Voet and Voet, 2011). This is carried out by a number of trafficking routes. Most commonly used is the intracellular exocytic machinery that is responsible for targeting of proteins to the plasma membrane and for the protein secretion (see **Figure 5**).

This machinery is also called **membrane protein sorting** and is responsible for the directed protein trafficking but also for checking the quality of transported proteins. There are many quality checkpoints on the exocytic pathway. Protein quality control is based on its tertiary/quaternary structure and on its post-translational modifications, especially glycosylation.

First check occurs already in the rough ER, where the formation of proper disulphide bonds is verified. Protein interactions with ions and core N-glycosylation take place also in the ER. Further checkpoints are in the Golgi apparatus. Proteins also undergo extensive N- and O-glycosylation there. Proteins with inappropriate folding or glycosylation are tagged for re-processing or degradation (Chen *et al.*, 2020; Goder and Melero, 2011; McCaffrey and Braakman, 2016; Proszynski *et al.*, 2004).

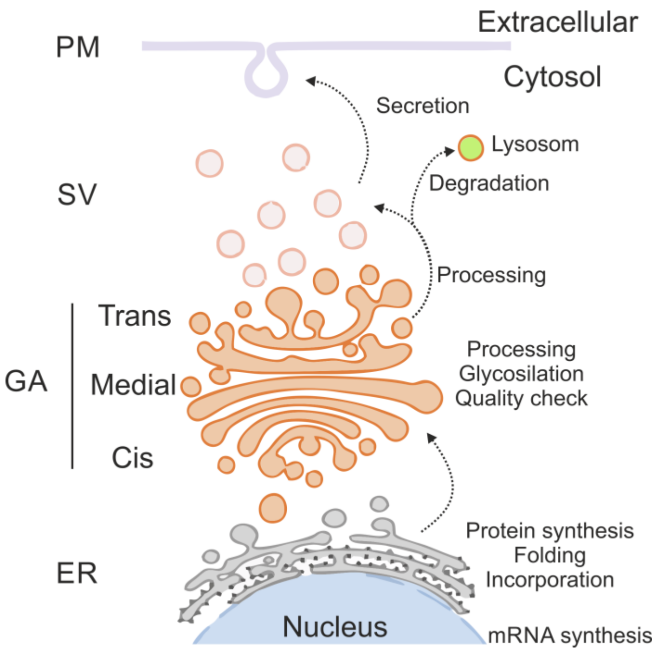

FIGURE 5: Scheme of a general exocytotic pathway used by integral membrane proteins

Membrane proteins are translated from mRNA by ribosomes at the rough endoplasmic reticulum (ER). Proteins are folded and incorporated into the phospholipid bilayer there. They further continue to the Golgi apparatus (GA), where most of secreted proteins undergo complex glycosylation and quality checks. Properly folded proteins are transferred via secretory vesicles (SV) from the trans-Golgi network to the plasma membrane (PM). After a fusion of vesicles with the PM, the luminal side of integral membrane proteins is facing the extracellular space. Incorrectly folded/matured proteins are sent for controlled degradation to lysosomes.

Both the ER and Golgi apparatus are discontinuous membrane structures. Properly folded proteins leave the ER towards the Golgi apparatus through ER-Golgi intermediate compartment most often using COP II machinery, or other alternative routes (Behnia and Munro, 2005; Sato and Nakano, 2007; Zanetti *et al.*, 2013). A number of proteins using this route encode in their primary structure combined DxE and YxxΦ motifs (where x is any amino acid, and Ø is a bulky hydrophobic residue), which were described as **ER-exit motifs**. The presence of such a sequence provides comparative advantage for these proteins to be exported from the ER (Chum *et al.*, 2016; Giraudo and Maccioni, 2003; Sato and Nakano, 2007; Spear *et al.*, 2015). Similar simple amino acid sequence KDEL is described to help proteins to return back into the ER (Traub, 2009). However, no such a simple amino acid pattern directing proteins from the Golgi apparatus to the *trans*-Golgi network and to the plasma membrane was found to date. It is the quality of protein folding and, especially, of its glycosylation, which allows proteins to leave the Golgi apparatus and targets them to other cell compartments (Fiedler and Simons, 1995; Proszynski *et al.*, 2004).

In addition to post-translational modifications affecting the protein structure, there are other 'softer/secondary' sorting signals that regulate the transport of membrane proteins towards the plasma membrane. The best described soft sorting signal in membrane proteins is the length of their TMD. In the hydrophobic mismatch theory, it has been shown that the length of the protein TMD must correspond to the thickness of the phospholipid bilayer in the target compartment (Bretscher and Munro, 1993; Sharpe *et al.*, 2010). The thickness of the hydrophobic part of cellular membranes increases from the ER through the Golgi apparatus towards the plasma membrane (Bernardino de la Serna *et al.*, 2016; Cebecauer, 2012; Mitra *et al.*, 2004). As described palmitoylation could serve as the additional secondary signal during the transmembrane protein sorting as well (Chum *et al.*, 2016; Hundt *et al.*, 2009).

However, the ability of proteins to occupy diverse regions does not finish with the export from the Golgi apparatus. Majority of proteins leaving the Golgi apparatus is targeted to the plasma membrane or is secreted. Only a small fraction of proteins remains trapped in the *trans*-Golgi network to fulfil their function there (Proszynski *et al.*, 2004). Moreover, proteins localised to the plasma membrane are not distributed randomly. In fact, such proteins often clusters together to form higher order structures. The mechanisms behind such assemblies are known for some, but not all, proteins. Before naming some of the main mechanisms responsible for the organisation of proteins on the plasma membrane, it is important to describe briefly the structure and topography of the plasma membrane, which is common for a majority of mammalian cells.

1.6 A brief insight into the topography of the plasma membrane (surface of T cells)

Cell surface is usually illustrated as a flat feature (as shown on **Figure 6**). Sometimes, few bigger structures representing cilia, filopodia or lamellipodia are extending from the generally flat surface of illustrated cells. Unfortunately, this simplistic model have got standardised not only in the textbooks, but also in the scientific community studying the biological and biophysical properties of the plasma membrane and associated processes in various vertebrate cells (Levental *et al.*, 2010; Sevcsik *et al.*, 2015; Sezgin *et al.*, 2015).

FIGURE 6: Animal cell: A typical textbook illustration

The plasma membrane of animal cells is for simplification drawn as a featureless structure. No surface membrane morphology is usually provided. Intracellular compartments are described on margins.

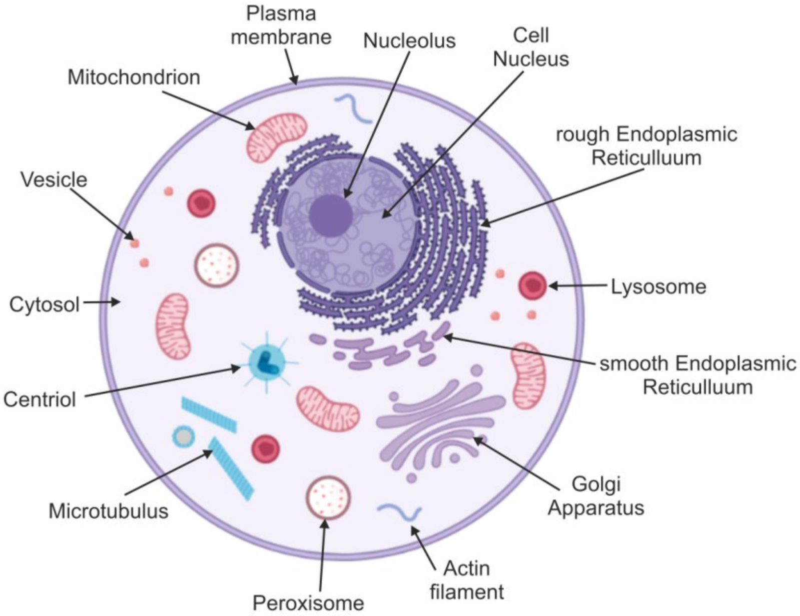

However, several reports, mostly based on the use of electron microscopy (EM) techniques, have shown that this simplified view of the cell surface is misleading (Fisher *et al.*, 2008; Gan and Jensen, 2012; Jung *et al.*, 2016; Kim *et al.*, 2018; Millington *et al.*, 1969). For example, the image from scaning electron microscope (SEM) of a primary T cell (see **Figure 7**) demonstrates the presence of numerous tiny protrusions on the surface of this cell. This indicates that the morphology of the cell surface, including the plasma membrane, can be much more complex. There is nowadays strong evidence that differentiated vertebrate cells are densely covered with numerous protrusions and invaginations exhibiting diverse physical and biochemical properties (**Figure 7**) (Fisher *et al.*, 2008; Jung *et al.*, 2016; Kim *et al.*, 2018; Lange, 2011; Lange and Gartzke, 2006).

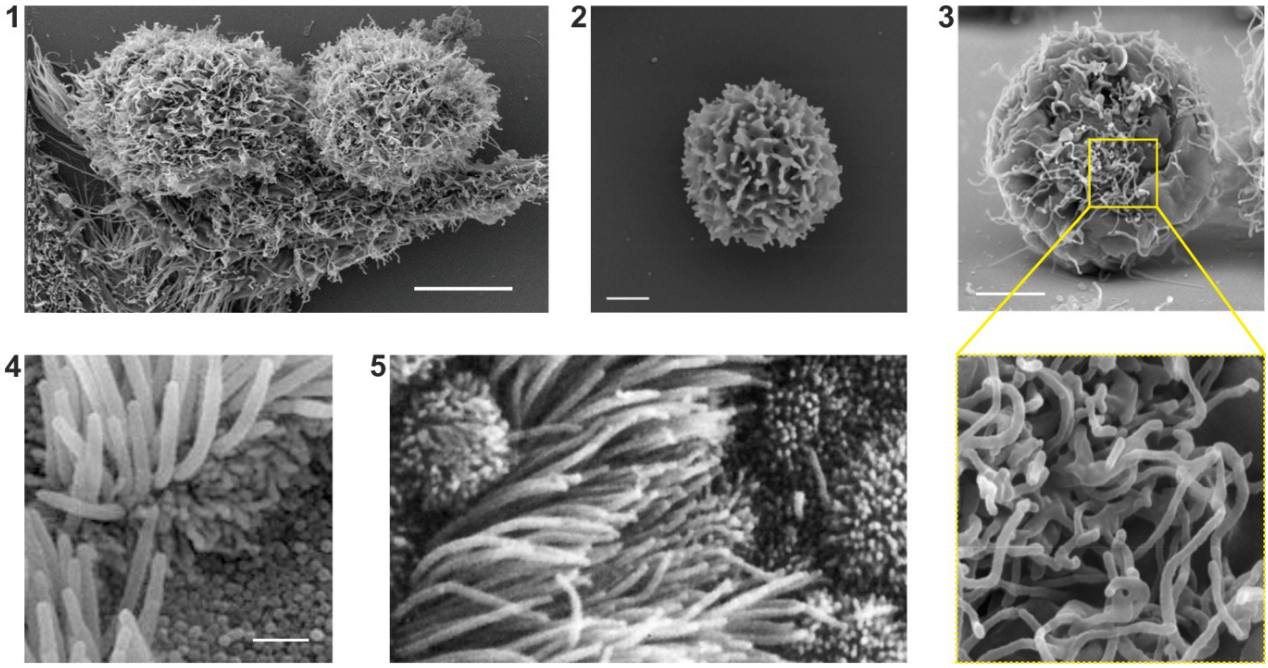

FIGURE 7: Examples of scanning electron micrographs of the surface on diverse human cells

SEM micrograph of (1) cultured HeLa cells with well-detectable complex surface nanomorphology (adopted from Capua *et al.*, 2010), (2) microvilli on the surface of primary resting T cell (adopted from Jung *et al.*, 2016), (3) microvilli on resting Jurkat T cell (a lower panel shows enlarged detail) (adapted from Kim *et al.*, 2018), (4) human bronchiolar epithelium showing cilia surrounded by a cell with a high density of microvilli (adapted from "The naked scientist," 2020), (5) a selected area of the SEM micrograph of the human uterine tube epithelium showing cells with long cilia surrounded by the cells covered with microvilli (adapted from "Embryology," 2020). Scale bars: 5 µm in (1, 3, 4), 1 µm in (2, 5).

The biggest structures are represented mostly by lamellipodia following fillopodia helping the cell during migration, but also big ruffles cover the plasma membrane (**Figure 8**). The most abundant surface protrusions increasing overall surface of the plasma membrane are small finger-like microvilli (see **Figure 8**, **Figure 9**). Additionally, clathrin-coated pits, caveolae and podosomes extend towards the cell interior and represent cell surface invaginations. Even though the potential role of lamellipodium, ruffles, cillium and podosomes in T cell physiology was reported (Nijhara *et al.*, 2004; Sage *et al.*, 2012;

Stephen *et al.*, 2018), microvilli and endocytic pits potentially dominate the effect on surface protein organisation in these cells. This is mainly due to the number of these structures present at the surface (Cai *et al.*, 2017; Compeer *et al.*, 2018; Kim *et al.*, 2018; Lou *et al.*, 2016).

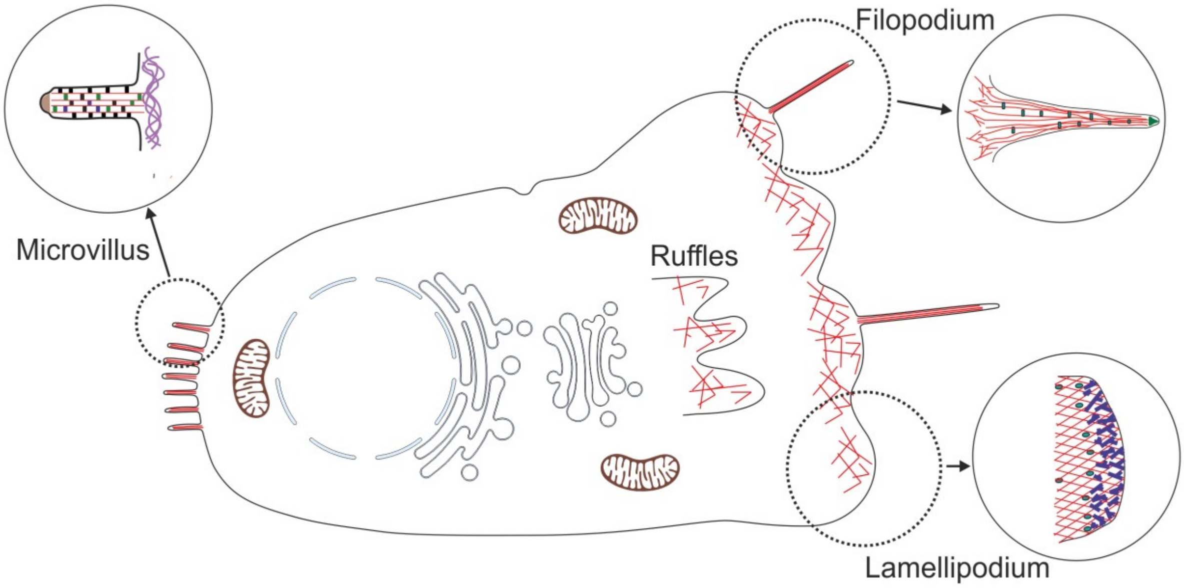

FIGURE 8: Schematic illustration of main plasma membrane morphological structures

Scheme shows main membrane structures responsible for roughness of the cell surface. Filopodia are structures on anterior site of the moving polarized cell supported by disorganized actin bundle-like structures involved in a search for a substrate. Lamellipodia are large plasma membrane protrusions made by dense disorganized actin cytoskeleton. These structures are involved in the to forward-oreinted cell mobility. Ruffles are sheet-like structures on the apical side of the plasma membrane, which are supported by disorganized actin cytoskeleton. Microvilli are finger-like structures made of densely packed actin bundles covering a large part of the cell surface (adapted from Chhabra and Higgs, 2007).

Clathrin-dependent and clathrin-independent endocytosis modulate the accessibility of receptors at the T-cell surface. In general, these processes are associated with the formation of small invaginations (50-200 nm in diameter), which may lead to the formation of endosomes after their maturation and successful fission from the plasma membrane (Lou *et al.*, 2016). These endocytic processes influence the distribution of surface molecules by accumulation and active removal of activated receptors from the surface.

Microvilli are dynamic finger-like protrusions with ~100 nm in diameter and varying length between 0.5-5 μm made of plasma membrane supported by the actin bundles with a half-life of about 10 minutes in cultured cells (see **Figure 8**, **Figure 9**; Gorelik *et al.*, 2003). Surface membrane of the microvillus is tightly connected to the actin bundles via myosins and proteins of the ezrin, radixin, moesin (ERM) family (for more details, see **Figure 9**; Chhabra and Higgs, 2007; Lange, 2011). This rigid structure may cause the same diffusion barrier in longer microvilli as observed in the cilia (Lin *et al.*, 2013). Tips of micro villi have a potential to accumulate membrane receptors in small domains with diameter smaller than 200 nm, which was observed for signalling receptors and ion channels in the epithelial and sensory cells (Lange, 2011). This phenomenon is less well understood in immune cells and more detailed studies are needed.

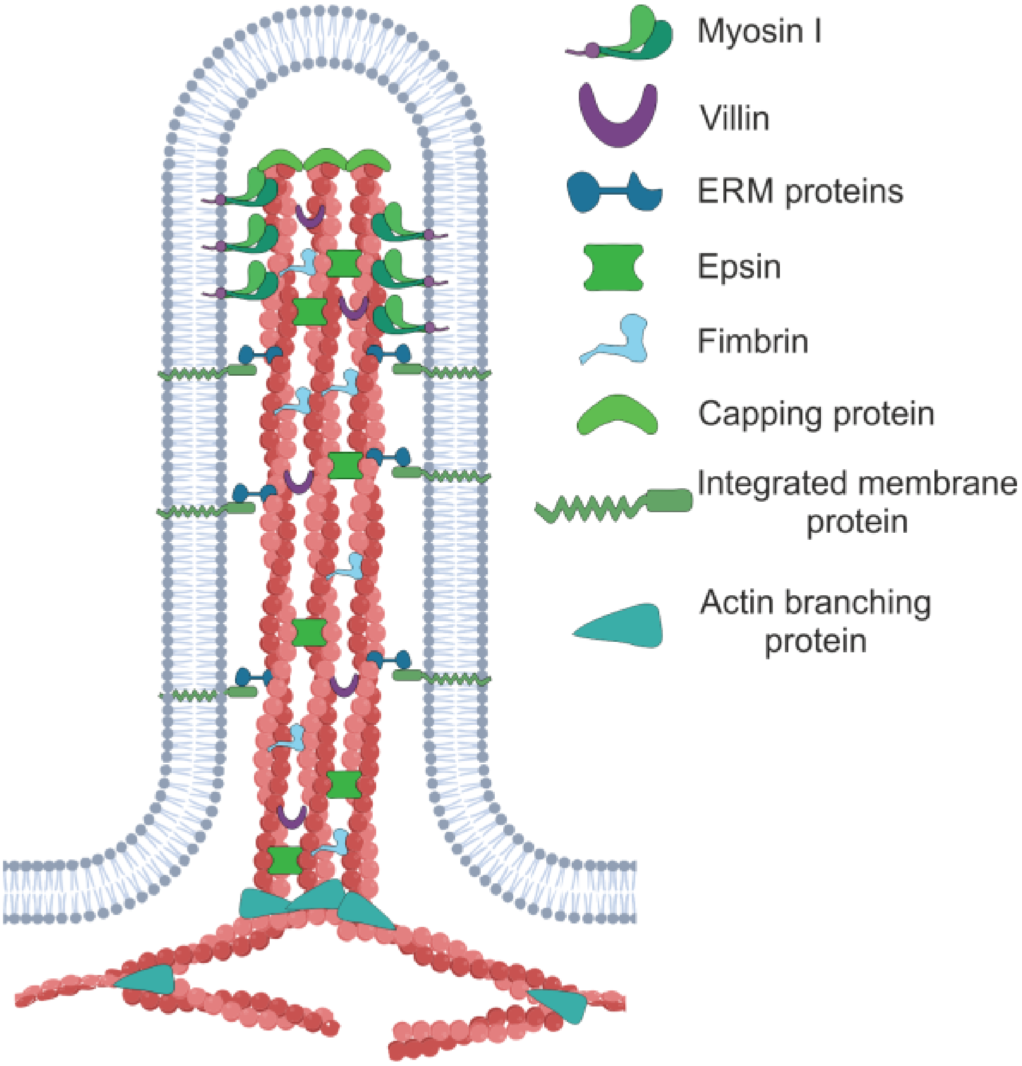

FIGURE 9: ***Inner structure of a microvillus***

Microvillus is a cell protrusion with a diameter of around 100 nm and a varying length of 0.5-5 µm. Microvilli have dynamic character and a complex structure, which is supported by actin bundles tightly connected with several different proteins (villin, epsin, fimbrin etc.). Actin bundles grow from the basal part supported by the cortical actin. Actin bundles in microvilli are directly connected to the plasma membrane via myosin-I or indirectly via ERM proteins interacting with diverse integral membrane proteins. This connection with a membrane and a tight actin bundling generate a diffusion barrier in the microvillar interior that extensively lowers the mobility of molecules from the basal segment towards the tip of the microvillus.

1.7 Organisation of proteins at the plasma membrane of T cells

As mentioned above cell surface morphology is quite complex. Effect of this complexity on protein distribution at the cell surface is totally underestimated except of the endocytic events (Johannes *et al.*, 2015). This is caused mostly due the lack of available methods for the molecular 3D analysis in the cells. Therefore, the available literature on surface protein organisation is dominated by those focused on the impact of the cytoskeleton and membrane lipid composition (Sevcsik and Schütz, 2016; Sezgin *et al.*, 2015). The plasma membrane is underlined by a fine network of cortical cytoskeleton which divides the membrane into small regions with sizes between 50-500 nm. It was shown in the phenomenal works of Akihiro Kusumi and colleagues that protein diffusion in living cells exhibits anomalous behaviour, when proteins diffuse rapidly in a small membrane compartments and only infrequently jump to another one defined by the cortical cytoskeleton (Kusumi *et al.*, 2010, 2005b, 2005a; Kusumi and Suzuki, 2005). This led to the definition of picket-and-fence model of the plasma membrane organisation (see **Figure 10** for more details; Kusumi *et al.*, 2005b).

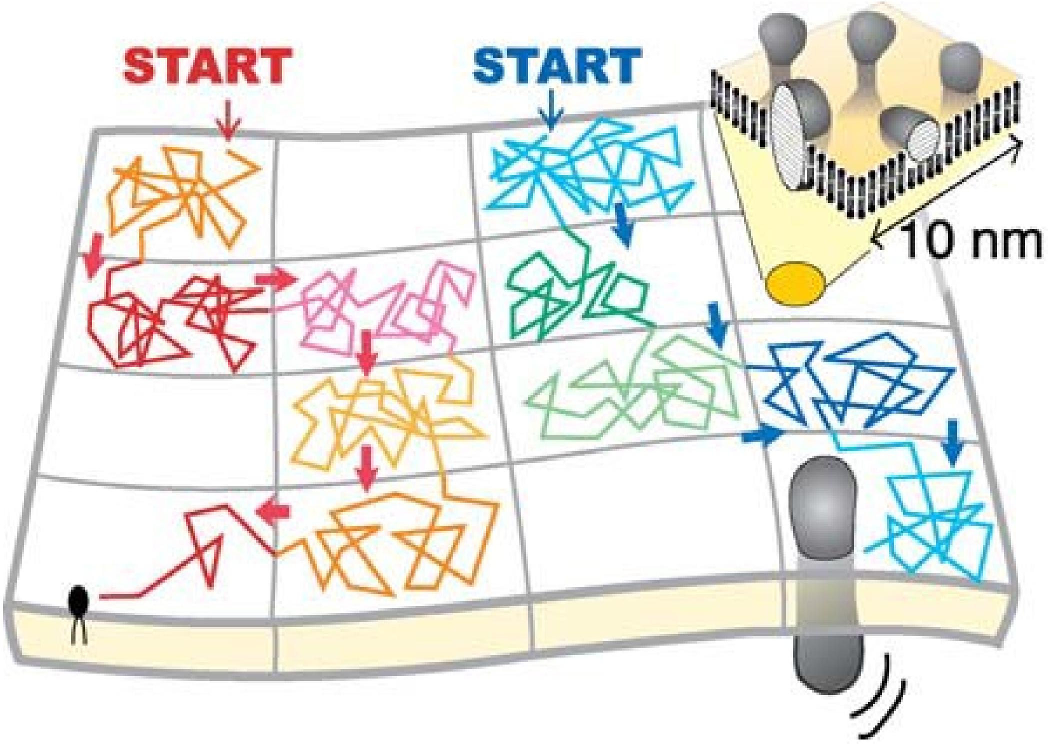

FIGURE 10: Picket-and-fence model of the plasma membrane organisation

The plasma membrane is partitioned into many submicron-sized compartments with regard to the translational diffusion of membrane-incorporated molecules. Many of the molecules undergo macroscopic diffusion by repeating their confinement within a compartment and hopping to an adjacent one. Within the limited area of 10 nm (inset), the original two-dimensional fluid model of Singer & Nicolson is still valid (adopted from Kusumi *et al.*, 2005b).

In addition, many proteins, such as spectrin, anchor the cellular cytoskeletal framework to the plasma membrane. These proteins and their associated structures contribute to the compartmentalisation of membrane proteins (Bernardino de la Serna *et al.*, 2016). An elegant example of a cytoskeleton-driven large membrane protein assembly are focal adhesions (Bertocchi *et al.*, 2017). Their tight connection to the actin cytoskeleton leads to a reduced local diffusion of membrane components, followed by the assembly of highly immobile structure. The size and low diffusibility of focal adhesions and spectrin compartments further influences the free molecules in their neighbourhood due to the obstacle effect (Saxton, 1987) and the roughness of the surface of protein TMDs (Olšinová *et al.*, 2018).

Whereas the impact of cytoskeleton on membrane protein organisation can be directly visualised, only a few works managed to observe similar effect based on a specific local membrane lipid composition, such as presence of phosphoinositides (Fairn *et al.*, 2011; Yeung *et al.*, 2008). Most of the lipid-based membrane organisation models, like existence of lipid rafts or mattress model, were defined on the biophysical data from synthetic or cell-derived model membranes. Comparable experiments on cells were only done after treatment with various small-molecule agent (Bernardino de la Serna *et al.*, 2016; Diaz-Rohrer *et al.*, 2014; Levental *et al.*, 2010; Sezgin *et al.*, 2015). It is generally accepted today that the overly complex lipid composition is distributed in cellular membranes non-homogenously (Almén *et al.*, 2009; Ariöz, 2014; Bernardino de la Serna *et al.*, 2016; Cebecauer *et al.*, 2018).

This applies to the lateral distribution of phospholipids, but also to the different composition of the two leaflets of the plasma membrane bilayer. In addition biophysical data indicate that membrane curvature affect the distribution of proteins and lipids in model membranes and therefore increase the complexity of the whole system (Beber *et al.*, 2019; Johannes *et al.*, 2015; Pezeshkian *et al.*, 2017; Saletti *et al.*, 2017). But little is known about how the bending influences the overall inhomogenous nature.

How membrane properties, including its nanotopography, influence the dynamic organisation of surface receptors regulating function of immune cells are the main questions in the Laboratory of Membrane Physical Biology. Some of these aspects were investigated with implementation of several advanced imaging techniques in our laboratory.

1.8 How to study cellular proteins

Even though proteins were experimentally approached already in antiquity (e.g., by Gaius Plinius Secundus of the early Roman Empire in the 1st century AD), any protein structure represented by amino acid sequence was not published until the middle of the 20th century AD (Sanger and Thompson, 1953; Sanger and Tuppy, 1951). Later, the X-ray crystallography provided insight into the 3D structure of myoglobin at the atomistic level (Kendrew *et al.*, 1958). This breakthrough discovery was awarded the Nobel Prize in Chemistry 1962 to Max Ferdinand Perutz and John Cowdery Kendrew.

Protein structural 3D studies were dependent on dry crystal production followed by the X-ray analysis until 1985, when the first 3D structure of a small protein in solution was determined by the nuclear magnetic resonance (NMR) spectroscopy (Williamson *et al.*, 1985). Recent computational improvements paved the way to studies of larger proteins or macromolecular complexes.

However, it was the entry of cryo-electron microscopy (cryo-EM) techniques into the field of protein complexes, which enabled characterisation of large, multiprotein structures with a near atomistic precision (Adrian *et al.*, 1984; Musacchio *et al.*, 1999; Stagg *et al.*, 2006) All these methods, X-ray crystallography, NMR spectroscopy and cryo-EM, are physical methods using a beam with a very high energy for studying the biological sample.

Under specific circumstances biochemical assays based on protein electrophoresis followed by immunodetection of proteins and their complexes, can provide the information about the protein amount and its interacting partners. To some extent, it also allow us to localisation in cellular structures (Brdička *et al., 2000*; Brdička *et al.*, 2002; Finco *et al.*, 1998). Nevertheless, biochemical methods cannot provide the information on the properties of proteins at the level of individual molecules and their behaviour in the native environment (living cells or organisms). For such studies the application of light microscopy techniques is required. Further enhancement of nowadays high end microscopy methods involving high quality objectives and detectors sensing single photons can provide details at the single molecule level in the cell. In connection with the hardware evolution, the development of some physical and mathematical tricks led to emergence of new super-resolution imaging science, as will be described in the later sections.

The discovery of a microscope was the first step towards the visualisation for a human eye inaccessible biostructures such as cells. The first proper microscope usable for observation of tiny creatures was presented by Antonie van Leeuwenhoek in 1670's (Tunnacliffe and Lapinski, 2003). Since then, the microscopy has undergone a significant evolution. First simple microscopes were using transmitted light. This was a limiting factor for their application in studies focused on specific details of biological samples. Despite the fact that early microscopes were rather simple from today's point of view, they reached quite quickly the diffraction limit of optics at ~250-500 nm as presented by Ernst Abbe in 1873. His postulate says that a maximal achievable resolution corresponds approximately to a half of the used wavelength of light (see **Note 1** for more details; Abbe, 1873).

NOTE 1. ***The maximal resolution***

The term resolution describes the minimum distance between the two separate point objects which can be distinguished by any image-forming device (telescope, microscope, camera, eye etc.). This phenomenon was first described by German physicist Ernst Abbe (1840-1905) and more precisely defined by Lord Rayleigh (born as John William Strutt, 1842-1919). It states that the two point sources of the equal strength are resolved when the principal diffraction maximum of one image coincides with the first minimum of the other one. As illustrated in **Note figure 1**, if the two points are separated by the distance significantly greater than a half of the wavelength of the light, the two points are seen as separate. With the distance getting smaller (closer to the half of the wavelength), the points are gradually merging into one blurred spot with a double the strength of the signal (Rayleigh, 1879). In principle, the maximal achievable resolution is very similar to the half of the wavelength of the used light. This also means that when the light of a shorter wavelength is used, a better maximal resolution can be achieved (Abbe, 1873; Rayleigh, 1879).

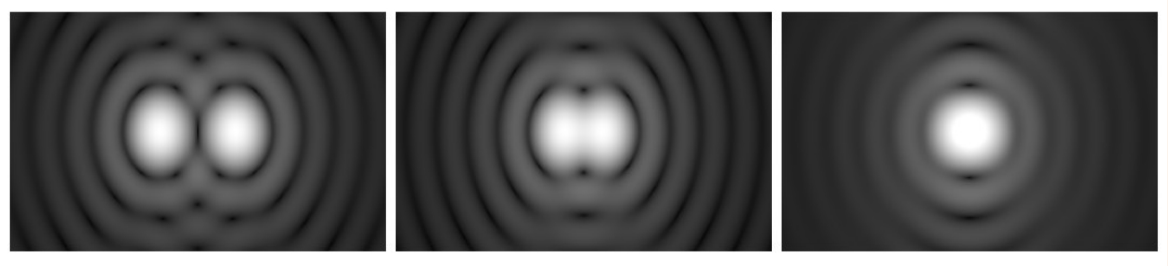

NOTE FIGURE 1: The effect of a distance on resolution of two separated spots

(Adapted from "Angular resolution," 2020)

Throughout the 20th century, the bright-field microscopy has constantly evolved. Bright-field microscope is the simplest microscopy equipment, where the transmitted light coming either from a lamp or reflected day light goes through the whole sample. The sample is enlarged by combination of lenses in the objective and eyepiece, where the biological specimen is observed. Combination of light diffraction and absorption by the sample allows us to see directly the detailed structures. More optical elements were introduced into the illumination and detection paths to achieve a better quality of images; for example: phase contrast, differential interference contrast (DIC; also known as Nomarski interference contrast), interference reflection, dark field etc. (Bradbury and Bracegirdle, 1998). For a long time, the light microscopy was merely used for visualisation of cellular and histological samples. The access to the molecular specificity was limited due the fact that available staining techniques were mainly applied to increase the contrast of the specimen. Only a few chemical staining methods enabled to visualise some definite structures of the biological sample, but they still lack the specificity required for analysis of selected proteins in the cell.

The breakthrough came in 1941 when Albert Coons first applied antibodies to capture specific proteins in a tissue (Coons *et al.*, 1941). The term immunohistochemistry became known and the localisation studies of selected proteins could start. Applied antibodies alone do not provide any additional contrast to the sample, therefore they have to be first chemically labelled to provide specific information. This was first tested by Obermeyer and Pick already in 1906, who chemically modified proteins to alter their properties (in this case antigenicity). Already in 1939, Florence Sabin used proteins modified with coloured chemicals to visualise the position of their binding partners in inoculated rabbits. He expected to find the antibodies binding his stained proteins (Sabin, 1939). Even though, his presented photographs exhibit unbelievable quality, it is obvious that this technique does not provide enough contrast for subcellular localisation of proteins.

Only thanks to the implementation of fluorescence (for more on fluorescence, see **Note 2**) or more precisely fluorescently labelled antibodies (Coons *et al.*, 1941) the way to the new age of microscopy of cells was fully opened. However, the use of labelled antibodies requires fixation of cells and in many cases also their permeabilization. Therefore, application of immunohistochemistry is significantly limited in living cells.

NOTE 2. *Fluorescence*

The term fluorescence describes the ability of particles to absorb light of a particular wavelength followed by release of the surplus energy in the form of light with longer wavelength. It was first described by Sir George G. Stokes in 1852, who showed that a mineral fluorspar emits red light upon the illumination by a UV light (Stokes, 1852). The principle of fluorescence is best explained by Jablonski diagram (**Note figure** 2; Lakowicz, 2006).

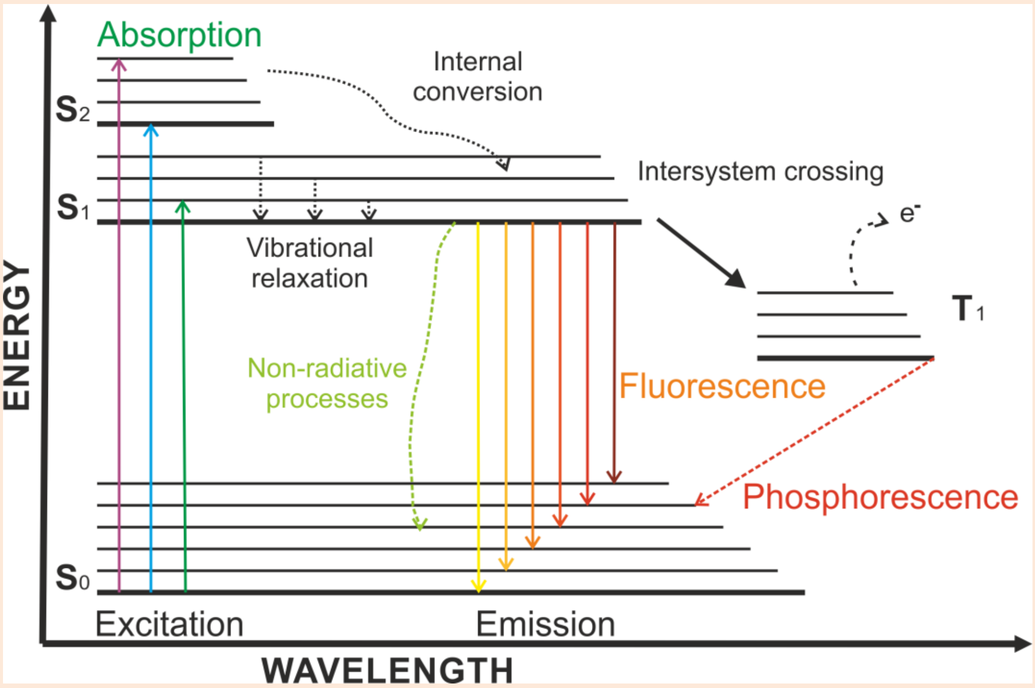

NOTE FIGURE 2: Jablonski diagram

Generally, molecules are at the lowest energy level called ground state S0. When a photon of an appropriate energy hits the molecule (purple, blue and green arrows), it is absorbed, and one electron is excited to a higher electronic singlet states S1, S2. During very fast non-radiative internal conversion and vibrational relaxation it drops to the lowest vibrational level S1 (black doted arrows). From this state the molecule can either undergo a non-radiative release of energy (light green dashed arrow), emit photon during fluorescent radiation (yellow to dark red arrows) or go through an intersystem crossing from excited singlet state to triplet state T1 (black arrow). From the triplet state it can be oxidized by oxidizing agents present in the solution (dashed black arrow), or the electron can get back through slower phosphorescence and emit a photon (red dashed arrow). The red-shift of emitted photons during fluorescence is dependent on the surrounding properties (adapted from Lakowicz, 2006).

For the imaging of living biological objects, probably the biggest breakthrough came in the 1992, when the primary sequence of the green fluorescent protein (GFP) was characterised (Prasher *et al.*, 1992). A couple of years later, the enhanced GFP (eGFP) with improved fluorescence properties was cloned by mutagenesis of the original GFP (Heim *et al.*, 1995). The availability of eGFP and genetic engineering techniques opened the path to study individual proteins in living cells (for more on fluorescent proteins and fluorescent organic dyes, see **Note 3**).

Note 3. *Labels used in fluorescence microscopy*

Chromophores including fluorophores are fluorescent compounds that can release light upon the excitation (see principles of the fluorescence in **Note 2**). Fluorophores are most often made of several conjugated double (π) bonds mostly building the aromatic groups, which can absorb photon energy and send it back as a lower-energy photon (Lichtman and Conchello, 2005). Organic molecules or fluorescent proteins (see **Note figure 3**), but also nanomaterials as nanodiamonds or quantum-dots (Q-dots) are used for imaging in cell biology. Small molecule fluorescent labels are mainly organic compounds derived from rhodamine, coumarin, cyanine etc. which are attached mostly to the antibody or another binding partner providing molecular specificity.

The other option is to modify the protein of interest directly on the genetic level by its fusion to the green fluorescent protein (or its variants). GFP was discovered in *Aequorea Victoria* already in early 1960's (Shimomura *et al.*, 1962) as a companion of the chemiluminescent protein *aequirin*. GFP was purified and spectroscopically characterised in 1974 (Morise *et al.*, 1974) and its primary sequence was described in 1992 (Prasher *et al.*, 1992). Since this time point, many mutant versions extending the applicability of fluorescent proteins have been obtained. These mutants brought a higher stability, more efficient folding, stronger fluorescence (higher quantum yields), other fluorescence spectra and behaviour etc. (Lambert, 2020).

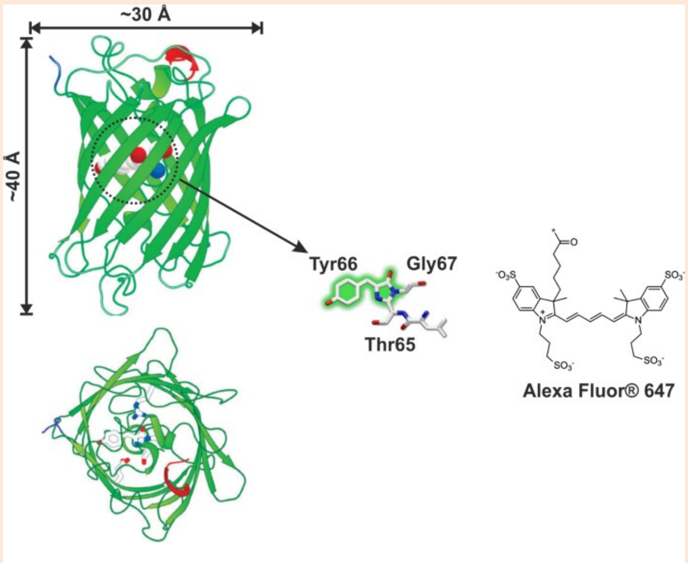

NOTE FIGURE 3: Examples of fluorophores employed in cell biology

Left: Green fluorescent protein from *Aequorea Victoria* that allows direct labelling of proteins using gene-modifying technologies. A side-view with a highlighted fluorophore (dotted circle) enclosed in the β-barrel structure(upper panel). Top-view on the protein with well recognizable fluorophore (lower panel). Middle: Chemical structure of the chromophore (covalently bound Thr65, Tyr66 and Gly67) in the structure of GFP. Right: For a comparison, the chemical structure of an organic dye most often used for dSTORM – Alexa Fluor® 647 (adapted from "Atdbio," 2020; Bullas, 2017; Craggs, 2009).

The new sample preparation using the fluorescent probes enabled to switch from collecting of the scattered light to recording images of light sources representing fluorescently labelled specific structures. The first fluorescence microscope (UV light microscope) was introduced already in 1913. But the difficulties connected to the UV light source made its wider application almost impossible. First fluorescence microscope in the 'modern' configuration, which lasted with small improvements till today, was presented in 1948. Thanks to the implementation of selective dichroic optical filters developed in 1940's, the transmitted excitation light, which was used before, was exchanged for incident excitation illumination coming from the objective (for more details on transmission and epifluorescence microscope see **Note 4**). In 1982, the first laser scanning fluorescent microscope was introduced (Masters, 2010). For more information about the most used microscopy technologies in biology, please see section **Fluorescence microscopy methods**.

Until the development of super-resolution (SR) methods, the fluorescence microscopy techniques were diffraction limited. The maximal achievable resolution of approximately 250 nm did not allow studying proteins at the single molecular level (Betzig *et al.*, 2006; Hell and Wichmann, 1994). The only way how to beat this limit was to use the irradiation source with shorter wavelengths. Because the basic principles of electron microscopy were known since 1930's (Kruger *et al.*, 2000), the EM was used to localise molecules with nanoscopic precision in cells and organisms.

Transmission electron microscope (TEM) uses a beam of high energy electrons with wavelength ~1.23 nm instead of visible light, several hundred times smaller than photons. Therefore, the limiting resolution of TEM is much higher (about single molecules and atoms) than that of an optical microscope. In basics principles, the transmission electron microscope is comparable to the light microscope, where the light beam is focused to the focal plane of the sample. In the case of TEM represented by an ultrathin slice (thickness ~100-200 nm) of the cell or tissue saturated with heavy metal ions lying on a metal grid. Radiated electrons are absorbed and diffracted by high density parts of the sample (containing big amount of metal ions). Accordingly, the acquired image is a negative representation of denser and less dense regions of the sample.

The technique was further developed for scanning and recording of secondary electrons reflected from the gold plated surface of the sample. Scanning electron microscope is able to reproduce the information about the sample topography at nanometer scale (see **Figure 7** for some examples; Von Ardenne and Beischer, 1940). Electron microscopy techniques provide almost atomistic details about biological samples. But it cannot visualise specific proteins efficiently. Firstly, samples have to undergo a rather harsh treatment during the preparation for imaging, when the samples have to be embedded into a hard resin and sliced after the fixation. Secondly, immunohistochemistry has to be applied on these planar and poorly permeable slices. Therefore the sample suffer from the low labelling densities due the imperfect access of labels to the appropriate structures (Franke *et al.*, 2019; Griffiths and Lucocq, 2014; Schwarz and Humbel, 2014).

From the biology point of view, there was a need to combine ultra-structural insight into the cell with the single molecule information. This generated a pressure on the development of light microscopy techniques with resolution surpassing the diffraction limit. Several approaches were suggested during 1980's and 1990's. But the results represented by different super-resolution microscopy techniques became available for biologists since the year 2000 (Betzig *et al.*, 2006; Gustafsson, 2005; Hess *et al.*, 2006; Klar *et al.*, 2000; Rust *et al.*, 2006). The application of super-resolution microscopy opened up possibilities for new discoveries such as the molecular structure of the nuclear pore complex (Dultz and Ellenberg, 2010) or dendritic spine plasticity (Wegner *et al.*, 2018). The distribution of receptors on the surface of immune cells was also investigated using super-resolution microscopy (for example in Lillemeier *et al.*, 2006; Rossboth *et al.*, 2018). These and other works employed usually two-dimensional (2D) methods projecting the space into planar maps (or images). Real 3D super-resolution microscopy methods became broadly available only within the last 2-3 years (as of 2020; including commercial instruments). Further improvements were done also by the development of correlative microscopy methods combining super-resolution techniques with the electron microscopy (super-resolution correlative light electron microscopy; SR-CLEM) (Franke *et al.*, 2019). The most commonly used super-resolution methods are explained into more details in the section **Fluorescence microscopy methods**.

Note 4. *Bright-field vs. epifluorescence microscopy*

Bright-field microscope is the simplest microscopy equipment. It uses the transmitted light (can be formally also called as transmitted light microscopy) going through the specimen. The light is transmitted through the optics of the microscope into the ocular lens in eyepiece, after some portion of it is absorbed or scattered specimen. Therefore the image of the sample finally appears darker than the surrounding brightly illuminated field of view (Bradbury and Bracegirdle, 1998). For the best contrast and illumination homogeneity the proper alignment of the transmitting light and objective in the same path is required (see **Note figure 4**). Nowadays' standard illumination follows the Köhler principle of totally defocused bulb filament with totally focused light beam at the sample plane (Köhler, 1893). As the biological sample lacks high contrast, often additional staining or alternative illumination scheme is required in the bright-field microscopy.

Epifluorescence microscopy uses the incidence light of a selected wavelength going most often through the objective lens (transmission scheme is also possible but used exceptionally). This light activates fluorophores in the specimen. The emitted light is collected by the objective and follows the same path until it hits the dichroic mirror that separates the emission from the excitation. The fluorescence signal is cleaned by additional emission filters blocking the excitation light. The specimen appears then bright in the surrounding black field of view (Rost, 2017).

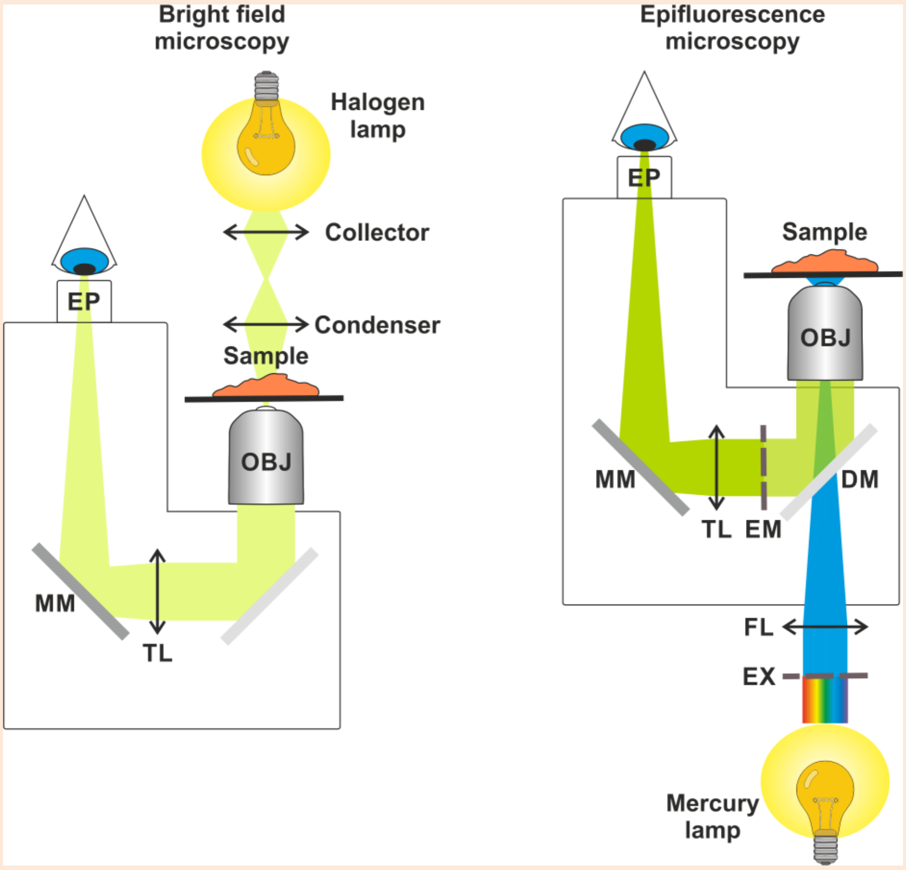

NOTE FIGURE 4: Difference between bright field and epifluorescence microscopy

In the bright-field microscope the transmitted light from halogen lamp is focused into the sample plane by the collector and condenser. The light scattered at the sample is collected by the objective and focused with the tube lens (TL). A set of mirrors (MM) directs the signal towards the eyepieces (EP). Epifluorescence uses for example mercury lamp as a light source. The proper wavelenght selected with the excitation filter (EX) is focused with the focus lens (FL) and objective into the sample plane. Emission light is collected by the objective and separate from excitation light on dichroic mirror (DM). Excitation is additionaly blocked by the emission filter (EM) and follows the path into the eyepiece.

1.9 Fluorescence microscopy methods

There are a number of microscopy techniques, many of which employ fluorescent or phosphorescent molecules and materials. In the following sections, I will briefly describe the two main principles of fluorescence imaging: widefield and confocal microscopy. All four main super-resolution methods are described in the later sections. The chapter is finished with a brief discussion about the axial resolution of super-resolution methods and the available options for 3D super-resolution imaging.

1.9.1 Widefield fluorescence microscopy

Widefield microscopes are the simplest fluorescence microscopes. In microscopy, the rule is that the finest images are obtained when the condenser in the excitation (illumination) path shares the same optical properties with the objective in the emission path – numerical aperture (NA; see **Note 5** for more details) and magnification. This is best achieved when a single objective serves both optical pathways in an epifluorescence mode (See **Note 4** and **Note figure 4**). To evenly distribute the illumination in the entire sample, the excitation light is focused on the back aperture of the objective to be finally spread over the focal plane.

In the standard setups, no spatial barriers are placed within the emission path before a detector. Currently, super-sensitive monochromatic cameras (either complementary metal oxide semiconductor (CMOS) devices with quantum efficiency (QE) higher than 80% or charge coupled devices (CCD) with QE > 95%) are used to collect the emitted light and convert it into electric signals for the computer to be processed into the images. The spectrum of detected light and therefore the 'colour' of the imaged object is defined by the appropriate spectral filter sets and dichroic mirrors. The dichroic mirror separates different spectra with a cut off wavelength into reflected and transmitted paths. Such setup can be used due to the fact that most of the fluorophores exhibit significant Stokes' shift between their excitation and emission spectrum (see **Note 6** for more details).

Due to the implementation of a very few optical elements, widefield microscopy is the most sensitive of fluorescence microscopy methods. It is also amazingly fast as the speed is limited only by the number of emitted photons (brightness of the sample) and the maximal camera frame rate. Current cameras can collect and transfer images within less than a millisecond. On the other hand, the biggest disadvantage of the widefield microscopy is the illumination of the whole sample. Fluorophores located out of focus are therefore excited together with molecules in the focal plane. The acquired image is thus often blurry due the signal coming from the out-of-focus areas.

NOTE 5. *Numerical aperture*

The numerical aperture (NA) of an optical system is a dimensionless number characterising the angular acceptance of the system for incoming light. It is based on geometrical considerations and is thus a theoretical parameter, which is calculated from the optical design. It cannot be directly measured, except in limiting cases with rather large apertures and negligible diffraction effects. NA is mathematically defined as the product of the refractive index of the media, from which the beam enters the system ($\boldsymbol{n}$) and the sine of the maximum ray angle against the optical axis ($\boldsymbol{\alpha}_{(\mathbf{max})}$).

$$NA = n\, sin\alpha(max)$$

For the maximum incidence angle, it is demanded that the light can get through the whole system and not only through an entrance aperture Different light entrance angle of the objective influences its numerical aperture, maximal magnification and also the working distance (see **Note figure 5;** "MicroscopyU," 2020).

It follows from the above equation that the numerical aperture, maximum resolution and brightness of the system also correlate with the light input medium used. **Table 1** shows the refractive indexes for media most often used in microscopy

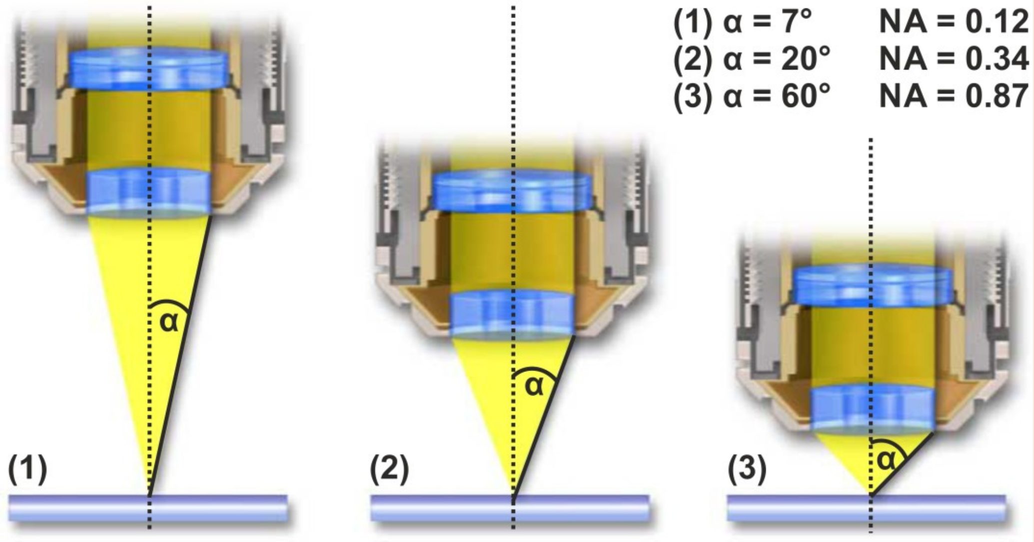

NOTE FIGURE 5: Scheme of the maximal entrance angle and NA of the objective

Adapted from "MicroscopyU," 2020.

TABLE 1: Refractive indexes for different microscopy media

Medium	n	Medium	n
Air	1.00	ProLong®	1.44
Water	1.33	Mowiol®	1.41-1.49
Glycerol 100%	1.47	Cell culture medium	1.31-1.33
Cedar oil	1.51	Glass (borosilicate)	1.47
Commercial Immersion oil	1.51	Glass (soda-lime; crown)	1.51
Vectashield®	1.46	Glass (High precision)	1.52-1.53

NOTE 6. *The Stokes‘ shift*

All fluorophores can be excited with a varying efficiency by the light lying within the full range of wavelengths surrounding the maximum of the excitation spectra (the optimal wavelength of the excitation light). This is due the fact that there exist several vibrational states upon excitation. The emission spectrum of the fluorophore typically mirrors its absorption (excitation) spectrum. Because of the intramolecular transition changes in the excited fluorophore, some excitation energy is released in non-radiational way and the emitted photons have a lower energy, therefore the wavelength(s) is shifted towards higher value(s) (see **Note figure 6**). The difference between the absorption and emission maxima was first described by George Gabriel Stokes. For the fluorescence microscopy, this phenomenon is of utmost importance, since it is easier to exclude (filter out) the excitation light from the collected emission for the fluorophores with a larger Stokes’ shift (Lakowicz, 2006; Stokes, 1852).

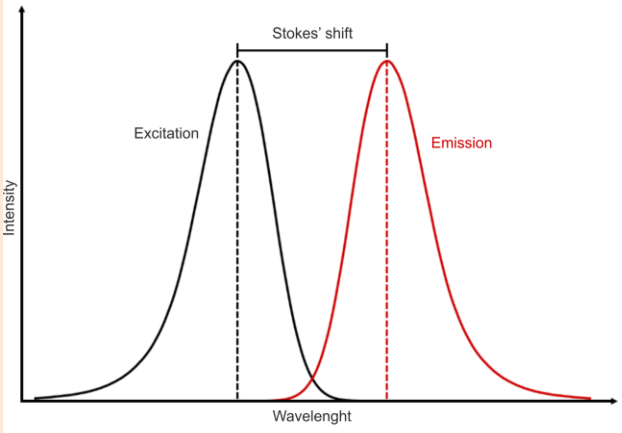

NOTE FIGURE 6: The Stokes' shift diagram

Strong illumination light has to be often applied to excite poor fluorophores. Since a small fraction of the excitation light is reflected through the objective back to the optical path and could interfere with the emission detection, it has to be blocked by additional blocking filters (see **Note 4**). Nowadays the polychromic lamps (mercury or xenon) as the light sources are more often replaced either by modern light emitting diodes (LED) or monochromatic lasers. This upgrade in combination with the up-to-date detectors (see below) allow new specialized applications that require highly controlled illumination conditions like very fast light ‘bursts’.

1.9.2 Laser scanning confocal microscopy

Confocal imaging aims to overcome the limitations of the traditional widefield fluorescence microscopes. There are two main differences between widefield and confocal microscopes.

Firstly, the confocal illuminates a single point instead of the whole sample, because the excitation light is focused into the sample by the objective. Therefore, it is able to illuminate only diffraction limited spot at the sample level (see **Figure 11**). Since lasers are used as a light source, a highly predictable illumination pattern can be achieved in the confocal setup. In the case of pulsed lasers, extremely short bursts of light up to femto-second time-scale can be applied for the illumination.

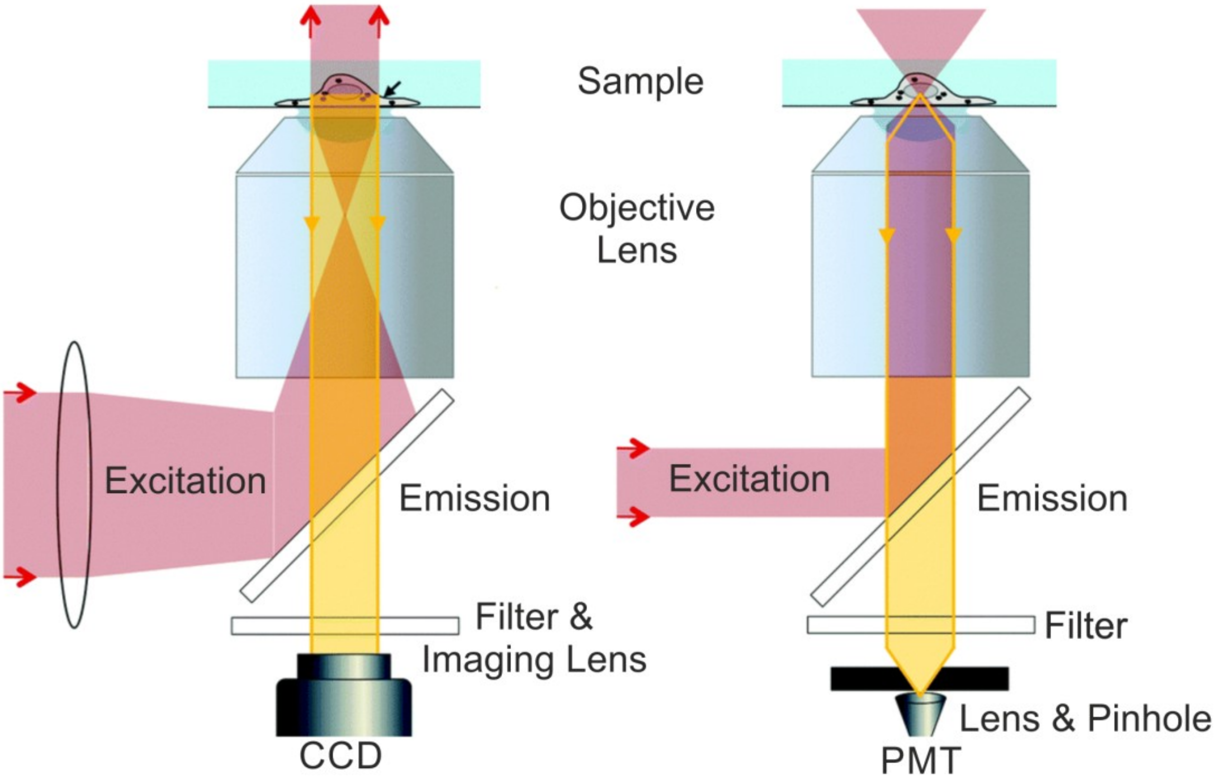

FIGURE 11: Comparison of a widefield and a confocal microscope

The excitation light in the widefield/epifluorescence microscope (left side) is focused on the back-focal plane of the objective. At the sample plane, the light is distributed over the whole sample area which is consequently captured on a camera chip. Since all fluorophores in the whole sample volume are excited simultaneously, the out-of-focus fluorescence is recorded along those from the focal plane in widefield microscopes. The excitation light in the confocal microscope (right side) is focused into the sample plane, where it forms a small excitation spot. Thus, such illumination mode excites fluorophores only in a very small confocal volume. Emission is detected by a photomultiplier tube (or single photon avalanche photodiodes or hybrid detector) positioned behind a pinhole aperture that blocks out-of-focus fluorescence. To acquire an image, moveable mirrors have to scan the object point-by-point to acquire the information about the whole sample (e.g., a cell). Adapted from Park *et al.*, 2015.

Secondly, an emission pinhole aperture is positioned in front of the detector (detection pathway) and blocks a majority of the out-of-focus signal. Such optical setup select only signal coming from the excitation spot. These enhancements improve the optical resolution of the image up to the diffraction limit, but at the cost of losing a large amount of the signal (Pawley, 2006). Confocal microscopes work in so-called point detection mode. Their (dis)advantage is the need of scanning of the sample point by point in a single matrix for 2D or multiple parallel matrixes for 3D imaging. Images are then reconstructed by the post-processing software.

When acquiring the cross-sections, the thickness of final individual focal planes is defined by the wavelength of the light divided by the objective NA and by the optical properties of the specimen. Confocal microscopes, with their ability to apply a thin optical sectioning, provide a direct, non-invasive method for studying biological samples and creating their 3D images (Fellers and Davidson, 2020; Pawley, 2006).

To offset the drop of the signal and the time-demanding scanning process, the emitted light is detected by sensitive and super-fast detectors. Today, simple single point photomultiplier tubes (PMT) with low background and sensitive single photon avalanche photodiodes (SPAD) are replaced by hybrid detectors and detector arrays, which combine the advantages of these two technologies (sensitivity and low background noise). All these detectors have the capacity to sense the single photon impact and convert it into an electrical signal (Fellers and Davidson, 2020).

Even more advanced measurement modalities are possible with contemporary photon detectors and using time-resolved photon counting electronics. Fluorescence lifetime is an intrinsic characteristic of the emitter. It can be regarded as the average time a fluorophore spends in the excited state before it returns to ground state. This quantity is solely determined by the emitter and its environment. It is independent on signal intensity and various emitters can be resolved from each other despite of their overlapping emission spectra (Lakowicz, 2006). Using pulsed excitation light and detecting the precise photon arrival times, it is possible to map the fluorescence lifetime. This is the basis for fluorescence lifetime imaging microscopy (FLIM), a powerful method used for mapping molecular interactions. Especially FLIM in combination with Förster resonance energy transfer (FLIM-FRET), an imaging method that maps the efficiency of FRET, became very popular, because it can be used as a molecular ruler to measure small (< 10 nm) distances between interacting molecules, e.g. to quantify the extent of binding (Algar *et al.*, 2019).

Another confocal measurement technique that has become available due to recent developments in the field of time resolved photon counting is fluorescence correlation spectroscopy (FCS). In this method, the confocal volume is typically stationary, although there are scanning modalities, too. The primary observable is the fluctuation of fluorescence intensity in the confocal volume. The size, mobility, molecular concentration and interactions between molecules can be determined using suitable analysis (Elson, 2011).

These abilities of confocal microscopy were recently expanded by the development of SPAD-detector arrays, which can offer a complex spectral analysis of imaged samples. The implementation of SPAD detectors into camera-like devices (SPAD-CMOS) may, in the future, expand the ability of confocal imaging beyond its current limitations (especially its speed; Castello *et al.*, 2018).

1.9.3 Super-resolution microscopy techniques

Standard fluorescence microscopes are diffraction limited by the nature of light at around the half of the used wavelength. Therefore the minimal distance between two distinguishable imaged spots is within a range of 200-500 nm, as defined by Abbe and Rayleigh (see **Note 1**; Abbe, 1873; Rayleigh, 1879). Using basic microscopy methods described above, it is technically impossible to resolve objects (particles) separated by a distance below this range. However, such distances are quite common in biology. As a result, enormous demand for microscopes with improved resolution stimulated research, which led to the development of super-resolution imaging techniques.

In 1990s' a few concepts were proposed to overcome diffraction limit of fluorescence microscopes (Bradl *et al.*, 1996; Heintzmann and Cremer, 1999; Hell and Wichmann, 1994). It took another decade to convert these principles into microscopes, which can be readily employed for biological research (Betzig *et al.*, 2006; Gustafsson, 2000). The impact of these methods on life sciences is enormous and Eric Betzig, William Esco Moerner and Stefan Hell were awarded the Nobel Prize in Chemistry in 2014 for their achievements during the development of these methods.

There are three basic technically separated super-resolution methods and one based on software implementation (see **Figure 12**). The principle that some fluorophores have to be kept in the non-fluorescent OFF state is the unifying point. Distinct physical, mathematical or combined tricks are applied to achieve this state and subsequently bypass the diffraction limit. In addition, the methods differ in their applicability for specific scientific questions and in their requirements for the system setup and fluorophore properties. In the following sections the basic principles, main applications, advantages and limitations will be described. As well as some new tools further expanding their capabilities in biological or medical research will be mentioned.

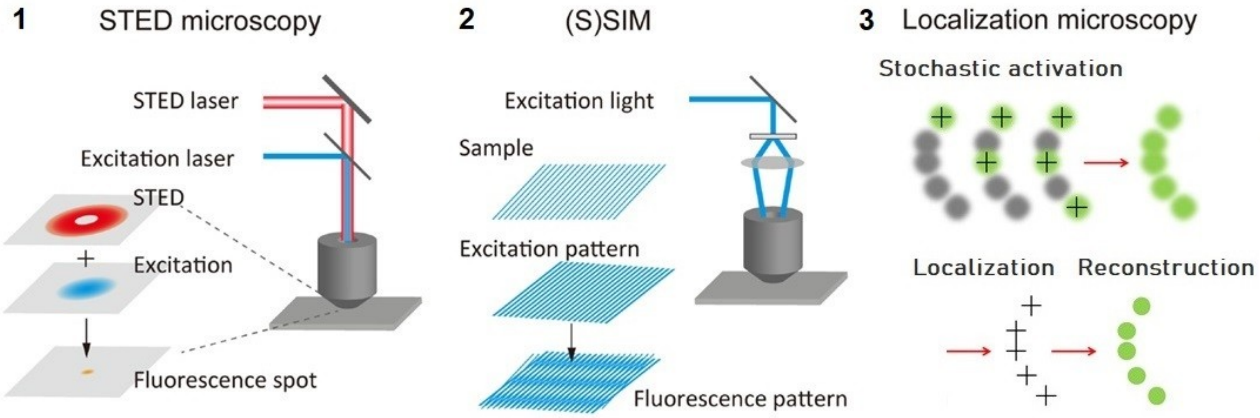

FIGURE 12: Scheme of the principle of main super-resolution microscopy techniques

Cartoons represent the basics of (1) stimulated emission depletion (STED), (2) structured illumination microscopy (SIM), (3) single molecule localisation microscopy. The basic principle of super-resolution optical fluctuation microscopy technically overlaps with localisation microscopy. The difference is the follow up software based analysis of the data acquired in the same way (see below) (adapted from Habuchi, 2014; Ziaowei, 2017).

1.9.3.1 Stimulated emission depletion

Stimulated emission depletion (STED) represents technique based on deterministic non-linear behavior of fluorophores. This approach was invented by Victor Okhonin and put into praxis by Stefan Hell and colleagues. STED is in fact a result of an evolutionary development of the confocal microscope (Hell and Wichmann, 1994; Klar and Hell, 1999; Okhonin, 1991). Confocal microscopes have a slightly better resolution compared to the widefield microscopes, but at the expense of signal loss caused by the pinhole placed in front of the detector (see **Figure 11**; Gu and Sheppard, 1992). Theoretically, lateral resolution of confocal microscopes is almost infinite by applying smaller and smaller pinhole(s) into the emission pathway (Wilson, 1995). Fluorescence emission of a real biological sample is too weak to be further extremely reduced, therefore the only way how to improve resolution is to reduce the excitation confocal volume.

Constraining the space in the sample where fluorophores can emit photons is a basic principle of STED. Fluorophores are excited in a standard way by appropriate laser wavelength corresponding to their excitation spectrum. In parallel, very high intensity depletion light with a wavelength corresponding to the red edge of the emission spectra is applied. The depletion light field surrounds the excitation laser spot in a form of a doughnut (for more details, see **Figure 13**). By means of stimulated emission, the intense depleting light depopulates the ensemble of excited molecules everywhere nearby, except in the very centre of excitation focus volume (Hell and Wichmann, 1994; Müller *et al.*, 2012).

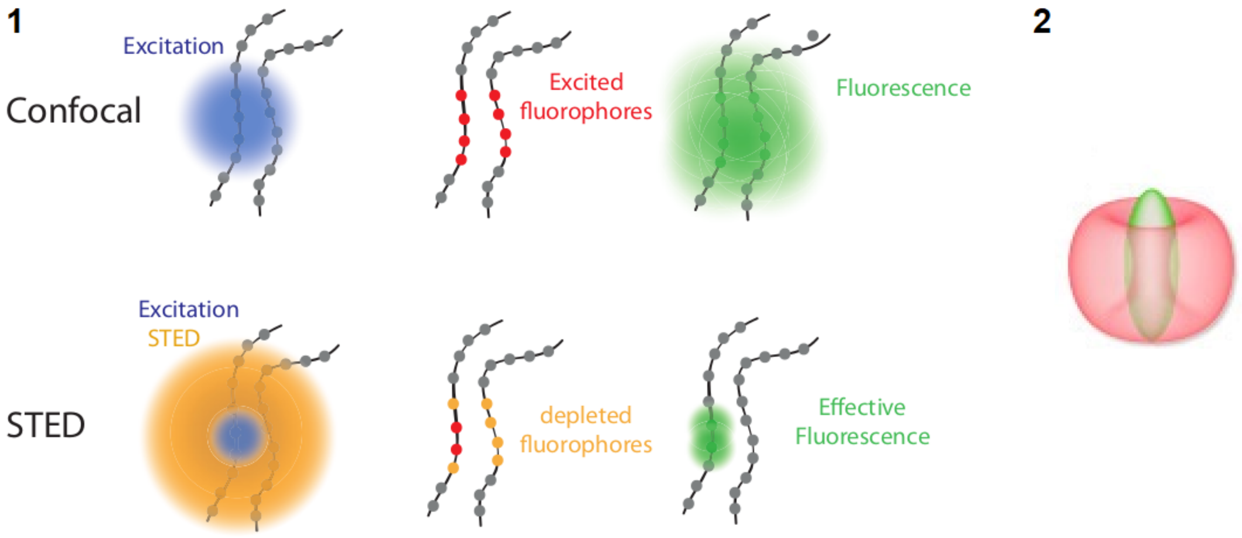

FIGURE 13: Schematic illustration of the STED principle compared to confocal

(1) Two thin wire-like structures are labeled with fluorophores (grey dots). In conventional confocal microscopy most of the fluorophores in the focal region are excited (red) and are able to emit fluorescence resulting in a fuzzy structure in the image. When STED laser illumination is applied, the doughnut shaped beam overlaps the excitation spot in the focal region. Additional energy depletes most of the excited fluorophores in the overlapping region (yellow dots). Only the fluorophores in the centre of the doughnut finally emit fluorescence (green). (2) Rendering of the STED doughnut 3D PSF pattern (adapted from Price and Davidson, 2020; SVI, 2020).

The improved resolution achieved in STED microscopy is typically 30-80 nm, but in theory it can be unlimited as it correlates with the intensity of depletion laser light (Wildanger *et al.*, 2012). In practise, such intensities cannot be used for imaging of biological samples, because the high-intensity light beam causes photo-damage of the biological structures. Moreover, increasing intensity of the used light induces irreversible photobleaching of the fluorophores caused by their oxidation. This is the main limiting factor for the application of several dyes in STED. Therefore the special requirements for the particular fluorophore behaviour led to the development of new dyes for STED.

Firstly, rhodamine B was used in STED experiments (Hell and Wichmann, 1994). However, its application capabilities are weak for imaging complex biological samples. In the literature, 40 different standard fluorescent dyes more or less suitable for single- or multi-colour STED microscopy covering the spectra were described (Müller *et al.*, 2012).

Due to the fact that STED does not require any complex sample preparation, it can be used for imaging of living objects. In past, STED was employed to image structures and processes in living mammalian cells (Hein *et al.*, 2008; Hoopmann *et al.*, 2010; Mueller *et al.*, 2011), living plant cells (Kleine-Vehn *et al.*, 2011) or in complex living tissues (Nagerl and Bonhoeffer, 2010; Rankin *et al.*, 2011; Urban *et al.*, 2011).

To minimize the photodamage of the imaged tissues and bleaching of fluorophores, new variants of STED microscopes equipped with pulsed lasers were developed. These allow either also pulsing of the depletion lasers (pSTED), or set up the time-gating of the fluorescence detection (gSTED) or the application of depletion light only in the regions with high fluorophore density (RESCue) (Vicidomini *et al.*, 2018). All these improvements led to the decrease in the required intensity of depletion lasers and, often consequently, the improved resolution of the method.

1.9.3.2 Structured illumination microscopy

The concept of <u>s</u>tructured <u>i</u>llumination <u>m</u>icroscopy (SIM) can be understood in terms of so-called moiré effect (see **Figure 14** for more details). Multiplicative moiré fringes appear as the product of superposition of two fine patterns with a small angular shift. Unlike STED, SIM uses widefield microscope setup with a line grated mask positioned in the excitation pathway (see **Figure 12** for the comparison). The line scheme is then projected onto the sample with the spacing close to the diffraction limit. SIM uses the well-defined mask introducing structured intensity changes of the illumination light as one of the super-positioned patterns. The second pattern is the unknown spatial distribution of fluorophores in the sample. As a result, the recorded emission figure is a product of the two overlaid patterns with moiré fringes. These moiré fringes are detectable by the microscope even if one or both of the original sources are too fine to be resolved separately. Since the illumination figure is known, the moiré fringes can be used to get the information about the unknown patterning. Thus, under the carefully-controlled illumination scheme, SIM opens access to the high resolution information about the fluorescently labelled shape in the sample (Gustafsson, 2005, 2000).

In order to get an super-resolution image, six to nine images of the same field of view are acquired with the mask being rotated in steps of 60° and 40°(Gustafsson, 2000). These different ‘snapshots’ are then used for image reconstruction by a rather complex mathematical algorithm(s) (Heintzmann, 2010). The most important advantage of SIM is its independence on specific fluorescent dye(s). SIM has relatively fast acquisition rates that are limited only by the amount of photons detected by the camera. Upgrade of setup by the electronic spatial light modulator instead of moveable mask is capable to image fast cellular processes with reasonable high resolution ~100 nm at the frame rate of 162 frame/s (corresponds to 6 ms/frame) (Lu-Walther *et al.*, 2015). The drawback of SIM is the limited improvement of the resolution, which is usually only 1.6-2 times better. As SIM acquistion dramatically improves the signal-to-noise ratio (SNR) of the image, this can be easily further processed using deconvolution approach to get highly appreciated data.

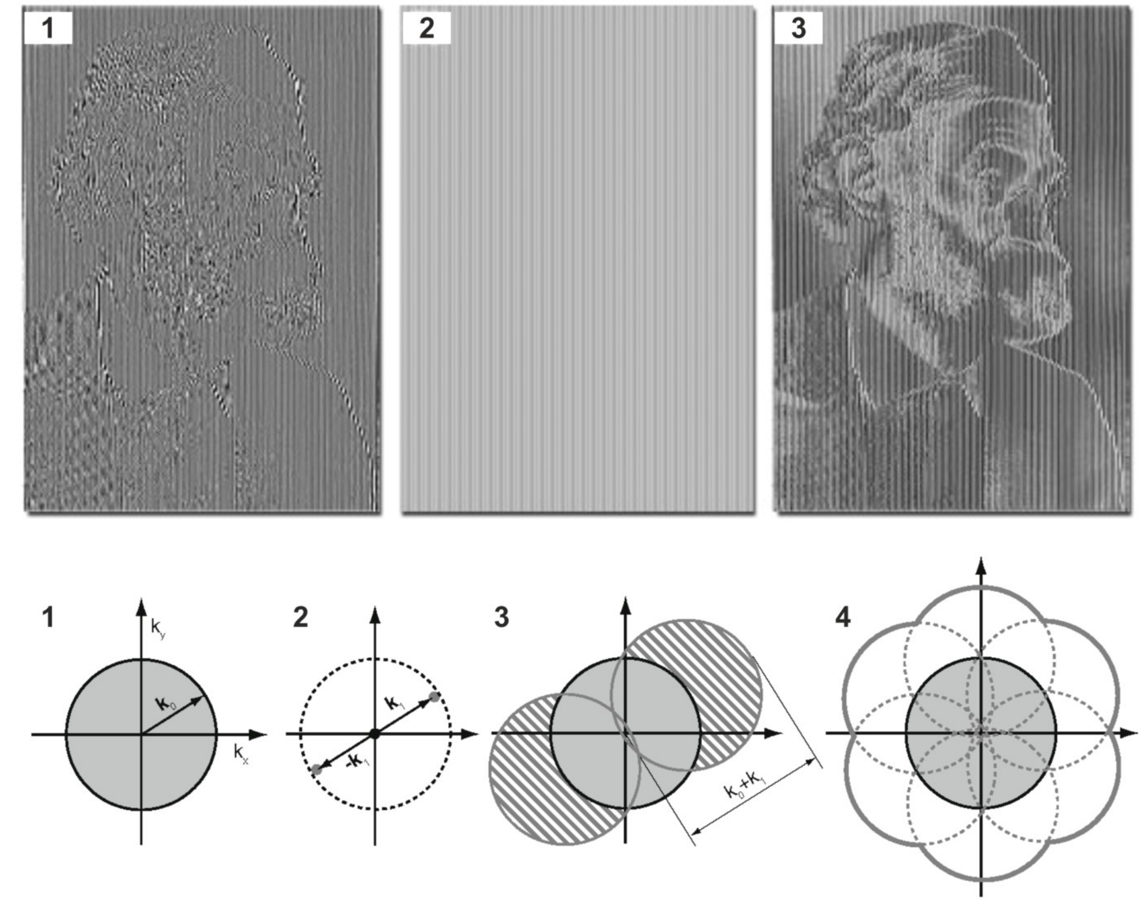

Figure 14: Scheme of the SIM principle

Upper panel shows the principle of visualisation of fine spatial information via moiré fringes. (1) Image consists of fine spatial details. (2) Linear structured mask to be overlaid. (3) Upon mixing those patterns together, the detailed portrait of Ernst Abbe (1840-1905) comes up. Lower panel shows principle of SIM-lateral resolution enhancement. (1) Planar representation of the resolution of the microscope, where the resolution limit (k0) lies at the border. (2) The first order components at the diffraction limit border (k1/-k1) form a line together with the zero order component in the centre. (3) Due to frequency mixing, the observable regions contains, in addition to the normal image of spatial frequencies (centre circle), two new offsets with higher spatial frequencies images (dashed circles) centred on the edges of the original field. These new centres double the final resolution (k0 + k1). (4) Set of images prepared from three phases at 120° orientations, which after processing extend the lateral resolution isotropically (adapted from (Gustafsson *et al.*, 2020).

The new development of SIM microscopes combining the light patterning with light-sheet microscopy (see **Note 7** for more details) is called lattice light sheet structured illumination microscopy (LLS-SIM) (Chen *et al.*, 2014). This combination uses the spatial light modulators to generate diverse non-linear illumination scheme that is introduced throughout the whole sample. LLS-SIM microscopes are probably one of the most promising developments for the imaging of living objects with high resolution and low impact on the studied organisms.

NOTE 7. *Light sheet fluorescence microscopy*

Light sheet fluorescence microscopy (LSFM) is a fluorescence microscopy technique combining an intermediate to high resolution with fine optical sectioning of the sample and very high speed recording. Only a thin slice (usually a few hundred nanometres to a few micrometers) of the sample is illuminated perpendicularly to the direction of observation (for the principle see **Note figure 7**). The sample is trans-illuminated with excitation light focused only in one direction into form of a light sheet. This principle brings very low photo-destruction of the sample and fast acquisition of the whole section in single frame (Olarte *et al.*, 2018). Light sheet microscope combined with spatial light modulators generating diverse non linear patterns throughout the whole sample nowadays opened the paths for higher resolution comparable to structured illumination microscopes and led to development of lattice light sheet SIM (Chen *et al.*, 2014).

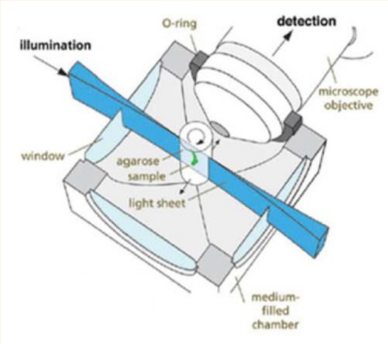

NOTE FIGURE 7: Scheme of the light sheet microscopy principle

Illumination of the sample in the form of thin light sheet is perpendicular to the microscope objective collecting the emitted light. Very often is light microscopy performed in the closed chamber fulfilled with medium (adapted from Olarte *et al.*, 2018).

1.9.3.3 Single molecule localisation microscopy

The ultimate goal of molecular biologists is to observe activity of individual (single) molecules in their native cellular environment. Widefield microscopes equipped with highly sensitive and fast cameras followed by a complex image analysis made this type of biological research possible. Recording and localising of individual fluorophores is the basic principle of single molecule localisation microscopy (SMLM; see **Figure 12** and **Figure 15**).

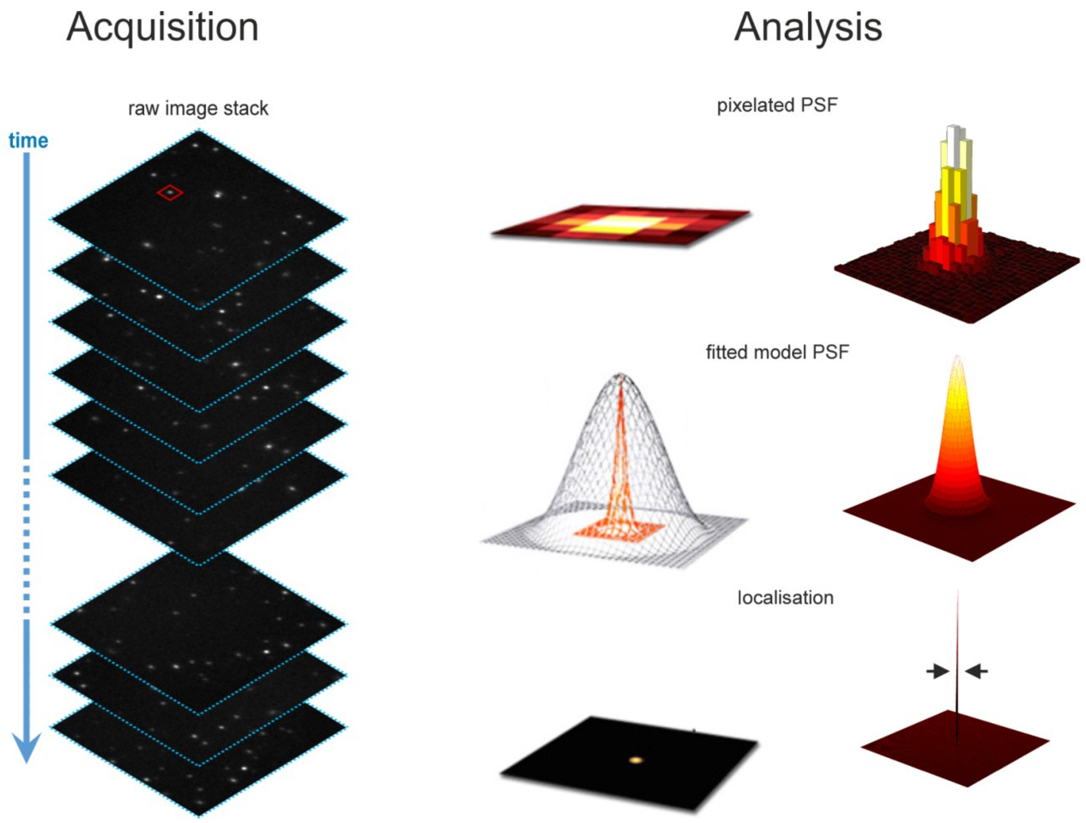

FIGURE 15: Scheme of the SMLM principle

Acquisition of data is represented by a stack of temporally separated snapshots of spatially distributed single emitters. For analysis single emitters are selected from the dataset. Their signal point spread function profile is interpolated as a real Gaussian profile. Original profile is fitted with ideal model point spread function and the centre is analysed concerning the full width at half maximum analysis. After that, the position is found and localized in 2D matrix with very narrow localisation precision (adapted from Franke, 2017).

The first images of immobilised single fluorescent molecules were generated using the near-field scanning optical microscope (NSOM; Betzig and Chichester, 1993). Later, similar results were achieved in the group of Toshio Yanagida using conventional fluorescence microscope, which is more convenient for biological research (Funatsu *et al.*, 1995). Imaging of mobile single molecules (fluorophores) on standard widefield microscope was then achieved by employing fast, liquid nitrogen-cooled CCD camera resulting in an image time of 35 ms/frame (Schmidt *et al.*, 1996). Following analysis of point-spread functions (PSF; see **Note 8** for details) provided localisation precision of 30 nm for individual molecules, about two times lower compared to 14 nm from original NSOM analysis of immobilised molecules (Betzig and Chichester, 1993). The final resolution is seven times better than diffraction limited spot of the utilised optical setup.

NOTE 8. *Point spread function*

Point spread function (PSF) is a physical equation describing the response of an imaging system to a point source of light. More general term is system's impulse response, where the ideal PSF is achieved on the focused optical system (see **Note figure 8**). But in many contexts it can be thought of as extended blob in an image that represents single point source of light. It is a useful concept in Fourier optics, astronomical imaging, medical imaging, electron microscopy as well as fluorescence and 3D microscopy. The degree of spreading of the signal (blurring) is a measure for the quality of an imaging system (Born and Wolf, 1999).

NOTE FIGURE 8: Image of a point spread function system response

Simulated point spred function for a system with a 1-mm pupil, based on its monochromatic aberrations during focusing and defocusing in steps ± 12, ± 8,7, ± 5,14 and ± 1,71 diopter (adapted form Wilson *et al.*, 2002).

In all these experiments, sparsely distributed fluorescent molecules were analysed, compared to that the real biological sample often includes nanometric (sub-resolution) dense structures. To generate an image of such a sample with localisation precision reaching the values of these early single molecule fluorescence studies, it is important to separate the molecules into discrete loci. A handful of approaches were suggested to date. The two main principles: photoactivated localisation microscopy (PALM) and stochastic optical reconstruction microscopy (STORM) will be described below. Some potentially superior approaches and methods specific for particular scientific questions will be mentioned at the end of this section.

It is known that the emission of a single fluorescent entity (organic fluorophore, fluorescent protein, fluorescent nanomaterial) shows random interruptions (Dickson *et al.*, 1997; Tinnefeld and Sauer, 2005). This is caused by the deterministic or stochastic alteration of the chromophore between a dark (non-fluorescent, OFF-) and a bright (fluorescent, ON-) states. These natural ON/OFF cycles are too fast for super-resolution imaging. The essential condition for improving the image resolution is a presence of less than one flourophore in a diffraction limites spot per frame. Therefore it was important to generate circumstances, which prolong the OFF state of most of the fluorophores. Such conditions can be accomplished in at least two ways. First is to change the spectral characteristics (photoconvertible) or quantum yield (photoactivable) of the fluorophore, usually a fluorescent protein. Second way is to control the oxido-reduction state of the chromophore (photoswitchable) by the composition of the imaging solution (usually organic dyes) (see **Figure 16**). Switching of the fluorophores to the ON state has to go through in a stochastic manner. This ensures that only a small number of active fluorophores are recorded on each frame, while allowing all labeled molecules to be recorded sequentially. Fluorescent molecules within a diffraction limited spot are thus temporally separated and can be individually localised with a high precision (see below). Such double separation of individual fluorophores paved the way for resolving more emitters that are less than half the wavelength of light apart (Abbe, 1873; Galbraith and Galbraith, 2011; Sauer, 2013; Tinnefeld and Sauer, 2005). The key for bypassing the diffraction barrier is a precise software single-molecule localisation and analysis from the acquired data. Recorded stochastically photoswitched, photoactivated or photoconverted fluorophores attached to the structure of interest are then reconstructed into high resolution image. It allows insight into details of (bio)structures at a resolution that is otherwise unmatched so far.

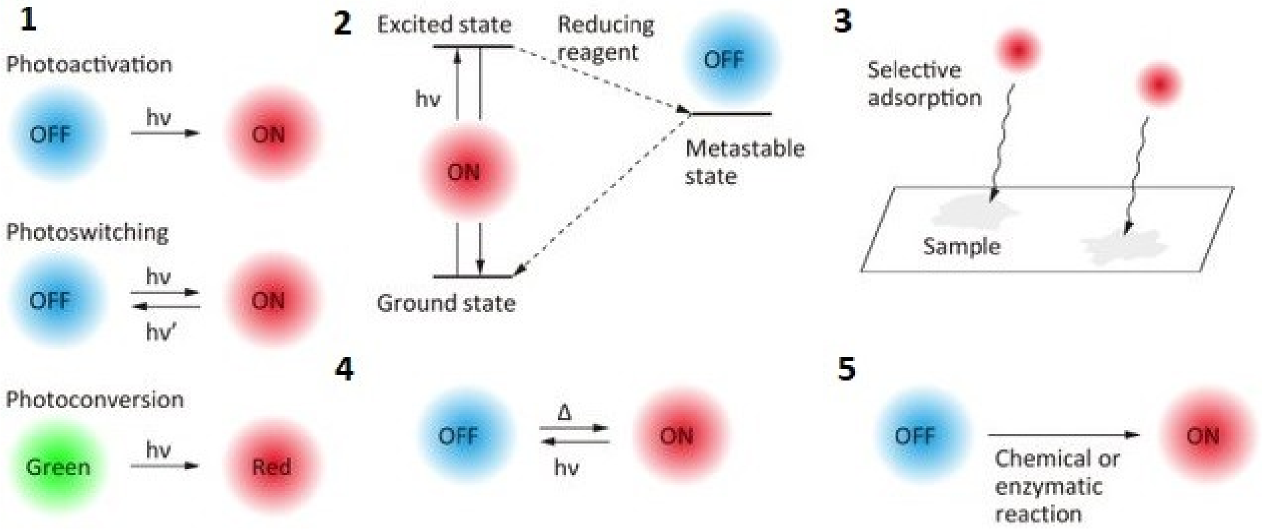

FIGURE 16: Scheme of different types of switching of fluorophores used in SMLM

(1) Different fluorophore state changes induced by the pulse of high energy light, (2) photo-induced redox switching, (3) selective adsorption of fluorescently labelled molecule, (4) thermal-induced switching and (5) chemical or enzymatic reaction-induced switching (adopted from Habuchi, 2014).

Molecules of interest are in praxis labelled either by fusion with photoconvertible or photoactivable fluorescent proteins for PALM or by antibodies or ligands conjugated with an organic dye for STORM. Almost all fluorophores are kept in the dark state naturally or by the composition of the imaging buffer. Only a minute number of molecules switch to the bright state in the absence of any stimulus which would be inconvenient for everyday imaging. Therefore for stimulus of the state-change process, activation energy from the outside has to be applied. This energy is usually added in the form of a high intensity laser pulse (lower wavelength). The intensity of an activating laser has to be adjusted during the acquisition to control the switching behaviour of the fluorophores. The goal is to switch ON only a few emitters in a single frame, which is recorded on the chip of a highly sensitive camera. These used to be mostly electron multiplying charge coupled devices (EMCCD) due to their high quantum efficiency and ability to effectively suppress the noise. The development of nowadays' scientific complementary metal oxide semiconductors (sCMOS) cameras with low noise and quantum efficiencies exceeding 80% led to their spread in the field of SMLM as well.

For the proper image reconstruction a sufficient amount and density of recorded fluorophores is needed. This means in praxis tens of thousands of frames has to be collected. Acquired image stacks are then computationally processed to find the proper localisations of the single emitters and generate a list (table) of coordinates of all molecules. The principle of localisation is based on fitting the PSF of each emitter with an ideal Gaussian profile function. For finding the proper centre of the Gaussian profile, its full width at half maximum (FWHM, see **Note 9** for more information) is calculated for each spot (see **Figure 15**).

NOTE 9. *Full width at half maximum*

When a signal is taken as normal Gaussian distribution, full width at half maximum (FWHM) is commonly used parameter describing the width of the Gaussian function (see **Note figure 9**). It is given by the distance between points on the curve at which the function reaches half of its maximum value. For microscopy (especially for SMLM and deconvolution) this parameter is used as default value for localisation of the centre of any single spot defined by the PSF on the image.

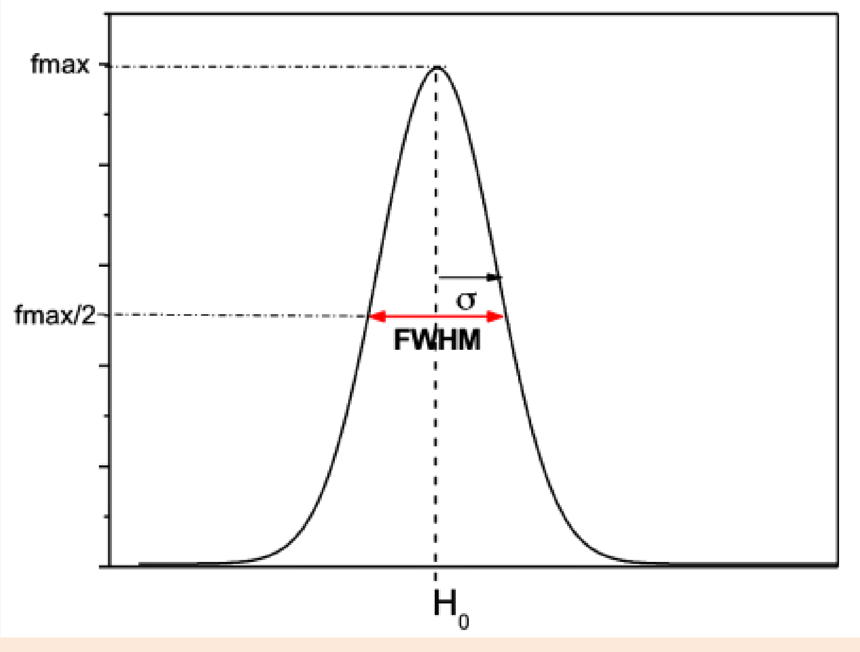

NOTE FIGURE 9: Diagram of FWHM of a normal Gaussian distribution

Point H_0 on the X axis represents the maximal value of the Gaussian distribution fmax. FWHM represents the value that describes the Gaussian distribution at the value fmax/2.

The centre of a Gaussian profile forms the XY coordinates of the emitter localisation. These are obtained for all emitters in all frames of the stack. In addition, for each emitter, the localisation precision representing the emitter localisation accuracy is calculated using the equation:

$$\boldsymbol{\sigma 2x, y} = \left[\frac{\left(\boldsymbol{s}^2 + \frac{\boldsymbol{q}^2}{\mathbf{12}}\right)}{\boldsymbol{N}}\right] + \left[\frac{(\mathbf{8}\boldsymbol{\pi s}^4\boldsymbol{b}^2)}{(\boldsymbol{q}^2\boldsymbol{N}^2)}\right]$$

where **$\sigma_{x,y}$** is the localisation precision of a fluorescent probe in the lateral dimensions, **s** is the standard deviation of the point-spread function, **N** is the total number of photons gathered (note: this does not represent the number of photons per pixel), **q** is the pixel size in the image space, and **b** is the background noise per pixel (not the background intensity).

When conducting PALM experiments with small pixel sizes (similar to those found in high-performance cameras) and negligible background noise from dark emitters and autofluorescence, basic equation can be approximated by formula:

$$\boldsymbol{\sigma}^2\mathbf{2}\boldsymbol{x, y} \approx \frac{\boldsymbol{s}^2}{\boldsymbol{N}}$$

which can be considered in this situation as governing the localisation precision of single molecules imaged by fluorescence microscopy (Shroff *et al.*, 2020).

The final high resolution image, or more precisely the localisation map, is generated by plotting points using coordinates of all detected molecules. Applying of the Gaussian function corresponding to the localisation precision of each point determines the signal spreading in the final position.

Since the localisation precision depends on the strength of the specific signal compared to the surrounding background. This makes all single molecule localisation microscopy methods very sensitive on signal-to-noise ratio. However, a few hundreds of photons from a single molecule allow the localisation of an emitter with a nanometre precision (Mortensen *et al.*, 2010; Thompson *et al.*, 2002; Yildiz and Selvin, 2005). To suppress the unwanted out-of-focus background, there are several alternative illumination schemes applied. These are represented by total internal reflection fluorescence (TIRF), highly inclined and laminated optical sheet illumination (HILO) (see **Note 10** for more details) or light sheet illumination (including lattice light sheet; see **Note 7**), which are reducing a volume where emitters are excited simultaneously. Reduction of unwanted fluorescence significantly increases the final SNR of recorded dataset.

NOTE 10. *Total internal reflection fluorescence and highly inclined thin illumination*

On an objective based total internal reflection fluorescence microscopy (TIRFM) principle uses high numerical aperture objective (with NA ≥ 1.4) for epifluorescence illumination. Excitation light is moved out of the optical centre to reach the edge of the objective lens system. At the point of supercritical angle highly inclined excitation rays propagate through the glass surface onto a sample plane, where it is reflected back at the glass-aqueous medium interface because of a big difference in the refraction indexes. At the place of incident the evanescence energy wave is penetrating the sample into several hundreds of nm (400-600 nm). This approach allow us to acquire fluorophores located close to the optical surface without unwanted background light coming from more distant parts of the samples (see **Note figure 10**; Stout and Axelrod, 1989). Just before getting TIRF illumination the different variable angle epifluorescence microscopy schemes (VAEM) penetrating through the sample are achieved (Sinkó *et al.*, 2014). With minor setup improvements highly inclined and laminated optical sheet illumination (HILO) can be used for optical sectioning throughout the sample in moving focal plane scheme. Also this system suppress the out of focus background light (Tokunaga *et al.*, 2008).

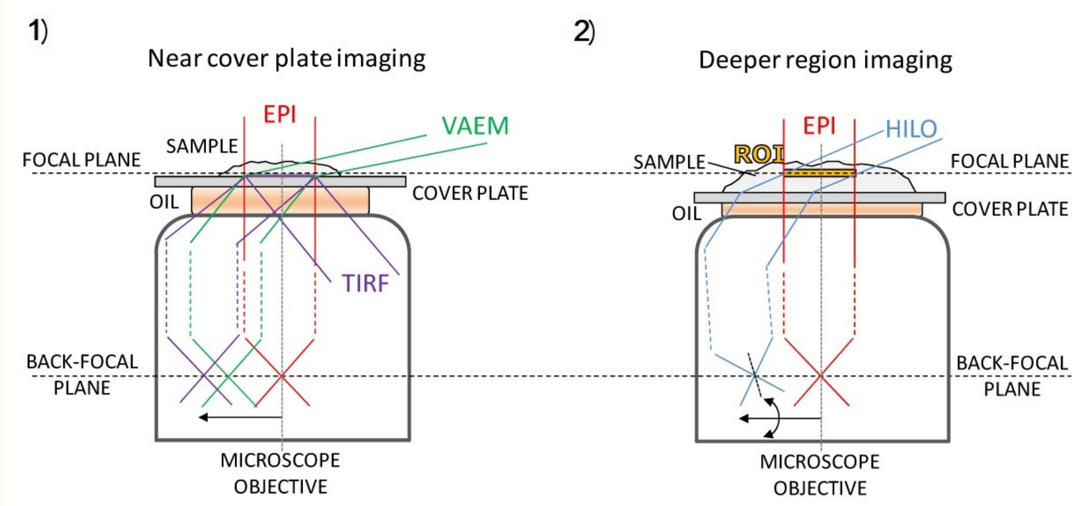

NOTE FIGURE 10: Scheme of an objective based total internal reflection microscopy

1) Excitation epifluorescence light (red lines) is always focused to the back-focal plane (lower black dashed line) of the microscope objective. VAEM illumination scheme (green lines) is reached by moving the light to the off-axis point. TIRF occurs after exceeding of the critical angle (purple lines). 2) HILO scheme is comparable with VAEM with tilted excitation light (blue lines), that suppresses unwanted illumination disruptions during movement of the focal plane (upper black dashed line) to the region of interest (ROI) hidden deeper in the sample (adapted from Sinkó *et al.*, 2014).

As mentioned above, two principles of SMLM methods were developed according the control of fluorophore switching mechanism between OFF- and ON-states. PALM (Betzig *et al.*, 2006; Hess *et al.*, 2007, 2006; Shroff *et al.*, 2008, 2007) is based on application of photoconvertible or photoactivated fluorescent proteins (Ando *et al.*, 2002; Lippincott-Schwartz and Patterson, 2009; Patterson, 2002). Direct stochastic optical reconstruction microcopy (dSTORM) uses the adaptation of photoswitching cycles of standard organic fluorophores coming from the discovery of Cy3-Cy5 photoswitching in nano-spaced conjugates (for more on different switching, see **Figure 16**; Bates *et al.*, 2005; Heilemann *et al.*, 2005). As organic dyes are small in size and have much higher fluorescence quantum yields (the higher amount of emitted photons) compared to fluorescent proteins, they are preferred fluorophores for the SMLM techniques. During the dSTORM measurement, fluorophores are transformed into the non-fluorescent triplet state by a fine-tuned reducing buffer. Upon a short irradiation pulse with a high energy light, a set of fluorophores gets to the ground S_0 state (see **Note 2** for more details). At this point fluorophores are ready to be illuminated with an intense beam of excitation light. Preferred is that emitters release the photons within the possible shortest time covering ideally a period of only one frame (Heilemann *et al.*, 2009, 2008; van de Linde *et al.*, 2011b, 2011a). The advantage of dSTORM is a better localisation precision compared to PALM thanks to its better SNR. The disadvantage is a need of permeabilization of cells before imaging of intracellular structures when using antibodies for staining. Sample for SMLM techniques usually has to be fixed due to sample preparation and long acquisition times needed. Therefore the application of PALM and dSTROM is limited for live cell imaging. Also the choice of appropriate fluorophores has to be taken into account (Heilemann *et al.*, 2009; van de Linde *et al.*, 2011a, 2011b, 2008). As the behaviour of such a molecule has to be controlled and well defined a majority of high-quality images were made with only a few dyes mostly based on cyanin backbone.

Several other SMLM methods using the principle that only a very few molecules can emit photons at the same time (in one frame) were developed over the last decade. The main attention achieved point accumulation for imaging in nanoscale topography (PAINT; Sharonov and Hochstrasser, 2006), especially its current variant DNA-PAINT (Schnitzbauer *et al.*, 2017). Its basis is a transient binding of fluorescent molecules to the molecule of interest (Schnitzbauer *et al.*, 2017; Sharonov and Hochstrasser, 2006).

Such temporary interactions generate brief period when the molecule is immobilised in the focus of the objective where it is taken as the bright state of the molecule (see **Figure 16**). For this approach DNA-PAINT uses short, complementary DNA oligonucleotides (9-12 bases) with specific affinity. The time a fluorophore spends in the illuminated space can be easily tuned by the affinity strength (Jungmann *et al.*, 2010). Similarly, complementation-activated light microscopy (CALM) takes advantage of weak fluorescence of the GFP missing M13 peptide that is normally part of the GFP primary structure (Pinaud and Dahan, 2011). GFP missing this part can be expressed in eukaryotic cells. After addition of the M13 peptide into the solution, the fluorescene of GFP increase rapidly. Stochastic binding of the peptide to the incomplete GFP turn the protein to the bright state and enables its precise localisation. Finally, expansion microscopy combined with standard SMLM methods potentially offers further improvement in the details, which can be imaged using those separate methods (Zwettler *et al.*, 2020). Fixed samples are immerged into highly hydrophilic polymeric material that expands 2-4 times with preserved original structures after adding aqueous solution to the sample. Structures are made larger and better resolvable then (Chen *et al.*, 2015). The biggest advantage of all SMLM is that the used instruments are simpler (and thus cheaper) compared to SIM or especially to STED.

1.9.3.4 Super-resolution optical fluctuation imaging

The principle of all SMLM techniques is precise localisation of spatially and temporally separated emitters. The biggest disadvantage of these methods is the data acquisition itself. For a proper high resolution image reconstruction a sufficient number of localisation, in other words emitting single molecules, is required. Therefore, tens of thousands of frames are needed (sometimes up to 60 000). To record so huge amount of snapshots is extremely time consuming even with the use of recent ultra fast sCMOS cameras and bright fluorophores.

To overcome this problem and to provide some new imaging options, super-resolution optical fluctuation imaging (SOFI) was developed in the group of Joerg Enderlein (Dertinger *et al.*, 2009). The basis of this method is statistical spatio-temporal analysis of signal fluctuations of the fluorophores grouped into so called cumulants. They combine all probability distributions with the same moment into one set as their resulting features are the same as well. This approach significantly lowers the computing power requirements of the method. Since SOFI analyses the signal fluctuations, emitter density has to be much higher and can overlap in contrast to SMLM techniques (Dertinger *et al.*, 2009) (for more details see **Figure 17**). To achieve a high resolution SOFI variant employing the employing 4th order cumulants up to 10 000 frames is sufficient. One image with reasonable increased resolution can be obtained in around 2-3 minutes, which means significant degrease of time needed. In the first step of the following mathematical analysis the uncorrelated background signal is eliminated out of the data. Finally, SOFI offers a moderate resolution gain with a significant contrast enhancement and much reduced light exposure needed in comparison to the SMLM and STED methods.

SOFI is often understood as a software-based microscopy technique. It can be performed on all imaging platforms without necessary adaptations. The choice of the imaging platform and signal processing can be carefully optimized for a given scientific task. Still the widefield fluorescence microscopes offer the best combination of high enough sensitivity and speed. In our laboratory, we took advantage of balanced super-resolution optical fluctuation imaging (bSOFI) variant. bSOFI bypasses the biggest drawback of standard SOFI. The nonlinear response to brightness and blinking heterogeneities in the sample limits the use of higher cumulants improving the final resolution. bSOFI analyses several cumulant orders for extracting molecular parameter maps. These can be the molecular fluorescence lifetimes, concentrations and brightness distribution of fluorophores within the biological sample. Estimated blinking statistics are then used for balancing the image contrast. Finally, after application the linearized brightness, blinking response and improved resolution correspond to the cumulant order (Geissbuehler *et al.*, 2012). Therefore it also directly provides quantitative data about the density of emitters in any area of the image and it can show accumulation of receptors in high density regions at the T cell surface (Lukeš *et al.*, 2017).

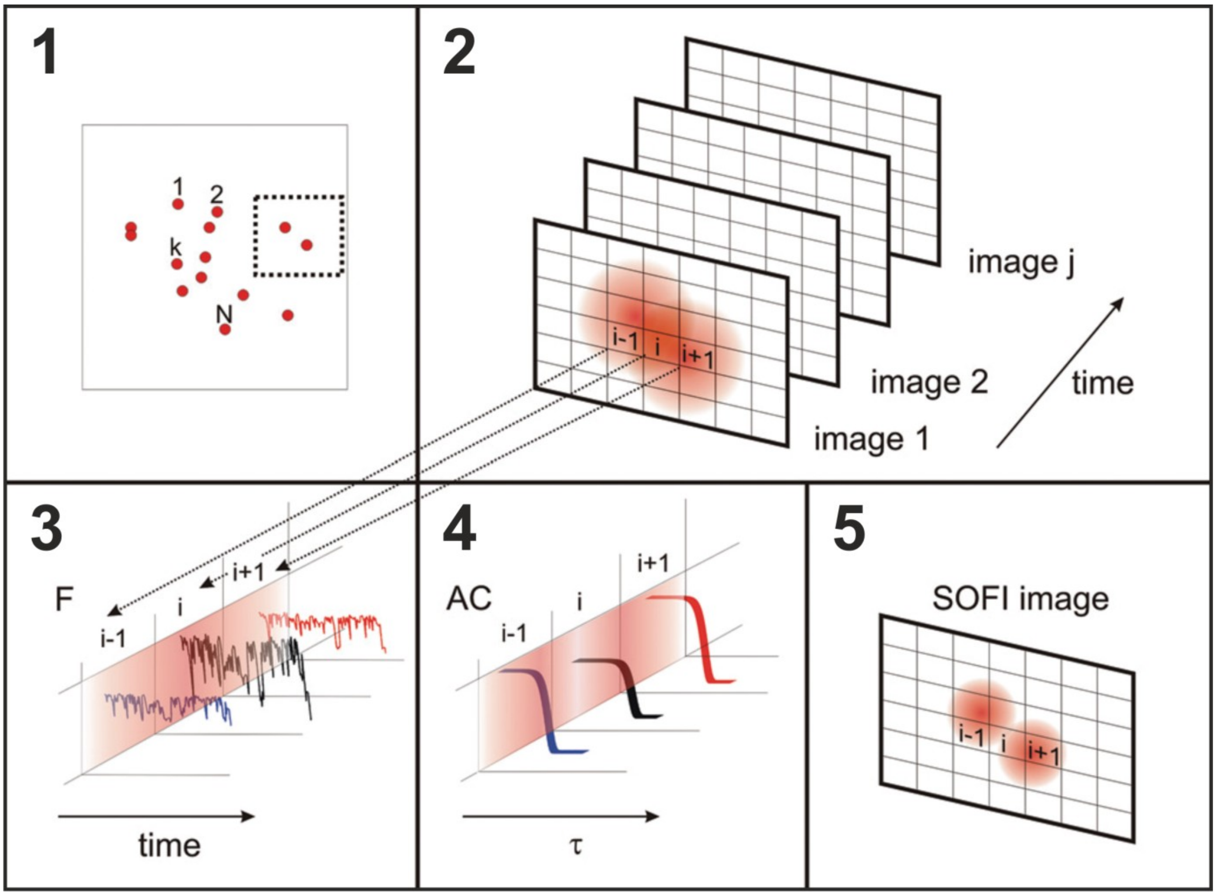

FIGURE 17: Scheme of the SOFI principle

(**1**) Simulated emitter distribution in the object plane. Each emitter exhibits fluorescence intermittency, which is uncorrelated with the others. (**2**) A magnified detail of the dotted box in 1. The signal from the emitter fluorescence distribution is convolved with the system PSF and recorded on a sub-diffraction grid (pixels of the CCD-camera). Two neighbouring emitters, for example, cannot be resolved because of the optical diffraction limit. The fluorescence fluctuations are recorded in a time-lapse image stack. (**3**) A time-trace for each pixel is encoded in the image stack. The time-trace is generated by the sum of individual emitter signals, whose PSF are reaching into the pixel. (**4**) The second-order autocorrelation function is calculated from the fluorescence fluctuations for each pixel. (**5**) The SOFI intensity value assigned for each pixel is given by the integral over the second-order correlation function. The second-order correlation function is proportional to the squared PSF, thus increasing the resolution of the imaging system by a factor of √2 (adopted from Dertinger *et al.*, 2009).

1.9.4 Super-resolution imaging in three dimensions

Super-resolution imaging significantly helped scientists to understand many biological processes in their native environment represented by the subcellular compartments. The triumphs mentioned above are prevalently related to the improvement of a lateral resolution. However, several super-resolution microscopy techniques with slightly modified properties are able to visualise the objects with high resolution also in 3D and in addition in some cases in living cells (Chen *et al.*, 2014; Geissbuehler *et al.*, 2011; Li *et al.*, 2015). Specialized 3D shape of the depletion laser focal spot is required for 3D STED to acquire images with axial resolution of 100 nm or below. Only a modest improvement in axial resolution is achieved by the most of SIM adaptations that end up at ~300 nm (see **Figure 18**; Lukeš *et al.*, 2014). In a way, the worst axial resolution with of ~500 nm is achieved using the 3D adaptation of SOFI (Dertinger *et al.*, 2012, 2009; Geissbuehler *et al.*, 2014).

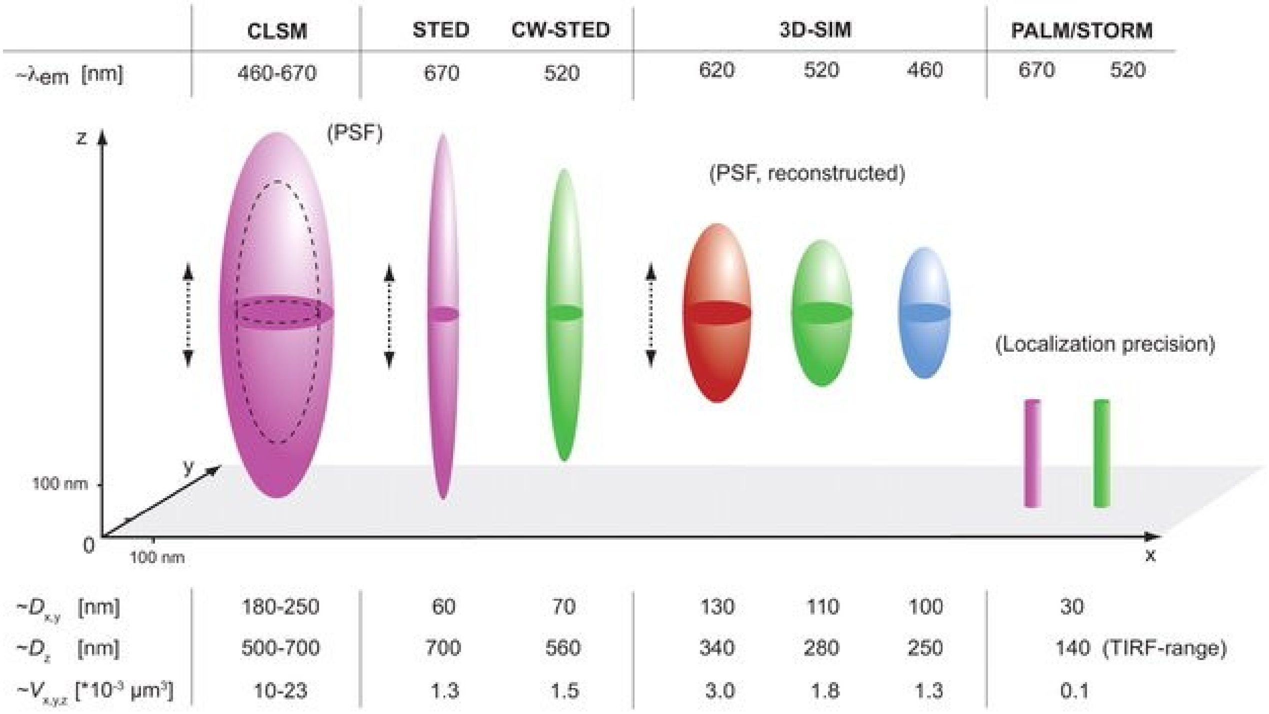

	CLSM	STED	CW-STED	3D-SIM			PALM/STORM	
~λem [nm]	460-670	670	520	620	520	460	670	520
$\sim D_{x,y}$ [nm]	180-250	60	70	130	110	100	30	
$\sim D_z$ [nm]	500-700	700	560	340	280	250	140 (TIRF-range)	
$\sim V_{x,y,z}$ [$*10^{-3}$ µm^3]	10-23	1.3	1.5	3.0	1.8	1.3	0.1	

FIGURE 18: Theoretically maximal resolvable volume obtained with different types of microscopes

Schematic 3D representation of focal volumes is shown for the indicated emission maxima. The approximate lateral (x,y) and axial (z) resolution and resolvable volumes are listed and compared to the confocal laser scanning microscope (CLSM). Note that STED/CW-STED and 3D-SIM can reach up to 20 µm into the sample, whereas PALM/STORM is usually confined to the evanescent wave field near the sample bottom. It should be noted that deconvolution approach can further improve STED resolution. For comparison the "focal volume" for PALM/STORM was estimated based on the localisation precision combined with the z-range of TIRF illumination (adopted from Schermelleh *et al.*, 2010).

Nevertheless, the SMLM techniques probably offer the greatest potential to get excellent 3D information about studied objects. Several adaptations were suggested to improve the final axial resolution (von Diezmann *et al.*, 2017). Among them, the best results were achieved with astigmatism (Huang *et al.*, 2008), biplane imaging (BP; Juette *et al.*, 2008; Ram *et al.*, 2008), double-helix point spread function (Pavani *et al.*, 2009) or interferometric photoactivated localisation microscopy (iPALM; Shtengel *et al.*, 2009). Apart from iPALM, these adaptations of the super-resolution methods lead to a significant improvement of axial resolution (5-20 times), but never to the visualisation of biological structures with isotropic accuracy. The maximum achieved axial resolution was always 5-10 times lower than the lateral resolution. This limits the final application.

To study the distribution of proteins on nanometric-sized structures representing microvillus dimensions, it is important to have methods that reach a resolution bellow 50 nm in all dimensions. This resolution can be provided by iPALM with axial resolution below 25 nm but the final precision is strongly dependent on the local environment of the imaged sample (Shtengel *et al.*, 2009). Axial resolution can also be improved by limiting the illuminated volume in the sample as applied in 3D STED or 3D SIM methods. TIRF and HILO offer such a restricted illumination for SMLM (see **Note 10**).

The system's ability to achieve HILO and TIRF illumination can be applied to the 'nano-topography' using varying angle total internal reflection fluorescence (VA-TIRF) illumination. In this way, the group of Dr. Haran determines the distance from the optical interface (coverslip) for the laterally located surface molecules (Jung *et al.*, 2016). However, this method does not exceed the standard 3D SMLM approaches mentioned above. Finally the temporal, radial-aperture-based intensity estimation (TRABI) is a software adaptation of the SMLM method that offers probably the best localisation precision in a real biological samples (Franke *et al.*, 2017). As our laboratory contributed to the development of a new, simplified version of TRABI, this method will be described into more details below.

1.9.4.1 Temporal, radial-aperture-based intensity estimation

TRABI is a computational technique for 3D SMLM image processing based on photometric analysis of the single molecule PSF distortions. The basic principle is any conventional SMLM method in a combination with state-of-the-art localisation software packages such as rapidSTORM (Wolter *et al.*, 2012) or ThunderSTORM (Ovesný *et al.*, 2014). In addition, to determining the localisation coordinates and localisation precision, these programs determine relatively accurate intensities for each molecule (the number of emitted photons). After adding these information to the TRABI algorithm, it defines the axial position using the distribution of photons over the PSF of each fluorescence molecule (see **Figure 19**). This approach makes possible to determine the positions of individual molecules with an axial depth of up to 300 nm in both directions from the focus plane (Franke *et al.*, 2017). An intermediate step in the development of TRABI was the application of a biplanedetection mode, which expands the possible localisation detection depth up to 500 nm on both sides of the focus. Moreover the global information on the molecules in the sample were improved by the structural density analysis (Franke *et al.*, 2020). This intermediate step led to establishment of the collaboration with our group and the development of direct temporal, radial-aperture-based intensity estimation (dTRABI). This is a computationally simplified and for quantitative analysis equipped method for isotropic super-resolution imaging of molecules near the optical surface in all three dimensions (see **Results** for more details). The application of dTRABI to analyze nanoscopic organisation of receptors on T-cell surface was one of the aims of my PhD studies.

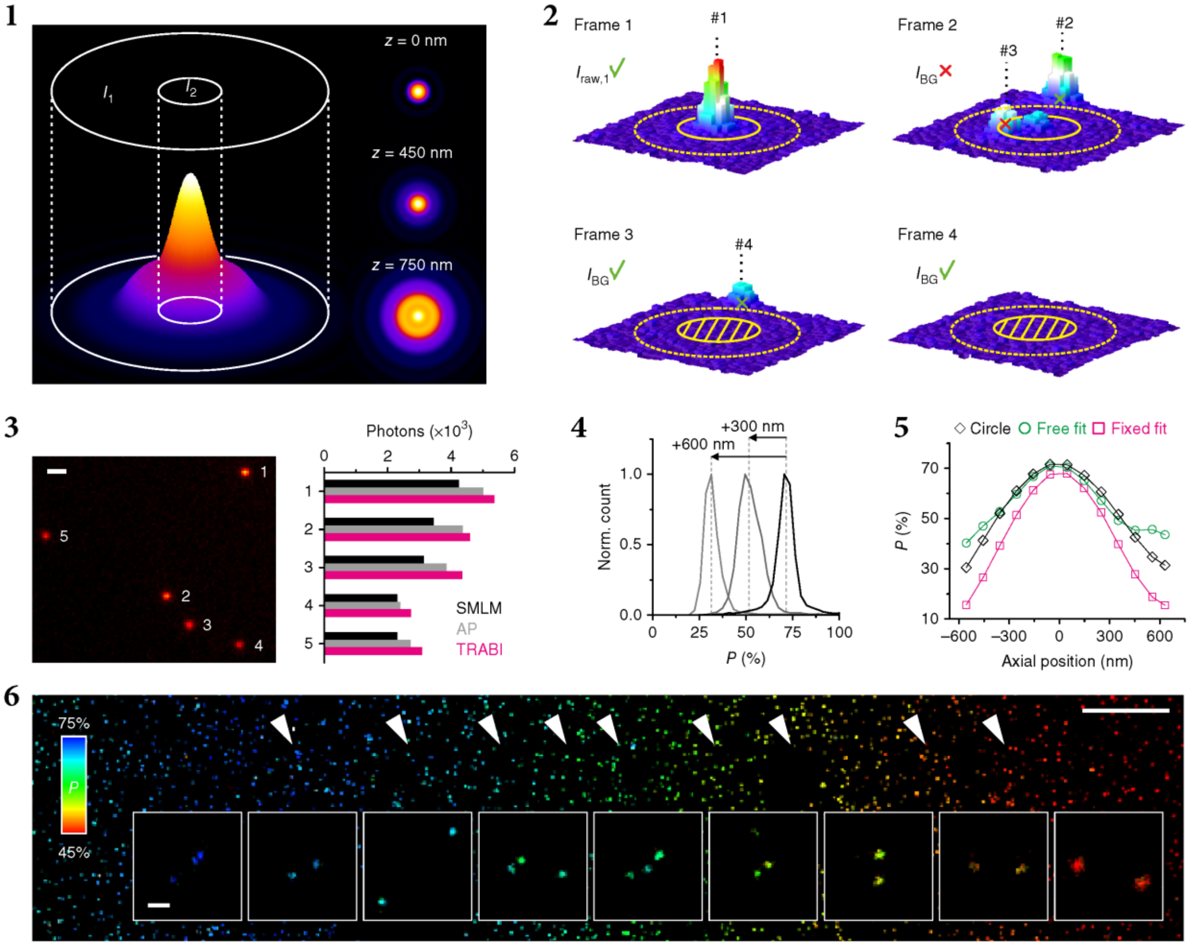

FIGURE 19: Photometry based 3D super-resolution imaging

(**1**) The photometric parameter P dependent on axial position of the localized emitter is determined by the intensities in the two apertures of the molecule's emission pattern according to $P = I_2\ I_1{-}1$. (**2**) Principle of the original TRABI approach, which uses a circular aperture with radius r_1 (solid circle) and an exclusion zone defined by $2r_1$ (dashed circle). I_1 is determined by subtracting background (I_{BG}) from raw intensity ($I_{raw,1}$). $I_{raw,1}$ and I_{BG} are not estimated in frames where localisations from neighbouring spots interfere. (**3**) Left, dSTORM image of surface-immobilised Cy5-labeled DNA. Right, number of photons obtained by fitting using rapidSTORM (free fit; black), classical aperture photometry (r_1 = 865 nm, r_2 = 1,131 nm; gray) and TRABI method (r_1 = 865 nm, n_{BG} = 7; magenta). (**4**) Histograms of P values for different axial positions of the single-molecule surface adjusted with a piezo-scanner. Dashed lines indicate the median of the distribution. (**5**) P as a function of the axial emitter position. Dots represent the median of the distribution, solid lines are used to guide an eye; I_1 was determined by TRABI (r_1 = 865 nm) and I_2 was determined either by TRABI (r_2 = 333 nm, black curve) or through free (green) or fixed fitting (magenta, FWHM = 300 nm) in rapidSTORM. (**6**) Reconstructed dSTORM image of a single-molecule surface tilted by an angle of 0.56°, colour-coded by P. Arrowheads indicate x positions of the magnified single-molecule localisation patterns (insets). Scale bars represent 1 μm (**3**), 5 μm (**6**) and 100 nm (**6**, insets) (adopted from Franke *et al.*, 2017).

1.10 Sample preparation and cell morphology preservation

To image simple, unicellular organisms, one has to immobilise the organism at the optical surface (glass coverslip) and apply the light. For basic morphological characterisation, such samples are usually fully sufficient. However, many of these organisms exhibit large glycostructures at their surface, which interfere with the applied light and reduce the ability of an experimenter to achieve the best optical resolution (the effect of light scattering). Several tricks have to be applied to avoid scattering at the surface of such organisms for high precision imaging of specific molecules. In the case of mutlicellular organisms, including humans, this problematic is more complex. Because cells are the building blocks of every living creature, proteins should be studied at the cellular level and the discoveries applied to the whole concept of the body, if possible.

In our laboratory, we investigate proteins at the surface of human or rodent lymphocytes. Our access to individual cells is thus straightforward. For those, studying cells of the brain or musculature, the only option often is to use model cell lines, which grow as single cells or as a single cell layer in tissue culture flasks or Petri dishes. In the following text, I will focus on what is known about the preparation of samples for imaging surface or intracellular molecules of cultured cells growing in suspension.

Usually, suspension-growing cells are immobilised to the coverslips using polycations such as poly-L/D-lysine (PLL, PDL). Surface of cells is negatively charged due to the presence of anionic glycocalyx structures (Maverakis *et al.*, 2015). Electrostatic interactions with PLL-coated surface help to immobilise cells for imaging of living or fixed cells. The interaction of cells with the coated coverslip is so strong that it allows the application of fixation (and permeabilization) solutions without disturbing the cells. Fixation additionally strengthens the interaction by chemical crosslinking of cellular structures and the surface. The whole process is often followed by antibody labelling of cellular structures and several washing steps.

An alternative approach is when antibodies specific for surface molecules (e.g., integrins or CD43) or ligands of adhesive molecules (e.g., ICAM-1 for LFA-1 or fibronectin for other integrins) are attached to the coverslip and cells are immobilised via their interaction with these anchor proteins (Bunnell *et al.*, 2002; Dustin, 2009). This configuration does not reflect the fact that cell to cell contacts are driven by receptors and ligands, which can be fully mobile. In order to avoid immobilisation of anchoring molecules supported planar bilayers (SPB) with ligands or antibodies conjugated with the lipid headgroups were developed. This led to creating of so-called functionalised SPBs (Dustin, 2009). Adhesive molecules are fully mobile on SPBs and, thus better mimic mobility of interacting molecules in the cellular context. However, irrespective to the mobility of anchoring molecules, immobilised cells undergo active stretching on such functionalised surfaces (Bunnell *et al.*, 2001; Mazia *et al.*, 1975; Rossboth *et al.*, 2018). This can affect their overall morphology but also the nanotopography of the surface membrane at the interface. Such immobilisation procedures are therefore inadequate for studies of the cell surface receptor organisation. In addition, contact of cells with present polycations and immobilised/lipid-anchored ligands/antibodies activate the cells (Bunnell *et al.*, 2002; Santos *et al.*, 2018; Varma *et al.*, 2006). Therefore, for studies of resting (non-stimulated) lymphocytes, these methods have to be avoided. In our laboratory, we are primarily studying receptors on resting T cells, hence we were looking for alternative approaches which do not stimulate cells during their immobilisation on coverslips.

Immobilisation of lymphocytes in a hydrogel or Matrigel does not lead to their stimulation (Santos *et al.*, 2018) and cells placed into these materials do not exhibit any detectable morphological changes. Unfortunately, Matrigel exhibits high background fluorescence, which is incompatible with single molecule fluorescence techniques. Moreover, the 3D matrix of hydrogels leads to a random axial distribution of cells. A longer distance of cells from the optical surface limits the selection of available techniques for high resolution studies to just two: STED and SIM (Cavo *et al.*, 2018; Fritzsche *et al.*, 2017). Above that the precision of all microscopy techniques declines with the distance from the optical surface due to the diffraction of the intermediate material (Lakowicz, 2006). Widefield microscopy-based single-molecule fluorescence techniques such as SOFI and TRABI used in our laboratory are especially sensitive to this effect. Therefore, we had to develop a new method for coating of coverslips with glycine that immobilises the cells to the optical surface, minimizes cell activation and prevents damage of the cellular surface morphological features like microvilli, cilia or ruffles.

1.11 Receptors, signalling molecules and artificial proteins studied in the studies

The main aim of our Laboratory of Membrane Physical Biology is to characterise the nanoscopic organisation of proteins on the plasma membrane. This aspect can also influence the signalling events and capacity of human T lymphocytes to respond to diverse stimuli. To this end, we apply advanced fluorescence microscopy and spectroscopy techniques to determine position and/or mobility of signalling molecules in their native environment. I have contributed to the two critical questions investigated in our laboratory. Firstly, what determines the sorting of molecules from their place of origin (the endoplasmic reticulum) to the plasma membrane. For this purpose, we have selected representatives from the topologically related group of single spanning membrane proteins. All of them are facing their N-terminus out of the cell. The studied proteins own a single transmembrane domain and the intracellular C-terminal domain often contains amino-acid residues or motifs directly involved in signal transduction (see **Figure 20**).

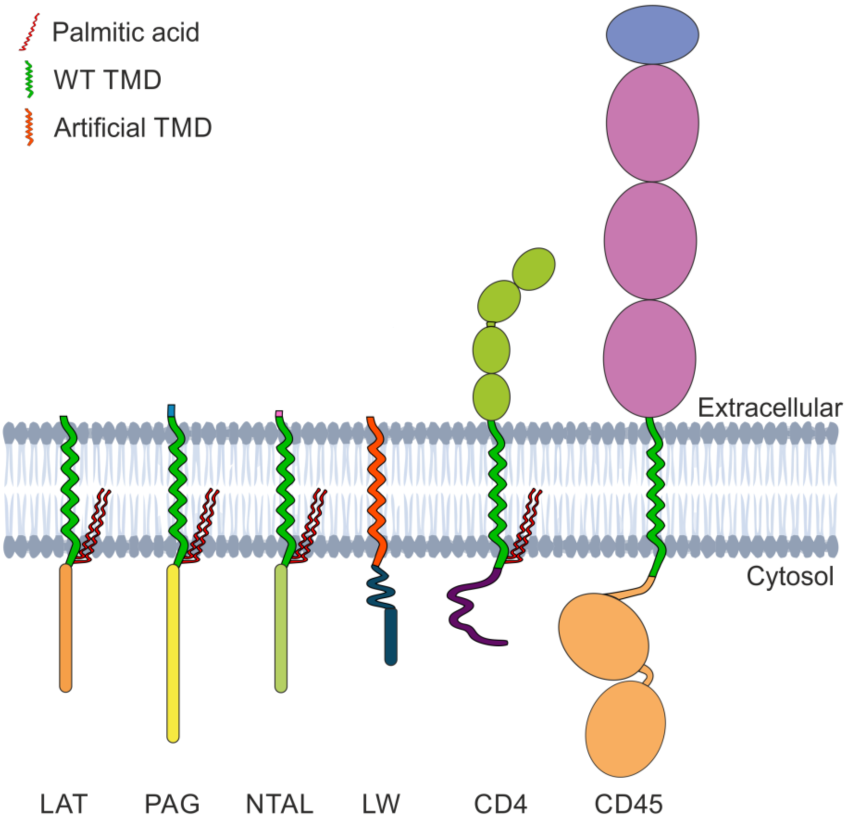

FIGURE 20: Schematic illustration of single spanning proteins tested in the study

LAT, PAG and NTAL are proteins from the type III family of integrated proteins – leaderless. LW is an artificial protein composed of a transmembrane domain (TMD) based on LW19/LW21 highly hydrophobic peptides and a backbone derived from CD247. CD4 and CD45 proteins have a huge highly glycosylated extracellular domain. Glycans are not shown. The extracellular domain of CD4 consists of 4 immunoglobulin-like domains (light green), the one of CD45 of 3 fibronectin-II-like domains (pink) and a Cys-rich domain (blue). LAT, PAG, NTAL and CD4 can be palmitoylated in the juxtamembrane region. Intracellular domains of LAT, PAG, NTAL and CD247 are phosphorylated upon T-cell activation and serve as scaffold for downstream signal transducers. Lck kinase associates with the intracellular part of CD4. The intracellular part of CD45 has phosphatase activity (membrane-proximal D1 domain).

First group of selected proteins belongs to the family of transmembrane adaptor proteins (TRAPs) – linker of activation of T lymphocytes (LAT), phosphoprotein associated with glycosphingolipid-enriched membrane microdomains (PAG) and non-T-cell activation linker (NTAL). These proteins do not have any enzymatic activity but rather serve as a scaffold for other active players in cell signalling. Importantly, selected TRAPs carry CxxC motif in their intracellular juxtamembrane region that can be palmitoylated and belong to type III membrane proteins so called leaderless. This means that the proteins do not have a separate sequence (signal peptide) for their positioning into the membrane bilayer. The proteins also lack any larger extracellular domain. The maximum length of their extracellular domain is 25 amino acids (Hořejší *et al.*, 2004; Štěpánek *et al.*, 2014). Those properties make them an ideal model for studying the impact of TMD and proximal sequences on protein sorting in cellular membranes. Due to a simple structure of these proteins, our mutagenesis experiments can be more easily interpreted with respect to the structural motifs involved.

As the second group we have tested typical type I membrane proteins, such as CD2, CD4 and CD8, in our plasma membrane sorting studies. However, generated mutants did not exhibit any interesting alterations in their trafficking to the predicted cellular membranes. Finally, we have produced ‘artificial TRAP-like proteins’, which carry so-called ideal transmembrane domain usually tested in synthetic membranes using biophysical methods (Olšinová *et al.*, 2018). These constructs were used as controls in our protein trafficking studies.

Also the nanometric surface organisation of receptors and its effect on the T-cell function was studied. For this purpose, CD4 and CD45, which play a crucial role in T-lymphocyte development and activation (Glatzová and Cebecauer, 2019; Holmes, 2006), were selected. The pilot studies were performed to establish the appropriate technologies for studying receptors in membrane nanotopography in non-stimulated T cells. Brief decription and some specific structural features will be described in the following sections.

LAT

Human linker of activation of T lymphocytes is a 38 kDa phosphoprotein expressed in T and natural killer (NK) cells. Lower levels were also found in the other immune cell types, including pre-B cells but not in B cells. It has only 3 amino acids in its extracellular part, which is extremely unusual for membrane proteins (for the simplified structure, see **Figure 20**). LAT also lacks any leader sequence for its positioning into the lipid bilayer. Indeed a mechanism, by which LAT incorporates into cell membranes, is not known yet. Mature protein undergoes palmitoylation of its membrane-proximal cysteines (Štěpánek *et al.*, 2014). LAT is best known for its rapid phosphorylation on tyrosine residues upon T-cell activation (Sieh *et al.*, 1994; Wange, 2000). LAT function is to bring together and close to the membrane several important players involved in TCR-induced signalling. Early after antigen recognition by T-cell receptor (TCR), LAT is phosphorylated by protein-tyrosine family kinase ZAP70 and serves as a scaffold for SH2 domain-containing proteins (e.g., PLCγ1, GRB2, SOS1, VAV) (Hořejší *et al.*, 2004). A specific and tuneable binding of all these interacting partners is probably achieved by distinct phosphorylation profiles on the available 9 intracellular tyrosine residues. Moreover, exact localisation of LAT before and during T-cell activation is not known. LAT knock-out mice exhibit impaired thymic development of T lymphocytes. Patients with mutant LAT often have compromised immune system.

PAG

Phosphoprotein associated with Glycosphingolipid-enriched membrane micro-domains, also known as Csk-binding protein (Cbp), belongs like many other TRAPs into the type III transmembrane protein family. It is ubiquitously expressed throughout human tissues. PAG comprises a small extracellular domain of 16 amino acids followed by 23 hydrophobic amino acids forming the intra-membrane α-helical structure tightly connected to the palmitoylation CxxC motif and a cytoplasmic C-terminal domain (for the simplified structure, see **Figure 20**). Intracellular tail of PAG contains 10 tyrosine residues that are likely to be phosphorylated by Src-family kinases and Csk (Hrdinka and Hořejší, 2014). PAG binds and brings to the membrane a major negative regulator of Src kinases – Csk. Csk is a tyrosine kinase which phosphorylates C-terminal tyrosine residue of Src kinases. This residue, in its phosphorylated form, negatively regulates enzymatic activity of Src kinases, including a critical player in T-cell activation – Lck kinase. In the absence of (antigenic) stimulus, PAG-Csk complex transmits negative regulatory signals to Src kinases and helps to keep resting cells in a quiescent state. Upon activation, PAG becomes rapidly dephosphorylated and dissociates from Csk. This leads to the release of a negative control and activation of Src kinases involved in signal transduction (Brdicka *et al.*, *2000*). Conventional PAG knock-out mice exhibit embryonic lethality.

NTAL

Non-T-cell activation linker is a transmembrane adaptor protein similar to LAT. It is also known under the names LAT2 and LAB. Both proteins belong to the type III – leaderless transmembrane protein family. It is expressed in many splenic and peripheral blood immune cells, but not in T lymphocytes. The protein is less well studied than LAT or PAG/Cbp. NTAL consists of a 5 amino acid long N-terminal domain followed by TMD containing 21 residues and a potential palmitoylation site CxxC. (for the simplified structure see **Figure 20**) Predicted cytoplasmic domain contains 10 tyrosines, which can be phosphorylated. No other recognisable motif was described in the intracellular part yet. NTAL shows analogous behaviour to LAT. Both are rapidly tyrosine-phosphorylated by Lyn upon triggering the reaction by immunoreceptors. This can be caused by cross-linking of the B-cell receptor (BCR), or high-affinity Fcγ- and Fcε-receptors in myeloid cells, respectively. The main function of NTAL is to make a scaffold for signalling molecules Grb2, Sos1, Gab1 and c-Cbl. These molecules together with C-C chemokine receptor type-5 (CCR5) send forward the signal downstream into the cytosol. NTAL is partially able to compensate the LAT deficiency in T cells due the fact that they interact with the same Src-family kinases (Lck, Lyn, Hck, Yes, Syk or ZAP-70; Brdička *et al.*, *2002*).

Artificial LW proteins

We have also generated several TRAP-like proteins, which contain artificial TMD designed based on the studies of synthetic transmembrane peptides like LW19. Such hydrophobic peptide(s) are often used as an *in vitro* TMD model for biophysical studies (Fastenberg *et al.*, 2003; Kaiser *et al.*, 2011; Macháň *et al.*, 2014). Importantly, these artificial TMDs exhibit transbilayer orientation *in vivo* and *in vitro* (Chum *et al.*, 2016; Macháň *et al.*, 2014). Our TRAP-like proteins are built around the CD247 backbone with varying TMDs. According to the literature (Sharpe *et al.*, 2010), proteins containing LW19 TMD should not naturally show plasma membrane localisation due to the suboptimal length of their TMD (see **Figure 20**). Proteins with LW21 TMD contain 2 more hydrophobic residues and should localize to the plasma membrane. Thus, we used these proteins as the tools for verification of the principles responsible for the plasma membrane protein targeting (see **Results** for more information).

CD4

Cluster of differentiation 4 glycoprotein is a co-receptor of main T lymphocyte receptor – TCR. Its molecular weight is 55 kDa and it belongs to the type I membrane protein family. First 25 amino acids of the protoprotein are the signal peptide. The extracellular part of CD4 is formed by four globular Ig-like domains (D1-D4), which can be extensively N-glycosylated. Extracellular part is followed by 23 amino acids forming an α-helical structure of TMD anchoring the protein into the plasma membrane lipid bilayer. Palmitoylation CxxC motif is in the cytosolic membrane proximal segment (see **Figure 20** for the structure). The intracellular part contains basic-rich motif and the Lck-binding site, which is formed by two cysteines, residues 445 and 447. Zinc coordinates binding between CD4 and Lck (containing also double cysteine motif in the binding site). There are 3 serine residues, which can be potentially phosphorylated. Phosphorylation of serine at the position 433 (human protein) regulates internalisation of CD4 from the cell surface (Shin *et al.*, 1990).

CD4 is expressed in a subset of T lymphocytes, NK cells, monocytes and macrophages. It is essential for the normal development of T cells in the thymus and for the antigen recognition in the periphery. CD4-knock-out mice lack normal presence of peripheral T cells. During T-cell activation, CD4 stabilizes the contact of TCR with major histocompatibility complex class II (MHCII), present on antigen presenting cells. The other important role of CD4 is to bring the main activating Src-family kinase, Lck, to the close contact with TCR. In quiescent T cells, a large fraction of cellular Lck is associated with CD4. Lck is the primary molecule that phosphorylates critical residues on TCR and activate downstream signaling together with ZAP-70 and many other important players after activation (LAT, Vav1, Sos1 etc.; Glatzová and Cebecauer, 2019). In macrophages and NK cells, CD4 plays a role in their differentiation, migration and cytokine expression. Additionally, CD4 with CCR5 are the two main receptors for HIV entry into human cells.

CD45

Protein tyrosine phosphatase receptor type C (PTPRC), known also as a cluster of differentiation 45 (CD45) or leukocyte common antigen, is present in various isoforms on all differentiated hematopoietic cells except of erythrocytes and plasma cells. Again, first 25 amino acids form the signal peptide, thus, CD45 belongs to the type I membrane protein family. It comprises a large and extensively glycosylated extracellular domain. Both, N- and O-glycosylation sites are present in the extracellular domain of CD45. The extracellular domain is followed by a single transmembrane domain (22 residues) and two tandem intracellular phosphatase domains. Several data indicate that membrane-distal domain (D2) is catalytically inactive (Streuli *et al.*, 1990). CD45 appeared on the lists of palmitoylated proteins in some high-throughput studies (Martin and Cravatt, 2009). However, no palmitoylation has been demonstrated in a direct experiment yet. Membrane proximal region of CD45 lacks cysteine residues to be palmitoylated. CD45 is an essential regulator of antigen receptor signalling in T and B cells. It regulates activity of lymphocytes either via a direct contact with extracellular domains of antigen receptor complexes or via its active cytoplasmic phosphatase domain (D1), which dephosphorylates tyrosine of Src-family kinases, including Lck and Lyn (Holmes, 2006).

2 AIMS OF THE WORK

The objective of this work was to demonstrate the impact of TMD and proximal sequences of single-spanning membrane proteins on their higher order organisation on the T-cell plasma membrane. For the ability to study single cells and to avoid biochemical methods, we used advanced fluorescence microscopy techniques. In addition to methodological development, two biological questions were studied in this work.

Biological Aim 1: How does protein palmitoylation and transmembrane domain properties influence sorting of TRAPs to the plasma membrane?

Experimental approach: Expressing of a large panel of fluorescent fusion proteins and their mutants in T cells together with markers of subcellular compartments. Subsequent quantitative analysis of protein localisation together with the markers. Application of super-resolution microscopy to further determine nanoscopic organisation of proteins at the T-cell surface.

Biological Aim 2: How are signalling receptors CD4 and CD45 organised at the T-cell plasma membrane with complex morphology determining nanotopography of CD4 and CD45 on the surface of resting T cells?

Experimental approach: New surface coating development to preserve the 3D nanostructures at the T-cell surface. Adaptation of the original TRABI method for quantitative, three-dimensional single molecule localisation analysis of receptor nanotopography.

Methodological Problem 1: How to adapt sample preparation protocols to improve the signal-to-noise by reducing background and achieve reproducibility in super-resolution microscopy?

Experimental approach: Extensive optimalisation of coverslip cleaning, storage and liquid handling protocols.

Methodological Problem 2: How to adapt sample preparation for super-resolution microscopy and preserve complex morphology of studied cells?

Experimental approach: Development, optimisation and in-depth characterisation of a new coverslip coating method together with the protocols for immunohistochemistry of the cells.

3 MATERIALS AND METHODS

3.1 Cell culture

3.1.1 HeLa cells

HeLa cell line (RRID: CVCL_0030; a kind present from J. Malinský – IEM Prague) was cultured in high-glucose DMEM (Sigma-Aldrich, D6429) supplemented with 10% heat-inactivated foetal bovine serum (FBS; Gibco, 10270-106) and 10mM HEPES (Sigma-Aldrich, H4034) under controlled conditions in humidified incubator at 37 °C and 5% CO_2 (Eppendorf). Treated T25 cm^2 culture flasks (Eppendorf, 0030710126) were used for expansion of the cell line. The cells were split regularly 3 times a week at 80-90% confluence using 0,25% Trypsin (Sigma-Aldrich, T4799) and 0.01% EDTA (Sigma-Aldrich, E6758) in PBS solution (Sigma-Aldrich, 56054C).

3.1.2 Jurkat cell line and its derivatives

Jurkat T-cell line (Clone E6.1, RRID: CVCL_0367; ATCC) and its variants (J.CaM2.5 and J.CD4 KO) were cultured in RPMI-1640 medium (Gibco, 61870036) supplemented with 10% heat-inactivated FBS, mix of non-essential amino-acids (NEA, Sigma-Aldrich, M7145), 10mM sodium pyruvate (Sigma-Aldrich, P5280) and 10mM HEPES in humidified incubator at 37 °C, and 5% CO_2 in non-treated T25 cm^2 culture flasks (Eppendorf, 0030710029). All these cell lines were split 3 times a week and never let to overgrow the density of 1×10^6 cells/ml. The minimum density in culture was 1.5×10^5 cells/ml. The cells were tested for polarization of centriole during the development of the immunological synapse in the conjugation with superantigen bearing APCs (Raji cell line; RRID: CVCL_0511).

The J.CaM2.5 (RRID: CVCL_DR61) cell line (kind present from T. Brdička – IMG Prague) and its parent cell line J.CaM2 (RRID: CVCL_R862) are deficient in LAT expression (Finco *et al.*, 1998) and were derived from Jurkat E6.1 cell line (RRID:CVCL_0367) using Cesium-137 gamma irradiation. The Jurkat CD4 knocked-out (J.CD4 KO) cell line was derived from Jurkat cell line, using CRISPR/Cas9 technology as described (Kornete *et al.*, 2018). Before settling the cell line, cells were several times checked for CD4 marker positivity on Flow cytometer (BD LSR II).

All cell lines were periodically tested for mycoplasma contamination using modified, highly sensitive BrdU assay (Dessi *et al.*, 2005), checked for their morphology and never kept in the culture for longer than 4 months.

3.2 Transient transfection

3.2.1 HeLa cells

For transfecting HeLa cell line, 8×105 of cells were seeded into 1 well of the ibiTreated 8-well chamber (ibidi, 80826) and grown overnight to reach approximately 70% confluence. According to the optimised manufacturer protocol, 150 ng of DNA was gently mixed in 50 µl of Opti-MEM Reduced Serum Media (Gibco, 51985-034) with 0.5 µl of Lipofectamin LTX (ThermoFisher Scientific, 15338100), or TransIT-X2® (Mirus, MIR 6004), respectively. The mixture was incubated for 30 minutes at room temperature.

Prior adding the lipoplex-DNA mixture to cells, the medium was replaced with the pre-warmed, fresh one. Cells were then incubated in the incubator overnight before imaging.

3.2.2 Jurkat cells and its variants

The Jurkat cell line and its variants were transfected using Neon™ Transfection System (ThermoFisher Scientific) following the manufacturer's protocol. Briefly, cells were harvested (400 rcf, 3 minuntes at room temperature) and washed once with PBS. Cells were then resuspended in the electroporation T buffer to final concentration of 2.5×107 cells/ml and mixed with 1 μg of vector DNA for each shot. Ten μl of cell suspension was electroporated (1400 V, 3 pulses, 10 ms width each) and gently transferred into 0.5 ml of incubated pre-warmed full growth media. Cells were incubated overnight in the incubator.

3.3 Cloning of fluorescent fusion proteins

Genes (cDNA) encoding the proteins of interest were introduced into pXJ41 vector (Xiao *et al.*, 1991) with an open reading frame fused to a fluorescent protein via GSGGGS amino-acid spacer at the 3' end (corresponds to C-terminus of the protein). The sequence encoding GFP (or its variants) was subcloned into the vector using BamHI and XhoI restriction sites. Protein of interest was inserted between EcoRI and BamHI restriction sites. For LAT and PAG proteins, the intracellular part (C-terminal) had to be inserted into the construct using BamHI cloning site due to the presence of this motif in their coding sequence. More details in (Chum *et al.*, 2016; Lukeš *et al.*, 2017).

3.4 Microscopy sample preparation

3.4.1 Preparation of solutions

Solutions for microscopy sample preparations were always prepared from the most concentrated available stocks (PBS 20x, PFA 36%) delivered from verified commercial sources or directly from the components in form of a powder. Powder components were dissolved in Milli-Q® ultrapure water (Merck-Millipore) to the desired concentration and filtered through a 0.22 μm syringe filter into piranha-treated glassware (see below). Stock solutions were stored at +4 °C or -20 °C. To prepare solutions from concentrated stocks, these were diluted with ultrapure water and filtered through a 0.22 μm syringe filter (TPP, 99722) into piranha-treated glassware. Purity of all used solutions, including the ultrapure water, was periodically tested on a single molecule microscope setup.

All glassware was cleaned by the treatment with piranha solution (a mixture of concentrated sulphuric acid (Lach:ner, 10055-A96) and 30% hydrogen peroxide (Lach:ner, 10064-A30), ratio 3:1) for at least 45 minutes followed by several washes with ultrapure water, until all traces of acidic solution were removed. This treatment was done in a periodical way with all used glassware to ensure its quality for storage of solutions intended for SMLM imaging.

3.4.2 Imaging surface preparation

For fluorescence microscopy, we used superfine glass coverslips (Marienfeld; High Precision thickness no. 1.5H, 12 mm 0117520, 18 mm 0117580, 25 mm 0117650). SMLM microscopy also requires extremely clean optical surface to avoid uncontrolled background signal. The most effective and rapid method is to submerge coverslips for 30 minutes into freshly prepared piranha solution. Preparation of fresh piranha solution is strongly exothermic reaction; the solution is highly corrosive. To avoid corrosion of metal-based racks, highly resistant racks made out of Teflon were used. After piranha solution treatment, coverslips were extensively washed with ultrapure water (5-10 rounds). For security reasons, the piranha treatment is often replaced by a less aggressive method (see below).

In many laboratories, washing of coverslips is performed with strong alkaline solutions (1M KOH) combined with sonication. This method was not sufficient for our purpose. Therefore, we evaluated the method employing Hellmanex solution, which is often used in fluorescence spectroscopy laboratories for cleaning cuvettes. Fortunately, the method produced coverslips which could be used for SMLM. In brief, coverslips stacked in Teflon racks and placed in a beaker, were submerged into Helmanex III solution (HelmaAnalytics) diluted to 2% in ultrapure water and incubated at 56-80 °C overnight using temperature-controlled water-bath. Afterwards, the coverslips in a beaker were sonicated in a heated sonication bath for 30 minutes at 80 °C. Hellmanex solution was aspirated and washed in the ultrapure water 5 times. Another 30 minutes sonication was applied for coverslips in ultrapure water. Again, coverslips were washed 5 times with ultrapure water. Quality of cleaning was regularly controlled using the single molecule surface and SMLM imaging and compared to piranha-cleaned coverslips. Cleaned coverslips can be stored for maximum 3 weeks but has to be kept submerged in the ultrapure water with a cover.

It is very important to omit (or minimise) the use of any plasticware for single molecule fluorescence microscopy, including SMLM. Plasticware contains residues of plasticizers used during their production. Their organic nature interferes with single molecule measurements since they often exhibit fluorescence. These molecules are released into the solutions stored in the plasticware.

3.4.3 Coating of imaging surface

Imaging surface was coated with a freshly prepared and filtered 0.001% poly-*L*-lysine (Sigma-Aldrich, P4707) solution in ultrapure water or 2M glycine (Sigma-Aldrich, G7126) solution in the ultrapure water. The incubation last for 15-30 minutes in the closed glass Petri dishes or multi-well plate at room temperature in the laminar flow box. Afterwards, the coating solution was removed, and the coverslips were washed once with the ultrapure water prior to the seeding of cells. PLL-coated coverslips could be dried and stored for several weeks. Only freshly prepared glycine-coated coverslips were used. Drying of glycine-coated coverslips would lead to the precipitation of glycine and deformation of the coating structure.

3.4.4 Immobilisation of cells on coverslips and fixation

Transfected cells from two shots (1 million of cells) were collected by centrifugation at 500 rcf for 5 minutes. After a brief wash with warm PBS, cells were resuspended in 500 μl of PBS or colour free RPMI, respectively and spread over the imaging surface. For live-cell imaging, cells were immediately imaged on the microscope. For imaging of fixed cells, the cells were allowed to attach to the coated surface for 10 minutes at 37 °C. Afterwards, the PBS was replaced with filtered, pre-warmed (37 °C) fixation solution composed of 4% formaldehyde (Electron Microscopy Sciences, 15714) and 2% sucrose (Sigma-Aldrich, S7903) dissolved in PBS. Samples were incubated for 30-45 minutes at room temperature. Fixation was stopped by a quick wash with the bleaching solution composed of 50 mM NH4Cl (Merck, 101145) in PBS, followed by another wash with the same solution. Second wash included the incubation of the sample for 5 minutes. The cells were further washed by three rounds of PBS. The specimens, which were not labelled with antibodies, were imaged after loading of fiducials.

3.4.5 Fiducial markers loading

For drift correction during the SMLM data analysis we used in-sample included fiducial markers. For this purpose we loaded 200 nm colloid gold beads (British-Biocell International, EM.GC200) into the sample. Coverslips mounted in ChamLide holder (Live Cell Instruments, CM-B25-1) were once washed with solution of 0.9% NaCl (Merck, 7710) in ultrapure water. Samples were then incubated with gold beads diluted to 1:10 in 500 μl of 0.9% NaCl for 5 minutes. Resting fiducials were removed and quickly washed once with 0.9% NaCl and PBS. For imaging PBS was used.

3.4.6 Immunohistochemistry

Fixed cells were first blocked with blocking solution, composed of 5% bovine serum albumin (BSA; Sigma-Aldrich,) in PBS, for 1 hour. Afterwards, the staining with Alexa® Fluor 647-conjugated primary antibodies against human CD4 (OKT4, 1:100, Biolegend) or human CD45 (MEM-28, 1:2 000, ExBio) was started. The antibody stock solutions were diluted in Blocking Solution. Staining was performed at ambient temperature overnight in dark in a humidity chamber to avoid drying of the solutions. After removing surplus antibodies by washing cells three times for 5 minutes in PBS, the cells were post-fixed with fixation solution for 5 minutes at room temperature and washed 5 times in PBS.

3.5 Fluorescence microscopy

Several microscopy approaches were used in this work. In the following sections, the methods will be described including minor deviations from the sample preparation described above, microscope setups (hardware), imaging conditions, data processing and data analysis. The methods are noted according to the projects.

3.5.1 Software equipment

For SMLM analysis rapidSTORM (Wolter *et al.*, 2012), and ThundersTORM ImageJ plugin (Ovesný *et al.*, 2014) was used.

For 3D analysis TRABI/dTRABI ImageJ written plugin/macros were used (Franke *et al.*, 2020, 2017; van de Linde, 2019).

For SOFI analysis a MATLAB script package was used (Geissbuehler *et al.*, 2012; Lukeš *et al.*, 2017).

MATLAB® (ver. 2016a, MathWorks®) was used to run home written image analysis and data analysis scripts.

ImageJ/FIJI software package (Rasband, 1997; Schindelin *et al.*, 2012) was used for processing of acquired data.

3.5.2 Project 1 and 2.

3.5.2.1 Confocal microscopy I: Single channel live cell imaging.

Imaging of living cells expressing fluorescently tagged proteins was routinely performed on a modified Olympus Fluoview 1000 setup (Olympus) equipped with environmental chamber (OKO-Lab) to keep cells at 37 °C and 60× objective (UPlanSApo, NA = 1.2 water immersion; Olympus). For excitation, 488 nm solid state laser (Sapphire, 20mW; Coherent) and 532 nm picosecond pulsed diode laser (TopTica, 4mW; PicoTA 532) were used. Fluorescence was detected in a single channel mode on PMT detectors equipped with selective dichroic mirrors and blocking filters (Olympus). Transmitted light detector was employed for a brightfield imaging. FluoView 1000 software (Olympus) was used to operate the microscope and for image acquisition.

Data processing.

The acquired images were only minimally corrected for brightness levels. Finally, the fluorescence and brightfield images of the cell were projected as a compound of individual images. All done in ImageJ/FIJI software package.

3.5.2.2 Confocal microscopy II: Live-cell colocalisation studies

A day before imaging, cells were transiently co-transfected with the proteins of interest fused to GFP and intracellular markers fused to mCherry/mRFP fluorescent protein. For colocalisation studies of proteins mutants with selected markers of cellular organelles, two-colour imaging of living cells was performed at the Microscopy Centre of IMG, Prague, Czech Republic. Leica SP5 TCS AOBS Tandem laser scanning confocal microscope equipped with hybrid detectors (HyD, Leica), 63× objective (HCX PLApo, NA = 1.3 glycerol immersion, temperature corrected; Leica) and the environmental chamber with temperature and CO_2 control (OKO-Lab) was used in a two-channel acquisition mode. Green and red fluorescent proteins were excited with 488 nm argon laser (100 mW, Leica) and 561 nm diode-pumped solid-state laser (DPSS, 10mW; Leica), respectively. Transmitted light detector was used for brightfield imaging. LAS AF image software (Leica) was used to operate the system.

Data processing.

Acquired images were corrected for brightness in all channels, where green represents signal from the protein of interest, red for the intracellular organelle marker and greyscale as brightfield image. Merged image was generated by overlaying the artificially coloured signals from fluorescent proteins. FIJI/ImageJ software package was used for all adjustments.

3.5.2.3 Confocal microscopy III: Quantitative membrane localisation analysis in living cells

A day before imaging, the cells were transiently co-transfected with the proteins of interest fused to GFP and wild-type LAT protein (LAT-WT) fused to mCherry fluorescent protein. LAT-WT was used as a control for the localisation of a native TRAP. Quantitative data on living cells were acquired at the IEM, Prague, Czech Republic. Zeiss LSM 510 laser scanning microscope was used in sequential two-channel image acquisition mode and the environmental chamber was set up to 37 °C and 5% CO_2 to support the vitality of studied cells. Fluorescence signals of GFP and mCherry were excited by 488 nm argon laser (50 mW, Zeiss) and 561 nm DPSS laser (20 mW, Zeiss), respectively. 100× objective (PlanApochromat, NA = 1.4 oil immersion; Zeiss) was used and the fluorescence was recorded on PMTs equipped with 505-550 nm band-pass and 580 nm long-pass filters, respectively. The system was operated by LSM software (Zeiss). Acquired images were analysed without a prior signal level adjustment.

Quantitative data analysis.

For the quantitative analysis of the protein localization at the plasma membrane, the acquired images were first manually thresholded to remove the noise detected outside of the cell. Then, the regions (pixels) of the cell body and cell cortex were manually selected in a synchronous manner for both channels. The relative plasma membrane localization for a protein of interest was calculated as the ratio of the green and red signal in each selected pixel, where red signal was taken as a reference for maximal plasma membrane expression of LAT WT in each cell (for more details see attached Chum *et al.*, 2016).

3.5.3 Project 3.

3.5.3.1 TIRF microscopy I: Cell spreading assay.

Cell spreading and viability experiments were performed on a home-build inverted microscope system (IX71, Olympus) equipped with the environmental chamber (OKO-Lab) set up to 37 °C. Original setup of the microscope built by Aleš Benda and described in previous work (Lukeš *et al.*, 2017) was largely redesigned and rebuild by myself to omit the original Olympus TIRF module, which was causing inhomogeneities in the illuminated area and dramatically reduced the laser power at the objective. Because high intensities are required for SR imaging, that was also performed on this setup (see below).

The single fluorescent molecule TIRF microscope setup as of 2020 (Figure 21; by Tomáš Chum and Peter Kapusta):

Lasers with dedicated maximal outputs 100mW 405 nm and 100mW 643 nm (both Cube, Coherent), 150mW 488 nm and 150mW 561 nm (both Sapphire, Coherent) were used for the excitation. There were two options for detection of the fluorescence emission. i) an EMCCD camera (iXon DU-897, Andor) connected to an image splitter output (Optosplit II, Cairn Research) for simultaneous recording of 2 channels and ii) a sCMOS camera (Zyla-4.2-CL10, Andor) connected to the eyepiece side port of the Olympus IX-71 microscope body. Two acousto-optic tuneable filters (AOTF; AOTFnC-400.650-TN, AA Optoelectronics) were controlled via digital-analogue fast switching pulse generator (DA4300, Technical Instruments) and provided fast laser line switching and synchronization with camera acquisition. One AOTF controlled grouped laser lines with 405 and 488 nm, the other one laser lines with 561 and 643 nm. The two laser line outputs were combined using a dichroic mirror in the illumination path and focused into the back focal plane of the objective. Three objectives were positioned on the objective carousel of the microscope: 10× objective (UPlanSApo, NA = 0.4 air; Olympus), 60x (UPlanSApo, NA = 1.2 water immersion; Olympus) and 100x (UApoN, NA = 1.49 oil immersion; Olympus). Objective-based total internal reflection illumination was obtained using manual micrometre-scale tilting mirror mechanism in the excitation pathway (KCB2C/M, Thorlabs).To achieve maximum pixel size of a 100 nm per pixel, the system is further equipped with a 1.6 times magnifying lens in the emission path. The system was operated and synchronised by a home written control system based on Labview (programmed by Aleš Benda; version 2011) or by µManager software (version 1.4.22, resp. version 2.0-beta; Edelstein *et al.*, 2014).

Sample preparation.

Cultured Jurkat CD4 KO transiently transfected with pXJ41-CD4-wt-eGFP and eGFP-LifeAct-mRuby2 plasmids were harvested and transferred into colour-free RMPI medium supplemented with 2mM L-glutamine, 10mM HEPES pre-warmed to 37 °C. Ultraclean coverslips were placed into a ChamLide holder equipped with tubing adaptors (Live Cell Instruments) and covered with a coating solution. Cells were injected onto the ChamLide chamber attached to the microscope stage immediately after the removal of the coating fluid through the connected tubing. Landing cells were followed under the transmitted light and the fluorescence was recorded on EMCCD camera using TIRF illumination immediately after forming the first contact with the coated coverslip. Fluorescence signal was split into two distinct areas of the camera chip by the OptoSplit II emission light splitter. Optosplit was equipped with a filter cube holding a 562 nm long-pass dichroic mirror (Semrock, FF562-Di03-25x36), a green filter in the GFP channel (Semrock, FF02-525/50-25) and an orange filter in the mRuby channel (Semrock, FF01-607/70-25). The system was operated by µManager software (version 1.4.22). The imaging was performed at 37 °C.

For each cell 1 200 frames were taken at one second intervals with 50ms exposure time and EM gain set up to 100. Time lapse image stacks were used for line profiles analysis set and generation of video sequences.

Line profiles.

Distribution of signal intensity over the areas covered with T-cell body was analysed by at least three line profiles per cell using commands of the FIJI/ImageJ software package.

Video editing.

Captured time lapse stack was manually thresholded to adjust the brightness of all images to the same level and then converted into movie file using command FIJI/ImageJ software package.

3.5.3.2 Bright-field microscopy: Cell viability assay

Cells transfected with mTurquoise-Farnesyl-5 (Addgene bank, #55551) were transferred into colour-free RPMI medium (Gibco) supplemented with 2mM L-glutamine, 10mM HEPES, NEA and 10% FBS containing 25 µg/ml (w/v) Calcein-AM viability stain (eBioscience, 65-0853-39) and incubated for 10 minutes in the incubator. Cells were transferred into fresh colour free-RPMI medium supplemented with 2mM L-glutamin and 1:20 diluted 7-Amino-Actinomycine D (7 AAD) viability stain (eBioscience, 00-6993-50) and incubated for 5 minutes. Cells were then transferred onto the coated coverslips placed in the ChamLide chamber. Imaging was performed from the time of landing for 30 minutes with ten-minute intervals. Two randomly selected regions of interest (ROIs) were acquired for each time point to avoid the effect of photo destruction. Acquisition was performed on the same setup as described in Project 1: Confocal microscopy I: Single channel live cell paging. In this case additionally equipped with mercury epifluorescence lamp (Olympus), appropriate selection filter sets for GFP and RFP imaging (Olympus), respectively, 10× objective (UPlanSApo, NA = 0.4 air; Olympus) and sCMOS camera (Zyla-4.2-CL10, Andor) connected to the right-hand side port of the microscope body. Calcein and 7AAD were excited with the epifluorescence lamp using GFP or RFP channel. Fluorescence was recorded with 100 ms exposure time. Cells were also imaged under the transmitted light to control their morphology. Acquisition was controlled by the µManager software (version 2.0 beta). The experiment was held on at 37 °C.

Data processing.

Five frames per channel and ROI were captured for each time point. Frames were then summed up to get the final image for analysis. Cells were counted as local maxima in each channel. The dying cells were calculated as a percentage of 7AAD-positive cells from all green calcein positive living cells. All handling and processing was performed using FIJI/ImageJ software package.

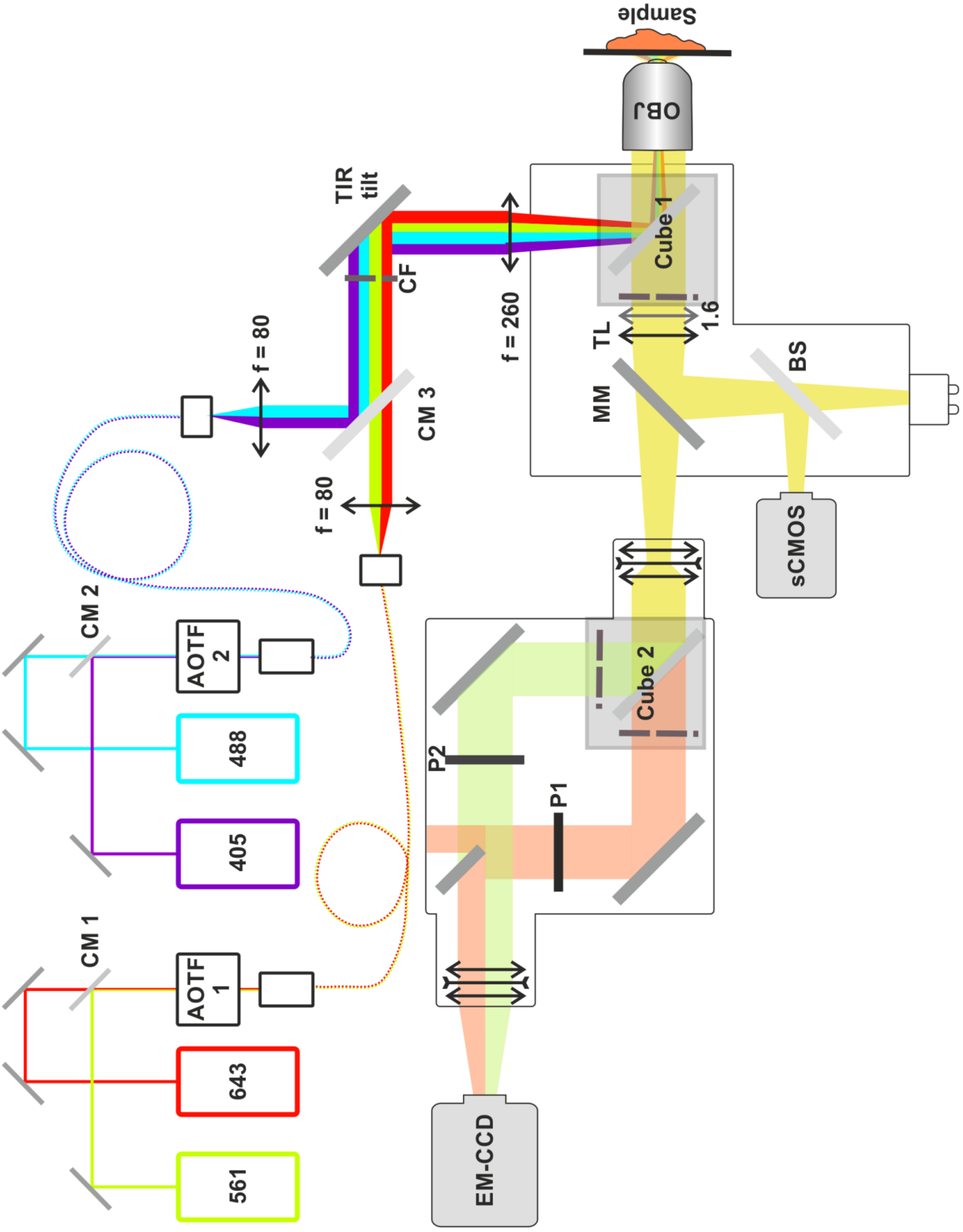
561
643
AOTF 1
CM 1
405
488
AOTF 2
CM 2
f = 80
f = 80
CM 3
CF
TIR tilt
f = 260
Cube 1
TL
1.6
MM
BS
OBJ
Sample
sCMOS
Cube 2
P1
P2
EM-CCD

FIGURE 21: Scheme of our home-built single-molecule widefield microscope

Excitation lasers (405, 488, 561 and 643 nm) are grouped into pairs and aligned into optical fibres (561 and 643 nm yellow-red, 405 and 488 nm violet-blue lines) using a combination of dichroic mirrors (CM1, CM2) and the acousto-optic tuneable filters (AOTF1, AOTF2). The output of the optical fibres is collimated with achromatic lenses (f = 80 mm). The two pairs of excitation paths are merged on the dichroic mirror CM3. The laser beam is spectrally cleaned up using the quad band laser cleanup filter (CF) and levelled up through a periscope to the back of the microscope body. Tilting mirror is used to laterally move the direction of the light beam required for the total internal reflection illumination (TIR tilt). At the entrance to the microscope body, the collimated laser beam is focused with achromatic lens (f = 260 mm) to the back focal plane of the objective. To separate the emitted fluorescence from the excitation light, a specific dichroic mirror is combined with the appropriate blocking filter in a filter cube (Cube 1). The fluorescence is then focused by the tube lens (TL) directly into the eyepiece or via the optional 50:50 beam-splitter (BS) onto a superfast sCMOS camera. Additional magnification can be introduced by sliding 1.6 times magnifying lens. By removing the moveable mirror (MM), the fluorescence is directed through a side-port of the microscope into the Optosplit II. There, the fluorescent light can be divided by the filter cube (Cube 2) using specific filters and dichroic mirror for the appropriate fluorescence wavelengths (simultaneous acquisition of two different fluorophores) or using 50:50-splitter for BP TRABI measurements. To achieve the light path difference for a BP mode, additional lenses are inserted into ports P1 and P2. For more details on the used optical and opto-/electromechanical components, please refer to the previous chapter.

3.5.3.3 TIRF microscopy II: Calcium measurements using genetic probe (with the help of Daniela Glatzová)

The microscope setup.

For imaging calcium influx, a home-built inverted microscope system (IX73, Olympus) equipped with 488 nm laser (Sapphire, 200 mW; Coherent) and AOTF was used. Fluorescence emission was detected by an EMCCD camera (iXon ULTRA DU-897U, Andor) connected to the camera port through two-channel image splitter (Optosplit II, Cairn Research). Laser was focused on the back focal plane of a 100x objective (UApoN, NA = 1.49 oil immersion; Olympus). TIRF illumination was achieved the same way as on the setup for live-cell imaging (see **TIRF microscopy I: Cell spreading assay.** for details) and the system was controlled by μManager software (version 1.4.20). Images were taken in 500ms intervals with the exposure time of 50 ms and camera EM gain set to 200.

Sample preparation.

Source plasmid encoding genetic ultrafast calcium sensor GCaMP6f_u was a kind gift from Katalin Török and Silke Kerruth (St George's, University of London). Coding sequence was amplified using primers AATAGATCTGCCACCATGGGCTGCGTGTGCTCCTC and AATGGATCCTCACTTCGCTGTCATCATTTGTACAAA and subcloned into pXJ41 vector via BglII and BamHI restriction site as described before (see **Publication 1:** Chum *et al.*, 2016).

For the measurements, the coverslips were coated with PLL or Glycine solution as described above. For positive control, coverslips were coated with OKT3 (anti-CD3ε) antibody in the final concentration of 0.01 μg/μl in PBS for 30 minutes at 37 °C. Coverslips were fast washed with PBS and used within a day.

Coated coverslips were mounted into the ChamLide holder, filled up with 500 µl of colour-free medium, placed on the microscope and focused on the focal plane prior the acquisition. For the experiment, cells transfected with GCaMPf$_u$ were washed with PBS and resuspended in colour-free RPMI medium supplemented with 2mM L-glutamine, 10mM HEPES, 1mM $CaCl_2$ and 1mM $MgCl_2$ and dropped onto the prepared coverslip while running the image acquisition.

Data processing.

Calcium influx was quantified as a mean fluorescence in cells immobilised on coated coverslips over the period of 10 minutes. FIJI/ImageJ software was used for the analysis. The peak intensity maxima $I_{(max)}$ was determined as a maximal value using Excel® software (Microsoft). The kinetics of fluorescence representing the calcium influx was quantified as ratio:

$$\frac{I(\boldsymbol{max})}{I(\boldsymbol{max}+\mathbf{5}\boldsymbol{min})} \quad \text{and} \quad \frac{I(\boldsymbol{max})}{I(\boldsymbol{max}+\mathbf{10}\boldsymbol{min})}$$

The terms $\mathbf{I_{(max+5min)}}$ and $\mathbf{I_{(max+10min)}}$ represent time points 5 minutes and 10 minutes, respectively, after the maximum calcium response. To avoid the impact of fluorescence intensity fluctuations all intensity maxima were calculated as an average of 10 frames.

3.5.3.4 Confocal microscopy IV: 3D imaging of CD45 and CD4 in fixed Jurkat T cells

A day before imaging, the cells were transiently transfected with CD4-WT fused to GFP. Cells were then immobilised on glycine-coated coverslips, fixed and CD45 was stained using specific antibodies (see **Immunohistochemistry** for details). GFP signal was followed to localize CD4. Three-dimensional confocal imaging on fixed samples was performed on at the Imaging Methods Core Facility of BIOCEV, Vestec, Czech Republic. Leica TCS SP8 WLL SMD-FLIM microscope in tandem two-channel acquisition mode was used for acquisition. The excitation was done by white light laser source (WLL with 488/561/633 selected laser lines; Leica). The 63x objective (PL APO CS2, NA = 1.4 oil immersion; Leica) was used and the fluorescence was recorded on hybrid (HyD, Leica) detectors.

Data processing.

Acquired images were slightly corrected for brightness in all channels, where green represents signal from CD4 and magenta CD45. Merged image was generated by overlaying the artificially coloured recorded images of fluorescent proteins. FIJI/ImageJ software package was used for all adjustments.

3.5.3.5 Three-dimensional dTRABI microscopy

The microscope setup.

For recording dTRABI data, inverted microscope (IX71, Olympus) equipped with a nose-piece stage (IX2-NPS, Olympus) and a 60x objective (PlanApo, NA = 1.45 oil immersion; Olympus) was used. Biplane imaging was performed using a two-channel image splitter with twofold magnification (TwinCam, Cairn Research) equipped with a 50/50 beamsplitter (Cairn Research) and two EMCCD cameras (Ixon 897 and Ixon Ultra 897, Andor). Cameras were synchronized by a pulse generator (DG535, Stanford Research Systems). 3D calibration experiments were performed by moving the objective with a piezo scanner (Pifoc, Physik Instrumente) driven with a servo controller (LVPZT E-662, Physik Instrumente) (Franke *et al.*, 2017).

Data processing.

For the analysis in dTRABI the simplified equation of photometric ratio of both planes was used:

$$\boldsymbol{I_{Fit,1,2(Z)}} = \frac{\boldsymbol{I_{Fit,1}} - \boldsymbol{I_{Fit,2}}}{\boldsymbol{I_{Fit,1}} + \boldsymbol{I_{Fit,2}}}$$

Where $\mathbf{I_{Fit,1,2(Z)}}$ stays for the final ratio of both recorder planes. $\mathbf{I_{fit,1}}$ and $\mathbf{I_{fit,2}}$ represent fitted intensity of the signal in the first, and second plane, respectively. Simplification is based on the fact that for reasonable large radii the reference intensity converges in the same way for both planes, therefore it can be omitted. This simplified version reduces the computational power consumption, makes analysis quicker and do not cancel so many overlapping signals in denser regions like original TRABI analysis (Franke *et al.*, 2017).

Axial localisation distribution analysis.

Localisation files obtained from rapidSTORM were loaded and processed by FIJI/ImageJ custom written scripts (van de Linde, 2019). Localisation coordinates in x, y and z were used to generate a quantitative stack of 2D images with 20 nm pixel size with separation of 20 nm in z, where the numeric value in each pixel represented the number of localisations. Z-stacks were then segmented into defined ROIs. The interior of analysed cells without the edges was selected manually to serve as boundary ROI. Within the main ROI, a set of 2×2 µm areas was automatically generated. Only ROIs with more than 75% covering were kept for the analysis (≥3 μm^2). The localisation density of each ROI was analysed by accumulating the grey values within the stack and plotted as a function of z with double Gaussian profile fitting. More details in results and the attached paper (Franke *et al.*, 2020).

3.5.3.6 Two-colour lateral SMLM for surface receptor colocalisation

Two-channel SMLM experiments were performed on a Nikon Eclipse Ti microscope equipped with 405, 488, 561 and 640 nm laser lines. A 100x objective (CFI super-resolution Apo TIRF, NA = 1.49 oil immersion; Nikon) with 1.5x postmagnification lens was used to achieve an optical pixel size of 104 nm. Before imaging Tetraspeck beads (ThermoFisher Scientific) on glass surface were imaged with altering 561 nm and 647 nm excitation to create a nanometre precise map for correction of a chromatic shift.

Cells transiently transfected with pXJ41-CD4-WT-mEOS2 were prepared and stained for CD45 as described above. Prior to acquisition, cells were irradiated in the epifluorescence illumination mode to turn out-of-focus emitters into dark state. Then the system was turned into HILO illumination scheme. The length of recording was set to capture the majority of emitters. Typical acquisition lengths were 60 000-120 000 frames for Alexa Fluor 647 channel and 30 000-60 000 frames for mEos2 channel. The acquisition times were set to 20 ms and 16 ms in the single- and dual-colour cases, respectively. The fluorescent protein mEos2 was exited with 561 nm laser beam and activated by 405 nm laser pulses with increasing power density over time to create an almost homogenous signal density.

Data processing.

For localisation of emitters the FWHM was set as free parameter in the range of 275-750 nm for both channels. The 561 nm excitation channel was then mapped onto the 647 nm channel after the localisation by applying the correction nanometre scale map gained from the Tetraspeck beads measurements.

3.5.3.7 SOFI microscopy

For SOFI, cells were prepared and stained with antibodies as for SMLM (see section **Microscopy sample preparation**). For the imaging, the samples were covered with imaging buffer containing glucose oxidase scavenger system and thiol reduction agent (buffer composition attached). Measurements were performed on the home build setup described in the **TIRF microscopy I** section. First, the emitters were turned to the dark state by a fast and intense illumination in the widefield mode. Then the excitation 643 nm laser line was turned to the TIRF illumination mode. The activation 405 nm laser was tuned to achieve ~100-500 fluorescent events per frame over the whole acquisition of ~10 000 images, to get at least 3rd cumulants order of SOFI analysis. Analysis was performed using home-written scripts in Matlab (Lukeš *et al.*, 2017).

4 RESULTS

4.1 Project 1: Quantitative confocal microscopy as a tool for elucidating sorting mechanism(s) of TRAPs.

Transmembrane adaptor proteins (TRAPs) are integral membrane proteins which have no enzymatic activity on their own. Despite that, TRAPs are important signalling nodes regulating development and function of mammalian white blood cells (Hořejší *et al.*, 2004; Štěpánek *et al.*, 2014). Their function is primarily linked to the plasma membrane and signalling of surface receptors, but the determinants that regulate their targeting to the plasma membrane are not fully understood yet. Members of TRAP family have only a short extracellular part, which consist of 3-20 amino acids. Therefore, it is possible that their sorting motifs are hidden in the transmembrane domain (TMD) or in the intracellular part. We also expected the presence of some signals for the exit from the endoplasmic reticulum (ER-exit; discussed below) and protein internalisation (not studied in this work) in the intracellular part. For that reason, our study was focused on the impact of properties of TMDs with the proximal sequences including palmitoylation sites and, to some extent on the intracellular part during the sorting of TRAPs.

Based on findings from biochemical studies, palmitoylation is thought to be a protein targeting signal for lipid rafts. These putative sphingolipid and cholesterol-enriched membrane microdomains should serve as interaction pools during the development and activation of white blood cells (Hořejší, 2005, 2004; Hořejší *et al.*, 2010; Hořejší and Hrdinka, 2014; Levental *et al.*, 2010; Štěpánek *et al.*, 2014). Due to a small size and highly dynamic character of lipid rafts, any direct evidence of their existence and of accumulation of palmitoylated proteins therein is still missing.

Therefore, the impact of palmitoylation on the plasma membrane localisation of TRAPs in relation to the properties of their TMD was investigated. The quantitative fluorescence confocal microscopy was applied to determine the efficiency of protein sorting on a set of mutated TRAPs. For this purpose, the proteins of interest were fused with GFP. Such fluorescently labelled proteins were then introduced into living human T cells using genetic modification techniques. The design of mutants was adjusted to monitor the impact of the TMD length and amino acid sequence on sorting of LAT, PAG and NTAL (selected representative TRAPs) in the absence or presence of protein palmitoylation.

It was already reported that non-palmitoylated LAT is trapped in the Golgi apparatus, however, no comprehensive study has been performed to understand the mechanism or rules of how palmitoylation affects the process (Hundt *et al.*, 2009). Instead of higher stability of LAT mutant on the plasma membrane, the opposite was found. Our work confirmed mislocalisation of non-palmitoylated LAT mutant that carried serine residues instead of cysteines. This phenomenon was evident exclusively for LAT. The other studied TRAPs – PAG and NTAL – did not exhibit a significant block in sorting. The exchange of potential palmitoylation sites represented by cysteine residues for serines partially reduced their sorting efficiency to the plasma membrane. Moreover in case of PAG and NTAL this swap caused the toxicity of the mutant protein when expressed in T cells. Similarly, no effect was observed for non-palmitoylated mutants of CD4 and hybrid proteins composed of CD4 extracellular part fused to the TMD and the intracellular part of LAT.

In addition, a strong accumulation inside the cell of non-palmitoylated mutants of LAT and PAG lacking the intracellular part was observed. Such truncated LAT mutant lacking palmitoylation sites was completely stuck in the ER. Analogously truncated PAG was detected also in some other cell compartments. Using *in silico* sequence analysis, DxE an YxxØ motifs (where x is any amino acid, and Ø is a bulky hydrophobic residue) were found at their C-termini. These sequences represented by DYESIS in PAG and DYENL in LAT serve as ER-exit motifs (Sevier *et al.*, 2000). Whether the ER-exit motif is sufficient to release the truncated LAT version from the ER have been also tested. For confirmation of this hypothesis, the minimal segment carrying the exit motif (SYDSTSSDYENLN) was fused directly to the truncated version of LAT composed of only its N-terminus and the TMD. The data indicate that this minimal segment can significantly restore the efficiency release of LAT variants from the ER (see **Figure 22**).

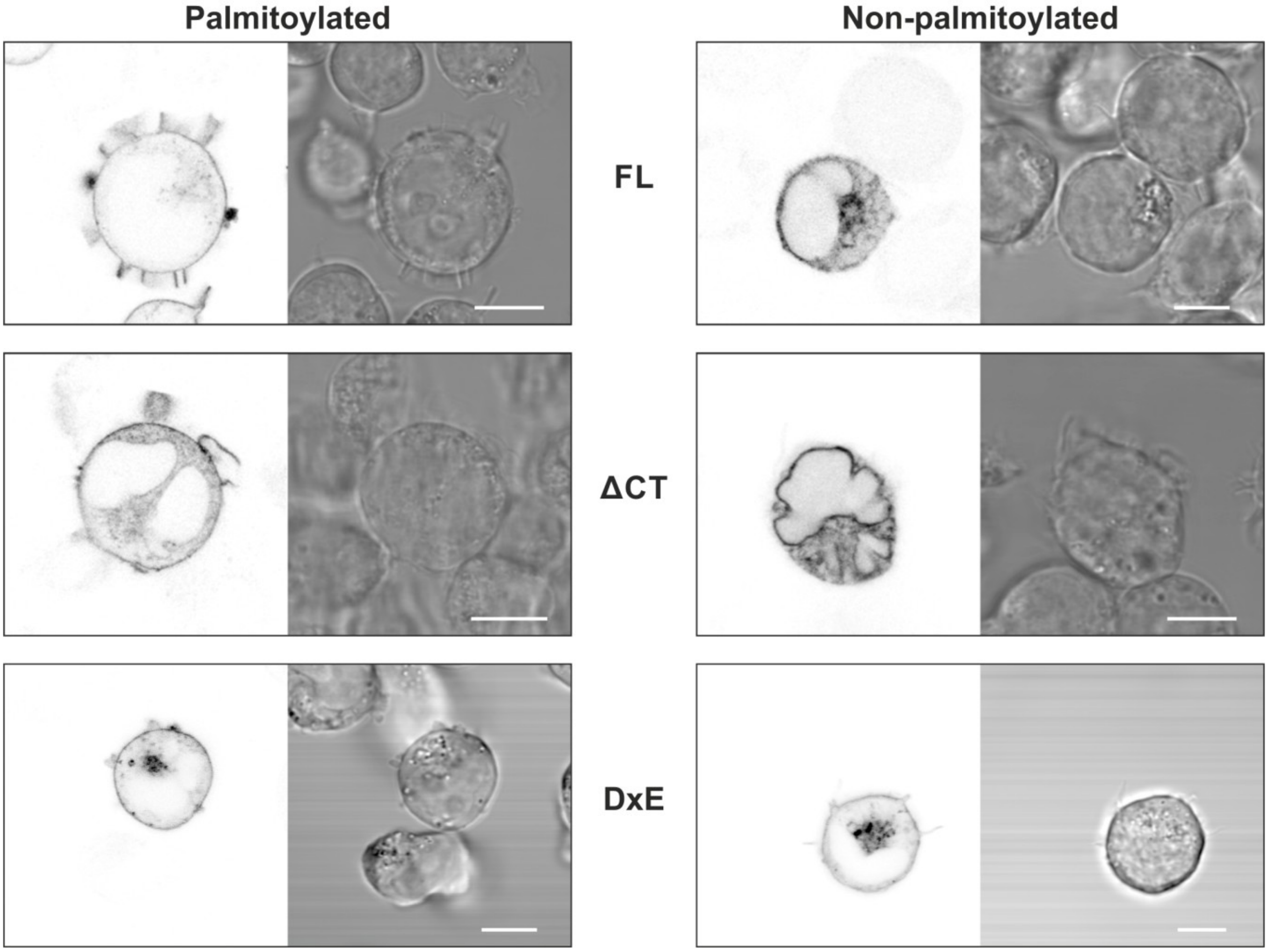

Figure 22: The impact of ER-exit motif on localisation of LAT

Confocal images of live Jurkat T cells transfected with GFP LAT mutant versions. First row: image of cells showing the impact of palmitoylation. Second row: impact of palmitoylation combined with C-terminal domain deletion. Third row: truncated version additionally carrying the DxE ER-exit motif on the intracellular part. Scale bars: 5 μm.

To test the impact of TMD physical properties on sorting of single spanning proteins, a model TRAP-like model protein with TMD composed of 19 hydrophobic amino acid residues (WWLLLLLLLLALLLLLLL) have been used. We expected that localisation of such a protein with suboptimal TMD would depend on some additional sorting signals. It was previously shown that proteins with TMD length of at least 21 hydrophobic amino acid residues are efficiently targeted to the plasma membrane (Sharpe *et al.*, 2010). We have designed and genetically engineered TRAP-like proteins based on the backbone from CD247 (also known as ζ chain of the T-cell receptor complex) but with its TMD replaced for the artificial LW19 sequence and some elements, which we expected to contribute to the protein localisation.

First, improved efficiency of the protein sorting to the plasma membrane by the electrostatic asymmetry of juxtamembrane sequences was demonstrated. The symmetric variant of LW19 TRAP-like protein with lysine residues on both sides was incompletely sorted to the plasma membrane. The protein was largely trapped in the intracellular compartments. The asymmetric variant with 2 glutamic acid residues at the luminal end of the TMD and 2 lysines at the cytosolic end were efficiently targeted to the cell surface. No such a difference was observed for TRAP-like proteins with TMD hydrophobic core extended to 25 amino acid residues.

Second, it was found that palmitoylation serves as a secondary signal for the plasma membrane sorting of TRAP-like proteins. Here, the TMD of LAT was replaced for LW19 sequence. This variant allowed the study of the effect of the absence or presence of the **C**VH**C** palmitoylation site from LAT on TRAP-like protein surface expression. Introduction of the palmitoylation motif in LAT with the symmetric LW19 TMD significantly improved its plasma membrane sorting compared to the non-palmitoylated variant with **S**VH**S** sequence. From the results a positive effect of palmitoylation on sorting of proteins with sub-optimal TMD length could be concluded.

In this work, it was shown that combination of quantitative 2-colour confocal fluorescence microscopy with DNA recombination techniques can provide a new insight into mechanisms regulating protein distribution in cells. For more details please refer to the attached **Publication 1:** Chum *et al.*, 2016.

4.2 Project 2: Confocal microscopy as a tool for elucidating the impact of kink-forming amino acids in the TMD of LAT (submitted)

The mechanism of LAT sorting control on the way to the plasma membrane is somehow different from other TRAPs, as shown in **Publication 1:** Chum *et al.*, 2016. Non-palmitoylated LAT variants are trapped in the Golgi apparatus and therefore they cannot perform their function. To further elucidate this difference, we focused on LAT TMD that contains highly conserved two proline and one glycine residues in the primary structure (ILV**P**CVL**G**LLLL**P**ILAMLMALCV). These amino acids were previously defined as typical helix-breakers (Levitt, 1978). The genetic engineering approach with confocal microscopy and all-atom molecular dynamic (MD) simulations were combined to determine function of these above mentioned helix destabilising amino acids in the α-helical structure of LAT TMD.

First, LAT TMD sequence was extended by adding six amino acids (LLLLLL or PILAML). Surprisingly, these changes did not overcome the essential role of palmitoylation in the LAT surface targeting. In addition, we found the accumulation of these variants in lysosomes, indicating increased degradation of the mutated protein.

Second, the role of Pro8, Gly12 and Pro17 residues was characterised using all-atom MD simulations. The data demonstrate a kink in the α-helix around the position Leu14, which was introduced by the presence of Gly12 and Pro17. The replacement of these conserved kink-forming amino acids for helix supporting residues (P8A, G12L, P17A and P8,17A) did not prevent the sorting of LAT mutants to the plasma membrane *in vivo*. Cells expressing LAT-P8A, LAT-G12L, LAT-P17A or LAT-P8,17A variants also indicated the same partial trapping of proteins in the Golgi aparratus as observed for LAT-WT. In addition, our model cell line J.Cam2.5 was lacking endogenous LAT, but its transfection with these LAT forms showed good calcium response to the activation stimulus indicating proper function of the mutants.

Interestingly, LAT-P8A, LAT-G12L and LAT-P17A mutation partially restored the surface localisation of the non-palmitoylated version (for more details, see **Publication 1:** Chum *et al.*, 2016). However, the plasma membrane sorting of these variants was incomplete. Large part of the expressed proteins remained in the intracellular membrane structures. No surface signal was detected in cells producing non-plamitoylated variant of LAT with native TMD (LAT-CS). Importantly, none of the non-palmitoylated LAT-P8A, LAT-G12L, LAT-P17A and LAT-CS mutants was able to respond to the stimulus, irrespective of their surface localisation.

We were thus interested in the organisation of LAT variants on T-cell surface. No differences in the nanoscopic organisation of palmitoylated LAT-P8A compared to LAT-WT were detected using super-resolution microscopy. Non-palmitoylated version of LAT-P8A formed patchy structures on the T-cell surface, but these cells were almost unable to make any contact with the imaging surface. This also indicates that T-cell interaction with the surface depends on LAT palmitoylation state or function (for more details see **Publication 3:** Glatzová *et al.*, 2020).

My contribution to this project was to characterise the colocalisation of prepared mutants with markers of intracellular compartments in living cells, live cell imaging of LAT versions with extended TMD and technical support and advice for the super-resolution microscopy measurements.

4.3 Project 3: Application of super-resolution fluorescence microscopy to study nanoscopic organisation of surface receptors on T cells (submitted)

CD4 delivers Lck kinase, which is crucial for T-cell development and activation, to the signalling hotspots of these immune cells. Therefore, it is important to understand the organisation of CD4 on the surface of T cells before and after stimulation.

To better understand the organisation of CD4 on the surface, super-resolution microscopy techniques were applied, as they allow the recognition of structures reaching the size of several tens of nanometres, well below the resolution limit of standard light microscopic methods.

In the previous work, T-cell surface distribution of CD4 and its non-palmitoylated mutant was projected onto planar 2D maps. Using 2D SOFI, The accumulation of CD4 in so-called high density regions (HDR; Lukeš *et al.*, 2017) have been demonstrated. But the surface of differentiated metazoan cells exhibits a 3D morphology (for mote details, see chapter **A brief insight into the topography of the plasma membrane (surface of T cells)**; Jung *et al.*, 2016).

Therefore there was a need for a quantitative 3D microscopy method with nanoscopic resolution. Collaboration with the founders of temporal, radial-aperture-based intensity estimation (TRABI; Franke *et al.*, 2017), Christian Franke (Max Planck Institute for CBG in Dresden) and Sebastian van de Linde (Strathclyde University in Glasgow) was established.

The original TRABI method achieved one of the best localisation precisions of all 3D super-resolution microscopic techniques. Its limitations were high demands on computational power, the problematic analysis of overlapping emitters and the lack of quantitative information about recorded molecules (Franke *et al.*, 2017). For our purpose, the original TRABI method required further development. The method was adapted for a rapid and direct analysis of axial emitter positions in combination with detailed quantitative analysis. These abilities were demonstrated in our work on nanotopography of receptors on the surface of immune cells.

The new and simplified approach is named direct TRABI (dTRABI) and is easily accessible for biologists (Franke *et al.*, 2020).

My role in this project was to develop and standardise sample preparation procedure that preserves the nanoscopic morphology of the cell surface during immobilisation on a glass surface (see also following chapters). I have prepared most of the samples for image analysis. This included, among other things, to provide a suitable labelling density to achieve the optimal dataset for reconstructing the distribution of receptors on the cell surface. In addition, I made a significant contribution to the interpretation of the measured data and, in close cooperation with our colleagues, created a reproducible protocol for image analysis using dTRABI. All these efforts led to the determination of nanoscopic 3D spatial organisation of CD4 and its non-palmitoylated variant on the surface of resting T cells.

It has been demonstrated that high density regions represents accumulation of CD4 on tips of microvilli-like structures of resting T cells. We have proven that this distribution is dependent on the palmitoylation state of CD4, since the non-palmitoylated mutant showed a random distribution over the rough T-cell surface. Segragation of CD45 molecule from the tips of microvilli-like structures was also demonstrated. CD45 localised to their shafts and basis. Overall, the results from resting cultured T cells indicate that these two molecules involved in TCR signalling are spatially separated from each other at the nanoscopic level. This spatial organisation may contribute to the regulation of their activity during T-cell activation.

The ability of dTRABI to characterise the spatial organisation of surface molecules at the single molecule level was proven using two different types of molecules with completely different behaviour. In addition, dTRABI provides quantitative information to the image of receptor distribution and offers a direct comparison of different molecules involved in membrane-related processes such as signal transmission. For more details, please refer to the attached **Publication 2:** Franke *et al.*, 2020.

4.4 Project 4: Development of a novel sample preparation method for 3D super-resolution imaging of cell surface molecules (manuscript in preparation)

Since single molecule localisation and super-resolution optical fluctuation imaging techniques are based on detection of particular fluorescent emitters, these methods are extremely sensitive to the signal-to-noise ratio (SNR). In other words, the image quality depends on the strength of non-specific background recorded together with the specific signal coming from labelled molecules of interest. The way to improve the SNR of super-resolution measurements was to maximally reduce the interfering background signal. This required identification of critical issues responsible for high background in tested samples (see **Figure 23**).

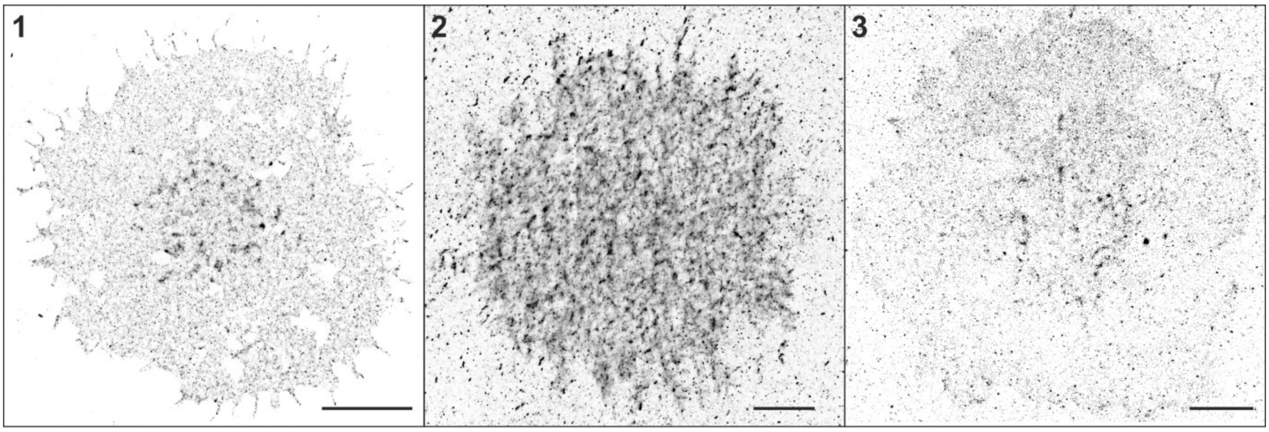

Figure 23: Sample preparation quality influences SMLM paging

J.CaM2.5 cells transiently transfected with LAT-WT-mEOS2 were immobilised on PLL-coated coverslips prepared using different approaches and analysed by PALM. (**1**) Image of a cell immobilised on the ultraclean coverslip. All solutions required for the sample preparation were made using ultraclean approach, which avoids the use of plasticware (see **Microscopy sample preparation** for more details). (2) Image of a cell immobilised on the PLL-coated coverslip cleaned using standard protocols. Solutions used for the sample preparation were stored in plastic tubes for several months at room temperature. Signal background originating from plasticware exhibits high fluorescence. High background is observed in cell-free areas. The signal originating from cellular structures was in this case strong enough for the super-resolution image reconstruction. (**3**) Image of a cell immobilised on PLL-coated coverslips cleaned using standard protocols as in (**2**). In this case background signal is comparable with a low signal emitted from specific structures on a cell. Such samples are nearly indistinguishable from the background in the cell-free areas. Scale bars: 3 μm in (**1**), 2 μm in (**2, 3**).

New procedure for the imaging surface treatment was developed. The protocol also includes the cleaning of the imaging surface itself, where the standard protocols used piranha solution or other chemically harsh conditions. To avoid the extremely oxidising piranha solution due the safety hazard linked to its use, the whole cleaning is now performed with Hellmanex solution. It is also a harsh chemical but the danger associated with its use is largely reduced. The cleaning is followed by extensive washing with ultrapure water (Note: only freshly prepared coverslips can be used for SMLM imaging; **Protocol 01** attached).

However, the critical discovery was that some fluorescent compounds are released from all plasticware; therefore plasticware needs to be omitted from the super-resolution sample preparation as much as possible. Essential is the storage of solutions, which should be always kept in ultra-clean glassware.

In addition, a new procedure of coating coverslips was developed. Extra treatment of the imaging surface with a glycine solution was previously used to suppress the non-specific background in single molecule imaging (Klein *et al.*, 2011; van de Linde *et al.*, 2011b). Nevertheless, when the 2M glycine solution is applied directly to the ultraclean glass surface, it forms the support that efficiently preserves the morphological details of seeded cells (**Protocol 02** attached). Currently, the proper physical nature of this coating is not fully understand yet, but based on atomic forced microcpy measurements, it behaves as a gel-like structure.

Several further characterisations of glycine-coated coverslips were performed, including stability tests under various conditions, in collaboration with Harsha Mavila from our laboratory. The coating is to some extent described in the **Publication 2**: Franke *et al.*, 2020. The experimental work is largely finished and the manuscript is being prepared for submission.

5 GENERAL CONCLUSIONS, DISCUSSION AND A FUTURE PERSPECTIVE

Today, proteins and their function were studied mainly by biochemical, biophysical and proteomic approaches (Hořejší, 2005; Hořejší *et al.*, 2004; Levental *et al.*, 2010; Štěpánek *et al.*, 2014). The disadvantage is that these methods are usually performed on a batch of thousands to millions of cells. Moreover, a complex sample preparation can destroy the information about the location of the studied protein. Therefore, the information about the single cell behaviour is lost.

In comparison, microscopic techniques can provide very detailed spatial information about molecules in individual cells. In their early days, microscopes used transmitted light from the sun or a bulb to illuminate a sample, and the obtained information was therefore limited to the overall shape of a studied organism. Since the introduction of fluorescence in the 1940s, the importance of microscopy in biology has further grown. The fluorescence enabled to label and visualise specific structures and molecules. The invention of laser scanning confocal microscopy in 1982 enabled imaging at the diffraction limit of the system. This opened new way to study subcellular structures such as mitochondria, Golgi apparatus, nucleus or centrioles. In contrast to electron microscopy, this can be done on a large number of samples (Masters, 2010). Even more, with the cloning and adaptation of green fluorescent protein (GFP) and its derivatives for cell biology (Prasher *et al.*, 1992), several structures could be imaged in living cells with high resolution and contrast.

The development of fluorescence microscopy continues and the state-of-the-art techniques are now able to overcome the diffraction limit of light. Some methods are able to provide the infomation at the level of single molecules. Alternatively, some methods allow to monitor the fast life events with acquisition speeds exceeding 50 Hz, or tracking of specific cells in the whole organisms or tissues, even though at the cost of lower resolution. As a result, biologists have become more independent of complex techniques such as electron microscopy, which is increasingly used for structural studies of molecules at atomic level.

My first work was focused on combination of molecular biology and standard fluorescence microscopy techniques (see **Publication 1:** Chum *et al.*, 2016). The aim was to understand new aspects of sorting of single spanning proteins in cellular membranes. Transmembrane adaptor proteins (TRAPs) were selected as model membrane proteins. These type III group proteins with a single transmembrane segment were selected because the influence of the transmembrane domain (TMD) and its physical properties on the protein distribution to and at the cell surface were studied. The effect of mutations in the TMD was readily identified and was not obscured by the presence of other TMDs, as would be the case of multi-spanning proteins. TRAPs also lack a larger extracellular domain that can be post-translationally modified. So, the effect of glycosylation, which was shown to affect protein sorting, could be disregarded.

According to the current model, which is based on the hydrophobic mismatch theory, the main sorting signal is encoded by the size (length) of the TMD. The length of the hydrophobic α-helical structure must correspond to the thickness of hydrophobic part of the target membrane compartment (Sharpe *et al.*, 2010). The composition of the phospholipid bilayer changes during the exocytic pathway from the endoplasmic reticulum (ER) to the plasma membrane. The amount of sphingolipids, cholesterol and other phospholipids with longer acyl chains increases and the thickness of the bilayer raises consequently (Bernardino de la Serna *et al.*, 2016; Cebecauer, 2012; Mitra *et al.*, 2004; Sharpe *et al.*, 2010). Also other membrane properties, such as asymmetry are dramatically changing along this pathway. Therefore, a set of GFP-fusion TRAP and TRAP-like proteins with mutations altering the length, hydrophobicity and membrane proximal sequences of their TMD was produced and those were studied with fluorescence microscopy in living or fixed human T cells.

Firstly, 3 proteins from TRAP family were selected: linker of activation of T lymphocytes (LAT), phosphoprotein associated with glycosphingolipid-enriched membrane microdomains (PAG) and non-T-cell activation linker (NTAL). TMD of these proteins have very similar hydrophobicity according to the HydrMCalc algorithm (Tossi *et al.*, 2002). The TMD of LAT and PAG is 23 amino acids long and thus corresponds to the thickness and properties of the plasma membrane as the target structure (Munro, 1995; Sharpe *et al.*, 2010). On the contrary, NTAL, with 19 amino acid-long TMD, should remain localised to the Golgi apparatus (Sharpe *et al.* 2010). All three proteins carry the internal proximal sequence containing the CxC or CxxC motif and are able to be palmitoylated (Štěpánek *et al.*, 2014). Despite the fact that no consensus palmitoylation motif has been found yet, it is generally accepted that similar sequence in the intracellular juxta-membrane position serves as a palmitoylation target (Roth *et al.*, 2002; Zeidman *et al.*, 2009). Indeed, palmitoylation of LAT, PAG and NTAL was experimentally proven (Brdicka *et al.*, *2000*; Brdička *et al.*, *2002*; Bunnell *et al.*, 2001). This is not common for all putative palmitoylated proteins listed in the database SwissPAlm (Blanc *et al.*, 2015).

The primary role of palmitoylation described so far is to regulate the association of myristoylated or farnesylated proteins with the membrane (Blaskovic *et al.*, 2014; Rocks *et al.*, 2010). Palmitoylation may also modify other protein properties such as conformation, formation of higher multiprotein complexes or cooperate with other posttranslational protein modifications in regulation of their function (Blaskovic *et al.*, 2013). Last but not least, palmitoylation is still considered as a protein targeting signal to putative sphingolipid and cholesterol-enriched membrane microdomains, also known as lipid rafts (Hořejší, 2005, 2004; Hořejší *et al.*, 2010; Hořejší and Hrdinka, 2014; Levental *et al.*, 2010; Štěpánek *et al.*, 2014). According to the bioinformatics data, this should mean that over 3 000 different human proteins localise to these dense structures. But direct and undisputable evidence of this phenomenon or even of the very existence of these structures in general is still missing.

Previous studies have shown that non-palmitoylated version of LAT is trapped in the inner membrane structures of the cell, mainly the Golgi apparatus (Hundt *et al.*, 2009). In this work, cysteine residues were exchanged for alanines. This means that they also affected the biophysical properties of the local environment, because alanines are non-polar and the presence of small alkyl side chain can change the local hydrophobic properties of the TMD. Theoretically, these properties should lead to the prolongation of the TMD and therefore to higher stability of such a protein. But the authors observed totally opposite result. Unfortunately, no more in-depth study has been performed to clarify this behaviour in the past studies (Hundt *et al.*, 2009; Tanimura *et al.*, 2006).

To avoid the interference with biophysical properties of the TMD, cysteines in the palmitoylation motif **C**VH**C** of LAT have been changed to serines, which share similar size, charge and hydrophobicity with the original amino. Similarly, **C**SS**C** motif in PAG and **C**VR**C** motif in NTAL were mutated accordingly to understand the effect of palmitoylation on TRAPs more generally.

Similar trapping of non-palmitoylated LAT in the Golgi apparatus as in the abovementioned study was observed and it indicated that the studied mutations probably did not lead to the TMD prolongation. This is also highlighted by the fact that similar mutations in the TMD of PAG and NTAL had negligible effect on sorting and both proteins readily localised to the plasma membrane. It is thus the specific character of LAT TMD, which causes dependency of the plasma membrane sorting of this protein on its palmitoylation state. LAT mutant CD4ex-LAT with fused glycosylated extracellular domain from CD4 did show the surface targeting independently on its palmitoylation state. This further indicated that palmitoylation can function as a secondary or minor sorting signal for proteins, which lack dominant determinants such as glycosylation, the appropriate TMD properties and/or TMD stability (see below).

Of note, the cells transfected with non-palmitoylated PAG and NTAL started to die after ~14 hours since transfection (data not shown). Only cells with low expression of these proteins were able to survive longer. We have not examined this phenomenon in more detail yet. The missing palmitoylation may alter nanoscopic organisation of non-palmitoylated PAG and NTAL on T-cell surface. First of all the conditions allowing higher expression of these mutants on the surface without affecting the viability of transfected cells has to be found. It will be also interesting to understand this phenomenon with respect to LAT, which behaves differently.

Interestingly, truncated versions of LAT and PAG lacking the intracellular C-terminal domain were partially trapped in the ER, with a significant predominance of LAT in the ER over its surface expression. PAG was distributed between the ER and surface almost equally. Similar difference between LAT and PAG was observed for the non-palmitoylated variants lacking the intracellular part. LAT was completely trapped in the ER but a small proportion of PAG still reached the surface. The intracellular part of both LAT and PAG contains the ER exit motif, specifically DYESIS in the C-terminal part of PAG and DYENL of LAT. These motifs fully comply with the rule that amino acid sequences DxE an YxxØ (where x is any amino acid, and Ø is a bulky hydrophobic residue) serve as a signal for membrane proteins to release the ER (ER-exit) (Sevier *et al.*, 2000). The positioning of these motifs to the C-terminus is evidently important for their function. The block of truncated LAT mutant in the ER was not completely released by the connection of outermost C-terminal sequence SYDSTSS**DYENL**N to the TMD. However, a significant increase in the localisation of such non-/palmitoylated LAT mutants on the surface confirmed the functionality of this motif in LAT (see **Figure 22**). It also supports the validity of this general rule.

This shows that sorting of these two proteins is evidently regulated by the primary sequence of their TMD in a different way. As mentioned above, sorting of LAT to the plasma membrane depends on palmitoylation and must be defined by the specific properties of its TMD, which must differ from the TMDs of other studied TRAPs (**Publication 1:** Chum *et al.*, 2016). LAT TMD contains two prolines and one glycine residues in its primary structure ILV**P**CVL**G**LLLL**P**ILAMLMALCV, which are highly conserved throughout the whole class of mammals. Proline and glycine are defined as helix-breakers in soluble and membrane proteins (Wilman *et al.*, 2014). No such amino acid is in the TMD of PAG, only single proline residue is in the luminal end of NTAL TMD.

All-atom molecular dynamics simulation of LAT TMD peptide embedded in a phospholipid bilayer indicate the presence of a kink at the Leu14 position, which is surrounded by the α-helix breaking amino acids glycine 12 and proline 17. The data were provided by the group of Prof. Lukasz Cwiklik in our institute. Simulation data thus support the influence of these typical helix-breakers on helical structures in water and membrane lipid environments (Levitt, 1978; Wilman *et al.*, 2014). It was also tested, whether mutating prolines or glycine in LAT TMD can stop LAT plasma membrane sorting dependence on palmitoylation (see **Publication 3:** Glatzová *et al.*, 2020).

The effect of shortening due the kink was tested by introducing 6 additional amino acids (LLLLLL and PILAML) next to the palmitoylation site and prolonging LAT TMD. However, this change did not overcome the dependence of LAT surface targeting on palmitoylation. Instead of better sorting driving LAT to the plasma membrane, these LAT variants were found in lysosomes and some unspecified intracellular structures which indicate further destabilisation of LAT. There are two possible scenarios what could have happened. First, another kink sould be introduced into the structure of TMD by adding another PILAML sequence to LAT TMD. However, similar results were observed for LAT with introduced six leucines. Second, LAT TMD could be prolonged to the extent that caused significant tilt and was recognised as an incorrectly folded protein in transfected cells. The undefined vesicular structures with found LAT variants with prolonged TMD, can be some form of storage compartment for proteins that cannot be degraded immediately and can also indicate a stress response of the cell. We did not observe any colocalisation of these LAT variants with autophagosomes (data not shown).

Again, aiming to understand the proper function of helix-breaking amino acids in LAT TMD, a set of GFP tagged mutants was prepared, in which proline residues have been exchanged for alanines (LAT-P8A, LAT-P17A). Alanines were selected since this amino acid is often used for mutagenesis in highly hydrophobic protein parts such as TMDs. Glycine in the position 12 was replaced by leucine (LAT-G12L) to prevent the impact on poly-leucine segment in its vicinity. According to the MD simulation data, mutation of proline 17, but not of the other proline 8 or glycine removed the kink from the structure of TMD. Interestingly, LAT-P8A mutant exhibited even higher dynamics than WT peptide. This indicates that the kink introduced by central proline 17 but the other helix-breaking residues fine tune the overall dynamic geometry of LAT TMD. Importantly, the expression of all mutants was similar to LAT-WT with a majority of protein at the surface and a small portion of the proteins trapped in the Golgi apparatus. No functional effect was observed when used to recover T-cell function in LAT-deficient Jurkat cell line J.CaM2.5. Interestingly, despite the fact that a large fraction remained in the intracellular compartments, all mutants partially restored the surface expression of the non-palmitoylated LAT. Non-palmitoylated LAT protein with native TMD did not exhibit the surface targeting in any of the analysed cells (including works of others). The level of expresion to the surface was insufficient for the cells to respond to the stimulus which is the contrast to the cells expressing the palmitoylated versions. The other interpretation could be that non-palmitoylated surface localised mutants exhibit different nanoscopic organisation than their palmitoylated counterparts.

This is partially supported by the fact that no difference in the protein organisation between LAT-P8A and LAT-WT using the superresolution microscopy with lateral localisation precision below 30 nm has been observed. Both proteins were homogeneously distributed over the surface without any signs of higher structural organisation. Results showing random distribution of native LAT are in conflict with previously published LAT clusters in non-stimulated T cells (Sherman *et al.*, 2011; Williamson *et al.*, 2011). However, we have used a superior method for T cell immobilisation on coverslips in terms non-specific stimulation and viability (see also **Publication 2**: and **Project 4: Development of a novel sample preparation method for 3D super-resolution imaging of cell surface molecules (manuscript** in preparation). Interestingly, non-palmitoylated LAT-P8A mutant formed patchy structures of the surface of T cells, but these cells were almost unable to make contact with the imaging surface as found by the interference reflection microscopy, a method that maps the contact between immobilised cells and optical surface. Untransfected LAT-deficient J.CaM2.5 and those transfected with non functional palmitoylation mutants were not spreading properly. One can thus speculate that spreading of T cells is dependent on LAT activity and its palmitoylation state (more in **Publication 3:** Glatzová *et al.*, 2020).

To study the effect of other physical properties of TMD on sorting of single spanning proteins, we have also prepared TRAP-like proteins composed of the model TMD with 19 hydrophobic amino acid residues (WWLLLLLLLLALLLLLLL) and of the CD247 protein backbone. CD247 was selected, because it cannot reach the surface without assembly with other component of the TCR/CD3 complex. Therefor it would not influence the final localisation of mutant proteins. Under normal circumstances, proteins with TMD shorter than 21 amino acid residues remain trapped in the Golgi apparatus or the ER (Bretscher and Munro, 1993; Sharpe *et al.*, 2010). It was expected that surface expression of TRAP-like protein with suboptimal TMD length will dependent on additional (secondary) sorting signals. Indeed, whereas fully symmetric variant with lysine residues on both sides of the transmembrane segment (**KK**WWL...L**KK** sequence) was trapped in the intracellular compartments, similar variant with negatively charged glutamic acid residues on the outer site (**EE**WWL...L**KK** sequence) reached the cell surface. The later variant follows the positive inside law that states that charged amino acids facing the cytosol are mostly basic (lysines or arginines; von Heijne, 1989). The difference between the surface localisation of symmetric and asymmetric variants was totally suppressed in TRAP-like proteins with prolonger hydrophobic part to 25 residues in total. With this outcome, it was found out that artificial TRAP-like proteins with highly hydrophobic TMD made of 19 amino acid residues serve as a useful model for a fine tuning of sorting motifs connected to the TMD. Even small changes in the amino acid sequence of the juxtamembrane region played a significant role in the distribution of the protein throughout the cell.

TRAP-like proteins based on the backbone from LAT with the above described model LW19 segment were also prepared. Such TRAP-like protein localised to the plasma membrane similar to native LAT. However, no localisation to the Golgi apparatus was observed using LAT with asymmetric model TMD (LAT-LW19$_{(Asym)}$). This indicates that the TMD determines sorting of this TRAP-like protein. This is further supported by the fact that non-palmitoylated TRAP-like protein with LAT backbone and asymmetric model TMD localised partially to the plasma membrane. As has been already stated many times, no such localisation was observed for non-palmitoylated LAT with its native TMD. TMD properties thus dominate over secondary sorting signals when regulating protein localisation in cells. This was also supported by the fact, that in presence of palmitoylation site, the truncated version of LAT-LW19(Asym) was quite efficiently delivered to the plasma membrane. In comparison, the non-palmitoylated version spread over the inner cell membrane compartments and surface distributed almost equally.

To understand the sorting efficiency and protein targeting under different conditions is very important deu the fact that the final position of proteins is crucial for their proper function in cellular processes. Mislocalisation of proteins can lead to a loss of their function and may eventually end up as a disease (Hung and Link, 2011; Lee *et al.*, 2013; Wang and Li, 2014). Especially, it is important to determine all the mechanisms responsible for the proper function of protein, including molecular organisation at the nanoscopic level.

For study of nanoscopic organisation of proteins super-resolution microscopy techniques has to be used. To characterise the nanoscopic organisation of LAT photoactivated localisation microscopy (PALM) was used. Several mutants used in Chum *et al.* (2016) were thus fused with mEos2. For other projects not discussed here, where antibodies with reasonable quality were available, the advantageous direct stochastic reconstruction microscopy (dSTROM) approach was applied. However, these techniques generate only two-dimensional (2D) maps of surface molecules recorded under TIRF illumination. Recostructed images lack the information about axial position of studied molecules which are important to generate the overall spatial visualisations. This simplified projection of three-dimensional surface organisation into planar maps was already discussed in the introductory part of this thesis (for more details, see section **A brief insight into the topography of the plasma membrane (surface of T** cells)). This reduction can lead to misinterpretation of acquired data as it was shown for example in Lukeš *et al.* (2017). Such projected 2D data can indicate clustering of membrane molecules. But the origin of these higher structures is not clear. Accumulation of proteins can be caused also by the nanotopography of the cell surface. Therefore, it is important to develop user-friendly super-reoslution microscopy methods capable to provide 3D localisation maps (or images) with nanoscopic resolution.

There were several modifications throughout the whole process required for imaging cells in 3D with nanoscopic precision. It included the modified sample preparation, data acquisition with subsequent processing and interpretation. The application of total internal reflection fluorescence (TIRF) illumination for 3D acquisition was restricted due its limited penetration depth coming up to 200 nm from the plane of coincidence. To achieve better penetration ability highly inclined and laminated optical sheet illumination (HILO) has to be applied, even though at the cost of higher background coming from the internal structures of the cell. Increased background remains to be a challenge, since signle molecule localisation microscopy (SMLM) techniques with the best achievable resolution are extremely sensitive to the background intensity. It was found that biplane recording mode is suitable for obtaining the information required to determine the axial positins of the emitters. Simplicity of this method offers advantages over other extensions needed for other 3D SMLM or super-resolution optical fluctuation imaging (SOFI) techniques in terms of hardware setup and data processing (see **Publication 2:** Franke *et al.*, 2020). Finally, the reconstruction of the image of the cell in 3D was followed by statisticall analysis of the recorded molecules.

The maximum amount of photons released by organic dyes is limited, even more so for fluorescent proteins. To echieve the best performance needed for 3D, the background has to be reduced to the minimum. When considering sample preparation, simple rinse of imaging glass (coverslips) was not sufficient for SMLM techniques. Therefore, harsh chemical conditions had to be applied for getting the surface without interfering noise signal. Usually, so-called piranha solution – mixture of concentrated sulphuric acid with hydrogen peroxide – is used to prepare glass surface comparable with application of high energy plasma. First, piranha treatment causes nanoscopic damage to the glass surface that is not detected by diffraction limited methods, but it decreases the quality of signal for SMLM techniques due to the light scattering. Second, the use of such mixtures also requires a special handling.

It was found that application of Hellmanex solution, commonly used in spectroscopy for cleaning of glass cuvettes, in combination with high temperature provides satisfactory results comparable with piranha solution. Lower risk for the user and glass surface is also connected to the treatment of glass with Hellmanex. High energy plasma application should be still the method of choice, if the user has acces to the proper instrumentation that is not common in biological laboratories.

Obtaining SMLM data in the best quality is not limited only by the cleaning efficiency, but also by the presence of other sources of background. The most common source of fluorescent background is plasticware used in the laboratory (see **Project 4: Development of a novel sample preparation method for 3D super-resolution imaging of cell surface molecules (manuscript in preparation)** for this problematic). The residuals were eluted from the plastic bottles or tubes during the storage of solutions. These often fluorescent contaminants are mostly the organic plasticizers and solvents used during the plastic production. Futher improvement was accomplished by avoiding any contact of solutions with plasticware, especially for long term storage. To additionally reduce the background coming form the solutions intended for super-resolution microscopy techniques, everything should be prepared from the most concentrated available stocks, or even better from powders and verified source of ultraclean water. Such handling of samples and solution reduced the overall background significantly.

To get proper 3D structural information, it is important to preserve the nanoscopic plasma membrane organisation. Morfology of the cells and plasma membrane is very often strongly disturbed by the presence of poly-lysine on coated coverslips. The charge of the surface overlay forces the cells to actively spread over and form the maximum contact with the glass (Maverakis *et al.*, 2015; Mazia *et al.*, 1975; Santos *et al.*, 2018). Similarly, the use of ligands or antibodies for surface molecules, whether directly immobilised or anchored in the supported planar bilayers, induces cell expansion over the surface. This stress leads to reduction of the cell surface complexity and disruption of the 3D organisation of surface molecules. Therefore, samples are often heterogenous and exhibit different results for the cells at diverse stages of landing and stretching.

This also means that the use of poly-lysine- or ligand/antibody-coated optical surfaces is impractical for 3D SMLM techniques. Several approaches, how to preserve the 3D nano- and micro-structural aspects of the cell surface were reported. Seeding of cells into Matrigel or hydrogels preserves their surface morphology (Santos *et al.*, 2018). But the distance of the cells from the optical surface limits the usage of such samples for confocal and STED microscopy (Cavo *et al.*, 2018; Fritzsche *et al.*, 2017) or structured illumination microscopy (SIM) that achieve only limited resolution improvements (Lukeš *et al.*, 2014). Enhanced diffraction of emitted light with the distance from the optical surface does not allow the use of single molecule techniques with these materials.

Therefore, a glycine treatment of coverslips, which was originally effectively used to suppress the background fluorescence (Klein *et al.*, 2011; van de Linde *et al.*, 2011b) was adapted. During the new coating procedure the 2M glycine solution was applied directly onto the ultraclean coverslip and totaly skip the poly-lysine treatment step. Surprisingly, the immobilised cells were more viable on such glycine-coated coverslips compared to the poly-lysine-coated surface and their morphology was better preserved for more than 5 minutes from the first contact. This offers a good time window for proper sample preparation. Moreover, cells can be fixed on glycine surface using the standard procedures.

Cells prepared in a new way of sample preparation combined with all the improvements described above were used for analysis of high density regions of CD4 on resting T cells. These clusters were demonstrated previously using 2D SOFI approach (Lukeš *et al.*, 2017). To acquire the best possible spatial information about such structures, a collaboration with the authors of temporal, radial-aperture-based intensity estimation method (TRABI; Franke *et al.*, 2017) was established. A minor disadvantage of TRABI is the requirement of the image splitting device in the emission path. Such device was adjusted for biplane recording mode, when a defined shift between the two recorded optical planes was introduced. This shift was achieved by placing of an appropriate lens in front of the detector(s). Recorded intensity data from the two shifted optical planes were then correlated with a calibration curve, which was obtained using defined single molecule surface. Received axial positions of single emitters were then used for 3D image reconstruction with near isotropic resolution. This newly simplified approach was called direct TRABI (sTRABI) and is described in **Publication 2:** Franke *et al.*, 2020. Because of highly reduced background, and therefore good signal-to-noise ratio (SNR), the measured data were usable for further quantitative statistical analysis of the axial distribution of recorded emitters in 3D space.

The method was used to reveal the structure of CD4, its non-palmitoylated mutant (Lukeš *et al.*, 2017) and CD45 on the surface of human T cells. It was found that the presence of high density regions is defined by the 3D structure of the plasma membrane, because CD4 molecules accumulate at the tips of microvilli. This accumulation seemed to be palmitoylation dependent since the non-palmitoylated CD4 mutant was distributed randomly over the cell surface without any detectable higher order structures. A similar distribution was observed for CD45 molecule. It was broadly distributed over the cell surface but almost exclusively in the shaft and basis of the protrusions and the plasma membrane. Spatial separation of CD4 and CD45 was further proven by 2-colour SMLM. Additional 2-colour dTRABI analysis of this phenomenon requires further improvement of the whole system and the method of analysis.

It was already shown that the main T cell receptor (TCR) accumulates at the tips of membrane protrusion (Jung *et al.*, 2020, 2016; Kim *et al.*, 2018) and that CD45 molecule is spread almost homogenously over the cell body except the regions of TCR accumulation sites (Jung *et al.*, 2020, 2016). This different behaviour can be one of the controlling mechanisms of T-cell activation as it would allow the cell to remove the CD45 phosphatase from the activation site. Similar behaviour was observed in our case with the difference that we used the main activation partner of TCR – CD4 coreceptor. From the cooperation of CD4 and TCR is often concluded that these two molecules occur together or in close proximity. Therefore, one can guess that the separation of CD4 and CD45 has the same background and purpose. However, the distribution of TCR was not tested using dTRABI yet.

According to the calcium measurements, the segregation of CD4 and CD45 in studied cells was not due to the activation of T cells by immobilisation on glycine. It was more likely caused by the physical properties of these molecules. The size of the CD45 extracellular domain may lead to its segregation from a limited space at the contact site. Alternatively, a short TMD of CD45 can limit the distribution of this receptor to the cell body (Jung *et al.*, 2020). Whatever is the mechanism, the receptor segregation is evident in all tested cells over the prolonged time of seeding to the surface on poly-lysine (Jung *et al.*, 2016) and glycine coating (**Publication 2:** Franke *et al.*, 2020), respectively. In order to understand early events of T-cell activation by antigen, localisation of molecules involved in this process needs to be studied further by applying diverse superresolution techniques. The activation of T cells is one of the most important steps involved in immune response of organisms to pathogens or malformations. Therefore, it is important to elucidate all the factors playing a role during the activation, since improper regulation of immune response can often lead to autoimmune disease or onset of allergic reactions.

Increasing accessibility of super-resolution imaging techniques can provide the insight into molecular mechanisms of diverse physiological processes at the single molecule level. In hand with the technology development, the sample preparation has to be optimised for a plethora of scientific questions. To get focus on the sample preparation is crucial step in experimental procedures avoiding generation of artefacts and data misinterpretation. The usability of our newly developed system of sample preparation was tested on diverse types of adherent and in suspension growing cells. After seeding their surface morphology was preserved. Nevertheless, the impact of glycine suface coating on protein distribution and dynamics has yet to be tested.

The disadvantage of the current protocol was dependence on labelling of receptors with antibodies, as the access to good quality antibodies is limited for some but not all surface molecules. Moreover, antibodies as voluminous molecules could alter the nanoscopic 3D organisation of the studied proteins. Therefore, the next step of the development will be introduction of small fluorophores for labelling using click chemistry. These should help to achieve a better localisation precision in all dimensions. In the future dTRABI should be extended for studies of more proteins in single cell to get information about interacting or cooperating partners. Here, the DNA point accumulation for imaging in nanoscale topography (DNA-PAINT) technique (Jungmann *et al.*, 2010) can open access to simultaneous ‘multi-colour’ 3D dTRABI analysis of receptors and effector molecules. Nowadays, relative easy access to the quantitative 3D information with very high resolution about one molecule is offered by the quite simple dTRABI technique (**Publication 2**: Franke *et al.*, 2020).

The final goal of every molecular biologist is to get the most natural image of studied cellular structures and process. The Holy Grail of cell biology is to see everything in living cells with natural temporal resolution using very complex techniques. But, the development is still far away from this stage.

6 REFERENCES

Abbe, E., 1873. Beiträge zur Theorie des Mikroskops und der mikroskopischen Wahrnehmung. Archiv füt Mikroskopische Anatomie 9, 413–418. https://doi.org/10.1007/BF02956173

Adrian, M., Dubochet, J., Lapault, J., McDowall, A.W., 1984. Cryo-electron microscopy of viruses. Nature 308, 32–36.

Algar, W.R., Hildebrandt, N., Vogel, S.S., Medintz, I.L., 2019. FRET as a biomolecular research tool — understanding its potential while avoiding pitfalls. Nat Methods 16, 815–829.
https://doi.org/10.1038/s41592-019-0530-8

Almén, M., Nordström, K.J., Fredriksson, R., Schiöth, H.B., 2009. Mapping the human membrane proteome: a majority of the human membrane proteins can be classified according to function and evolutionary origin. BMC Biol 7, 50. https://doi.org/10.1186/1741-7007-7-50

Ando, R., Hama, H., Yamamoto-Hino, M., Mizuno, H., Miyawaki, A., 2002. An optical marker based on the UV-induced green-to-red photoconversion of a fluorescent protein. Proceedings of the National Academy of Sciences 99, 12651–12656. https://doi.org/10.1073/pnas.202320599

Andreeva, A., Howorth, D., Chothia, C., Kulesha, E., Murzin, A.G., 2014. SCOP2 prototype: a new approach to protein structure mining. Nucl. Acids Res. 42, D310–D314. https://doi.org/10.1093/nar/gkt1242

Aon, M.A., Tocchetti, C.G., Bhatt, N., Paolocci, N., Cortassa, S., 2015. Protective Mechanisms of Mitochondria and Heart Function in Diabetes. Antioxidants & Redox Signaling 22, 1563–1586. https://doi.org/10.1089/ars.2014.6123

Ariöz, C., 2014. Exploring the Interplay of Lipids and Membrane Proteins. Department of Biochemistry and Biophysics, Stockholm University, Stockholm.

Bates, M., Blosser, T.R., Zhuang, X., 2005. Short-Range Spectroscopic Ruler Based on a Single-Molecule Optical Switch. Phys. Rev. Lett. 94, 108101. https://doi.org/10.1103/PhysRevLett.94.108101

Beber, A., Taveneau, C., Nania, M., Tsai, F.-C., Di Cicco, A., Bassereau, P., Lévy, D., Cabral, J.T., Isambert, H., Mangenot, S., Bertin, A., 2019. Membrane reshaping by micrometric curvature sensitive septin filaments. Nat Commun 10, 420. https://doi.org/10.1038/s41467-019-08344-5

Behnia, R., Munro, S., 2005. Organelle identity and the signposts for membrane traffic. Nature 438, 597–604. https://doi.org/10.1038/nature04397

Bernardino de la Serna, J., Schütz, G.J., Eggeling, C., Cebecauer, M., 2016. There Is No Simple Model of the Plasma Membrane Organization. Front. Cell Dev. Biol. 4. https://doi.org/10.3389/fcell.2016.00106

Bertocchi, C., Wang, Y., Ravasio, A., Hara, Y., Wu, Y., Sailov, T., Baird, M.A., Davidson, M.W., Zaidel-Bar, R., Toyama, Y., Ladoux, B., Mege, R.-M., Kanchanawong, P., 2017. Nanoscale architecture of cadherin-based cell adhesions. Nat Cell Biol 19, 28–37. https://doi.org/10.1038/ncb3456

Betzig, E., Chichester, R.J., 1993. Single Molecules Observed by Near-Field Scanning Optical Microscopy. Science 262, 1422–1425. https://doi.org/10.1126/science.262.5138.1422

Betzig, E., Patterson, G.H., Sougrat, R., Lindwasser, O.W., Olenych, S., Bonifacino, J.S., Davidson, M.W., Lippincott-Schwartz, J., Hess, H.F., 2006. Imaging Intracellular Fluorescent Proteins at Nanometer Resolution. Science 313, 1642–1645. https://doi.org/10.1126/science.1127344

Bijlmakers, M., 2003. The on–off story of protein palmitoylation. Trends in Cell Biology 13, 32–42.
https://doi.org/10.1016/S0962-8924(02)00008-9

Bijlmakers, M.-J., 2009. Protein acylation and localization in T cell signaling (Review). Molecular Membrane Biology 26, 93–103. https://doi.org/10.1080/09687680802650481

Blanc, M., David, F., Abrami, L., Migliozzi, D., Armand, F., Bürgi, J., van der Goot, F.G., 2015. SwissPalm: Protein Palmitoylation database. F1000Res 4, 261. https://doi.org/10.12688/f1000research.6464.1

Blaskovic, S., Adibekian, A., Blanc, M., van der Goot, G.F., 2014. Mechanistic effects of protein palmitoylation and the cellular consequences thereof. Chemistry and Physics of Lipids 180, 44–52. https://doi.org/10.1016/j.chemphyslip.2014.02.001

Blaskovic, S., Blanc, M., van der Goot, F.G., 2013. What does S-palmitoylation do to membrane proteins? FEBS J 280, 2766–2774. https://doi.org/10.1111/febs.12263

Bradbury, S., Bracegirdle, B., 1998. Introduction on Light Microscopy. BIOS Scientific Publisher.

Bradl, J., Rinke, B., Esa, A., Edelmann, P., Krieger, H., Schneider, B., Hausmann, M., Cremer, C.G., 1996. Comparative study of three-dimensional localization accuracy in conventional, confocal laser scanning and axial tomographic fluorescence light microscopy, in: Bigio, I.J., Grundfest, W.S., Schneckenburger, H., Svanberg, K., Viallet, P.M. (Eds.), . Presented at the BiOS Europe '96, Vienna, Austria, p. 201. https://doi.org/10.1117/12.260797

Brdička, T., Imrich, M., Angelisová, P., Brdičková, N., Horváth, O., Špička, J., Hilgert, I., Lusková, P., Dráber, P., Novák, P., Engels, N., Wienands, J., Simeoni, L., Österreicher, J., Aguado, E., Malissen, M., Schraven, B., Hořejší, V., 2002. Non–T Cell Activation Linker (NTAL). The Journal of Experimental Medicine 196, 1617–1626. https://doi.org/10.1084/jem.20021405

Brdic ka, T., Pavlis tová, D., Leo, A., Bruyns, E., Kor ínek, V., Angelisová, P., Scherer, J., Shevchenko, Andrej, Shevchenko, Anna, Hilgert, I., C erný, J., Drbal, K., Kuramitsu, Y., Kornacker, B., Hor ejs í, V., Schraven, B., *2000*. Phosphoprotein Associated with Glycosphingolipid-Enriched Microdomains (Pag), a Novel Ubiquitously Expressed Transmembrane Adaptor Protein, Binds the Protein Tyrosine Kinase Csk and Is Involved in Regulation of T Cell Activation. The Journal of Experimental Medicine 191, 1591–1604.
https://doi.org/10.1084/jem.191.9.1591

Bretscher, M.S., Munro, S., 1993. Cholesterol and the Golgi Apparatus. Science 1280–1281. https://doi.org/10.1126/science.8362242

Bunnell, S.C., Hong, D.I., Kardon, J.R., Yamazaki, T., McGlade, C.J., Barr, V.A., Samelson, L.E., 2002. T cell receptor ligation induces the formation of dynamically regulated signaling assemblies. The Journal of Cell Biology 158, 1263–1275. https://doi.org/10.1083/jcb.200203043

Bunnell, S.C., Kapoor, V., Trible, R.P., Zhang, W., Samelson, L.E., 2001. Dynamic Actin Polymerization Drives T Cell Receptor–Induced Spreading: A Role for the Signal Transduction Adaptor LAT. Immunity 315–329.

Cai, E., Marchuk, K., Beemiller, P., Beppler, C., Rubashkin, M.G., Weaver, V.M., Gérard, A., Liu, T.-L., Chen, B.-C., Betzig, E., Bartumeus, F., Krummel, M.F., 2017. Visualizing dynamic microvillar search and stabilization during ligand detection by T cells. Science 356, eaal3118. https://doi.org/10.1126/science.aal3118

Capua, C.J., Hopson, N.P., Stewart, C.M.M., Johnston, G.R., O'Neill, K.L., Schaalje, G.B., Lee, C.M., Booth, G.M., 2010. Cytotoxicity of *Atriplex confertifolia*. Journal of Toxicology 2010, 1–7. https://doi.org/10.1155/2010/976548

Castello, M., Tortarolo, G., Buttafava, M., Deguchi, T., Villa, F., Koho, S., Bianchini, P., Sheppard, C.J.R., Diaspro, A., Tosi, A., Vicidomini, G., 2018. Image Scanning Microscopy with Single-Photon Detector Array (preprint). Bioengineering. https://doi.org/10.1101/335596

Cavo, M., Caria, M., Pulsoni, I., Beltrame, F., Fato, M., Scaglione, S., 2018. A new cell-laden 3D Alginate-Matrigel hydrogel resembles human breast cancer cell malignant morphology, spread and invasion capability observed "in vivo." Sci Rep 8, 5333. https://doi.org/10.1038/s41598-018-23250-4

Cebecauer, M., 2012. Lipids and proteins in membranes: From *in silico* to *in vivo*. Molecular Membrane Biology 29, 115–117. https://doi.org/10.3109/09687688.2012.710344

Cebecauer, M., Amaro, M., Jurkiewicz, P., Sarmento, M.J., Šachl, R., Cwiklik, L., Hof, M., 2018. Membrane Lipid Nanodomains. Chem. Rev. 118, 11259–11297. https://doi.org/10.1021/acs.chemrev.8b00322

Chen, B.-C., Legant, W.R., Wang, K., Shao, L., Milkie, D.E., Davidson, M.W., Janetopoulos, C., Wu, X.S., Hammer, J.A., Liu, Z., English, B.P., Mimori-Kiyosue, Y., Romero, D.P., Ritter, A.T., Lippincott-Schwartz, J., Fritz-Laylin, L., Mullins, R.D., Mitchell, D.M., Bembenek, J.N., Reymann, A.-C., Böhme, R., Grill, S.W., Wang, J.T., Seydoux, G., Tulu, U.S., Kiehart, D.P., Betzig, E., 2014. Lattice light-sheet microscopy: Imaging molecules to embryos at high spatiotemporal resolution. Science 346, 1257998. https://doi.org/10.1126/science.1257998

Chen, F., Tillberg, P.W., Boyden, E.S., 2015. Expansion microscopy. Science 347, 543–548. https://doi.org/10.1126/science.1260088

Chen, X.-L., Liu, C., Tang, B., Ren, Z., Wang, G.-L., Liu, W., 2020. Quantitative proteomics analysis reveals important roles of N-glycosylation on ER quality control system for development and pathogenesis in Magnaporthe oryzae. PLoS Pathog 16, e1008355. https://doi.org/10.1371/journal.ppat.1008355

Chhabra, E.S., Higgs, H.N., 2007. The many faces of actin: matching assembly factors with cellular structures. Nat Cell Biol 9, 1110–1121. https://doi.org/10.1038/ncb1007-1110

Chou, K.-C., Cai, Y.-D., 2005. Prediction of Membrane Protein Types by Incorporating Amphipathic Effects. J. Chem. Inf. Model. 45, 407–413. https://doi.org/10.1021/ci049686v

Chou, K.-C., Elrod, D.W., 1999. Prediction of membrane protein types and subcellular locations 17.

Chou, K.-C., Shen, H.-B., 2009. REVIEW : Recent advances in developing web-servers for predicting protein attributes. NS 01, 63–92. https://doi.org/10.4236/ns.2009.12011

Chou, K.-C., Shen, H.-B., 2007. MemType-2L: A Web server for predicting membrane proteins and their types by incorporating evolution information through Pse-PSSM. Biochemical and Biophysical Research Communications 360, 339–345. https://doi.org/10.1016/j.bbrc.2007.06.027

Chum, T., Glatzová, D., Kvíčalová, Z., Malínský, J., Brdička, T., Cebecauer, M., 2016. The role of palmitoylation and transmembrane domain in sorting of transmembrane adaptor proteins. J Cell Sci 129, 3053–3053. https://doi.org/10.1242/jcs.194209

Cohen, P., 2002. The origins of protein phosphorylation. Nat Cell Biol 4, E127–E130. https://doi.org/10.1038/ncb0502-e127

Compeer, E.B., Kraus, F., Ecker, M., Redpath, G., Amiezer, M., Rother, N., Nicovich, P.R., Kapoor-Kaushik, N., Deng, Q., Samson, G.P.B., Yang, Z., Lou, J., Carnell, M., Vartoukian, H., Gaus, K., Rossy, J., 2018. A mobile endocytic network connects clathrin-independent receptor endocytosis to recycling and promotes T cell activation. Nat Commun 9, 1597. https://doi.org/10.1038/s41467-018-04088-w

Coons, A.H., Creech, H.J., Jones, R.N., 1941. Immunological Properties of an Antibody Containing a Fluorescent Group. Experimental Biology and Medicine 47, 200–202. https://doi.org/10.3181/00379727-47-13084P

Czuba, L.C., Hillgren, K.M., Swaan, P.W., 2018. Post-translational modifications of transporters. Pharmacology & Therapeutics 192, 88–99. https://doi.org/10.1016/j.pharmthera.2018.06.013

Dertinger, T., Colyer, R., Iyer, G., Weiss, S., Enderlein, J., 2009. Fast, background-free, 3D super-resolution optical fluctuation imaging (SOFI). PNAS 106, 22287–22292. https://doi.org/10.1073/pnas.0907866106

Dertinger, T., Xu, J., Naini, O., Vogel, R., Weiss, S., 2012. SOFI-based 3D superresolution sectioning with a widefield microscope. Opt Nanoscopy 1, 2. https://doi.org/10.1186/2192-2853-1-2

Dessi, D., Delogu, G., Emonte, E., Catania, M.R., Fiori, P.L., Rappelli, P., 2005. Long-Term Survival and Intracellular Replication of Mycoplasma hominis in Trichomonas vaginalis Cells: Potential Role of the Protozoon in Transmitting Bacterial Infection. Infection and Immunity 73, 1180–1186. https://doi.org/10.1128/IAI.73.2.1180-1186.2005

Diaz-Rohrer, B.B., Levental, K.R., Simons, K., Levental, I., 2014. Membrane raft association is a determinant of plasma membrane localization. Proceedings of the National Academy of Sciences 111, 8500–8505. https://doi.org/10.1073/pnas.1404582111

Dickson, R.M., Cubitt, A.B., Tsien, R.Y., Moerner, W.E., 1997. On/off blinking and switching behaviour of single molecules of green fluorescent protein. Nature 388, 355–358. https://doi.org/10.1038/41048

Dobson, C.M., 1999. Protein misfolding, evolution and disease. TIBS 24, 329–332. https://doi.org/10.1016/s0968-0004(99)01445-0

Dultz, E., Ellenberg, J., 2010. Live imaging of single nuclear pores reveals unique assembly kinetics and mechanism in interphase. The Journal of Cell Biology 191, 15–22. https://doi.org/10.1083/jcb.201007076

Dustin, M.L., 2009. Supported bilayers at the vanguard of immune cell activation studies. Journal of Structural Biology 168, 152–160. https://doi.org/10.1016/j.jsb.2009.05.007

Edelstein, A.D., Tsuchida, M.A., Amodaj, N., Pinkard, H., Vale, R.D., Stuurman, N., 2014. Advanced methods of microscope control using µManager software. J Biol Methods 1, 10. https://doi.org/10.14440/jbm.2014.36

Elson, E.L., 2011. Fluorescence Correlation Spectroscopy: Past, Present, Future. Biophysical Journal 101, 2855–2870. https://doi.org/10.1016/j.bpj.2011.11.012

Embryology [WWW Document], 2020. URL: https://embryology.med.unsw.edu.au/embryology/images/e/eb/Human_uterine_tube_ciliated_epithelium_SEM.jpg (accessed 4.22.20).

Fairn, G.D., Hermansson, M., Somerharju, P., Grinstein, S., 2011. Phosphatidylserine is polarized and required for proper Cdc42 localization and for development of cell polarity. Nat Cell Biol 13, 1424–1430. https://doi.org/10.1038/ncb2351

Fastenberg, M.E., Shogomori, H., Xu, X., Brown, D.A., London, E., 2003. Exclusion of a Transmembrane-Type Peptide from Ordered-Lipid Domains (Rafts) Detected by Fluorescence Quenching: Extension of Quenching Analysis to Account for the Effects of Domain Size and Domain Boundaries †. Biochemistry 42, 12376–12390. https://doi.org/10.1021/bi034718d

Fellers, T.J., Davidson, M.W., 2020. Introduction to Confocal Microscopy.

Fiedler, K., Simons, K., 1995. The role of n-glycans in the secretory pathway. Cell 81, 309–312. https://doi.org/10.1016/0092-8674(95)90380-1

Finco, T.S., Kadlecek, T., Zhang, W., Samelson, L.E., Weiss, A., 1998. LAT Is Required for TCR-Mediated Activation of PLC⍰1 and the Ras Pathway. Immunity 9, 10. https://doi.org/10.1016/S1074-7613(00)80659-7

Fisher, P.J., Bulur, P.A., Vuk-Pavlovic, S., Prendergast, F.G., Dietz, A.B., 2008. Dendritic cell microvilli: a novel membrane structure associated with the multifocal synapse and T-cell clustering. Blood 112, 5037–5045. https://doi.org/10.1182/blood-2008-04-149526

Foot, N., Henshall, T., Kumar, S., 2017. Ubiquitination and the Regulation of Membrane Proteins. Physiological Reviews 97, 253–281. https://doi.org/10.1152/physrev.00012.2016

Franke, C., 2017. Advancing Single-Molecule Localization Microscopy.

Franke, C., Chum, T., Kvicalova, Z., Glatzova, D., Rodriguez, A., Helmerich, D., Frank, O., Brdicka, T., van de Linde, S., Cebecauer, M., 2020. Unraveling nanotopography of cell surface receptors (preprint). Cell Biology. https://doi.org/10.1101/2019.12.23.884460

Franke, C., Repnik, U., Segeletz, S., Brouilly, N., Kalaidzidis, Y., Verbavatz, J., Zerial, M., 2019. Correlative single-molecule localization microscopy and electron tomography reveals endosome nanoscale domains. Traffic 20, 601–617. https://doi.org/10.1111/tra.12671

Franke, C., Sauer, M., van de Linde, S., 2017. Photometry unlocks 3D information from 2D localization microscopy data. Nat Methods 14, 41–44. https://doi.org/10.1038/nmeth.4073

Fritzsche, M., Fernandes, R.A., Chang, V.T., Colin-York, H., Clausen, M.P., Felce, J.H., Galiani, S., Erlenkämper, C., Santos, A.M., Heddleston, J.M., Pedroza-Pacheco, I., Waithe, D., de la Serna, J.B., Lagerholm, B.C., Liu, T., Chew, T.-L., Betzig, E., Davis, S.J., Eggeling, C., 2017. Cytoskeletal actin dynamics shape a ramifying actin network underpinning immunological synapse formation. Sci. Adv. 3, e1603032.
https://doi.org/10.1126/sciadv.1603032

Funatsu, T., Harada, Y., Tokunaga, M., Kiwamu, S., 1995. Imaging of single fluorescent molecules and individual ATP turnovers by single myosin molecules in aqueous solution. Nature 555–559.

Galbraith, C.G., Galbraith, J.A., 2011. Super-resolution microscopy at a glance. Journal of Cell Science 124, 1607–1611. https://doi.org/10.1242/jcs.080085

Gan, L., Jensen, G.J., 2012. Electron tomography of cells. Quart. Rev. Biophys. 45, 27–56. https://doi.org/10.1017/S0033583511000102

Geissbuehler, S., Bocchio, N.L., Dellagiacoma, C., Berclaz, C., Leutenegger, M., Lasser, T., 2012. Mapping molecular statistics with balanced super-resolution optical fluctuation imaging (bSOFI). Opt Nanoscopy 1, 4. https://doi.org/10.1186/2192-2853-1-4

Geissbuehler, S., Dellagiacoma, C., Lasser, T., 2011. Comparison between SOFI and STORM. Biomed. Opt. Express 2, 408. https://doi.org/10.1364/BOE.2.000408

Geissbuehler, S., Sharipov, A., Godinat, A., Bocchio, N.L., Sandoz, P.A., Huss, A., Jensen, N.A., Jakobs, S., Enderlein, J., Gisou van der Goot, F., Dubikovskaya, E.A., Lasser, T., Leutenegger, M., 2014. Live-cell multiplane three-dimensional super-resolution optical fluctuation imaging. Nat Commun 5, 5830. https://doi.org/10.1038/ncomms6830

Giraudo, C.G., Maccioni, H.J.F., 2003. Endoplasmic Reticulum Export of Glycosyltransferases Depends on Interaction of a Cytoplasmic Dibasic Motif with Sar1. MBoC 14, 3753–3766. https://doi.org/10.1091/mbc.e03-02-0101

Glatzová, D., Cebecauer, M., 2019. Dual Role of CD4 in Peripheral T Lymphocytes. Front. Immunol. 10, 618. https://doi.org/10.3389/fimmu.2019.00618

Glatzová, D., Mavila, H., Saija, M.C., Chum, T., Cwiklik, L., Brdic ka, T., Cebecauer, M., 2020. The role of prolines and glycine in transmembrane domain of LAT (preprint). Cell Biology. https://doi.org/10.1101/2020.08.10.244251

Goder, V., Melero, A., 2011. Protein O-mannosyltransferases participate in ER protein quality control. Journal of Cell Science 124, 144–153. https://doi.org/10.1242/jcs.072181

Gorelik, J., Shevchuk, A.I., Frolenkov, G.I., Diakonov, I.A., Lab, M.J., Kros, C.J., Richardson, G.P., Vodyanoy, I., Edwards, C.R.W., Klenerman, D., Korchev, Y.E., 2003. Dynamic assembly of surface structures in living cells. Proceedings of the National Academy of Sciences 100, 5819–5822. https://doi.org/10.1073/pnas.1030502100

Griffiths, G., Lucocq, J.M., 2014. Antibodies for immunolabeling by light and electron microscopy: not for the faint hearted. Histochem Cell Biol 142, 347–360. https://doi.org/10.1007/s00418-014-1263-5

Gu, M., Sheppard, C.J.R., 1992. Confocal fluorescent microscopy with a finite-sized circular detector. J. Opt. Soc. Am. A 9, 151. https://doi.org/10.1364/JOSAA.9.000151

Gustafsson, M.G.L., 2005. Nonlinear structured-illumination microscopy: Wide-field fluorescence imaging with theoretically unlimited resolution. Proceedings of the National Academy of Sciences 102, 13081–13086. https://doi.org/10.1073/pnas.0406877102

Gustafsson, M.G.L., 2000. Surpassing the lateral resolution limit by a factor of two using structured illumination microscopy. SHORT COMMUNICATION. J Microsc 198, 82–87. https://doi.org/10.1046/j.1365-2818.2000.00710.x

Gustafsson, M.G.L., Allen, J.R., Davidson, M.W., 2020. SIM-Zeiss [WWW Document]. URL http://zeiss-campus.magnet.fsu.edu/articles/superresolution/supersim.html (accessed 6.4.20).

Habuchi, S., 2014. Super-Resolution Molecular and Functional Imaging of Nanoscale Architectures in Life and Materials Science. Front. Bioeng. Biotechnol. 2. https://doi.org/10.3389/fbioe.2014.00020

Heijne, G., Gavel, Y., 1988. Topogenic signals in integral membrane proteins. Eur J Biochem 174, 671–678. https://doi.org/10.1111/j.1432-1033.1988.tb14150.x

Heilemann, M., Margeat, E., Kasper, R., Sauer, M., Tinnefeld, P., 2005. Carbocyanine Dyes as Efficient Reversible Single-Molecule Optical Switch. J. Am. Chem. Soc. 127, 3801–3806. https://doi.org/10.1021/ja044686x

Heilemann, M., van de Linde, S., Mukherjee, A., Sauer, M., 2009. Super-Resolution Imaging with Small Organic Fluorophores. Angew. Chem. Int. Ed. 48, 6903–6908. https://doi.org/10.1002/anie.200902073

Heilemann, M., van de Linde, S., Schüttpelz, M., Kasper, R., Seefeldt, B., Mukherjee, A., Tinnefeld, P., Sauer, M., 2008. Subdiffraction-Resolution Fluorescence Imaging with Conventional Fluorescent Probes. Angew. Chem. Int. Ed. 47, 6172–6176. https://doi.org/10.1002/anie.200802376

Heim, R., Cubbit, A.B., Tsien, Roger Y., 1995. Improved green fluorescence. Nature 373, 663–664. https://doi.org/10.1038/3736663b

Hein, B., Willig, K.I., Hell, S.W., 2008. Stimulated emission depletion (STED) nanoscopy of a fluorescent protein-labeled organelle inside a living cell. Proceedings of the National Academy of Sciences 105, 14271–14276. https://doi.org/10.1073/pnas.0807705105

Heintzmann, R., 2010. Correcting distorted optics: back to the basics. Nat Methods 7, 108–110. https://doi.org/10.1038/nmeth0210-108

Heintzmann, R., Cremer, C.G., 1999. Laterally modulated excitation microscopy: improvement of resolution by using a diffraction grating, in: Bigio, I.J., Schneckenburger, H., Slavik, J., Svanberg, K., Viallet, P.M. (Eds.), . Presented at the BiOS Europe ’98, Stockholm, Sweden, pp. 185–196. https://doi.org/10.1117/12.336833

Hell, S.W., Wichmann, J., 1994. Breaking the diffraction resolution limit by stimulated emission: stimulated-emission-depletion fluorescence microscopy. Opt. Lett. 19, 780. https://doi.org/10.1364/OL.19.000780

Hess, S.T., Girirajan, T.P.K., Mason, M.D., 2006. Ultra-High Resolution Imaging by Fluorescence Photoactivation Localization Microscopy. Biophysical Journal 91, 4258–4272. https://doi.org/10.1529/biophysj.106.091116

Hess, S.T., Gould, T.J., Gudheti, M.V., Maas, S.A., Mills, K.D., Zimmerberg, J., 2007. Dynamic clustered distribution of hemagglutinin resolved at 40 nm in living cell membranes discriminates between raft theories. Proceedings of the National Academy of Sciences 104, 17370–17375. https://doi.org/10.1073/pnas.0708066104

Holmes, N., 2006. CD45: all is not yet crystal clear. Immunology 117, 145–155. https://doi.org/10.1111/j.1365-2567.2005.02265.x

Hoopmann, P., Punge, A., Barysch, S.V., Westphal, V., Buckers, J., Opazo, F., Bethani, I., Lauterbach, M.A., Hell, S.W., Rizzoli, S.O., 2010. Endosomal sorting of readily releasable synaptic vesicles. Proceedings of the National Academy of Sciences 107, 19055–19060. https://doi.org/10.1073/pnas.1007037107

Hořejší, V., 2005. Lipid rafts and their roles in T-cell activation. Microbes and Infection 7, 310–316. https://doi.org/10.1016/j.micinf.2004.12.004

Hořejší, V., 2004. Transmembrane adaptor proteins in membrane microdomains: important regulators of immunoreceptor signaling. Immunology Letters 92, 43–49. https://doi.org/10.1016/j.imlet.2003.10.013

Hořejší, V., Hrdinka, M., 2014. Membrane microdomains in immunoreceptor signaling. FEBS Letters 588, 2392–2397. https://doi.org/10.1016/j.febslet.2014.05.047

Hořejší, V., Otáhal, P., Brdička, T., 2010. LAT - an important raft-associated transmembrane adaptor protein. Delivered on 6 July 2009 at the 34th FEBS Congress in Prague, Czech Republic: LAT, a key membrane raft-associated protein. FEBS Journal 277, 4383–4397. https://doi.org/10.1111/j.1742-4658.2010.07831.x

Hořejší, V., Zhang, W., Schraven, B., 2004. Transmembrane adaptor proteins: organizers of immunoreceptor signalling. Nat Rev Immunol 4, 603–616. https://doi.org/10.1038/nri1414

Hrdinka, M., Hořejší, V., 2014. PAG - a multipurpose transmembrane adaptor protein. Oncogene 33, 4881–4892. https://doi.org/10.1038/onc.2013.485

Huang, B., Wang, W., Bates, M., Zhuang, X., 2008. Three-Dimensional Super-Resolution Imaging by Stochastic Optical Reconstruction Microscopy. Science 319, 810–813. https://doi.org/10.1126/science.1153529

Hundt, M., Harada, Y., De Giorgio, L., Tanimura, N., Zhang, W., Altman, A., 2009. Palmitoylation-Dependent Plasma Membrane Transport but Lipid Raft-Independent Signaling by Linker for Activation of T Cells. J Immunol 183, 1685–1694. https://doi.org/10.4049/jimmunol.0803921

Hung, M.-C., Link, W., 2011. Protein localization in disease and therapy. Journal of Cell Science 124, 3381–3392. https://doi.org/10.1242/jcs.089110

Johannes, L., Parton, R.G., Bassereau, P., Mayor, S., 2015. Building endocytic pits without clathrin. Nat Rev Mol Cell Biol 16, 311–321. https://doi.org/10.1038/nrm3968

Juette, M.F., Gould, T.J., Lessard, M.D., Mlodzianoski, M.J., Nagpure, B.S., Bennett, B.T., Hess, S.T., Bewersdorf, J., 2008. Three-dimensional sub–100 nm resolution fluorescence microscopy of thick samples. Nat Methods 5, 527–529. https://doi.org/10.1038/nmeth.1211

Jung, H.R., Jensen, O.N., 2006. Proteomic analysis of GPI-anchored membrane proteins. Drug Discovery Today: Technologies 3, 339–346. https://doi.org/10.1016/j.ddtec.2006.09.011

Jung, Y., Riven, I., Feigelson, S.W., Kartvelishvily, E., Tohya, K., Miyasaka, M., Alon, R., Haran, G., 2016. Three-dimensional localization of T-cell receptors in relation to microvilli using a combination of superresolution microscopies. Proc Natl Acad Sci USA 113, E5916–E5924. https://doi.org/10.1073/pnas.1605399113

Jung, Y., Wen, L., Altman, A., Ley, K., 2020. CD45 pre-exclusion from the tips of microvilli establishes a phosphatase-free zone for early TCR triggering (preprint). Immunology. https://doi.org/10.1101/2020.05.21.109074

Jungmann, R., Steinhauer, C., Scheible, M., Kuzyk, A., Tinnefeld, P., Simmel, F.C., 2010. Single-Molecule Kinetics and Super-Resolution Microscopy by Fluorescence Imaging of Transient Binding on DNA Origami. Nano Lett. 10, 4756–4761. https://doi.org/10.1021/nl103427w

Kaiser, H.-J., Orlowski, A., Rog, T., Nyholm, T.K.M., Chai, W., Feizi, T., Lingwood, D., Vattulainen, I., Simons, K., 2011. Lateral sorting in model membranes by cholesterol-mediated hydrophobic matching. Proceedings of the National Academy of Sciences 108, 16628–16633. https://doi.org/10.1073/pnas.1103742108

Kendrew, J.C., Bodo, G., Dintzis, H.M., Parrish, R.G., Wyckoff, H., Phillips, D.C., 1958. A Three-Dimensional Model of the Myoglobin Molecule Obtained by X-Ray Analysis. Nature 181, 662–666. https://doi.org/10.1038/181662a0

Khoury, G.A., Baliban, R.C., Floudas, C.A., 2011. Proteome-wide post-translational modification statistics: frequency analysis and curation of the swiss-prot database. Sci Rep 1, 90. https://doi.org/10.1038/srep00090

Kim, H.-R., Mun, Y., Lee, K.-S., Park, Y.-J., Park, J.-S., Park, J.-H., Jeon, B.-N., Kim, C.-H., Jun, Y., Hyun, Y.-M., Kim, M., Lee, S.-M., Park, C.-S., Im, S.-H., Jun, C.-D., 2018. T cell microvilli constitute immunological synaptosomes that carry messages to antigen-presenting cells. Nat Commun 9, 3630. https://doi.org/10.1038/s41467-018-06090-8

Klar, T.A., Hell, S.W., 1999. Subdiffraction resolution in far-field fluorescence microscopy. Opt. Lett. 24, 954. https://doi.org/10.1364/OL.24.000954

Klar, T.A., Jakobs, S., Dyba, M., Egner, A., Hell, S.W., 2000. Fluorescence microscopy with diffraction resolution barrier broken by stimulated emission. Proceedings of the National Academy of Sciences 97, 8206–8210. https://doi.org/10.1073/pnas.97.15.8206

Klein, T., Löschberger, A., Proppert, S., Wolter, S., van de Linde, S., Sauer, M., 2011. Live-cell dSTORM with SNAP-tag fusion proteins. Nat Methods 8, 7–9. https://doi.org/10.1038/nmeth0111-7b

Kleine-Vehn, J., Wabnik, K., Martinière, A., Łangowski, Ł., Willig, K., Naramoto, S., Leitner, J., Tanaka, H., Jakobs, S., Robert, S., Luschnig, C., Govaerts, W., W Hell, S., Runions, J., Friml, J., 2011. Recycling, clustering, and endocytosis jointly maintain PIN auxin carrier polarity at the plasma membrane. Mol Syst Biol 7, 540. https://doi.org/10.1038/msb.2011.72

Knowles, T.P.J., Vendruscolo, M., Dobson, C.M., 2014. The amyloid state and its association with protein misfolding diseases. Nat Rev Mol Cell Biol 15, 384–396. https://doi.org/10.1038/nrm3810

Kornete, M., Marone, R., Jeker, L.T., 2018. Highly Efficient and Versatile Plasmid-Based Gene Editing in Primary T Cells. J.I. 200, 2489–2501. https://doi.org/10.4049/jimmunol.1701121

Kruger, D., Schneck, P., Gelderblom, H., 2000. Helmut Ruska and the visualisation of viruses. The Lancet 355, 1713–1717. https://doi.org/10.1016/S0140-6736(00)02250-9

Kusumi, A., Ike, H., Nakada, C., Murase, K., Fujiwara, T., 2005a. Single-molecule tracking of membrane molecules: plasma membrane compartmentalization and dynamic assembly of raft-philic signaling molecules. Seminars in Immunology 17, 3–21. https://doi.org/10.1016/j.smim.2004.09.004

Kusumi, A., Nakada, C., Ritchie, K., Murase, K., Suzuki, K., Murakoshi, H., Kasai, R.S., Kondo, J., Fujiwara, T., 2005b. Paradigm Shift of the Plasma Membrane Concept from the Two-Dimensional Continuum Fluid to the Partitioned Fluid: High-Speed Single-Molecule Tracking of Membrane Molecules. Annu. Rev. Biophys. Biomol. Struct. 34, 351–378. https://doi.org/10.1146/annurev.biophys.34.040204.144637

Kusumi, A., Shirai, Y.M., Koyama-Honda, I., Suzuki, K.G.N., Fujiwara, T.K., 2010. Hierarchical organization of the plasma membrane: Investigations by single-molecule tracking vs. fluorescence correlation spectroscopy. FEBS Letters 584, 1814–1823. https://doi.org/10.1016/j.febslet.2010.02.047

Kusumi, A., Suzuki, K., 2005. Toward understanding the dynamics of membrane-raft-based molecular interactions. Biochimica et Biophysica Acta (BBA) - Molecular Cell Research 1746, 234–251. https://doi.org/10.1016/j.bbamcr.2005.10.001

Labbadia, J., Morimoto, R.I., 2015. The Biology of Proteostasis in Aging and Disease. Annu. Rev. Biochem. 84, 435–464. https://doi.org/10.1146/annurev-biochem-060614-033955

Lakowicz, J.R., 2006. Principles of Fluorescence Spectroscopy, 3 rd. Edition. ed. Springer, Boston.

Lange, K., 2011. Fundamental role of microvilli in the main functions of differentiated cells: Outline of an universal regulating and signaling system at the cell periphery. J. Cell. Physiol. 226, 896–927. https://doi.org/10.1002/jcp.22302

Lange, K., Gartzke, J., 2006. F-actin-based Ca signaling—a critical comparison with the current concept of Ca signaling. J. Cell. Physiol. 209, 270–287. https://doi.org/10.1002/jcp.20717

Lee, K., Byun, K., Hong, W., Chuang, H.-Y., Pack, C.-G., Bayarsaikhan, E., Paek, S.H., Kim, H., Shin, H.Y., Ideker, T., Lee, B., 2013. Proteome-wide discovery of mislocated proteins in cancer. Genome Research 23, 1283–1294. https://doi.org/10.1101/gr.155499.113

Levental, I., Lingwood, D., Grzybek, M., Coskun, U., Simons, K., 2010. Palmitoylation regulates raft affinity for the majority of integral raft proteins. Proceedings of the National Academy of Sciences 107, 22050–22054. https://doi.org/10.1073/pnas.1016184107

Levitt, M., 1978. Conformational preferences of amino acids in globular proteins. Biochemistry 17, 4277–4285. https://doi.org/10.1021/bi00613a026

Li, D., Shao, L., Chen, B.-C., Zhang, X., Zhang, M., Moses, B., Milkie, D.E., Beach, J.R., Hammer, J.A., Pasham, M., Kirchhausen, T., Baird, M.A., Davidson, M.W., Xu, P., Betzig, E., 2015. Extended-resolution structured illumination imaging of endocytic and cytoskeletal dynamics. Science 349, aab3500–aab3500. https://doi.org/10.1126/science.aab3500

Lillemeier, B.F., Pfeiffer, J.R., Surviladze, Z., Wilson, B.S., Davis, M.M., 2006. Plasma membrane-associated proteins are clustered into islands attached to the cytoskeleton. Proceedings of the National Academy of Sciences 103, 18992–18997. https://doi.org/10.1073/pnas.0609009103

Lin, Y.-C., Niewiadomski, P., Lin, B., Nakamura, H., Phua, S.C., Jiao, J., Levchenko, A., Inoue, Takafumi, Rohatgi, R., Inoue, Takanari, 2013. Chemically inducible diffusion trap at cilia reveals molecular sieve–like barrier. Nat Chem Biol 9, 437–443. https://doi.org/10.1038/nchembio.1252

Lippincott-Schwartz, J., Patterson, G.H., 2009. Photoactivatable fluorescent proteins for diffraction-limited and super-resolution imaging. Trends in Cell Biology 19, 555–565. https://doi.org/10.1016/j.tcb.2009.09.003

Lobo, S., 2013. Discovery of Selective and Potent Inhibitors of Palmitoylation, in: El-Shemy, H. (Ed.), Drug Discovery. InTech. https://doi.org/10.5772/52503

Lodish, H., Berk, A., Kaiser, C.A., Krieger, M., Bretscher, A., Ploegh, H., Amon, A., Martin, K.C., 2016. Molecular Cell Biology, 8 th edition. ed. W. H. Freeman, New York.

Lorent, J.H., Diaz-Rohrer, B., Lin, X., Spring, K., Gorfe, A.A., Levental, K.R., Levental, I., 2017. Structural determinants and functional consequences of protein affinity for membrane rafts. Nat Commun 8, 1219. https://doi.org/10.1038/s41467-017-01328-3

Lou, J., Rossy, J., Deng, Q., Pageon, S.V., Gaus, K., 2016. New Insights into How Trafficking Regulates T Cell Receptor Signaling. Front. Cell Dev. Biol. 4. https://doi.org/10.3389/fcell.2016.00077

Lukeš, T., Glatzová, D., Kvíčalová, Z., Levet, F., Benda, A., Letschert, S., Sauer, M., Brdička, T., Lasser, T., Cebecauer, M., 2017. Quantifying protein densities on cell membranes using super-resolution optical fluctuation imaging. Nat Commun 8, 1731. https://doi.org/10.1038/s41467-017-01857-x

Lukeš, T., Křížek, P., Švindrych, Z., Benda, J., Ovesný, M., Fliegel, K., Klíma, M., Hagen, G.M., 2014. Three-dimensional super-resolution structured illumination microscopy with maximum a posteriori probability image estimation. Opt. Express 22, 29805. https://doi.org/10.1364/OE.22.029805

Lundby, A., Lage, K., Weinert, B.T., Bekker-Jensen, D.B., Secher, A., Skovgaard, T., Kelstrup, C.D., Dmytriyev, A., Choudhary, C., Lundby, C., Olsen, J.V., 2012. Proteomic Analysis of Lysine Acetylation Sites in Rat Tissues Reveals Organ Specificity and Subcellular Patterns. Cell Reports 2, 419–431. https://doi.org/10.1016/j.celrep.2012.07.006

Lu-Walther, H.-W., Kielhorn, M., Förster, R., Jost, A., Wicker, K., Heintzmann, R., 2015. fastSIM: a practical implementation of fast structured illumination microscopy. Methods Appl. Fluoresc. 3, 014001. https://doi.org/10.1088/2050-6120/3/1/014001

Macháň, R., Jurkiewicz, P., Olżyńska, A., Olšinová, M., Cebecauer, M., Marquette, A., Bechinger, B., Hof, M., 2014. Peripheral and Integral Membrane Binding of Peptides Characterized by Time-Dependent Fluorescence Shifts: Focus on Antimicrobial Peptide LAH $_4$. Langmuir 30, 6171–6179. https://doi.org/10.1021/la5006314

Martin, B.R., Cravatt, B.F., 2009. Large-scale profiling of protein palmitoylation in mammalian cells. Nat Methods 6, 135–138. https://doi.org/10.1038/nmeth.1293

Masters, B.R., 2010. The Development of Fluorescence Microscopy, in: John Wiley & Sons, Ltd (Ed.), Encyclopedia of Life Sciences. John Wiley & Sons, Ltd, Chichester, UK, p. a0022093. https://doi.org/10.1002/9780470015902.a0022093

Maverakis, E., Kim, K., Shimoda, M., Gershwin, M.E., Patel, F., Wilken, R., Raychaudhuri, S., Ruhaak, L.R., Lebrilla, C.B., 2015. Glycans in the immune system and The Altered Glycan Theory of Autoimmunity: A critical review. Journal of Autoimmunity 57, 1–13. https://doi.org/10.1016/j.jaut.2014.12.002

Mazia, D., Schatten, G., Sale, W., 1975. Adhesion of cells to surfaces coated with polylysine. Applications to electron microscopy. The Journal of Cell Biology 66, 198–200. https://doi.org/10.1083/jcb.66.1.198

McCaffrey, K., Braakman, I., 2016. Protein quality control at the endoplasmic reticulum. Essays in Biochemistry 60, 227–235. https://doi.org/10.1042/EBC20160003

Millington, P.F., Critchley, D.R., Tovell, P.W.A., Pearson, R., 1969. Scanning electron microscopy of intestinal microvilli. Journal of Microscopy 89, 339–344. https://doi.org/10.1111/j.1365-2818.1969.tb00681.x

Mitra, K., Ubarretxena-Belandia, I., Taguchi, T., Warren, G., Engelman, D.M., 2004. Modulation of the bilayer thickness of exocytic pathway membranes by membrane proteins rather than cholesterol. Proceedings of the National Academy of Sciences 101, 4083–4088. https://doi.org/10.1073/pnas.0307332101

Morimoto, R.I., Cuervo, A.M., 2014. Proteostasis and the Aging Proteome in Health and Disease. The Journals of Gerontology Series A: Biological Sciences and Medical Sciences 69, S33–S38. https://doi.org/10.1093/gerona/glu049

Mortensen, K.I., Churchman, L.S., Spudich, J.A., Flyvbjerg, H., 2010. Optimized localization analysis for single-molecule tracking and super-resolution microscopy. Nat Methods 7, 377–381. https://doi.org/10.1038/nmeth.1447

Mueller, V., Ringemann, C., Honigmann, A., Schwarzmann, G., Medda, R., Leutenegger, M., Polyakova, S., Belov, V.N., Hell, S.W., Eggeling, C., 2011. STED Nanoscopy Reveals Molecular Details of Cholesterol- and Cytoskeleton-Modulated Lipid Interactions in Living Cells. Biophysical Journal 101, 1651–1660. https://doi.org/10.1016/j.bpj.2011.09.006

Müller, T., Schumann, C., Kraegeloh, A., 2012. STED Microscopy and its Applications: New Insights into Cellular Processes on the Nanoscale. ChemPhysChem 13, 1986–2000. https://doi.org/10.1002/cphc.201100986

Munro, S., 1995. An investigation of the role of transmembrane domains in Golgi protein retention. The EMBO Journal 14, 4695–4704. https://doi.org/10.1002/j.1460-2075.1995.tb00151.x

Musacchio, A., Smith, C.J., Roseman, A.M., Harrison, S.C., Kirchhausen, T., Pearse, B.M.F., 1999. Functional Organization of Clathrin in Coats: Combining Electron Cryomicroscopy and X-Ray Crystallography. Molecular Cell 10.

Nagerl, U.V., Bonhoeffer, T., 2010. Imaging Living Synapses at the Nanoscale by STED Microscopy. Journal of Neuroscience 30, 9341–9346. https://doi.org/10.1523/JNEUROSCI.0990-10.2010

Nextprot database [WWW Document], 2020. URL https://www.nextprot.org/about/statistics (accessed 3.9.20).

Nijhara, R., van Hennik, P.B., Gignac, M.L., Kruhlak, M.J., Hordijk, P.L., Delon, J., Shaw, S., 2004. Rac1 Mediates Collapse of Microvilli on Chemokine-Activated T Lymphocytes. J Immunol 173, 4985–4993. https://doi.org/10.4049/jimmunol.173.8.4985

Okhonin, V., 1991. Method of investigating specimen microsctrucutre. SU1374922A1.

Olšinová, M., Jurkiewicz, P., Kishko, I., Sýkora, J., Sabó, J., Hof, M., Cwiklik, L., Cebecauer, M., 2018. Roughness of Transmembrane Helices Reduces Lipid Membrane Dynamics. iScience 10, 87–97. https://doi.org/10.1016/j.isci.2018.11.026

Ovesný, M., Křížek, P., Borkovec, J., Švindrych, Z., Hagen, G.M., 2014. ThunderSTORM: a comprehensive ImageJ plug-in for PALM and STORM data analysis and super-resolution imaging. Bioinformatics 30, 2389–2390. https://doi.org/10.1093/bioinformatics/btu202

Park, Y.I., Lee, K.T., Suh, Y.D., Hyeon, T., 2015. Upconverting nanoparticles: a versatile platform for wide-field two-photon microscopy and multi-modal in vivo imaging. Chem. Soc. Rev. 44, 1302–1317. https://doi.org/10.1039/C4CS00173G

Patterson, G.H., 2002. A Photoactivatable GFP for Selective Photolabeling of Proteins and Cells. Science 297, 1873–1877. https://doi.org/10.1126/science.1074952

Pavani, S.R.P., Thompson, M.A., Biteen, J.S., Lord, S.J., Liu, N., Twieg, R.J., Piestun, R., Moerner, W.E., 2009. Three-dimensional, single-molecule fluorescence imaging beyond the diffraction limit by using a double-helix point spread function. Proceedings of the National Academy of Sciences 106, 2995–2999. https://doi.org/10.1073/pnas.0900245106

Pawley, J.B., 2006. Handbook of Biological Confocal Microscopy, 3 rd. edition. ed. Springer, Berlin.

Pertea, M., Salzberg, S.L., 2010. Between a chicken and a grape: estimating the number of human genes 7.

Pezeshkian, W., Gao, H., Arumugam, S., Becken, U., Bassereau, P., Florent, J.-C., Ipsen, J.H., Johannes, L., Shillcock, J.C., 2017. Mechanism of Shiga Toxin Clustering on Membranes. ACS Nano 11, 314–324. https://doi.org/10.1021/acsnano.6b05706

Pinaud, F., Dahan, M., 2011. Targeting and imaging single biomolecules in living cells by complementation-activated light microscopy with split-fluorescent proteins. Proceedings of the National Academy of Sciences 108, E201–E210. https://doi.org/10.1073/pnas.1101929108

Prasher, D.C., Eckenrode, V.K., Ward, W.W., Prendergast, F.G., Cormier, M.J., 1992. Primary structure of the Aequorea victoria green-fluorescent protein. Gene 111, 229–233. https://doi.org/10.1016/0378-1119(92)90691-H

Price, S.P., Davidson, M.W., 2020. STED-Zeiss [WWW Document]. URL http://zeiss-campus.magnet.fsu.edu/tutorials/superresolution/stedconcept/indexflash.html (accessed 4.8.20).

Proszynski, T.J., Simons, K., Bagnat, M., 2004. *O* -Glycosylation as a Sorting Determinant for Cell Surface Delivery in Yeast. MBoC 15, 1533–1543. https://doi.org/10.1091/mbc.e03-07-0511

Quesnel, S., Silvius, J.R., 1994. Cysteine-Containing Peptide Sequences Exhibit Facile Uncatalyzed Transacylation and Acyl-CoA-dependent Acylation at the Lipid Bilayer Interfacet 45, 13340–13348.

Radak, Z., Chung, H.Y., Goto, S., 2005. Exercise and hormesis: oxidative stress-related adaptation for successful aging. Biogerontology 6, 71–75. https://doi.org/10.1007/s10522-004-7386-7

Ram, S., Prabhat, P., Chao, J., Sally Ward, E., Ober, R.J., 2008. High Accuracy 3D Quantum Dot Tracking with Multifocal Plane Microscopy for the Study of Fast Intracellular Dynamics in Live Cells. Biophysical Journal 95, 6025–6043. https://doi.org/10.1529/biophysj.108.140392

Rankin, B.R., Moneron, G., Wurm, C.A., Nelson, J.C., Walter, A., Schwarzer, D., Schroeder, J., Colón-Ramos, D.A., Hell, S.W., 2011. Nanoscopy in a Living Multicellular Organism Expressing GFP. Biophysical Journal 100, L63–L65. https://doi.org/10.1016/j.bpj.2011.05.020

Rasband, W.S., 1997. ImageJ. National Institutes of Health, Bethesda, Maryland, USA.

Rayleigh, Lord, 1879. Investigations in Optics, with special reference to the Spectroscope. Lond.Edinb.Dubl.Phil.Mag., 5th.

Rocks, O., Gerauer, M., Vartak, N., Koch, S., Huang, Z.-P., Pechlivanis, M., Kuhlmann, J., Brunsveld, L., Chandra, A., Ellinger, B., Waldmann, H., Bastiaens, P.I.H., 2010. The Palmitoylation Machinery Is a Spatially Organizing System for Peripheral Membrane Proteins. Cell 141, 458–471. https://doi.org/10.1016/j.cell.2010.04.007

Rocks, O., Peyker, A., Kahms, M., Verveer, P.J., Koerner, C., Lumbierres, M., Kuhlmann, J., Waldmann, H., Wittinghofer, A., Bastiaens, P.I.H., 2005. An Acylation Cycle Regulates Localization and Activity of Palmitoylated Ras Isoforms. Science 307, 1746–1752. https://doi.org/10.1126/science.1105654

Rossboth, B., Arnold, A.M., Ta, H., Platzer, R., Kellner, F., Huppa, J.B., Brameshuber, M., Baumgart, F., Schütz, G.J., 2018. TCRs are randomly distributed on the plasma membrane of resting antigen-experienced T cells. Nat Immunol 19, 821–827. https://doi.org/10.1038/s41590-018-0162-7

Roth, A.F., Feng, Y., Chen, L., Davis, N.G., 2002. The yeast DHHC cysteine-rich domain protein Akr1p is a palmitoyl transferase. The Journal of Cell Biology 159, 23–28. https://doi.org/10.1083/jcb.200206120

Rust, M.J., Bates, M., Zhuang, X., 2006. Sub-diffraction-limit imaging by stochastic optical reconstruction microscopy (STORM). Nat Methods 3, 793–796. https://doi.org/10.1038/nmeth929

Sabin, F.R., 1939. CELLULAR REACTIONS TO A DYE-PROTEIN WITH A CONCEPT OF THE MECHANISM OF ANTIBODY FORMATION. The Journal of Experimental Medicine 70, 67–82. https://doi.org/10.1084/jem.70.1.67

Sage, P.T., Varghese, L.M., Martinelli, R., Sciuto, T.E., Kamei, M., Dvorak, A.M., Springer, T.A., Sharpe, A.H., Carman, C.V., 2012. Antigen Recognition Is Facilitated by Invadosome-like Protrusions Formed by Memory/Effector T Cells. J.I. 188, 3686–3699. https://doi.org/10.4049/jimmunol.1102594

Saletti, D., Radzimanowski, J., Effantin, G., Midtvedt, D., Mangenot, S., Weissenhorn, W., Bassereau, P., Bally, M., 2017. The Matrix protein M1 from influenza C virus induces tubular membrane invaginations in an in vitro cell membrane model. Sci Rep 7, 40801. https://doi.org/10.1038/srep40801

Sanger, F., Thompson, E.O.P., 1953. The amino-acid sequence in the glycyl chain of insulin. 1. The identification of lower peptides from partial hydrolysates. Biochemical Journal 53, 353–366. https://doi.org/10.1042/bj0530353

Sanger, F., Tuppy, H., 1951. The amino-acid sequence in the phenylalanyl chain of insulin. 1. The identification of lower peptides from partial hydrolysates. Biochemical Journal 49, 463–481. https://doi.org/10.1042/bj0490463

Santos, A.M., Ponjavic, A., Fritzsche, M., Fernandes, R.A., de la Serna, J.B., Wilcock, M.J., Schneider, F., Urbančič, I., McColl, J., Anzilotti, C., Ganzinger, K.A., Aßmann, M., Depoil, D., Cornall, R.J., Dustin, M.L., Klenerman, D., Davis, S.J., Eggeling, C., Lee, S.F., 2018. Capturing resting T cells: the perils of PLL. Nat Immunol 19, 203–205. https://doi.org/10.1038/s41590-018-0048-8

Sato, K., Nakano, A., 2007. Mechanisms of COPII vesicle formation and protein sorting. FEBS Letters 581, 2076–2082. https://doi.org/10.1016/j.febslet.2007.01.091

Sauer, M., 2013. Localization microscopy coming of age: from concepts to biological impact. Journal of Cell Science 126, 3505–3513. https://doi.org/10.1242/jcs.123612

Saxton, M.J., 1987. The Effect of Mobile Obstacles 52, 9.

Schermelleh, L., Heintzmann, R., Leonhardt, H., 2010. A guide to super-resolution fluorescence microscopy. The Journal of Cell Biology 190, 165–175. https://doi.org/10.1083/jcb.201002018

Schindelin, J., Arganda-Carreras, I., Frise, E., Kaynig, V., Longair, M., Pietzsch, T., Preibisch, S., Rueden, C., Saalfeld, S., Schmid, B., Tinevez, J.-Y., White, D.J., Hartenstein, V., Eliceiri, K., Tomancak, P., Cardona, A., 2012. Fiji: an open-source platform for biological-image analysis. Nat Methods 9, 676–682. https://doi.org/10.1038/nmeth.2019

Schmidt, T., Schutz, G.J., Baumgartner, W., Gruber, H.J., Schindler, H., 1996. Imaging of single molecule diffusion. Proceedings of the National Academy of Sciences 93, 2926–2929. https://doi.org/10.1073/pnas.93.7.2926

Schnitzbauer, J., Strauss, M.T., Schlichthaerle, T., Schueder, F., Jungmann, R., 2017. Super-resolution microscopy with DNA-PAINT. Nat Protoc 12, 1198–1228. https://doi.org/10.1038/nprot.2017.024

Schwarz, H., Humbel, B.M., 2014. Correlative Light and Electron Microscopy Using Immunolabeled Sections, in: Kuo, J. (Ed.), Electron Microscopy: Methods and Protocols, Methods in Molecular Biology. Humana Press, Totowa, NJ, pp. 559–592. https://doi.org/10.1007/978-1-62703-776-1_25

Sevcsik, E., Brameshuber, M., Fölser, M., Weghuber, J., Honigmann, A., Schütz, G.J., 2015. GPI-anchored proteins do not reside in ordered domains in the live cell plasma membrane. Nat Commun 6, 6969. https://doi.org/10.1038/ncomms7969

Sevcsik, E., Schütz, G.J., 2016. With or without rafts? Alternative views on cell membranes. BioEssays 38, 129–139. https://doi.org/10.1002/bies.201500150

Sevier, C.S., Weisz, O.A., Davis, M., Machamer, C.E., 2000. Efficient Export of the Vesicular Stomatitis Virus G Protein from the Endoplasmic Reticulum Requires a Signal in the Cytoplasmic Tail That Includes Both Tyrosine-based and Di-acidic Motifs. MBoC 11, 13–22. https://doi.org/10.1091/mbc.11.1.13

Sezgin, E., Waithe, D., Bernardino de la Serna, J., Eggeling, C., 2015. Spectral Imaging to Measure Heterogeneity in Membrane Lipid Packing. ChemPhysChem 16, 1387–1394. https://doi.org/10.1002/cphc.201402794

Sharonov, A., Hochstrasser, R.M., 2006. Wide-field subdiffraction imaging by accumulated binding of diffusing probes. Proceedings of the National Academy of Sciences 103, 18911–18916. https://doi.org/10.1073/pnas.0609643104

Sharpe, H.J., Stevens, T.J., Munro, S., 2010. A Comprehensive Comparison of Transmembrane Domains Reveals Organelle-Specific Properties. Cell 142, 158–169. https://doi.org/10.1016/j.cell.2010.05.037

Sherman, E., Barr, V., Manley, S., Patterson, G., Balagopalan, L., Akpan, I., Regan, C.K., Merrill, R.K., Sommers, C.L., Lippincott-Schwartz, J., Samelson, L.E., 2011. Functional Nanoscale Organization of Signaling Molecules Downstream of the T Cell Antigen Receptor. Immunity 35, 705–720. https://doi.org/10.1016/j.immuni.2011.10.004

Shin, J., Doyle, C., Yang, Z., Kappes, D., Strominger, J.L., 1990. Structural features of the cytoplasmic region of CD4 required for internalization. The EMBO Journal 9, 425–434. https://doi.org/10.1002/j.1460-2075.1990.tb08127.x

Shroff, H., Galbraith, C.G., Galbraith, J.A., Betzig, E., 2008. Live-cell photoactivated localization microscopy of nanoscale adhesion dynamics. Nat Methods 5, 417–423. https://doi.org/10.1038/nmeth.1202

Shroff, H., Galbraith, C.G., Galbraith, J.A., White, H., Gillette, J., Olenych, S., Davidson, M.W., Betzig, E., 2007. Dual-color superresolution imaging of genetically expressed probes within individual adhesion complexes. Proceedings of the National Academy of Sciences 104, 20308–20313. https://doi.org/10.1073/pnas.0710517105

Shroff, H., Hess, S.T., Betzig, E., Hess, H.F., Patterson, G.H., Lippincott-Schwartz, J., Davidson, M.W., 2020. SMLM-Zeiss [WWW Document]. URL: http://zeiss-campus.magnet.fsu.edu/articles/superresolution/palm/practicalaspects.html (accessed 5.27.20).

Shtengel, G., Galbraith, J.A., Galbraith, C.G., Lippincott-Schwartz, J., Gillette, J.M., Manley, S., Sougrat, R., Waterman, C.M., Kanchanawong, P., Davidson, M.W., Fetter, R.D., Hess, H.F., 2009. Interferometric fluorescent super-resolution microscopy resolves 3D cellular ultrastructure. Proceedings of the National Academy of Sciences 106, 3125–3130. https://doi.org/10.1073/pnas.0813131106

Sieh, M., Batzer, A., Schlessinger, J., Weiss, A., 1994. GRB2 and Phospholipase C-yl Associate with a 36- to 38-Kilodalton Phosphotyrosine Protein after T-Cell Receptor Stimulation. MOL. CELL. BIOL. 14, 8.

Snyder, W.S., Cook, M.J., Nasset, E.S., Karhausen, L.R., Howells, G.P., Tipton, I.H., 1972. Report of the Task Group on Reference Man. Pergamon Press.

Spear, J.M., Koborssy, D.A., Schwartz, A.B., Johnson, A.J., Audhya, A., Fadool, D.A., Stagg, S.M., 2015. Kv1.3 contains an alternative C-terminal ER exit motif and is recruited into COPII vesicles by Sec24a. BMC Biochem 16, 16. https://doi.org/10.1186/s12858-015-0045-6

Spiess, M., 1995. Heads or tails - what determines the orientation of proteins in the membrane. FEBS Letters 369, 76–79. https://doi.org/10.1016/0014-5793(95)00551-J

Stagg, S.M., Gürkan, C., Fowler, D.M., LaPointe, P., Foss, T.R., Potter, C.S., Carragher, B., Balch, W.E., 2006. Structure of the Sec13/31 COPII coat cage. Nature 439, 234–238. https://doi.org/10.1038/nature04339

Štěpánek, O., Dráber, P., Hořejší, V., 2014. Palmitoylated transmembrane adaptor proteins in leukocyte signaling. Cellular Signalling 26, 895–902. https://doi.org/10.1016/j.cellsig.2014.01.007

Stephen, L.A., ElMaghloob, Y., McIlwraith, M.J., Yelland, T., Castro Sanchez, P., Roda-Navarro, P., Ismail, S., 2018. The Ciliary Machinery Is Repurposed for T Cell Immune Synapse Trafficking of LCK. Developmental Cell 47, 122-132.e4. https://doi.org/10.1016/j.devcel.2018.08.012

Streuli, M., Krueger, N.X., Thai, T., Tang, M., Saito, H., 1990. Distinct functional roles of the two intracellular phosphatase like domains of the receptor-linked protein tyrosine phosphatases LCA and LAR. The EMBO Journal 9, 2399–2407. https://doi.org/10.1002/j.1460-2075.1990.tb07415.x

SVI, 2020. Stimulated Emission Depletion (STED) Microscopy | Scientific Volume Imaging [WWW Document]. URL https://svi.nl/Stimulated-Emission-Depletion-(STED)-Microscopy (accessed 5.27.20).

Tanimura, N., Saitoh, S., Kawano, S., Kosugi, A., Miyake, K., 2006. Palmitoylation of LAT contributes to its subcellular localization and stability. Biochemical and Biophysical Research Communications 341, 1177–1183. https://doi.org/10.1016/j.bbrc.2006.01.076

The naked scientist [WWW Document], 2020. URL: https://www.thenakedscientists.com/files/images/bronchiolarepithelium3-semjpg (accessed 4.23.20).

Theocharis, A.D., Skandalis, S.S., Gialeli, C., Karamanos, N.K., 2016. Extracellular matrix structure. Advanced Drug Delivery Reviews 97, 4–27. https://doi.org/10.1016/j.addr.2015.11.001

Thompson, R.E., Larson, D.R., Webb, W.W., 2002. Precise Nanometer Localization Analysis for Individual Fluorescent Probes. Biophysical Journal 82, 2775–2783. https://doi.org/10.1016/S0006-3495(02)75618-X

Tinnefeld, P., Sauer, M., 2005. Branching Out of Single-Molecule Fluorescence Spectroscopy: Challenges for Chemistry and Influence on Biology. Angew. Chem. Int. Ed. 44, 2642–2671. https://doi.org/10.1002/anie.200300647

Tossi, A., Sandri, L., Giangaspero, A., 2002. New consensus hydrophobicity scale extended to non-proteinogenic amino acids, in: Peptides. Edizioni Ziino, Napoli, Italy, pp. 416–417.

Traub, L.M., 2009. Clathrin Couture: Fashioning Distinctive Membrane Coats at the Cell Surface. PLoS Biol 7, e1000192. https://doi.org/10.1371/journal.pbio.1000192

Tunnacliffe, A., Lapinski, J., 2003. Resurrecting Van Leeuwenhoek's rotifers: a reappraisal of the role of disaccharides in anhydrobiosis 17.

Urban, N.T., Willig, K.I., Hell, S.W., Nägerl, U.V., 2011. STED Nanoscopy of Actin Dynamics in Synapses Deep Inside Living Brain Slices. Biophysical Journal 101, 1277–1284. https://doi.org/10.1016/j.bpj.2011.07.027

van de Linde, S., 2019. Single-molecule localization microscopy analysis with ImageJ. J. Phys. D: Appl. Phys. 52, 203002. https://doi.org/10.1088/1361-6463/ab092f

van de Linde, S., Kasper, R., Heilemann, M., Sauer, M., 2008. Photoswitching microscopy with standard fluorophores. Appl. Phys. B 93, 725–731. https://doi.org/10.1007/s00340-008-3250-9

van de Linde, S., Krstić, I., Prisner, T., Doose, S., Heilemann, M., Sauer, M., 2011a. Photoinduced formation of reversible dye radicals and their impact on super-resolution imaging. Photochem. Photobiol. Sci. 10, 499–506. https://doi.org/10.1039/C0PP00317D

van de Linde, S., Löschberger, A., Klein, T., Heidbreder, M., Wolter, S., Heilemann, M., Sauer, M., 2011b. Direct stochastic optical reconstruction microscopy with standard fluorescent probes. Nat Protoc 6, 991–1009. https://doi.org/10.1038/nprot.2011.336

Varma, R., Campi, G., Yokosuka, T., Saito, T., Dustin, M.L., 2006. T Cell Receptor-Proximal Signals Are Sustained in Peripheral Microclusters and Terminated in the Central Supramolecular Activation Cluster. Immunity 25, 117–127. https://doi.org/10.1016/j.immuni.2006.04.010

Vicidomini, G., Bianchini, P., Diaspro, A., 2018. STED super-resolved microscopy. Nat Methods 15, 173–182. https://doi.org/10.1038/nmeth.4593

Videla, L.A., Rodrigo, R., Orellana, M., Fernandez, V., Tapia, G., Quiñones, L., Varela, N., Contreras, J., Lazarte, R., Csendes, A., Rojas, J., Maluenda, F., Burdiles, P., Diaz, J.C., Smok, G., Thielemann, L., Poniachik, J., 2004. Oxidative stress-related parameters in the liver of non-alcoholic fatty liver disease patients. Clinical Science 106, 261–268. https://doi.org/10.1042/CS20030285

Vlastaridis, P., Kyriakidou, P., Chaliotis, A., Van de Peer, Y., Oliver, S.G., Amoutzias, G.D., 2017. Estimating the total number of phosphoproteins and phosphorylation sites in eukaryotic proteomes. GigaScience 6.
https://doi.org/10.1093/gigascience/giw015

Voet, D., Voet, J.G., 2011. Biochemistry, 4th ed. ed. John Wiley & Sons, Hoboken, NJ.

Von Ardenne, M., Beischer, D., 1940. Untersuchung von Metalloxyd-Rauchen mit dem Universal-Elektronenmikroskop. Zeitschrift für Elektrochemie und angewandte physikalische Chemie 46, 270–277.
https://doi.org/10.1002/bbpc.19400460406

von Diezmann, A., Shechtman, Y., Moerner, W.E., 2017. Three-Dimensional Localization of Single Molecules for Super-Resolution Imaging and Single-Particle Tracking. Chem. Rev. 117, 7244–7275.
https://doi.org/10.1021/acs.chemrev.6b00629

von Heijne, G., 2007. The membrane protein universe: what's out there and why bother? J Intern Med 261, 543–557. https://doi.org/10.1111/j.1365-2796.2007.01792.x

von Heijne, G., 1989. Control of topology and mode of assembly of a polytopic membrane protein by positively charged residues. Nature 341, 456–458. https://doi.org/10.1038/341456a0

Wang, X., Li, S., 2014. Protein mislocalization: Mechanisms, functions and clinical applications in cancer. Biochimica et Biophysica Acta (BBA) - Reviews on Cancer 1846, 13–25.
https://doi.org/10.1016/j.bbcan.2014.03.006

Wange, R.L., 2000. LAT, the Linker for Activation of T Cells: A Bridge Between T Cell-Specific and General Signaling Pathways. Sci. Signal, re1 63, 14.

Wegner, W., Mott, A.C., Grant, S.G.N., Steffens, H., Willig, K.I., 2018. In vivo STED microscopy visualizes PSD95 sub-structures and morphological changes over several hours in the mouse visual cortex. Sci Rep 8, 219. https://doi.org/10.1038/s41598-017-18640-z

WHO statistics [WWW Document], 2018. Global Health Estimates 2016: Disease burden by Cause, Age, Sex, by Country and by Region, 2000-2016. Geneva, World Health Organization; 2018. URL:
http://www.who.int/healthinfo/global_burden_disease/estimates/en/ (accessed 3.18.20).

Wildanger, D., Patton, B.R., Schill, H., Marseglia, L., Hadden, J.P., Knauer, S., Schönle, A., Rarity, J.G., O'Brien, J.L., Hell, S.W., Smith, J.M., 2012. Solid Immersion Facilitates Fluorescence Microscopy with Nanometer Resolution and Sub-Ångström Emitter Localization. Adv. Mater. 24, OP309–OP313.
https://doi.org/10.1002/adma.201203033

Williamson, D.J., Owen, D.M., Rossy, J., Magenau, A., Wehrmann, M., Gooding, J.J., Gaus, K., 2011. Pre-existing clusters of the adaptor Lat do not participate in early T cell signaling events. Nat Immunol 12, 655–662. https://doi.org/10.1038/ni.2049

Williamson, M.P., Havel, T.F., Wiithrich, K., 1985. Solution Conformation of Proteinase Inhibitor IIA from Bull Seminal Plasma by ‘H Nuclear Magnetic Resonance and Distance Geometry. J. Mol. Biol. 182, 21.

Wilman, H.R., Shi, J., Deane, C.M., 2014. Helix kinks are equally prevalent in soluble and membrane proteins: Helix Kinks in Soluble and Membrane Helices. Proteins 82, 1960–1970. https://doi.org/10.1002/prot.24550

Wilson, T., 1995. The Role of the Pinhole in Confocal Imaging System, in: Pawley, J.B. (Ed.), Handbook of Biological Confocal Microscopy. Springer US, Boston, MA, pp. 167–182. https://doi.org/10.1007/978-1-4757-5348-6_11

Wold, F., 1981. In Vivo Chemical Modification of Proteins (Post-Translational Modification). Annu. Rev. Biochem. 50, 783–814. https://doi.org/10.1146/annurev.bi.50.070181.004031

Wolter, S., Löschberger, A., Holm, T., Aufmkolk, S., Dabauvalle, M.-C., van de Linde, S., Sauer, M., 2012. rapidSTORM: accurate, fast open-source software for localization microscopy. Nat Methods 9, 1040–1041. https://doi.org/10.1038/nmeth.2224

Xiao, J.H., Davidson, I., Matthes, H., Garnier, J.-M., Chambon, P., 1991. Cloning, expression, and transcriptional properties of the human enhancer factor TEF-1. Cell 65, 551–568. https://doi.org/10.1016/0092-8674(91)90088-G

Yeung, T., Gilbert, G.E., Shi, J., Silvius, J., Kapus, A., Grinstein, S., 2008. Membrane Phosphatidylserine Regulates Surface Charge and Protein Localization. Science 319, 210–213. https://doi.org/10.1126/science.1152066

Yildiz, A., Selvin, P.R., 2005. Fluorescence Imaging with One Nanometer Accuracy: Application to Molecular Motors. Acc. Chem. Res. 38, 574–582. https://doi.org/10.1021/ar040136s

Zanetti, G., Prinz, S., Daum, S., Meister, A., Schekman, R., Bacia, K., Briggs, J.A., 2013. The structure of the COPII transport-vesicle coat assembled on membranes. eLife 2, e00951. https://doi.org/10.7554/eLife.00951

Zeidman, R., Jackson, C.S., Magee, A.I., 2009. Protein acyl thioesterases (Review). Molecular Membrane Biology 26, 32–41. https://doi.org/10.1080/09687680802629329

Ziaowei, Z., 2017. Illuminating biology at the nanoscale with single-molecule and super-resolution imaging. Nanobiology Honours Programme News Blog. URL: https://nanobiologyhonoursprogrammeblog.wordpress.com/2017/02/02/illuminating-biology-at-the-nanoscale-with-single-molecule-and-super-resolution-imaging/ (accessed 5.27.20).

Zlatkine, P., Mehul, B., Magee, A.I., 1997. Retargeting of cytosolic proteins to the plasma membrane by the Lck protein tyrosine kinase dual acylation motif. Journal of Cell Science 110, 673–679.

Zwettler, F.U., Spindler, M.-C., Reinhard, S., Klein, T., Kurz, A., Benavente, R., Sauer, M., 2020. Tracking down the molecular architecture of the synaptonemal complex by expansion microscopy. Nat Commun 11, 3222. https://doi.org/10.1038/s41467-020-17017-7

7 APPENDICES

7.1 Protocols

Protocol 01: Cleaning of foverslips for SMLM

Protocol 02: Glycine coating of coverslips for SMLM

Protocol 03: dSTORM imaging buffer

Protocol 01: Cleaning of foverslips for SMLM

Materials

- Hellmanex III® (Helma Analytics)
- MilliQ® water (Merck)

1. Fill rack holder with coverslips (25 mm for PALM/dSTORM, fit to 6-well plate; 12 mm for 60x objective, fit to 12-well plate).

2. Place into beaker (Should be clean one), fill with 2% Hellmanex in MilliQ-water solution, cover top with aluminium foil.

3. Put into water tank, overnight incubation at 56-80 °C.

4. Sonicate for 30 minuntes, heating on.

5. Wash 3x with MilliQ-water (each wash: aspire solution), fill with MilliQ-water.

6. Sonicate 30 minutes, heating on.

7. Wash 5x with MilliQ-water (each wash: aspire solution), fill with MilliQ-water.

8. Store in MilliQ-water for max. 3 weeks covered with aluminium foil at room temperature.

Protocol 02: Glycine coating of coverslips for SMLM

Materials

- Glycine (powder), # G7126 (Sigma)
- MilliQ® water, (Merck)
- Ethanol 96%

1. Clean microscope slides (coverslips) with distilled water.

For adherent cells start here!

2. Then follow one of the two sterilization processes:
    a. Disinfect them by washing with 70% Et-OH.
    b. Wash once with distilled sterile water.

    a. Place the clean microscope slides into glass petri-dish and autoclave them.

   NOTE: Use **always sterile tweezers** for the whole following process (the best is to use autoclave).

For suspension cells start here!

3. Allow the slides to dry completely in the laminar box (suck all the resting fluid).
   Note: If slides are not dry completely, they stick to the plastic surface and are not able to be detached.

4. Lay down into petri-dish (more-well plate).

5. Cover the whole surface of the slide with 2M sterile glycine solution (placed in the fridge).

6. Incubate in the laminar box under cover for 15 min – 1 hour.
   Note: Try to avoid drying, as it leads to immediate glycine crystallization.

7. Suck out as much fluid as possible.
   Note: Work as fast as possible to avoid crystallization of resting glycine.

   (Recommended: Wash once with distilled sterile water to remove unbound glycine.)

8. Seed cells in desired number in serum free medium as fast as possible.

Protocol 03: dSTORM imaging buffer

Materials

- Cysteamine (MEA) #30070-10G (Sigma)- store at 4 °C
- Glucose oxidase type seven from Aspergillius #G2133-50KU (Sigma)-store at -20 °C
- Catalase from Bovine liver C40-100 mg (Sigma) - store at -20 °C
- 1M Tris pH 8.0 # 22638 500 ML (Affymetrix / USB) - store at room temperature
- NaCl
- Glucose

Stocks

- Buffer A: 50 mM Tris-HCl (pH 8.0) + 10 mM NaCl) - store at room temperature
- Buffer B: 50 mM Tris-HCl (pH 8.0) + 10 mM NaCl + 10% (w/v) glucose - store at 4 °C
- 1 M MEA: 77 mg MEA dissolved in 1 mL Buffer A - store at 4 °C
- Gloxy: glucose oxidase (Gluox)+catalase mixture dissolved in buffer A - store at 4 °C

- When making Gloxy stock, calculate the amount to add based on the active units (AU) since not all the protein in the bottle is active. Both the Catalase and Glucose from Sigma should have the information written on the tube. For 10x stock of Gloxy mix 1,688 AU Gluox + 14,040 AU Catalase into 1mL of 50 mM Tris+10 mM NaCl (pH 8.0) and vortex.

Imaging buffer – Make the mixture on ice or at 4 °C fresh before imaging

Typically 50 mM MEA + 1x Gloxy in buffer B

Mix 50 uL of 1 M MEA + 100 uL of 10x Gloxy + 850 uL of buffer B in a 1.5 ml centrifuge tube and vortex.

Buffer can be used at room temperature imaging for approximately 2 hours.

7.2 Lists of figures and notes

7.3 Publications

Publication 1:

Tomáš Chum, Daniela Glatzová, Zuzana Kvíčalová, Jan Malínský, Tomáš Brdička,
Marek Cebecauer

The role of palmitoylation and transmembrane domain in sorting of transmembrane adaptor proteins.

Journal of Cell Science, 2016.

https://doi.org/10.1242/jcs.194209

© 2016. Published by The Company of Biologists Ltd | Journal of Cell Science (2016) 129, 95-107 doi:10.1242/jcs.175190

RESEARCH ARTICLE

The role of palmitoylation and transmembrane domain in sorting of transmembrane adaptor proteins

Tomáš Chum[1], Daniela Glatzová[1,2], Zuzana Kvíčalová[1], Jan Malínský[3], Tomáš Brdička[2] and Marek Cebecauer[1,*]

ABSTRACT

Plasma membrane proteins synthesised at the endoplasmic reticulum are delivered to the cell surface via sorting pathways. Hydrophobic mismatch theory based on the length of the transmembrane domain (TMD) dominates discussion about determinants required for protein sorting to the plasma membrane. Transmembrane adaptor proteins (TRAP) are involved in signalling events which take place at the plasma membrane. Members of this protein family have TMDs of varying length. We were interested in whether palmitoylation or other motifs contribute to the effective sorting of TRAP proteins. We found that palmitoylation is essential for some, but not all, TRAP proteins independent of their TMD length. We also provide evidence that palmitoylation and proximal sequences can modulate sorting of artificial proteins with TMDs of suboptimal length. Our observations point to a unique character of each TMD defined by its primary amino acid sequence and its impact on membrane protein localisation. We conclude that, in addition to the TMD length, secondary sorting determinants such as palmitoylation or flanking sequences have evolved for the localisation of membrane proteins.

KEY WORDS: LAT, PAG, Palmitoylation, Plasma membrane, Protein sorting, Transmembrane domain

INTRODUCTION

Integral membrane proteins of eukaryotic cells comprise almost 30% of all proteins encoded by the human genome (Almén et al., 2009). These undergo sorting into target compartments such as the endoplasmic reticulum (ER), Golgi complex, mitochondria or the plasma membrane to perform their function. Mis-localisation can lead to a loss-of-function of these proteins, resulting in cell malfunction and even development of diseases (Howell et al., 2006). Structural and sequence motifs responsible for protein sorting events have been studied for more than 30 years. During that time a number of determinants of specific membrane protein localisation have been identified. These include sequence motifs in cytosolic and lumenal domains (e.g. KDEL for the ER or YxxØ for clathrin-dependent processes; Traub, 2009), N- and O-glycosylation of the extracellular domains (Fiedler and Simons, 1995; Potter et al., 2006; Proszynski et al., 2004), and physical properties of the transmembrane domain (TMD) such as length and hydrophobicity (Cosson et al., 2013; Sharpe et al., 2010). This wide variety of sorting signals is further extended by the fact that more than one determinant can define the localisation of proteins in the cell (Alonso et al., 1997; Duffield et al., 2008). No universal signal or motif has been demonstrated for the sorting of proteins to the plasma membrane. Therefore, all parts of the protein need to be tested for their impact on the proper localisation when investigating protein function using various mutants.

Transmembrane adaptor proteins (TRAPs) are topologically related type I integral membrane proteins that enable the association of signalling effectors and other enzymes with the plasma membrane of eukaryotic cells. They contain only a short extracellular part, single TMD and the cytosolic domain with multiple protein-protein interaction motifs mediating their functions (Fig. 1A). TRAPs do not have any enzymatic activity. In mammalian white blood cells, they function as crucial check-points or regulators of the main signalling events defining the basic function of these cells by facilitating the assembly of signalling complexes at the plasma membrane (Hořejší et al., 2004). Three TRAP subfamilies were defined in these cells: (i) monomeric, palmitoylated TRAPs (pTRAPs), (ii) monomeric, non-palmitoylated TRAPs and (iii) dimeric TRAPs frequently associated with large multisubunit receptor complexes (Stepanek et al., 2014). The latter group represents a challenge when studying the impact of various motifs on protein localisation because of their dimeric character and strong association with other subunits of receptor complexes. For example, CD247 dimer (ζ chain) facilitates the surface expression of the multi-subunit TCR/CD3 complex in T lymphocytes (Weissman et al., 1989). Non-palmitoylated, monomeric TRAPs (LAX1 and SIT1) have an extracellular part of intermediate size (38–40 residues) with potential glycosylation sites. Their glycosylation status can influence the plasma membrane localisation as shown for a number of surface glycoproteins (Fiedler and Simons, 1995). On the contrary, none of the known pTRAPs [LAT, PAG1, NTAL (also known as LAT2), LIME1, PRR7, SCIMP] are likely to be glycosylated because of their very short extracellular part (3–20 amino acids) and lack of glycosylation sites. In addition, pTRAPs are missing a signal peptide and use their unique TMD for membrane insertion, similar to type II membrane proteins. It can be hypothesised that it is the TMD length or composition that defines the localisation of such proteins to the plasma membrane, as observed for type II proteins in the past (Munro, 1991).

Palmitoylation, a reversible post-translational modification of eukaryotic proteins (Bijlmakers, 2009), is another factor that can contribute to plasma membrane targeting of pTRAPs. In the process of palmitoylation, palmitoyl-CoA produced by fatty acid metabolism at the ER membrane is enzymatically reacted with cysteine residues in the cytoplasmic parts of target proteins by the DHHC family of proteins (Zeidman et al., 2009). No consensus palmitoylation motif has been found to date (Zeidman et al., 2009). In all pTRAPs, the palmitoylation sites are thought to be the cytosolic cysteine residues within CxxC or CxC motifs adjacent to

---

[1]Department of Biophysical Chemistry, J. Heyrovsky Institute of Physical Chemistry, Czech Academy of Sciences, Dolejskova 3, 18223 Prague, Czech Republic. [2]Laboratory of Leukocyte Signaling, Institute of Molecule Genetics, Czech Academy of Sciences, Videnska 1083, Prague, Czech Republic. [3]Microscopy Unit, Institute of Experimental Medicine, Czech Academy of Sciences, Videnska 1083, 14220 Prague, Czech Republic.

*Author for correspondence (marek.cebecauer@jh-inst.cas.cz)

Received 2 June 2015; Accepted 13 November 2015

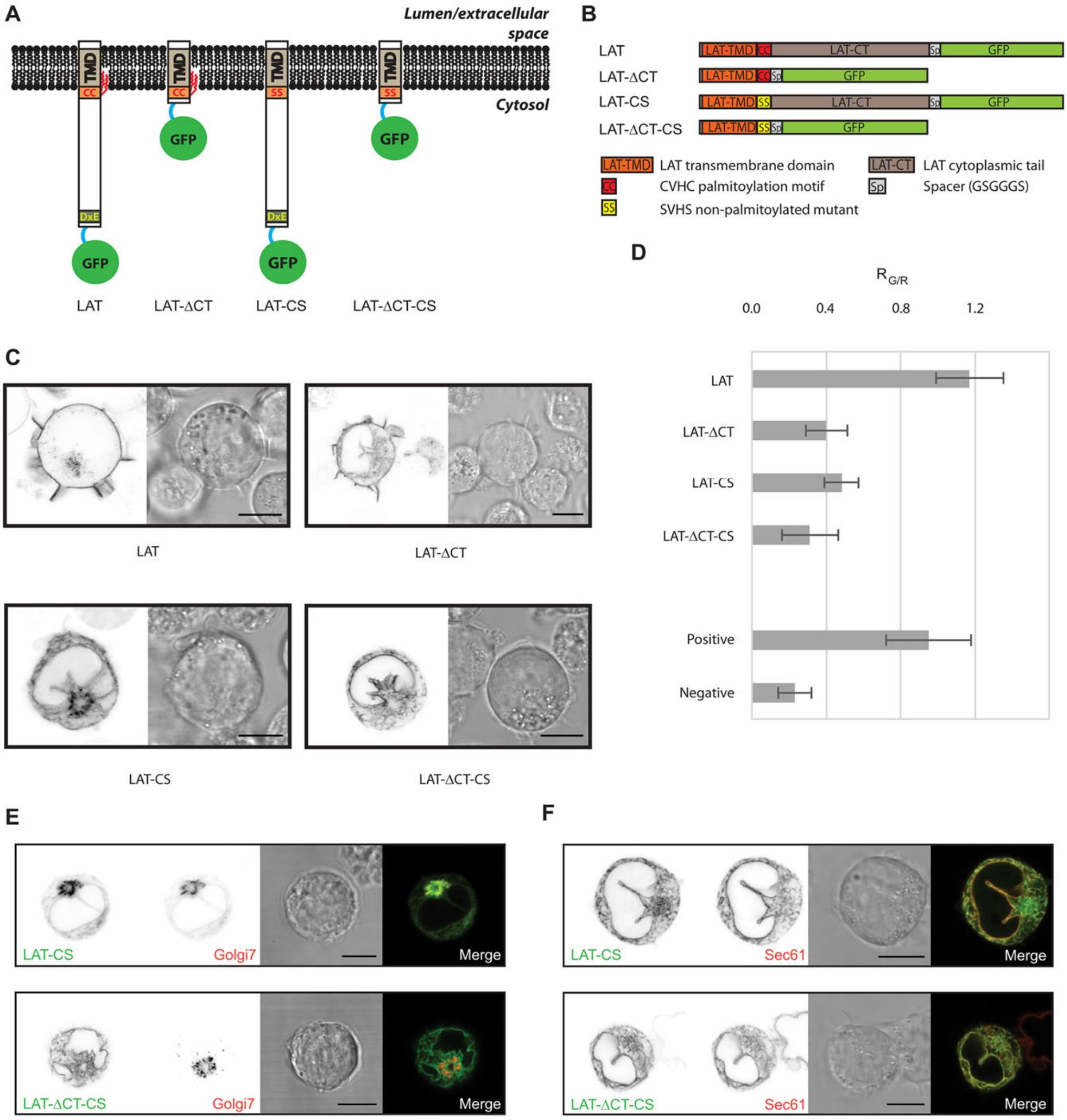

Fig. 1. Palmitoylation is essential for plasma membrane localisation of LAT. (A) Schematic illustration of LAT and its variants: lacking the intracellular domain (LAT-ΔCT), with mutated palmitoylation site (LAT-CS), and non-palmitoylated variant lacking the intracellular domain (LAT-ΔCT-CS). CC, CVHC motif for palmitoylation; SS, non-palmitoylatable SVHS motif; DxE, combined DxE/YxxΦ motif for the ER exit. (B) Schematic representation of wild-type LAT-GFP construct (LAT) and its variants: lacking the intracellular domain (LAT-ΔCT); palmitoylation mutant (LAT-CS) and combined palmitoylation mutant lacking the intracellular domain (LAT-ΔCT-CS). The lower part of the panel defines the colour coding for specific regions in LAT constructs. (C) Confocal images of live Jurkat T cells transfected with LAT (*n*=50), LAT-ΔCT (*n*=47), LAT-CS (*n*=25) and LAT-ΔCT-CS (*n*=26) GFP fusion proteins. The left side of each panel is a representative image acquired on the GFP channel, the right side is the corresponding bright-field image. (D) Quantitative plasma membrane localisation analysis of LAT variants in transfected Jurkat T cells (as in C). Relative values are shown where $R_{G/R}$~1 corresponds to plasma membrane localisation comparable to native LAT, $R_{G/R}$~0 indicates retention of proteins in the intracellular membranes. See Table 3 for details. Error bars represent s.d. For controls, Jurkat T cells were co-transfected with LAT-GFP/PAG-mCherry (Positive) or Sec61-GFP/LAT-mCherry (Negative). (E,F) Two-colour confocal images of LAT-CS (upper panel) and LAT-ΔCT-CS (lower panel) GFP fusion proteins (green) and markers for the Golgi complex (E; Golgi7, red) or ER (F; Sec61, red). Images from left to right represent GFP channel, marker channel, corresponding bright-field and merged image of GFP and red channels. Scale bars: 5 µm.

the transmembrane domain, although for some family members it has not yet been proven experimentally. Palmitoylation stabilises the plasma membrane localisation of a number of myristoylated or farnesylated peripheral membrane proteins such as Ras or Src family proteins (Rocks et al., 2010). The importance of palmitoylation for plasma membrane localisation of LAT, a member of the pTRAP subfamily, has also been reported (Hundt et al., 2009). Palmitoylation is also believed to target some pTRAPs to putative sphingolipid- and cholesterol-enriched membrane microdomains called lipid rafts (Hořejší et al., 2010; Levental et al., 2010). Levental and co-workers recently combined these two concepts and suggested that the capacity to associate with lipid rafts is a determinant of protein plasma membrane localisation (Diaz-Rohrer et al., 2014). In this study, we were interested in the impact of palmitoylation and TMD sequence (including adjacent sequences) on the plasma membrane localisation of pTRAP family proteins. Using a panel of mutant proteins and live cell imaging we reveal a complexity of determinants for plasma membrane targeting, specific for each individual membrane protein. Our data confirm the dominant impact of TMD length and/or hydrophobicity on plasma membrane localisation of proteins, but we also demonstrate that secondary sorting determinants such as palmitoylation, flanking sequences and the presence of the extracellular domain also contribute to plasma membrane localisation of proteins with suboptimal TMD length. We provide evidence that the intracellular domain (ER exit motifs) facilitates the flow of proteins towards the plasma membrane. The data indicate that more than one sorting determinant defines the dynamic localisation of proteins in cells.

RESULTS

Importance of palmitoylation and the intracellular domain for the plasma membrane localisation of LAT, PAG and NTAL proteins

The absence of a glycosylated extracellular domain suggests that TMD length and composition and/or other factors such as palmitoylation determine localisation of pTRAPs. The effect of TMD length and composition has recently been analysed by Munro and colleagues (Sharpe et al., 2010). They used a bioinformatics approach and found a strong correlation between the length and hydrophobicity of the TMD and the protein localisation. According to their results, TMDs of 22 residues and longer preferentially localise to the plasma membrane. In addition, specific distribution of side chain size and hydrophobicity throughout the TMD also correlated with protein subcellular distribution. Based on these data they created an algorithm (available online at www.tmdsonline.org as ‘TMD organelle predictor’) which predicts the localisation of membrane proteins in fungi and vertebrates to various cellular membranes (ER, Golgi complex and plasma membrane) based purely on the amino acid sequence. The algorithm has an overall success rate of 82% for prediction of plasma membrane localisation. However, analysis of all six human monomeric pTRAPs using this algorithm predicted the localisation of only three proteins to the plasma membrane, and localisation of the remaining three to the ER (Table 1). Five members of the pTRAP family have TMD lengths of 22–23 residues (Table 1) indicating that these proteins should be efficiently sorted to the plasma membrane. NTAL possesses a shorter TMD of 19 residues which falls outside of this range and was predicted to reside in the ER. LIME and PRR7, both with long TMDs, are also predicted to localise to the ER. As available data show that all these transmembrane adaptors are localised at the surface of human cells (Stepanek et al., 2014), we concluded that other determinants, not considered by the prediction algorithm, might contribute to the plasma membrane localisation of pTRAPs. It is worth noting that the bioinformatics tool ‘TMD organelle predictor’ was not designed for palmitoylated proteins.

In order to better characterise what determines plasma membrane localisation of these adaptors we selected three representative members of the pTRAP protein family: LAT, PAG and NTAL (Stepanek et al., 2014). To visualise sorting of these pTRAPs, green fluorescent protein (GFP) fusion variants (Fig 1A,B; Fig 2A; Fig. S1A) were expressed in a human T cell line (Jurkat, native environment) and cells of epithelial origin (HeLa, non-native environment) and imaged using live cell confocal microscopy. First, we verified the expression of wild-type variants of these fusion proteins and found that LAT, PAG and NTAL all almost exclusively localised in the plasma membrane of Jurkat (Fig 1C, Fig 2B; Fig. S1B) and HeLa cells (data not shown). Palmitoylation of pTRAPs is essential for their function (Stepanek et al., 2014) and is mainly thought to be a targeting signal for lipid rafts (Levental et al., 2010). Immunofluorescence of a non-palmitoylatable mutant of LAT revealed its mislocalisation to the intracellular membranes of human T cells (Hundt et al., 2009). We were, therefore, interested whether palmitoylation controls plasma membrane localisation of other pTRAPs, PAG and NTAL. pTRAPs are palmitoylated at the membrane proximal cysteines of the cytosolic tail (Fig. 1A). Transient expression of GFP fusion proteins with these cysteines mutated to serines (CS variants) demonstrated hindered plasma membrane localisation for non-palmitoylated LAT-CS (Fig. 1C,D, Table 3). Conversely, only a weak effect of Cys→Ser mutation was observed for PAG and NTAL proteins (Fig. 2B,C; Fig. S1B). Retention of LAT-CS in the Golgi complex was shown not to result from reduced kinetics of sorting; no plasma membrane localisation was observed in cells with blocked protein synthesis for 4–6 h (25 µg/ml cycloheximide; data not shown). Rather, LAT-CS mislocalisation led to its degradation. The surface expression of non-mutated LAT was unaffected in cyclohexamide-treated cells.

Changes in structure can cause re-orientation of proteins in membranes. Indeed, bioinformatics analysis (TMHMM 2.0; Krogh et al., 2001) suggests that non-palmitoylated LAT-CS is a type II membrane protein (cytosolic N-terminus). Native LAT protein is a type I protein (extracellular N-terminus). We, therefore, tested the orientation of LAT and LAT-CS proteins using a glycosylation assay (see Fig. S1C for more details) (van Geest and Lolkema, 2000). No difference in orientation between LAT and LAT-CS was observed (Fig. S1C).

Table 1. Predicted localisation of human pTRAP proteins

Protein name	UniProt* code	TMD length‡	Predicted localisation§	Prediction confidence§
LAT	O43561	23	Plasma membrane	Excellent
PAG	Q9NWQ8	23	Plasma membrane	Good
NTAL	Q9GZY6	19	Endoplasmic reticulum	Excellent
LIME	Q9H400	23	Endoplasmic reticulum	Excellent
PRR7	Q8TB68	22	Endoplasmic reticulum	Poor
SCIMP	Q6UWF3	23	Plasma membrane	Excellent

*UniProt database at http://www.uniprot.org/.

‡TMD length determined using TMHMM 2.0 algorithm available at http://www.cbs.dtu.dk/services/TMHMM/; verified at http://www.tmdsonline.org/.

§Prediction performed using bioinformatics tools at http://www.tmdsonline.org/.

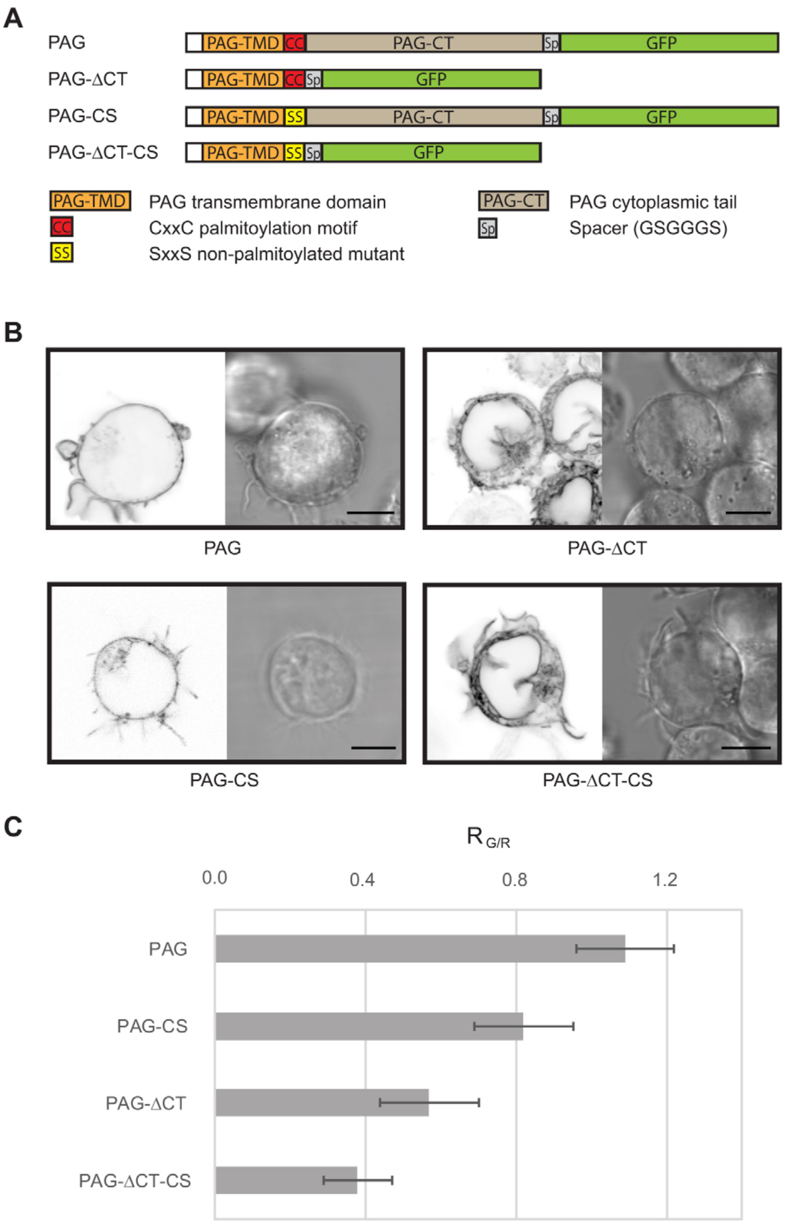

Fig. 2. PAG surface expression is independent of palmitoylation. (A) Schematic representation of wild-type PAG-GFP construct (PAG) and its variants: lacking the intracellular domain (PAG-ΔCT); palmitoylation mutant (PAG-CS) and combined palmitoylation mutant lacking the intracellular domain (PAG-ΔCT-CS). The lower part of the panel defines the colour coding for specific regions in PAG constructs. (B) Confocal images of live Jurkat T cells transfected with PAG (*n*=22), PAG-ΔCT (*n*=26), PAG-CS (*n*=16) and PAG-ΔCT-CS (*n*=24) GFP fusion proteins. The left side of each panel is a representative image acquired on the GFP channel, the right side is the corresponding bright-field image. Only cells with very low expression of PAG-CS mutants could be analysed because of a strong toxicity of these constructs in Jurkat T cells. Scale bars: 5 µm. (C) Quantitative plasma membrane localisation analysis of PAG variants in transfected Jurkat T cells (as in B). Relative values are shown where $R_{G/R}\sim 1$ corresponds to plasma membrane localisation comparable to native PAG, $R_{G/R}\sim 0$ indicates retention of proteins in the intracellular membranes. See Table 3 for details. Error bars represent s.d.

We were further interested in whether TMD, together with palmitoylation, are sufficient for plasma membrane localisation and generated LAT and PAG mutants missing the intracellular domain (LAT: Δ34–262 residues; PAG: Δ44–432 residues). Both palmitoylated and non-palmitoylated versions of short variants were tested. Fig. 1C,D shows poor plasma membrane localisation of palmitoylated short LAT variant and retention of its non-palmitoylated counterpart in the ER. Similarly to LAT, removal of the intracellular domain of PAG reduced sorting to the plasma membrane. By contrast, its palmitoylated and non-palmitoylated variants exhibited comparable distribution between the ER and plasma membrane, confirming that palmitoylation does not influence sorting of PAG to the plasma membrane (Fig. 2B). Co-localisation analysis with markers of the Golgi complex (Golgi7) and ER (Sec61) demonstrated that non-palmitoylated LAT remained localised to the Golgi complex (Fig. 1E) whereas non-palmitoylated LAT missing the intracellular domain was retained in the ER (Fig. 1F). This was supported by quantitative analysis of plasma membrane localisation efficiency. Plasma membrane localisation efficiency of non-palmitoylated LAT lacking the intracellular domain was comparable to the negative control represented by ER marker Sec61 (Fig. 1D). In summary, we demonstrate here that palmitoylation is essential for plasma membrane localisation of LAT but not for PAG and NTAL and that cytoplasmic domain of LAT and PAG also plays an important role in this process.

Addition of the extracellular glycosylated domain recovers plasma membrane localisation of non-palmitoylated LAT

The glycosylated extracellular domain of some proteins has been demonstrated to provide sufficient plasma membrane localisation signal (Potter et al., 2006; Proszynski et al., 2004). We were, therefore, interested in whether the lack of a large glycosylated extracellular domain in pTRAPs could be the reason for their increased dependence on palmitoylation and cytoplasmic sequences for plasma membrane localisation. To test the role of the extracellular domain on pTRAP localisation, we selected the extracellular region of T cell surface molecule CD4, which is relatively large, N-glycosylated and contains four immunoglobulin-like domains. In the native CD4 molecule it is followed by a transmembrane domain and a short cytoplasmic domain. The transmembrane domain is directly followed by a palmitoylation site (composed of two cysteine residues), which is very similar to the palmitoylation sites in pTRAPs. As shown in Fig. 3A, mutations of these cysteines did not have any effect on CD4 surface expression in human T cells. We fused the extracellular domain of CD4 (CD4ex) to the full coding sequence of LAT and its variants lacking the palmitoylation motif and/or cytoplasmic domain (Fig. 3B,C). The addition of the CD4 extracellular domain to the native LAT sequence (CD4ex-LAT) did not affect its surface expression in human T cells

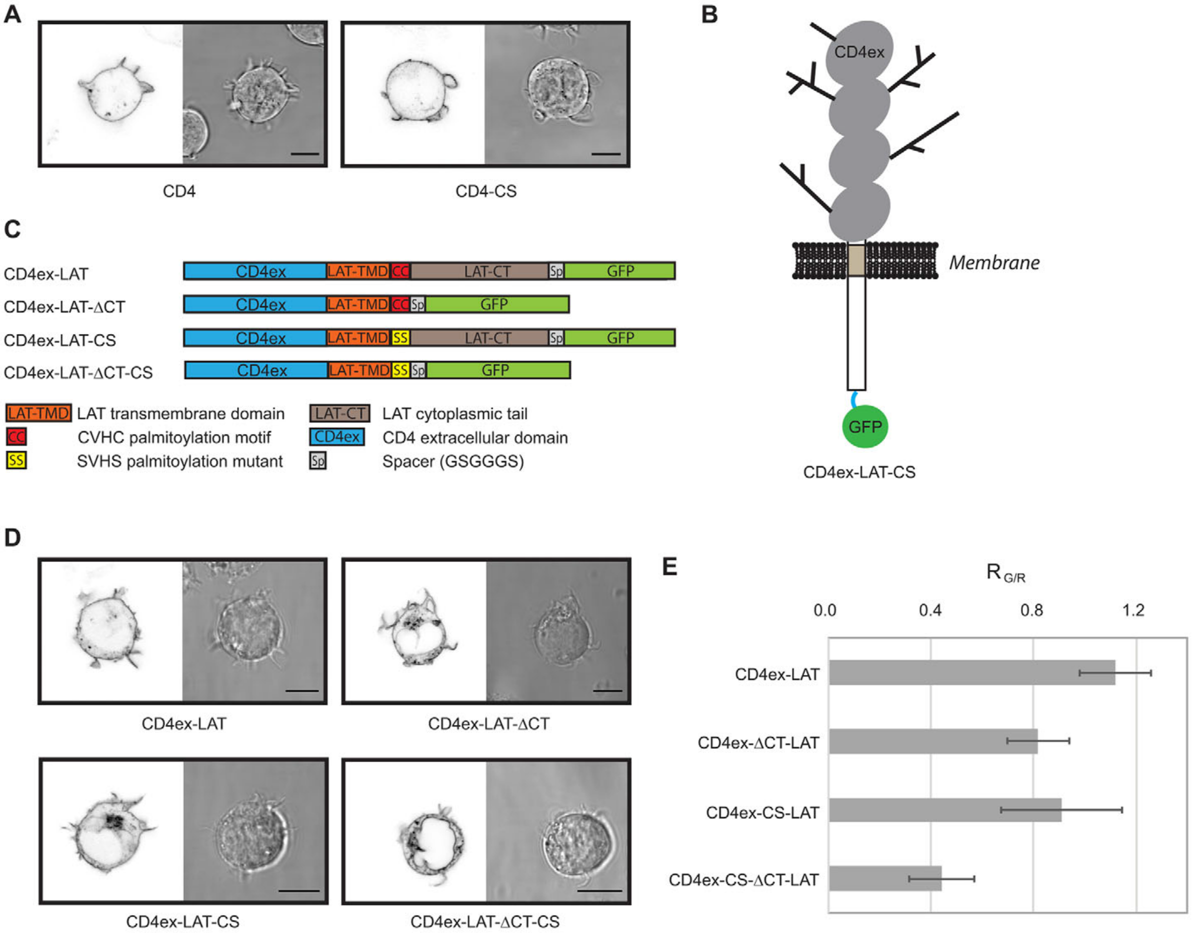

Fig. 3. Glycosylated extracellular domain facilitates sorting of LAT to the plasma membrane. (A) Confocal images of live Jurkat T cells transfected with GFP fusion proteins of wild-type human CD4 (*n*=15) and its palmitoylation mutant CD4-CS (*n*=12). The left side of each panel is a representative image acquired on the GFP channel, the right side is the corresponding bright-field image. (B) Schematic illustration of non-palmitoylated LAT mutant with added CD4 extracellular domain (CD4ex-LAT-CS; CD4ex, the extracellular domain of CD4). (C) Schematic representation of LAT-GFP variants: with added extracellular domain of human CD4 (CD4ex-LAT); with added extracellular domain of human CD4 but lacking the intracellular region of LAT (CD4ex-LAT-ΔCT); with extracellular domain of human CD4 added to the LAT palmitoylation mutant (CD4ex-LAT-CS); and with extracellular domain of human CD4 added to the combined palmitoylation mutant lacking the intracellular region (CD4ex-LAT-ΔCT-CS). The lower part of the panel defines the colour coding for specific regions in CD4ex-LAT constructs. (D) Confocal images of live Jurkat T cells transfected with CD4ex-LAT (*n*=14), CD4ex-LAT-ΔCT (*n*=18), CD4ex-LAT-CS (*n*=21) and CD4ex-LAT-ΔCT-CS (*n*=22) GFP fusion proteins. The left side of each panel is a representative image acquired on the GFP channel, the right side is the corresponding bright-field image. Scale bars: 5 µm in A,D. (E) Quantitative plasma membrane localisation analysis of CD4ex-LAT variants in transfected Jurkat T cells (as in D). Relative values are shown where $R_{G/R}$~1 corresponds to plasma membrane localisation comparable to native LAT, $R_{G/R}$~0 indicates retention of proteins in the intracellular membranes. See Table 3 for details. Error bars represent s.d.

(Fig. 3D, upper left panel). Conversely, when this domain was attached to the non-palmitoylated LAT-CS mutant (CD4ex-LAT-CS), clear plasma membrane localisation was observed (Fig. 3D, lower left panel). This is in contrast to LAT-CS lacking the extracellular domain which exhibited no plasma membrane localisation (Fig. 1C). Similarly, the presence of the CD4 extracellular domain in the non-palmitoylatable CD4ex-LAT-ΔCT-CS variant missing the intracellular domain of LAT caused its weak but reproducible plasma membrane localisation (Fig. 3D, lower right panel). These data demonstrate the role of a glycosylated extracellular domain in plasma membrane localisation of proteins lacking other sorting determinants. Moreover, the additional effect of protein palmitoylation on the surface expression was reproduced by chimeric LAT proteins containing the extracellular domain of CD4.

Asymmetry of the artificial TMD augments plasma membrane localisation of TRAP-like proteins

Characterisation of chimeric and mutant LAT and PAG proteins suggests important roles for palmitoylation and both extra- and intracellular domains in protein sorting (Figs 1–3). To further address this effect we designed model TRAP-like proteins containing artificial TMDs followed by the intracellular domain of CD247, and transiently expressed these proteins in Jurkat cells. ‘TRAP-like’ here refers to an overall topological similarity to TRAP family proteins: monomers with a very short extracellular domain, a single transmembrane domain and an intracellular domain lacking enzymatic function. Our work was inspired by earlier findings that highly hydrophobic artificial sequences can provide a signal for membrane anchorage of model proteins (Munro, 1991, 1995). In these studies, the model TMDs were fused to the extracellular and intracellular domain of CD8α (UniProt ID P01732) and alpha-2,6-sialyltransferase (ST6GALNAC2), non-palmitoylated membrane proteins of type I and type II, respectively. The lengths of these TMDs were found to be important for protein sorting, with longer TMDs preferentially localising to the plasma membrane and shorter TMDs to the Golgi complex. Other parts of these proteins outside TMDs were also shown to play a role.

For our experiments we selected variants of peptide LW21 as an artificial transmembrane domain. LW21 has 21 hydrophobic residues and has been used *in vitro* as a model transmembrane peptide in a number of biophysical studies (Fastenberg et al., 2003; Kaiser et al., 2011; Macháň et al., 2014). The length of this peptide is close to the optimal TMD length for plasma membrane localisation of vertebrate membrane proteins (Sharpe et al., 2010). We found TRAP-like proteins with LW21 to be expressed at the surface of transiently transfected Jurkat cells (data not shown), and subsequently designed a TMD of 19 hydrophobic residues to represent a suboptimal (short) plasma membrane localisation signal. LW19 TMD was obtained by modifying the LW21 sequence by removing two C-terminal tryptophan residues (Table 2). The remaining tryptophan residues at the extracellular end of the hydrophobic stretch mimic the TMDs of PAG and NTAL. We generated TRAP-like protein variants composed of LW19 TMD, the intracellular domain of CD247 and C-terminal GFP for visualisation. CD247 was selected to limit the impact of ‘backbone’ on plasma membrane localisation. A GFP fusion protein of CD247 is retained in the ER in the absence of remaining subunits of the TCR/CD3 complex (Fig. S2), suggesting that CD247 does not contain any dominant sorting sequence mediating its transport further down the exocytic pathway. In addition, CD247 is not palmitoylated. However, it shares a similar overall structure with other TRAP proteins such as LAT. Because the sequence of LW19 TMD is symmetric but the plasma membrane is asymmetric, we therefore generated two versions of LW19 TMD, one of which was made symmetric by adding 2 lysine residues at both ends of the hydrophobic core, and one of which was made asymmetric by adding 2 glutamic acid residues at the N-terminus (extracellular end) and 2 lysine residues at the C-terminus (intracellular end) of the hydrophobic core (Table 2; Fig. 4A,B). Designed model proteins [LW19(Sym)] maintained type I protein orientation in the membrane (Fig. S1C). Asymmetric TRAP-like protein LW19(Asym) localised at the plasma membrane and Golgi complex but not in the ER in Jurkat cells (Fig. 4C,D). By contrast, symmetric TRAP-like protein LW19(Sym) was largely maintained at the level of Golgi complex and ER (Fig. 4C,D). Weak surface expression was detected for this protein, but on very few cells (<10%). A less prominent difference in membrane distribution was observed for LW19 TRAP-like proteins lacking the intracellular domain (Fig. 4C–E). A small proportion (~20%) of cells expressing LW19-ΔCT protein with the asymmetric TMD [LW19(Asym)-ΔCT] exhibited detectable sorting to the plasma membrane (Fig. 4E), but GA and ER localisation was observed in the remaining cells (Fig. 4C). However, no surface expression was observed for symmetric variant LW19(Sym)-ΔCT even though >200 cells were inspected. These data experimentally demonstrate the importance of asymmetry for the plasma membrane protein sorting of proteins with suboptimal TMDs (Fig. 4C,D). However, a longer and highly hydrophobic asymmetric TMD was sufficient for plasma membrane localisation of TRAP-like proteins regardless of

Table 2. Sequences of TMDs of TRAP and TRAP-like proteins tested in this study

Protein	TMD sequence plus flanking residues*	Mean hydrophobicity‡
LAT	**EEAILVPCVLGLLLLPILAMLMALCVHCHRLP**	5
PAG	**GQMQITLWGSLAAVAIFFVITFLIFLCSSCDREK**	5
NTAL	**SSGTELLWPGAALLVLLGVAASLCVRCSRP**	4
LW19(Sym)	GLLDPKK**WWLLLLLLLLALLLLLLLL**KKFSRS	9
LW19(Asym)	GLLDPEE**WWLLLLLLLLALLLLLLLL**KKFSRS	9
LW21(Sym)	GLLDPKK**WWLLLLLLLLALLLLLLLLWW**KKFSRS	ND
LW25(Sym)	GLLDPKK**WWLLLLLLLLLLALLLLLLLLLLLL**KKFSRS	9.3
LW25(Asym)	GLLDPEE**WWLLLLLLLLLLALLLLLLLLLLLL**KKFSRS	9.3
LAT-LW19(Asym)	DLGTEE**WWLLLLLLLLLLALLLLLLLLLLL**KKGSYD	9
LAT-LW19(Asym$_{CVHC}$)	DLGTEE**WWLLLLLLLLLLALLLLLLLLLLL**CVHCHR	9
LAT-LW19(Asym$_{SVHS}$)	DLGTEE**WWLLLLLLLLLLALLLLLLLLLLL**SVHSHR	9

*Hydrophobic stretch is highlighted in bold. Putative palmitoylation sites (cysteines) are underlined.

‡Mean hydrophobicity of the hydrophobic stretch (bold) was calculated using HydroMCalc algorithm (Tossi et al., 2002). Hydrophobicity scale is −10 to +10. An average value calculated for randomly selected 20 amino acids is ~−3. ND, not determined.

Table 3. Quantitation of plasma membrane localisation

Protein variant (GFP fusion)	$R_{G/R}$	$\sigma_{R(G/R)}$	*n* (cells)	Plasma membrane GFP expression [%]*	$\sigma_{R(GFP)}$ [%]	Plasma membrane mCherry expression [%][‡]	$\sigma_{R(mCherry)}$ [%]
LAT	1.17	0.18	15	32.5	12.0	27.6	9.4
LAT-CS	0.39	0.11	31	12.2	4.6	31.4	8.4
LAT-ΔCT	0.48	0.09	10	13.1	3.8	27.5	8.0
LAT-ΔCT-CS	0.31	0.15	17	8.4	5.2	27.2	7.6
PAG	1.09	0.13	18	39.2	13.8	35.8	11.9
PAG-CS	0.82	0.13	19	24.3	9.3	30.2	11.2
PAG-ΔCT	0.57	0.13	12	15.9	6.1	28.2	10.4
PAG-ΔCT-CS	0.38	0.09	20	10.3	3.1	27.1	5.1
CD4ex-LAT	1.12	0.14	19	31.4	5.9	28.2	4.7
CD4ex-LAT-CS	0.91	0.24	23	26.4	7.1	29.3	4.9
CD4ex-LAT-ΔCT	0.82	0.12	22	20.9	3.7	26.0	5.5
CD4ex-LAT-ΔCT-CS	0.44	0.13	18	12.3	3.8	29.0	7.8
CD4	1.32	0.18	16	30.5	8.5	23.4	6.8
CD4-CS	1.22	0.10	13	33.4	7.5	27.6	6.8
LW19(Sym)	0.75	0.33	25	15.3	6.8	21.5	5.9
LW19(Asym)	1.19	0.33	12	22.8	7.4	19.6	4.7
LW19(Sym)-ΔCT	0.53	0.09	22	12.8	4.1	24.0	6.7
LW19(Asym)-ΔCT	0.61	0.14	23	14.2	6.9	22.8	9.1
LW25(Sym)	1.18	0.23	17	34.1	10.1	29.4	8.8
LW25(Asym)	1.35	0.15	17	41.8	8.6	30.9	5.4
LW25(Sym)-ΔCT	0.63	0.05	19	17.6	4.7	28.0	6.5
LW25(Asym)-ΔCT	0.72	0.09	20	16.3	5.0	22.6	6.3
LAT-LW19(Asym)	1.30	0.14	16	38.5	5.9	29.7	3.8
LAT-LW19(Asym)-ΔCT	0.59	0.10	41	14.7	4.2	25.1	6.5
LAT_LW19(Asym)$_{CVHC}$-ΔCT	0.72	0.11	14	17.2	5.3	24.6	7.8
LAT_LW19(Asym)$_{SVHS}$-ΔCT	0.36	0.10	15	8.3	2.1	25.1	10.5
Positive control	0.95	0.12	11	28.1	5.2	29.0	5.4
Negative control	0.23	0.09	6	5.5	2.8	25.0	6.6

*Percentage of GFP expressed at the plasma membrane, calculated as $R(GFP)=(I_{PM}(GFP)/I_{Cell}(GFP))$.

[‡] Percentage of mCherry expressed at the plasma membrane, calculated as $R(mCherry)=[I^{PM}(mCherry)/I^{Cell}(mCherry)]$.

$\sigma_{R(G/R)}$, $\sigma_{R(GFP)}$ and $\sigma_{R(mCherry)}$ are standard deviations (σ) calculated from two or three independent experiments.

whether symmetric and asymmetric versions of LW25 TRAP-like proteins were tested (Fig. 4D,F,G).

Plasma membrane localisation of palmitoylated TRAP-like proteins with the artificial TMD

Figs 1, 2 and Fig. S1 demonstrate the importance of palmitoylation for the plasma membrane sorting of LAT, but not of PAG and NTAL proteins. Because asymmetric LW19 TMD was able to mediate efficient sorting of our CD247-based artificial TRAP-like protein to the plasma membrane, we were interested in whether this TMD could rescue plasma membrane targeting of non-palmitoylated LAT. For this purpose, we replaced the TMD and palmitoylation motif in LAT with asymmetric LW19 TMD (Fig. 5A). Interestingly, the exchange of the TMD sequence of LAT protein for the highly hydrophobic, asymmetric LW19 sequence led to it sorting to the plasma membrane in the absence of palmitoylation (Fig. 5B). We did not observe any difference between asymmetric LW19 variants with CD247 or LAT 'backbones' (compare Fig. 4C with Fig. 5B). However, the absence of the intracellular domain again caused a reduction of LAT-LW19(Asym)-ΔCT plasma membrane localisation (Fig. 5B,D). Thus, we next tested whether palmitoylation can improve plasma membrane localisation of this variant. For this experiment we inserted a LAT palmitoylation site (CVHC sequence) into LAT-LW19(Asym)-ΔCT TRAP-like protein. Palmitoylation increased its plasma membrane localisation to almost complete surface expression level, comparable to native LAT (compare Fig. 1C with Fig. 5C). This effect was caused by the palmitoylation since the insertion of a non-palmitoylatable SVHS sequence had no impact (Fig. 5C,D). Our observations support the view that plasma membrane localisation of proteins is primarily determined by their TMD but supplementary signals, such as palmitoylation, can increase sorting efficiency.

DISCUSSION

In this study we have investigated the impact of the TMD, its flanking sequences and palmitoylation on the plasma membrane localisation of pTRAP family proteins. These proteins are essential for the proper function of various cells, facilitating signalling processes taking place at the plasma membrane. Their plasma membrane localisation is, therefore, a prerequisite for their function.

We studied the localisation of three pTRAP proteins: LAT, PAG and NTAL. Based on published data describing the correlation between TMD length and protein sorting to various cellular compartments (Sharpe et al., 2010), one would expect that in the absence of palmitoylation LAT and PAG, with TMDs of 23 residues, would localise to the plasma membrane, whereas NTAL, with a 19 amino acid TMD, would localise to the ER and Golgi complex. Intriguingly, our live cell imaging data showed that these predictions were valid only for PAG, whereas non-palmitoylated LAT was retained mainly in the Golgi complex, in agreement with data published by Hundt et al. (2009). Non-palmitoylated NTAL was sorted to the plasma membrane. Moreover, mislocalisation of LAT-CS to the Golgi complex caused its degradation. These experiments demonstrated that, in addition to TMD length, other sorting determinants such as palmitoylation also define the behaviour of pTRAPs in cell membranes.

Palmitoylation is essential for the proper function of LAT, PAG and NTAL (Brdicka et al., 2002, 2000; Posevitz-Fejfár et al., 2008; Zhang

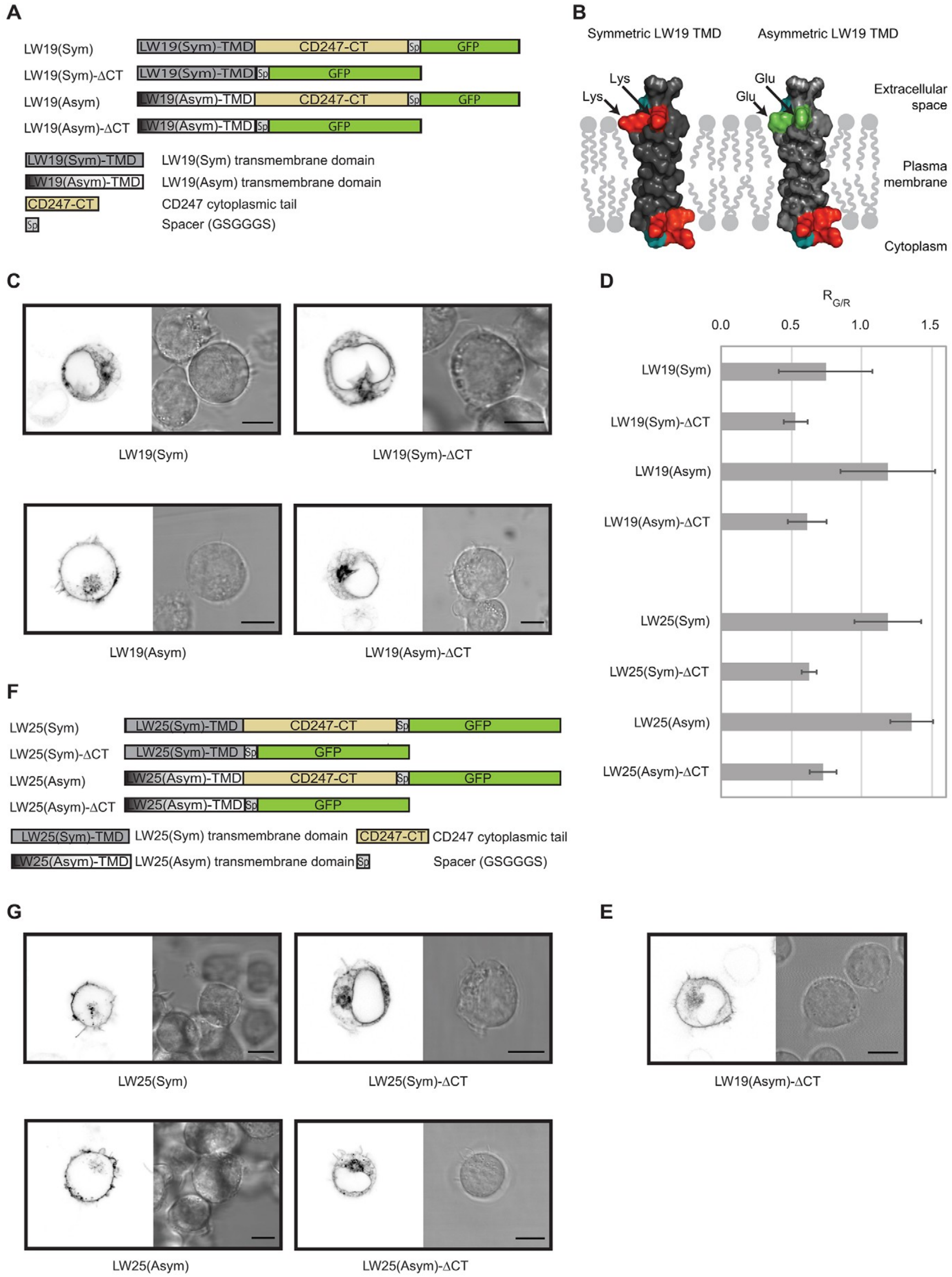

Fig. 4. See next page for legend.

Journal of Cell Science

Fig. 4. Asymmetry promotes plasma membrane localisation of TRAP-like proteins with a suboptimal TMD. (A) Schematic representation of model TRAP-like GFP fusion proteins: symmetric LW19 TMD with the intracellular part of CD247 [LW19(Sym)]; symmetric LW19 TMD missing the intracellular part of CD247 [LW19(Sym)-ΔCT]; asymmetric LW19 TMD with the intracellular part of CD247 [LW19(Asym)]; and asymmetric LW19 TMD missing the intracellular part of CD247 [LW19(Asym)-ΔCT]. All LW-based constructs contain a short extracellular domain (20 residues of c-Myc tag and CD247), a model TMD and C-terminal GFP fused to the protein via a short GSGGGS spacer (Fig. S2; Table 2). The lower part of the panel defines the colour coding for specific regions in TRAP-like protein variants. (B) Charged residues are evenly distributed in symmetric but not asymmetric LW19 TMDs. PyMOL models of α-helical TMD structures illustrate symmetric and asymmetric distribution of basic (red, Lys) and acidic (green, Glu) amino acid residues in LW19(Sym) and LW19(Asym) constructs, respectively. (C) Confocal images of live Jurkat T cells transfected with LW19(Sym) (*n*=63), LW19(Sym)-ΔCT (*n*=56), LW19(Asym) (*n*=71) and LW19(Asym)-ΔCT (*n*=58) GFP fusion proteins. The left side of each panel is a representative image acquired on the GFP channel, the right side is the corresponding brightfield image. (D) Quantitative plasma membrane localisation analysis of TRAP-like proteins in transfected Jurkat T cells (as in C and G). Relative values are shown where $R_{G/R}$~1 corresponds to plasma membrane localisation comparable to native LAT, $R_{G/R}$~0 indicates retention of proteins in the intracellular membranes. See Table 3 for details. Error bars represent s.d. (E) Approximately one-fifth of cells expressing LW19(Asym)-ΔCT variant showed surface expression (selected confocal image; as in panel C). (F) Schematic representation of model TRAP-like GFP fusion proteins: composed of a symmetric LW25 TMD and the intracellular region of CD247 [LW25(Sym)]; with a symmetric LW25 TMD lacking the intracellular region [LW25(Sym)-ΔCT]; composed of an asymmetric LW25 TMD and the intracellular region of CD247 [LW25(Asym)]; with an asymmetric LW25 TMD lacking the intracellular region [LW25(Asym)-ΔCT]. The lower part of the panel defines the colour coding for specific regions in TRAP-like protein constructs. (G) Confocal images of live Jurkat T cells transfected with LW25(Sym) (*n*=23), LW25(Sym)-ΔCT (*n*=25), LW25(Asym) (*n*=18) and LW25(Asym)-ΔCT (*n*=19) GFP fusion proteins. The left side of each panel is a representative image acquired on the GFP channel, the right side is the corresponding brightfield image. Scale bars: 5 µm in C,E,G.

et al., 1998). Here we demonstrated that non-palmitoylated PAG and NTAL showed unaltered sorting. These observations indicate that plasma membrane localisation is important but not sufficient for the function of pTRAPs in lymphocyte signalling. Super-resolution microscopy recently identified non-homogenous distribution of palmitoylated proteins in the plasma membrane (Fukata et al., 2013; Owen et al., 2010; Saka et al., 2014). This suggests that palmitoylation of PAG and NTAL, which is unresolvable using confocal microscopy, could determine their precise localisation at the plasma membrane. A loss of palmitoylation would then result in incorrect distribution of PAG and NTAL at the plasma membrane of Jurkat cells and consequently disrupt the spatio-temporal control required for their proper involvement in cell signalling (Cebecauer et al., 2010).

All LAT and PAG variants lacking the intracellular domain showed inefficient release from the ER. This was especially the case for non-palmitoylated LAT-CS-ΔCT, which was almost exclusively resident in the ER (Fig. 1F). The data suggest that the intracellular domain encodes signals for ER exit whereas TMD and proximal sequences define the fate of membrane proteins further down the exocytic pathway. Both, LAT and PAG proteins contain DxE and YxxΦ motifs reported to provide signals for efficient exit of some proteins from the ER (Sevier et al., 2000). It was shown that mutation or deletion of a larger sequence containing these motifs, enables recycling of membrane proteins between the ER and Golgi complex and limits their sorting to the surface (Fossati et al., 2014). We speculate that by deletion of the entire intracellular domain, including combined DxE and YxxΦ motifs, we have reduced the ability of these variants to enter the later sorting machinery of the trans-Golgi/endosomal network.

We also designed artificial TRAP-like proteins containing a short model LW19 TMD and showed that, similarly to a previously used TMD composed of a stretch of 17 leucine residues (Munro, 1995), it was insufficient for sorting to the plasma membrane. Because the addition of two more hydrophobic residues in LW21 led to weak but detectable expression in the plasma membrane (data not shown), we concluded that LW19 is a suboptimal TMD for plasma membrane localisation, positioned at the borderline of the sorting length scale. This unique feature allowed us to investigate the impact of palmitoylation and proximal sequence(s) on sorting of TRAP-like proteins in more detail. For TMD proximal sequences, basic residues are enriched near the cytosolic end of the TMD of integral membrane proteins. These residues play a role during the insertion of the hydrophobic stretch of a nascent protein into the membrane (Andersson et al., 1992; Nilsson et al., 2005). By contrast, a slight increase in the presence of acidic residues near the extracellular end of the TMD was found in a comprehensive study with >700 vertebrate plasma membrane proteins analysed (Sharpe et al., 2010). Indeed, acidic amino acids are found close to the extracellular end of the TMD in some single-spanning membrane proteins of human lymphocytes (e.g. LAT, NTAL, CD8α, DAP-12). Interestingly, replacement of lysine residues with glutamic acid at the extracellular end of suboptimal LW19 TMD, and thereby generation of asymmetric LW19(Asym), led to an increase in plasma membrane localisation. Together with the preference of less voluminous hydrophobic amino acids for the exoplasmic half of the plasma membrane (Quiroga et al., 2013; Sharpe et al., 2010), these data support the importance of asymmetry in proteins with a suboptimal TMD. In addition, the increased surface localisation of palmitoylated LAT-LW19(Asym$_{CVHC}$)-ΔCT compared with its non-palmitoylatable variant LAT-LW19(Asym$_{SVHS}$)-ΔCT again supports the view that palmitoylation can facilitate protein sorting.

In this study we show the importance of the unique primary sequence of TMDs for the localisation of integral proteins in cell membranes. As such, we provide a novel standpoint for discussion on why so many TMDs have evolved when a handful would be sufficient for targeting membrane proteins to their proper cellular compartments (Spira et al., 2012). By contrast, no conclusive data were obtained to uncover the difference between LAT and PAG TMDs, which are formed of the same number of amino acids (23 residues). TMD sequence analysis shows that all tested TRAP proteins contain a similar number of hydrophobic (~ 80%) and no charged residues. No clear difference could be found by calculating mean hydrophobicity of their TMDs (Table 2) (Tossi et al., 2002). Further experiments are required to uncover the exclusive character of these TMDs, especially whether the limited presence of bulky amino acids in the hydrophobic core or the asymmetric distribution of charged residues flanking the TMD provide sufficient signal, comparable to asymmetric LW19 TRAP-like proteins tested herein. It would also be interesting to investigate how the exceptionally short 19 residue TMD of NTAL drives plasma membrane localisation in the absence of palmitoylation.

To summarise, we have confirmed the dominant impact of TMD length and hydrophobicity on plasma membrane localisation of proteins, but also provided evidence that secondary sorting determinants such as palmitoylation or flanking sequences have evolved for proteins with suboptimal TMD length. We additionally demonstrate that the presence of ER exit motifs in the intracellular domain further influences the transport of proteins towards the plasma membrane, supporting the view that more than one

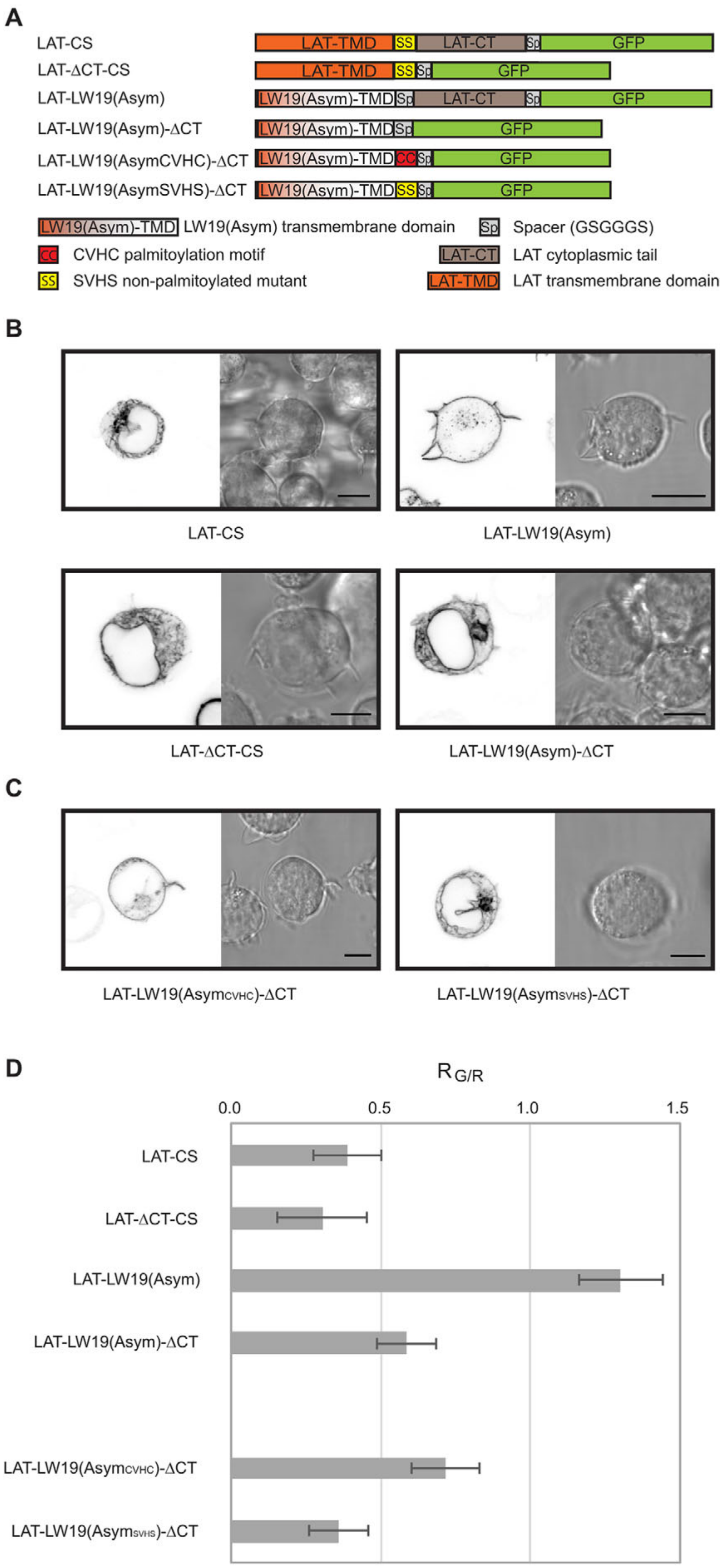

Fig. 5. Palmitoylation facilitates plasma membrane localisation of TRAP-like proteins. (A) Schematic representation of non-palmitoylated LAT variants (LAT-CS and LAT-ΔCT-CS; as in Fig. 1B) and model TRAP-like GFP fusion proteins based on the LAT protein 'backbone'. LAT-LW19(Asym)$_{LAT}$: TMD and palmitoylation site of LAT was replaced with asymmetric LW19 TMD; LAT-LW19(Asym)-ΔCT: LAT-LW19(Asym) lacking the intracellular region; LAT-LW19(Asym$_{CVHC}$)-ΔCT: LAT-LW19(Asym)-ΔCT with CVHC palmitoylation motif; LAT-LW19(Asym$_{SVHS}$)-ΔCT: LAT-LW19(Asym)-ΔCT with non-palmitoylatable SVHS motif. All LW-based LAT 'backbone' constructs contain short extracellular domains (18 residues of c-Myc tag and LAT), a model TMD and C-terminal GFP fused to the protein via a short GSGGGS spacer (Fig. S3; Table 2). The lower part of the panel defines the colour coding for specific regions of TRAP-like protein constructs. (B) Confocal images of live Jurkat T cells transfected with LAT-CS (*n*=26), LAT-ΔCT-CS (*n*=25), LAT-LW19(Asym) (*n*=13) and LAT-LW19(Asym)-ΔCT (*n*=17) GFP fusion proteins. (C) Confocal images of live Jurkat T cells transfected with LAT-LW19(Asym$_{CVHC}$)-ΔCT (*n*=21) and LAT-LW19(Asym$_{SVHS}$)-ΔCT (*n*=19) GFP fusion proteins. The left side of each panel is a representative image acquired on the GFP channel, the right side is the corresponding bright-field image. Scale bars: 5 µm in B,C. (D) Quantitative plasma membrane localisation analysis of LAT mutants in transfected Jurkat T cells (as in B and C). Relative values are shown where $R_{G/R}$~1 corresponds to plasma membrane localisation comparable to native LAT, $R_{G/R}$~0 indicates retention of proteins in the intracellular membranes. See Table 3 for details. Error bars represent s.d.

determinant plays in concert to define the precise localisation of proteins in cells.

MATERIALS AND METHODS

Cell culture, transfection and biochemical procedures

Jurkat T and HeLa (or HEK293) cell lines were grown in RPMI-1640 and DMEM media, respectively (Sigma-Aldrich), supplemented with glutamine and 10% foetal calf serum (Life Technologies) at 37°C under 5% CO_2 in a humidified incubator. These cells originate from the cell bank of the Institute of Molecular Genetics in Prague, Czech Republic, are regularly tested for surface markers, morphology and contamination.

Jurkat cells were transiently transfected using Neon® transfection system (Life Technologies). According the manufacturer's instructions, 1 µg of vector DNA per shot per 50,000 cells was used. HeLa and HEK293 cells were grown at >50% confluency on clean coverslips for minimum of 18 h before transfection. For transfection, 500 ng of DNA was mixed with 1.5 µl of Fugene HD transfection reagent (Promega) in 25 µl OptiMEM, incubated for 20 min at ambient temperature and dispersed onto cultured cells in 24-well plates. Live cell imaging was performed 16–24 h after transfection.

To immunoprecipitate GFP-tagged proteins from the transfected cells, transfectants were lysed in lysis buffer [50 mM Tris pH 7.5, 150 mM NaCl, 1 mM AEBSF (Sigma-Aldrich)] containing 1% n-dodecyl-β-D-maltoside followed by immunoprecipitation with GFP-specific rabbit antisera (kind gift from Llewelyn Roderick, University of Wales). The immunoprecipitated proteins were detected by immunoblotting with the same anti-GFP antibody.

DNA cloning

Plasmid pXJ41-EGFP was prepared by PCR amplification of the EGFP sequence of vector pEGFP-N1 with a spacer (GSGGGS) attached to the N-terminus (primers T198 and T199; see list of all primers in Table S1) and sub-cloning into the *Bam*HI and *Xho*I restriction sites of vector pXJ41 (Xiao et al., 1991). For further cloning, restriction sites *Kpn*I and *Bgl*II in the pXJ41-EGFP construct were eliminated by mutation. We designed a modular system for cloning of pTRAP variants with or without the intracellular domain and with the possibility to exchange the sequence encoding the TMD and flanking 4–5 residues (Fig. S3A). A DNA fragment encoding the LAT sequence was synthesised by GeneArt (Invitrogen) and includes the 5′ UTR and leader sequence of human CD148, followed by a Myc-tag and the entire coding sequence of LAT without the ATG start codon. The Myc-tag sequence and the coding sequence of LAT were separated by a *Kpn*I restriction site. A silent mutation was inserted into the LAT sequence (residues GGC→GGA) to introduce a *Bam*HI restriction site between the TMD and the intracellular domain. Restriction sites *Not*I and *Bam*HI (partial digestion) were used for sub-cloning and generation of a pXJ41-LAT-EGFP vector. A pXJ41-LAT-ΔCT-EGFP variant was generated by deletion of the sequence encoding the intracellular domain using *Bam*HI restriction sites and self-ligation. CS mutation was introduced into the pXJ41-LAT-ΔCT-EGFP vector by amplification of its TMD sequence (using primers T255 and T256) and sub-cloning of the LAT-CS TMD sequence instead of the LAT TMD using *Kpn*I and *Bam*HI cloning sites. A full length version was generated by sub-cloning of the LAT intracellular sequence into pXJ41-LAT-ΔCT-CS-EGFP using *Bam*HI restriction sites.

A pXJ41-PAG-ΔCT-EGFP vector was prepared by amplification of the PAG TMD sequence (using primers T257 and T258) from plasmid PAG/pEFIRES-N1 and sub-cloning it into vector pXJ41-LAT-ΔCT-EGFP instead of the LAT TMD sequence using cloning sites *Kpn*I and *Bam*HI. The PAG intracellular region was amplified from PAG/pEFIRES-N1 (using primers T259 and T260) and sub-cloned into vector pXJ41-PAG-ΔCT-EGFP using *Bam*HI restriction sites to generate pXJ41-PAG-EGFP. A CS version of PAG-ΔCT was prepared the same way except for the use of primer T263 instead of T258 to introduce the CS mutation. The PAG intracellular region amplified from plasmid PAG/pEFIRES-N1 was than sub-cloned into vector pXJ41-PAG-ΔCT-CS-EGFP to generate pXJ41-PAG-CS-EGFP. Full-length LAT and PAG sequences were also cloned as fusions with mCherry fluorescent protein by replacing the EGFP sequence in pXJ41-LAT-EGFP and pPAG-EGFP with a sequence encoding mCherry from plasmid pcDNA3.1-mCherry (kind gift from Marco Purbhoo, Imperial College London).

The DNA sequence of the CD4 extracellular region was amplified (using primers T246 and T297) from plasmid CD4/pEGFP-N1 and sub-cloned into vectors pXJ41-LAT-EGFP, pXJ41-LAT-CS-EGFP, pXJ41-LAT-ΔCT-EGFP and pXJ41-LAT-ΔCT-CS-EGFP through *Eco*RI and *Kpn*I restriction sites, to generate pXJ41-CD4ex-LAT-EGFP, pXJ41-CD4ex-LAT-CS-EGFP, pXJ41-CD4ex-LAT-ΔCT-EGFP and pXJ41-CD4ex-LAT-ΔCT-CS-EGFP constructs.

To generate pXJ41-LW19(Sym)-EGFP and pXJ41-LW19(Asym)-EGFP, DNA fragments encoding symmetric and asymmetric variants of LW19 fused to the CD247 intracellular domain were synthesised by GeneArt (Invitrogen) and sub-cloned into plasmid pXJ41-LAT-EGFP using restriction sites *Kpn*I and *Bam*HI, replacing the coding sequence of LAT. During the fragment synthesis, the native *Bam*HI site in the CD247 sequence was removed and a *Bgl*II restriction site newly inserted into the CD247 sequence (AGGAGC→AGATCT) to separate the TMD and the intracellular domain. pXJ41-LW25(Sym)-EGFP and pXJ41-LW25(Asym)-EGFP constructs were generated from respective LW19 constructs by site-directed mutagenesis. To achieve this, from each template [pXJ41-LW19 (Sym)-EGFP or pXJ41-LW19(Asym)-EGFP], two separate overlapping cDNA fragments were synthesised by PCR with primer pairs T295/T292, and T291/T296. These fragments were then fused in a subsequent PCR reaction using flanking primers T295 and T296 and subcloned into the *Kpn*I and *Bam*HI sites of pXJ41-LAT-EGFP, replacing the coding sequence of LAT. ΔCT variants of all these LW constructs were generated by deletion of the sequence encoding the intracellular domain using *Bgl*II and *Bam*HI restriction and self-ligation for the generation of constructs pXJ41-LW19 (Sym)-ΔCT-EGFP, pXJ41-LW19(Asym)-ΔCT-EGFP, pXJ41-LW25 (Sym)-ΔCT-EGFP and pXJ41-LW25(Asym)-ΔCT-EGFP.

The asymmetric variant of LW19 in a LAT 'backbone' was amplified from the pXJ41-LW19(Asym)-EGFP construct (using primers T289 and T290) and sub-cloned into vectors pXJ41-LAT-EGFP and pXJ41-LAT-ΔCT-EGFP using restriction sites *Eco*RI and *Bam*HI to generate vectors LAT-LW19(Asym) and LW19(Asym)LAT-ΔCT, respectively. To introduce the CVHC motif into the sequence of LAT-LW19(Asym)-ΔCT construct we amplified its TMD sequence using primers T290 and T294, and then sub-cloned the mutated sequence into the pXJ41-LAT-ΔCT-EGFP vector using *Eco*RI and *Bam*HI restriction sites to generate the LAT-LW19(Asym$_{CVHC}$) LAT-ΔCT construct. The cloning strategy for LAT-LW19(Asym$_{SVHS}$)LAT-ΔCT construct was the same with the exception of using a different set of primers (T290, T298).

The pXJ41-NTAL-EGFP vector was generated by amplification of the NTAL coding sequence (using primers NTAL wt fwd *Eco*RI, NTAL rev *Bam*HI) from the NTAL-pFLAG-CMV plasmid and sub-cloning into vector pXJ41-LAT-EGFP through *Eco*RI and *Bam*HI restriction sites. We inserted the CS mutation in the NTAL sequence by linking PCR (using primers NTAL wt fwd *Eco*RI, NTAL rev *Bam*HI, NTAL CS fwd, NTAL CS rev) using NTAL-pFLAG-CMV plasmid as a template. The PCR product was sub-cloned into vector pXJ41-LAT-EGFP through *Eco*RI and *Bam*HI restriction sites to generate pXJ41-NTAL-CS-EGFP.

A version of pXJ41-LAT-ΔCT-EGFP without the CD148 leader, c-Myc and 5′ UTR was generated by amplification of the LAT-EGFP sequence (using primers T287 and LAT *Bam*HI rev) and sub-cloning into the former pXJ41-LAT-ΔCT-EGFP vector using *Eco*RI and *Bam*HI restriction sites. pXJ41-LAT-ΔCT-CS-EGFP* without the CD148 leader, c-Myc and 5′ UTR was generated using the same cloning strategy (with use of primers T287 and T255). No difference between plasma membrane localisation of LAT variants with and without the CD148 leader, c-Myc and 5′ UTR was detected (Fig. S3B,C).

Live cell imaging and cyclohexamide treatment

Cells were imaged on poly-L-lysine-coated (to immobilise cells) glass-bottom 8-well chamber slides (Lab-Tek®, Thermo Scientific) supplemented with pre-heated, colour-free RPMI-1640 medium. Images were taken using a Leica SP5 TCS AOBS Tandem laser scanning confocal microscope equipped with Leica HyD hybrid detector, 63×1.3 NA glycerine immersion objective (Leica PLAN APO) and live cell support chamber. LAS AF image software (Leica Microsystems) was used for acquisition. 3–4 sections were taken per cell, focused on the Golgi complex, ER and the plasma membrane. Minor contrast and/or level adjustments were applied and images were processed for publishing by Fiji/ImageJ (Schindelin et al., 2012).

For colocalisation studies, markers for the ER (Sec61-mCherry) and Golgi complex (Golgi 7-mApple) were co-transfected into Jurkat cells and imaged in parallel with GFP constructs using the TRIC channel setup (Leica Microsystems). mApple-Golgi-7 was a gift from Michael Davidson (Addgene plasmid #54907) and mCherry-Sec61 beta from Gia Voeltz (Addgene plasmid #49155).

Kinetic studies were performed using transiently transfected Jurkat T cells. After 16 h of culture, 25 µg/ml cyclohexamide was added to media and live cell imaging was performed after 0, 2, 4, 6 and 20 h.

Quantitative image analysis of plasma membrane localisation

In order to quantitate plasma membrane localisation, the proportion of plasma membrane signal on total cell fluorescence was calculated for each protein variant and compared with native LAT or PAG proteins (Fig. S4). Protein variants (with GFP) were transiently co-expressed with LAT-mCherry or PAG-mCherry in Jurkat T cells. Native LAT and PAG proteins were selected as positive controls as they reproducibly showed the most efficient plasma membrane localisation (Figs 1, 2). Sequential 2-colour live cell imaging was performed using a Zeiss LSM 510 laser scanning confocal microscope with a 100×1.4 NA PlanApochromat oil-immersion objective. Fluorescence signals of GFP and mCherry excited at 488 nm by Ar laser and 561 nm by DPSS laser were detected using the 505–550 nm band-pass and 580 nm long-pass emission filters, respectively. Acquired images were manually thresholded to remove signal noise detected outside of the cell. Then, total cell intensity (I_{Cell}) and plasma membrane signal (I_{PM}) were calculated in MATLAB by integration of fluorescence intensities in pixels of manually selected areas encompassing the whole cell body and the cell cortex, respectively. Relative plasma membrane localisation efficiency $R_{G/R}$ was calculated as

$$R_{G/R} = \frac{(I_{PM}(GFP)/I_{Cell}(GFP))}{(I_{PM}(mCherry)/I_{Cell}(mCherry))},$$

where mCherry-tagged proteins were treated as reference (positive control). Positive (PAG versus LAT) and negative (ER marker Sec61 versus LAT) controls of plasma membrane localisation generated $R_{G/R}$ values of 0.95±0.12 and 0.23±0.09, respectively (Fig. 1D).

In silico analysis of TMD and protein properties

The hydrophobic core or TMD of all tested proteins (Table 2) were determined using the bioinformatics tool TMHMM 2.0 prediction of transmembrane helices in proteins (http://www.cbs.dtu.dk/services/TMHMM-2.0/) (Krogh et al., 2001). For *in silico* prediction of protein membrane compartmentalisation we employed http://www.tmdsonline.org/predict.html#0 (Sharpe et al., 2010). Mean hydrophobicity of protein TMDs was calculated using HydroMCalc algorithm provided by A. Tossi (University of Trieste). No difference in mean hydrophobicity of TMDs was found when an alternative algorithm was used (Fauchere and Pliska, 1983).

Acknowledgements

We would like to thank Anthony I. Magee (Imperial College London) and Kvido Stříšovský (IOCB, Prague) for critical reading of the manuscript. We would also like to thank Radek Šachl for help with MATLAB script development.

Competing interests

The authors declare no competing or financial interests.

Author contributions

T.B. and M.C. designed experiments; T.C., D.G., T.B. and M.C. performed experiments and data processing; T.C., Z.K. and J.M. performed quantitative image analysis; T.B. and M.C. wrote the paper.

Funding

This study received funding from the Czech Science Foundation [P305/11/0459] and Purkyne Fellowship to M.C.

Supplementary information

Supplementary information available online at
http://jcs.biologists.org/lookup/suppl/doi:10.1242/jcs.175190/-/DC1

References

Almén, M. S., Nordström, K. J., Fredriksson, R. and Schiöth, H. B. (2009). Mapping the human membrane proteome: a majority of the human membrane proteins can be classified according to function and evolutionary origin. *BMC Biol.* **7**, 50.

Alonso, M. A., Fan, L. and Alarcon, B. (1997). Multiple sorting signals determine apical localization of a nonglycosylated integral membrane protein. *J. Biol. Chem.* **272**, 30748-30752.

Andersson, H., Bakker, E. and von Heijne, G. (1992). Different positively charged amino acids have similar effects on the topology of a polytopic transmembrane protein in Escherichia coli. *J. Biol. Chem.* **267**, 1491-1495.

Bijlmakers, M.-J. (2009). Protein acylation and localization in T cell signaling (Review). *Mol. Membr. Biol.* **26**, 93-103.

Brdicka, T., Pavlistova, D., Leo, A., Bruyns, E., Korinek, V., Angelisova, P., Scherer, J., Shevchenko, A., Hilgert, I., Cerny, J. et al. (2000). Phosphoprotein associated with glycosphingolipid-enriched microdomains (PAG), a novel ubiquitously expressed transmembrane adaptor protein, binds the protein tyrosine kinase csk and is involved in regulation of T cell activation. *J. Exp. Med.* **191**, 1591-1604.

Brdicka, T., Imrich, M., Angelisova, P., Brdickova, N., Horvath, O., Spicka, J., Hilgert, I., Luskova, P., Draber, P., Novak, P. et al. (2002). Non-T cell activation linker (NTAL): a transmembrane adaptor protein involved in immunoreceptor signaling. *J. Exp. Med.* **196**, 1617-1626.

Cebecauer, M., Spitaler, M., Serge, A. and Magee, A. I. (2010). Signalling complexes and clusters: functional advantages and methodological hurdles. *J. Cell Sci.* **123**, 309-320.

Cosson, P., Perrin, J. and Bonifacino, J. S. (2013). Anchors aweigh: protein localization and transport mediated by transmembrane domains. *Trends Cell Biol.* **23**, 511-517.

Diaz-Rohrer, B. B., Levental, K. R., Simons, K. and Levental, I. (2014). Membrane raft association is a determinant of plasma membrane localization. *Proc. Natl. Acad. Sci. USA* **111**, 8500-8505.

Duffield, A., Caplan, M. J. and Muth, T. R. (2008). Protein trafficking in polarized cells. *Int. Rev. Cell. Mol. Biol.* **270**, 145-179.

Fastenberg, M. E., Shogomori, H., Xu, X., Brown, D. A. and London, E. (2003). Exclusion of a transmembrane-type peptide from ordered-lipid domains (rafts) detected by fluorescence quenching: extension of quenching analysis to account for the effects of domain size and domain boundaries. *Biochemistry* **42**, 12376-12390.

Fauchere, J. L. and Pliska, V. (1983). ProtScale tool. Amino acid scale: hydrophobicity scale (pi-r). *Eur. J. Med. Chem.* **18**, 369-375.

Fiedler, K. and Simons, K. (1995). The role of N-glycans in the secretory pathway. *Cell* **81**, 309-312.

Fossati, M., Colombo, S. F. and Borgese, N. (2014). A positive signal prevents secretory membrane cargo from recycling between the Golgi and the ER. *EMBO J.* **33**, 2080-2097.

Fukata, Y., Dimitrov, A., Boncompain, G., Vielemeyer, O., Perez, F. and Fukata, M. (2013). Local palmitoylation cycles define activity-regulated postsynaptic subdomains. *J. Cell Biol.* **202**, 145-161.

Hořejší, V. V., Zhang, W. and Schraven, B. (2004). Transmembrane adaptor proteins: organizers of immunoreceptor signalling. *Nat. Rev. Immunol.* **4**, 603-616.

Hořejší, V., Otáhal, P. and Brdička, T. (2010). LAT - an important raft-associated transmembrane adaptor protein. Delivered on 6 July 2009 at the 34th FEBS Congress in Prague, Czech Republic. *FEBS J.* **277**, 4383-4397.

Howell, G. J., Holloway, Z. G., Cobbold, C., Monaco, A. P. and Ponnambalam, S. (2006). Cell biology of membrane trafficking in human disease. *Int. Rev. Cytol.* **252**, 1-69.

Hundt, M., Harada, Y., De Giorgio, L., Tanimura, N., Zhang, W. and Altman, A. (2009). Palmitoylation-dependent plasma membrane transport but lipid raft-independent signaling by linker for activation of T cells. *J. Immunol.* **183**, 1685-1694.

Kaiser, H.-J., Orlowski, A., Rog, T., Nyholm, T. K., Chai, W., Feizi, T., Lingwood, D., Vattulainen, I. and Simons, K. (2011). Lateral sorting in model membranes by cholesterol-mediated hydrophobic matching. *Proc. Natl. Acad. Sci. USA* **108**, 16628-16633.

Krogh, A., Larsson, B., von Heijne, G. and Sonnhammer, E. L. L. (2001). Predicting transmembrane protein topology with a hidden Markov model: application to complete genomes. *J. Mol. Biol.* **305**, 567-580.

Levental, I., Lingwood, D., Grzybek, M., Coskun, U. and Simons, K. (2010). Palmitoylation regulates raft affinity for the majority of integral raft proteins. *Proc. Natl. Acad. Sci. USA* **107**, 22050-22054.

Macháň, R., Jurkiewicz, P., Olżyńska, A., Olšinová, M., Cebecauer, M., Marquette, A., Bechinger, B. and Hof, M. (2014). Peripheral and integral membrane binding of peptides characterized by time-dependent fluorescence shifts: focus on antimicrobial peptide LAH(4). *Langmuir* **30**, 6171-6179.

Munro, S. (1991). Sequences within and adjacent to the transmembrane segment of alpha-2,6-sialyltransferase specify Golgi retention. *EMBO J.* **10**, 3577-3588.

Munro, S. (1995). An investigation of the role of transmembrane domains in Golgi protein retention. *EMBO J.* **14**, 4695-4704.

Nilsson, J., Persson, B. and von Heijne, G. (2005). Comparative analysis of amino acid distributions in integral membrane proteins from 107 genomes. *Proteins* **60**, 606-616.

Owen, D. M., Rentero, C., Rossy, J., Magenau, A., Williamson, D., Rodriguez, M. and Gaus, K. (2010). PALM imaging and cluster analysis of protein heterogeneity at the cell surface. *J. Biophotonics* **3**, 6-454.

Posevitz-Fejfár, A., Šmída, M., Kliche, S., Hartig, R., Schraven, B. and Lindquist, J. A. (2008). A displaced PAG enhances proximal signaling and SDF-1-induced T cell migration. *Eur. J. Immunol.* **38**, 250-259.

Potter, B. A., Hughey, R. P. and Weisz, O. A. (2006). Role of N- and O-glycans in polarized biosynthetic sorting. *Am. J. Physiol. Cell Physiol.* **290**, C1-C10.

Proszynski, T. J., Simons, K. and Bagnat, M. (2004). O-glycosylation as a sorting determinant for cell surface delivery in yeast. *Mol. Biol. Cell* **15**, 1533-1543.

Quiroga, R., Trenchi, A., Gonzalez Montoro, A., Valdez Taubas, J. and Maccioni, H. J. F. (2013). Short transmembrane domains with high-volume exoplasmic halves determine retention of Type II membrane proteins in the Golgi complex. *J. Cell Sci.* **126**, 5344-5349.

Rocks, O., Gerauer, M., Vartak, N., Koch, S., Huang, Z.-P., Pechlivanis, M., Kuhlmann, J., Brunsveld, L., Chandra, A., Ellinger, B. et al. (2010). The palmitoylation machinery is a spatially organizing system for peripheral membrane proteins. *Cell* **141**, 458-471.

Saka, S. K., Honigmann, A., Eggeling, C., Hell, S. W., Lang, T. and Rizzoli, S. O. (2014). Multi-protein assemblies underlie the mesoscale organization of the plasma membrane. *Nat. Commun.* **5**, 4509.

Schindelin, J., Arganda-Carreras, I., Frise, E., Kaynig, V., Longair, M., Pietzsch, T., Preibisch, S., Rueden, C., Saalfeld, S., Schmid, B. et al. (2012). Fiji: an open-source platform for biological-image analysis. *Nat. Methods* **9**, 676-682.

Sevier, C. S., Weisz, O. A., Davis, M. and Machamer, C. E. (2000). Efficient export of the vesicular stomatitis virus G protein from the endoplasmic reticulum requires a signal in the cytoplasmic tail that includes both tyrosine-based and di-acidic motifs. *Mol. Biol. Cell* **11**, 13-22.

Sharpe, H. J., Stevens, T. J. and Munro, S. (2010). A comprehensive comparison of transmembrane domains reveals organelle-specific properties. *Cell* **142**, 158-169.

Spira, F., Mueller, N. S., Beck, G., von Olshausen, P., Beig, J. and Wedlich-Söldner, R. (2012). Patchwork organization of the yeast plasma membrane into numerous coexisting domains. *Nat. Cell Biol.* **14**, 640-648.

Stepanek, O., Draber, P. and Horejsi, V. (2014). Palmitoylated transmembrane adaptor proteins in leukocyte signaling. *Cell Signal.* **26**, 895-902.

Tossi, A., Sandri, L. and Giangaspero, A. (2002). New consensus hydrophobicity scale extended to non-proteinogenic amino acids. In *PEPTIDES 2002* (ed. E. Benedetti and C. Pedone). Napoli, Italy: Edizioni Ziino, 416-417.

Traub, L. M. (2009). Tickets to ride: selecting cargo for clathrin-regulated internalization. *Nat. Rev. Mol. Cell Biol.* **10**, 583-596.

van Geest, M. and Lolkema, J. S. (2000). Membrane topology and insertion of membrane proteins: search for topogenic signals. *Microbiol. Mol. Biol. Rev.* **64**, 13-33.

Weissman, A. M., Frank, S. J., Orloff, D. G., Mercep, M., Ashwell, J. D. and Klausner, R. D. (1989). Role of the zeta chain in the expression of the T cell antigen receptor: genetic reconstitution studies. *EMBO J.* **8**, 3651-3656.

Xiao, J. H., Davidson, I., Matthes, H., Garnier, J.-M. and Chambon, P. (1991). Cloning, expression, and transcriptional properties of the human enhancer factor TEF-1. *Cell* **65**, 551-568.

Zeidman, R., Jackson, C. S. and Magee, A. I. (2009). Protein acyl thioesterases (Review). *Mol. Membr. Biol.* **26**, 32-41.

Zhang, W., Trible, R. P. and Samelson, L. E. (1998). LAT palmitoylation: its essential role in membrane microdomain targeting and tyrosine phosphorylation during T cell activation. *Immunity* **9**, 239-246.

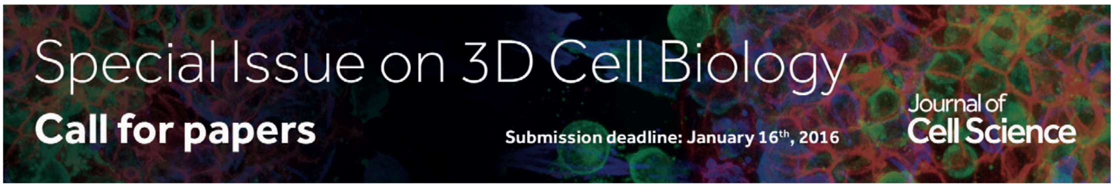

© 2016. Published by The Company of Biologists Ltd | Journal of Cell Science (2016) 129, 3053 doi:10.1242/jcs.194209

CORRECTION

The role of palmitoylation and transmembrane domain in sorting of transmembrane adaptor proteins

Tomáš Chum, Daniela Glatzová, Zuzana Kvíčalová, Jan Malínský, Tomáš Brdička and Marek Cebecauer

There was an error published in *J. Cell Sci.* **129**, 95–107.

In Fig. S1C, the labels for the location of the glycosylation site were inadvertently swapped. The correct image is shown below. There are no changes to the figure legend, which is accurate. This error does not affect the conclusions of the study.

The authors apologise to the readers for any confusion that this error might have caused.

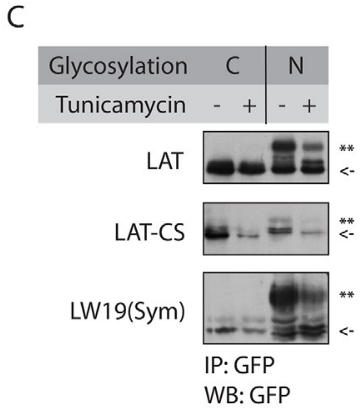

Fig. S1. (C) Membrane orientation of TRAP and TRAP-like protein variants. LAT, LAT-CS and LW19 (Sym) were designed to include N-glycosylation site (NNSS) at their N- or C-terminal end linked via a flexible linker (GGSGG). All constructs were prepared as C-terminal fusion proteins with GFP (as for all tested proteins in this work; Fig. S3) for sorting of transiently transfected cells.

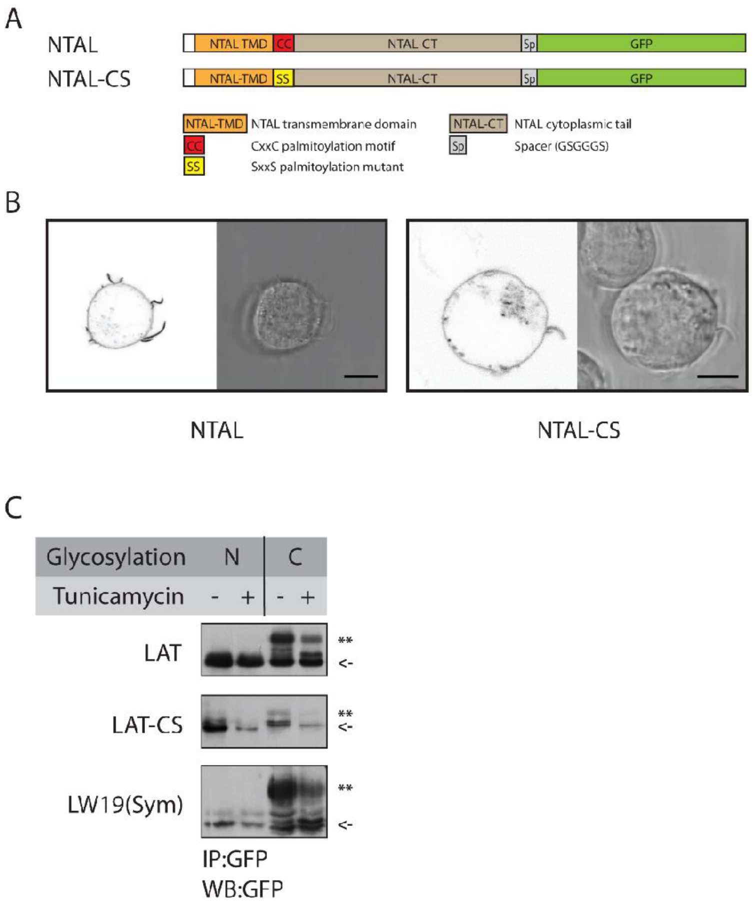

Figure S1. NTAL surface expression is independent of its palmitoylation. A. Schematic representation of native NTAL-GFP construct (NTAL) and its palmitoylation mutant (NTAL-CS). The lower part of the panel indicates colour coding for specific parts in NTAL constructs. **B**. Confocal images of live Jurkat T cells transfected with NTAL (n=18) and NTAL-CS (n=11). The left side of each panel is a representative image acquired for GFP channel, the right side corresponding bright-field image. Only cells with a very low expression of NTAL-CS mutants could be analysed due to a strong toxicity of these constructs for Jurkat T cells. Scale bars: 5 µm. **C. Membrane orientation of TRAP and TRAP-like protein variants.** LAT, LAT-CS and LW19 (Sym) were designed to include N-glycosylation site (NNSS) at their N- or C-terminal end linked via a flexible linker (GGSGG). All constructs were prepared as C-terminal fusion proteins with GFP (as for all tested proteins in this work; Fig. S3) for sorting of transiently transfected cells. **C**. Half of the cells was treated with tunicamycin (1 µg/ml) 16h after transfection. After another 24h of culture, cells were lysed and proteins were immunoprecipitated using anti-GFP antiserum. Proteins were detected by immunoblotting (non-glycosylated forms labelled with <-) using the same anti-GFP antiserum. Glycosylated proteins exhibited secondary band with a slower mobility (labelled **). In all cases, tunicamycin treatment caused reduction of the presence of glycosylated proteins. Representative data out of three independent experiments performed in doublets are shown.

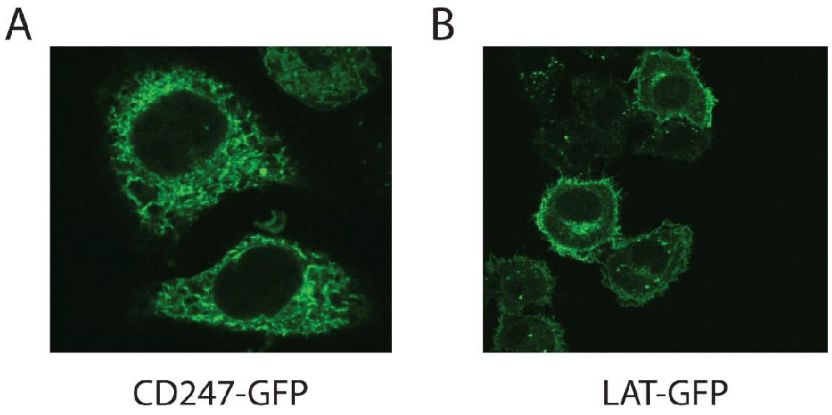

Figure S2. ER localisation of CD247-GFP fusion protein. A. Representative confocal image of HeLa cells transiently transfected with CD247(TCRζ chain)-GFP encoding plasmid. HeLa cells transfected with LAT-GFP fusion protein are shown for comparison (**B**).

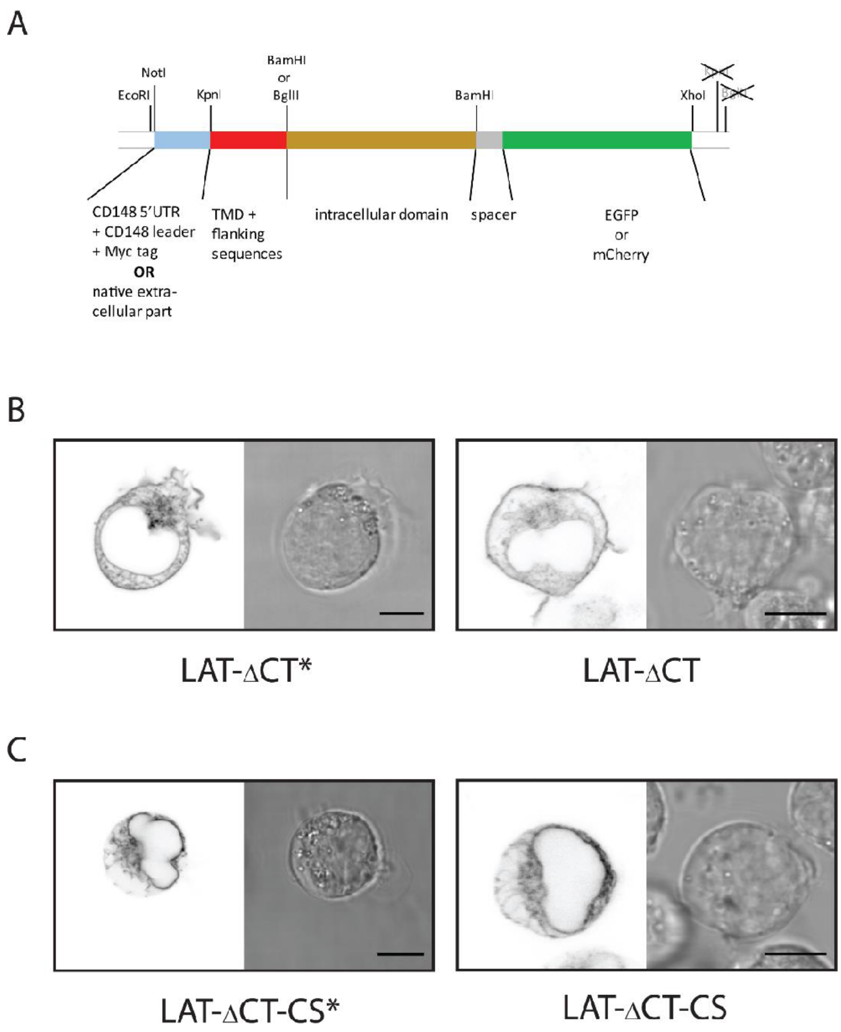

Figure S3. A. Schematic illustration of cloning strategy. Generalised schematic illustration of the modular cloning system used for generation of the majority of the constructs. It shows the position of restriction sites with respect to individual protein domains and the modified poly-linker of pXJ41. Jurkat T cells transiently co-transfected with control (LAT-mCherry or PAG-mCherry) and GFP fusion protein of interest were imaged using confocal microscopy. **B and C.** Presence of CD148 leader and c-Myc tag sequence at the N terminus does not impact sorting of LAT constructs. Confocal images of live Jurkat T cells transfected with **B:** LAT-ΔCT* (n=8) and LAT-ΔCT (n=47), and **C:** LAT-ΔCT-CS* (n=10) and LAT-ΔCT-CS (n=26) GFP fusion proteins. Asterisks indicate constructs generated without CD148 leader and c-myc tag sequence. The left side of each panel is a representative image acquired for GFP channel, the right side corresponding bright-field image. Scale bars: 5 µm.

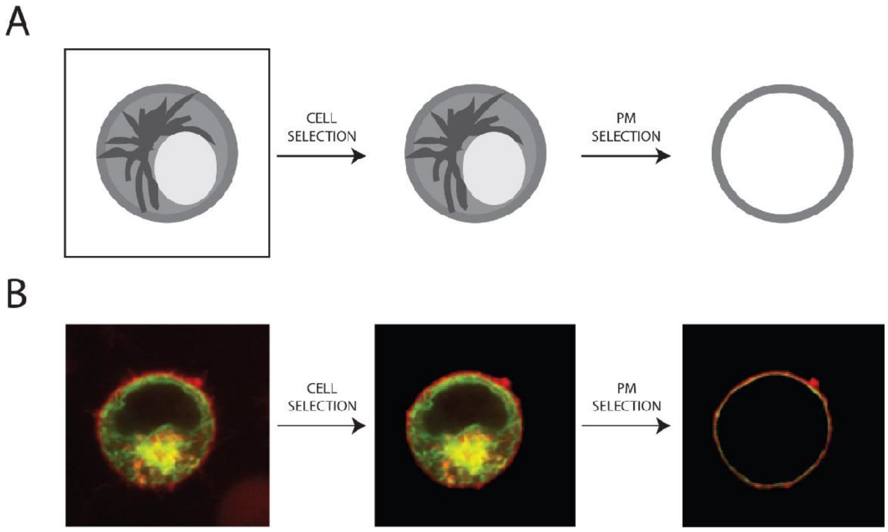

Figure S4. Schematic illustrations of quantitative image analysis of PM sorting. A cell cross-section was acquired at the position where GA and ER are well detectable. Images were first manually thresholded to remove background noise outside of the cell. Manual selection of pixels including total cell area and those of PM only followed by intensity signal integration was performed using custom MATLAB script. PM sorting efficiency was calculated as described in Material and Methods. Schematic illustration of image processing (**A**). Representative example of image processing (**B**).

Publication 2:

Christian Franke, **Tomáš Chum**, Zuzana Kvíčalová, Daniela Glatzová, Alvaro Rodriguez,
Dominic Helmerich, Otakar Frank, Tomáš Brdička,
Sebastian van de Linde, Marek Cebecauer

Unraveling nanotopography of cell surface receptors

(preprint). bioRxiv, Cell Biology, 2020

https://doi.org/10.1101/2019.12.23.884460

Unraveling nanotopography of cell surface receptors

Christian Franke[1,7,*], Tomáš Chum[2,7], Zuzana Kvíčalová[2], Daniela Glatzová[2,3], Alvaro Rodriguez[4], Dominic A. Helmerich[5], Otakar Frank[4], Tomáš Brdička[3], Sebastian van de Linde[6,8,*] and Marek Cebecauer[2,8,*]

[1] Max Planck Institute of Molecular Cell Biology and Genetics, Dresden, Germany

[2] Department of Biophysical Chemistry, J. Heyrovsky Institute of Physical Chemistry, Czech Academy of Sciences, Prague, Czech Republic

[3] Laboratory of Leukocyte Signalling, Department of Institute of Molecular Genetics, Czech Academy of Sciences, Prague, Czech Republic

[4] Department of Electrochemical Materials, J. Heyrovsky Institute of Physical Chemistry, Czech Academy of Sciences, Prague, Czech Republic

[5] Department of Biotechnology and Biophysics, Biocenter, University of Würzburg, Würzburg, Germany

[6] Department of Physics, SUPA, University of Strathclyde, Glasgow, United Kingdom

[7] These authors contributed equally: Christian Franke and Tomáš Chum.

[8] These authors contributed equally: Sebastian van de Linde and Marek Cebecauer.

* Corresponding authors: Ch.F. cfranke@mpi-cbg.de, S.v.d.L. s.vandelinde@strath.ac.uk and M.C. marek.cebecauer@jh-inst.cas.cz

ABSTRACT

Cells communicate with their environment via surface receptors, but nanoscopic receptor organization with respect to complex cell surface morphology remains unclear. This is mainly due to a lack of accessible, robust and high-resolution methods. Here, we present an approach for mapping the topography of receptors at the cell surface with nanometer precision. The method involves coating glass coverslips with glycine, which preserves the fine membrane morphology while allowing immobilized cells to be positioned close to the optical surface. We developed an advanced and simplified algorithm for the analysis of single-molecule localization data acquired in a biplane detection scheme. These advancements enable direct and quantitative mapping of protein distribution on ruffled plasma membranes with near isotropic 3D nanometer resolution. As demonstrated successfully for CD4 and CD45 receptors, the described workflow is a straightforward quantitative technique to study molecules and their interactions at the complex surface nanomorphology of differentiated metazoan cells.

INTRODUCTION

Supramolecular complexes drive numerous vital processes in cells, such as gene expression, molecular transport or signal transduction. Cellular membranes provide an excellent platform to assemble molecules into complex structures. Indeed, membrane-associated molecules, including surface receptors, have been found to form clusters with nanometric dimensions[1-5]. Lateral interactions and/or actin-cytoskeleton anchorage drive clustering of some receptors (e.g., tetraspanin platforms, focal adhesion complexes). However, the mechanism of cluster assembly for other receptors remains unknown and proposed theories are often controversial (e.g., receptor microclusters on lymphocytes). Indeed, receptor clustering is the subject of intense debate[6-8]. Several works have provided evidence for the monomeric character of receptors, which were shown to cluster using different experimental setups[9-11]. Thus, understanding their origins can help to unravel the very existence of receptor clusters. In this work, we focused on receptor clustering on the plasma membrane of lymphocytes, but the method and general principles discussed herein apply to the surface of any cell, including those of prokaryotes.

A common feature of supramolecular structures, including membrane receptor clusters, is their size (< 200 nm), too small to be analyzed by standard light microscopy. Therefore, molecular assemblies in cells are often studied indirectly. For example, total internal reflection fluorescence (TIRF) microscopy enabled dynamic receptor microclusters to be visualized in B and T cells[12,13]. It was the lateral mobility of these entities that indicated the very existence of clusters in these cells. The size and shape of the observed clusters were irresolvable because the spatial resolution of TIRF microscopy is diffraction limited. Later, super-resolution (SR) microscopy techniques were developed to surpass the diffraction limit and offered a more detailed insight into the architecture of cell receptor clusters (for example, refs: [5,14-16]).

Currently, single-molecule localization microscopy (SMLM) is the method of choice to study the organization of membrane receptors due to its ability to localize emitters (i.e., labelled receptors) with nanometer precision and its potential for quantitative assessments of protein distribution and number[17-20]. SMLM-based studies confirmed the earlier observations using TIRF microscopy that receptors and associated signaling molecules can cluster in non-stimulated and stimulated immune cells[21-25]. However, there is an intense discussion about the feasibility of SMLM for the cluster analysis of membrane molecules[26-28]. Recently, procedures aiming to minimize the impact of methodological artefacts on the SMLM results were developed[29-31].

In most of these studies, the SMLM methods were used to generate localization maps by projecting the presumably three-dimensional receptor distribution onto a two-dimensional plane. The precise information about the axial position of emitters (e.g., receptors), and therefore their distribution, is missing. This was an accepted trade-off due to the limited axial resolution of the applied SR methods (including STED and SIM; ref.[32]). Moreover, the plasma membrane is routinely depicted as a rather featureless structure (for example, refs.[33,34]). Yet differentiated cells of vertebrates are densely covered with membrane protrusions and invaginations, thus resulting in a highly three-dimensional surface[35]. For example, scanning electron microscopy micrographs have demonstrated that finger-like membrane protrusions reminiscent of microvilli dominate the surface of lymphocytes[36-38]. Microvilli are dynamic structures ~100 nm in diameter and 0.5–5 µm long[39]. Although less well understood on immune cells, tips of microvilli can potentially accumulate membrane receptors in domains with a diameter ~100 nm, analogous to signaling receptors and channels on epithelial and sensory cells[40].

Electron microscopy (EM), with its ability to provide information about ultrastructural details, was the key method for microvilli characterization in the pioneering works[41]. However, EM cannot visualize specific proteins efficiently, since the labelling densities are limited by ligand/antigen accessibility, steric hindrance and electron repulsion[42-44]. A rapid development of SR light microscopy techniques enabled the visualization of three-dimensional objects with high precision, with the use of highly specific and frequently efficient labelling methods and on living cells (e.g., refs.[45,46]). However, to characterize receptor distribution on nanometric membrane structures such as microvilli, it is crucial to develop three-dimensional SR techniques with axial resolution well below 50 nm. Several SMLM based methods have been suggested[47], such as astigmatism[48], multiplane[46] or biplane imaging[49,50], double-helix point spread function[51] or interferometric PALM[52].

Although microscopy techniques with dramatically improved spatial resolution recently became available, the (cell) sample preparation for SR imaging still suffers from several caveats. The spatial resolution offered by SMLM comes with the tradeoff of time resolution since thousands of camera frames are needed to render a map sufficiently representing, for example, a receptor distribution on a cell[53]. Thus, the movement of imaged objects (e.g., proteins) has to be minimized. This is usually accomplished by the fixation of cells prior to imaging. Importantly, cells grown or isolated initially in suspension must be attached to the optical surface (e.g., coverslips). Poly-*L*-lysine (PLL, or its isomer poly-*D*-lysine) is used for the immobilization of suspension cells in standard protocols[54]. However, attachment to a surface via interaction with PLL leads to the deformation of cells[55]. Similarly, the flattening of cell surfaces is observed when positioning immune cells on adhesion molecules (e.g., ICAMs) directly coated on coverslips or linked to a supported planar lipid bilayer[56,57]. The use of hydrogel or Matrigel enables cell stabilization for imaging without observable morphological changes[58,59]. However, these materials submerge cells into a three-dimensional matrix which leads to their random axial distribution. Single-molecule fluorescence microscopy techniques (including SMLM) depend on efficient transmission of photons from emitters and thus, provide the best results for molecules close to the optical surface, especially when aiming for a subsequent quantitative analysis[47]. Currently, none of the available methods can immobilize cells close to the optical surface without interfering with their complex surface morphology.

CD4 is a surface glycoprotein involved in T-cell development and function. It is associated with Lck kinase, which drives antigen-specific T-cell activation[60,61]. CD4 also mediates T-cell adhesion to the cells which express major histocompatibility complex class II (MHCII) proteins on their surface. We have recently shown that CD4 accumulates in clusters on the surface of non-stimulated T cells in a palmitoylation-dependent manner[28]. The origin of these CD4 clusters remains unknown. CD45, another glycoprotein that is three times larger than CD4, is expressed at the surface of all lymphocytes[62]. Its intracellular phosphatase domain regulates Lck kinase activity. CD45 has been found to segregate from signaling molecules in activated T cells, as predicted by the kinetic segregation model of T-cell activation[63,64]. However, the mechanism responsible for such segregation is incompletely understood due to a lack of information about its precise localization at the surface of immune cells.

Here, we describe a new method for mapping receptors at the nano-topography of the plasma membrane with near isotropic three-dimensional resolution. The workflow involves a newly developed, optimized coating of glass coverslips, which preserves the complex morphology of a cell surface while allowing for the positioning of immobilized cells close to the optical surface. Moreover, we advanced the recently reported TRABI method[65] for nanometer precise three-dimensional SMLM imaging to improve data acquisition, processing and drift correction, as well as the integrity of the three-dimensional SMLM data set. This allowed us to employ a straightforward quantitative assessment of the axial distributions of selected cell surface receptors at the nanoscale. We applied this method to reveal the three-dimensional nature of CD4 receptor clusters in non-stimulated T cells. Also, we discovered the importance of membrane protrusions for the segregation of CD45 phosphatase from CD4 involved in T-cell signaling. The presented method enables molecular studies of cell surface nano-morphology but also of other fluorescent nanoscopic structures.

RESULTS

Preservation of membrane morphology and resting state during cell immobilization on coverslips

To map receptor distribution at the complex surface of cells and the nanoscale, the experimental setup must include quantitative labelling of target molecules, an appropriate sample preparation, and a nanometer precise three-dimensional imaging method. In this work, labeling of surface receptors was performed by standard immunofluorescence protocols using directly labelled, highly specific primary antibodies to avoid artificial clustering by high level crosslinking with secondary antibodies[66-68]. To prevent visualization of intracellular molecules, fixed T cells were labelled in the absence of membrane permeabilization.

Cells grown or isolated in suspension, e.g., T cells, must be immobilized on the optical surface (e.g., coverslips; Fig. 1a-b) to facilitate imaging approaches, which require long acquisition times. This is true for most SMLM techniques[69]. Commonly, PLL-coating of glass coverslips is used to adhere suspension cells to the optical surface[55]. Negatively charged biomolecules at the cell surface electrostatically interact with the polycationic layer formed by PLL on coverslips[70,71]. However, such interaction can deform the cell surface (Fig. 1a; ref.[55]). Indeed, we have repeatedly observed a rapid flattening of a T-cell surface upon settling on the PLL-coated coverslip, visualized by TIRF microscopy of CD4-GFP fusion protein (for example, Fig. 1c and Supplementary Movie 1). With small exceptions (red arrowhead), a homogenous distribution of CD4-GFP signal dominated in such cells within 1-5 minutes after the first detectable contact with the optical surface (blue arrowheads; and Supplementary Fig. S1a). Continuous and homogenous fluorescence signal indicated a lack of CD4-GFP accumulation on membrane protrusions and invaginations. These data suggest that immobilization on PLL-coated coverslips can cause the flattening of the T-cell surface.

We thus required an alternative method for coating of coverslips, which better preserves their native morphology. Coating of an optical surface with glycine has been previously used to minimize non-specific background signals in single-molecule fluorescence imaging[72,73]. However, when applied without prior PLL treatment, glycine formed a gel-like layer on a glass surface (Supplementary Fig. S2a). Our atomic force microscopy (AFM) measurements indicated a continuous surface coating with glycine (Supplementary Fig. S2b). However, the AFM measurements were limited by the softness of the glycine layer and a tendency of this material to adhere to the AFM tip. We were thus unable to determine the exact thickness and stiffness of the glycine layer. The few holes, probably caused by gas bubbles, observed in the tested samples indicated that the average thickness of the glycine layer was at least 15 nm (Supplementary Fig. S2c). We further observed crystals on coverslips coated with glycine that were subsequently dried. On the contrary, no such precipitate was observed on dried PLL-coated coverslips (Supplementary Fig. S2d). We thus conclude that glycine forms a narrow, gel-like structure on the glass surface, which functions as a semi-soft cushion upon cell landing.

To investigate the impact of glycine coating on cell surface morphology, we imaged T cells expressing CD4-GFP during landing on coverslips in analogy to the cells on PLL-coated coverslips (Fig. 1c). Interestingly, a highly heterogeneous CD4-GFP signal was detected in a majority of cells immobilized on glycine-coated coverslips for more than 5 minutes since the first contact with the optical surface (Fig. 1d and Supplementary Movie 2). Intensity line profiles measured across the surface of such T cells exhibited large deviations (Supplementary Fig. S1b). These data indicate that glycine coating allows immobilization of cells close to the optical surface and improves the preservation of cellular morphology better, and for longer, than PLL-coating. Such properties open access to live-cell imaging of cell surface morphology or more convenient sample preparation, e.g., fixation.

We further examined the impact of the newly developed coating method on the resting state and viability of immobilized T cells. PLL was reported to induce calcium response in cells attached to the coated surface[74]. Our measurements confirmed that PLL induces calcium mobilization in T cells, albeit much less than antigenic stimulation mimicked by the coverslip coated with specific antibodies (anti-CD3ε) (Fig. 1e and Supplementary Fig. S3). In turn, the immobilization of T cells on glycine-coated coverslips stimulated only a negligible calcium response (Fig. 1e and Supplementary Fig. S3). We have employed the highly-sensitive, genetically encoded membrane-associated fluorescent calcium indicator GCaMP6f_u, which enables detection of weak and rapid signals from cell surface receptors and channels[75]. Glycine-coating of coverslips, thus, prevents non-specific stimulation of T cells observed on PLL-coated surfaces. Moreover, for longer cultivation times (> 10 min) we found a significantly improved viability for T cells incubated on glycine-coated coverslips compared to those on PLL-coated coverslips (Fig. 1f).

In summary, our findings indicate that coating of optical surfaces with glycine reduces the stress generated by the charged surface of, for example, PLL-coated coverslips. Moreover, the gel-like structure of the glycine coating better preserves the surface morphology of immobilized cells and enables quantitative analysis of the three-dimensional receptor distribution on the surface of resting T cells with SMLM.

The three-dimensional SMLM method

To capture the entire nanoscopic three-dimensional organization of receptors at the cell surface, we acquired image sequences with a highly inclined and laminated optical sheet (HILO) illumination, which enables single-molecule detection in cells much deeper than in TIRF microscopy (Fig. 2a). At the same time, it restricts the out-of-focus fluorescence from the remaining parts of a cell, thus improving the local signal-to-noise ratio[76]. Prior to the acquisition, we briefly irradiated the whole cell in epifluorescence to further minimize out-of-focus contributions (see **Methods**).

Intensity-based biplane SMLM imaging - dTRABI. Previously, we reported the temporal, radial-aperture-based intensity estimation (TRABI) method in combination with a biplane detection as a powerful three-dimensional imaging tool with nanometer precision[65,77]. In short, TRABI comprised fitting single-molecule spots by a Gaussian model with an invariant width, a subsequent independent photometric analysis of these spots and a final allocation of the axial coordinate based on a calibration curve. The photometric value was determined from the intensity obtained by the established Gaussian fitting procedure (I_{Fit}) and background-subtracted reference intensity of the spot (I_{R}), with $I_{\mathrm{Fit}} < I_{\mathrm{R}}$.

Here, we used a simplified but superior version of the TRABI method in which solely the intensity information obtained by the Gaussian fit (I_{Fit}) was used as metric for both channels in a biplane imaging scheme. Synchronized image stacks of the two channels (transmitted and reflected) generated by dividing the emitted fluorescence equally with a 50/50 beam-splitter, were analyzed by the same Gaussian function with an invariant width for every spot. Spots in the reflected channel were mapped to the corresponding spots in the transmitted channel by the nearest neighbor algorithm (Fig. 2b, see **Methods**). By omitting the standard photometric analysis[65], the computation time was reduced, and the allowed number of localizations per frame was significantly increased. Therefore, as demonstrated by Fourier Ring Correlation (FRC) of according data sets, we achieve an improved structural resolution while maintaining the same axial localization precision as with the original TRABI approach (Supplementary Figs.

S4 and S5, see also **Methods**)[78]. While this resolution-enhancement is more pronounced for structures with a medium or high local signal density, e.g., microtubules, and less distinct, but still apparent, for lower-density structures such as CD4 clusters (Supplementary Fig. S6), there is an additional implication for molecular quantification approaches. We subsequently called the new method dTRABI (for *direct* TRABI; Fig. 2c).

Fiducial-free drift and tilt correction. To ensure optimal axial localization over an extended imaging time as well as accounting for subtle sample drift, we developed a fiducial free approach for its correction (see **Methods**). In short, the axial footprint of the entire structure is tracked over time, resulting in a spatio-temporal drift trace (Fig. 3a). This trace is fitted with a high-order polynomial, which serves as the correction term for the raw localizations by linearization. We assumed that in a thin sample layer like the plasma membrane, the spatio-temporal distribution of active photo-switches that reside in their on-state is constant over time. The selection of appropriate regions in axially more extended samples can include structures, where the local z-dimension is restricted. Most data sets that were used to conclude the results in the following paragraphs showed axial drift with different orders of magnitude and non-linearity, which could be accounted for by the described correction approach. However, an additional linear axial tilt was observable in some data sets, most likely due to minor imperfections of the sample holder. Since we assumed the layer closest to the coverslip to be axially flat on the whole-cell scale, we fitted an inclined plane to the raw image, thereby determining its gradient and thus enabling the linearization of the raw localization data (see **Methods** and Fig. 3b).

Quantitative axial localization analysis. For the analysis of the axial receptor distribution, localization files were loaded and processed in Fiji with custom written scripts (see **Methods**)[79,80]. The analysis comprised three steps: generation of quantitative image stacks, segmentation in regions of interest (ROIs) and axial quantification of individual ROIs. (i) A quantitative 3D image stack (z-stack) was generated with 20 nm pixel size in *x*, *y* and *z*. (ii) These stacks were then segmented by automatically generating multiple regions of interest (ROIs) with an area of 4 µm² within the interior of the cell (Supplementary Fig. S6). (iii) Then, the axial distribution of localizations was analyzed by counting all localizations per ROI along the z-stack. For each ROI, the resulting distribution was fitted to a superposition of two Gaussians (Supplementary Fig. S6). By analyzing the properties of these fits, we acquired parameters that provide quantitative information about the axial distribution of surface receptors (see **Methods**).

Imaging CD45 nano-topography using the dTRABI approach

To demonstrate the applicability of dTRABI, we labelled CD45 receptors, which are highly expressed on the surface of T cells (> 100.000 copies/cell; ref.[81]) with Alexa Fluor 647-conjugated antibody (MEM-28) and imaged as described above. Cells were immobilized on glycine-coated coverslips to preserve cell surface morphology. Resulting three-dimensional images with color-coded z-axis represent a footprint of a cell on a coverslip (Fig. 4a). The apparent optical depth, which varies between cells (300–650 nm), depends on the available structure in the individual field of view. CD45-labelled cells exhibited a variety of features that can extend far from the coverslip. However, the entire extent of the basal membrane resting on the surface was captured in all displayed and analyzed cells. Fig. 4b shows the three-dimensional image of CD45 which indicates a complex morphology of the cell surface. Magnified images and the corresponding *xz*-projections (Fig. 4c) demonstrate the ability of dTRABI to visualize large membrane protrusions at the edge of the cell (ROIs 1 and 3; blue arrowheads), as well as more subtle membrane extensions towards the exterior (ROIs 1-4; magenta arrowheads) and interior (ROIs 3 and 5; green arrowheads) of the cell.

The origin of CD4 microclusters on the surface of unstimulated T cells

Next, we aimed at examining the origin of previously reported receptor (signaling) microclusters[1,4,5]. We recently showed that CD4 receptors accumulate in high-density regions on unstimulated T cells using two-dimensional SR imaging[28], while the three-dimensional organization of these clusters remained unclear. First, we confirmed that CD4 accumulates in high-density regions on T cells immobilized on glycine-coated coverslips using 2D *d*STORM (Supplementary Fig. S7). Next, high-resolution three-dimensional maps of the CD4 surface distribution were acquired by analyzing the same data sets with the dTRABI approach (Fig. 5a). The high-precision, nanoscopic three-dimensional view of wild-type CD4 indicates that the receptor is clustered and preferentially localized to one topographical level of the membrane (Fig. 5a). This is also demonstrated by plotting the relative z-position of CD4 molecules in the central area, which avoids cell edges (Fig. 5b). On the contrary, a broad surface distribution is evident from the three-dimensional view of a CD4 variant, which cannot be palmitoylated and was previously shown to exhibit random distribution in such unstimulated T cells (CD4 CS1; Fig. 5c-d; ref.[28]). Though these plots provide useful information about axial distribution of receptors in individual cells, their utility for the global distribution analysis is limited by a variation in surface complexity of individual cells. Therefore, the propensity of CD4 molecules to accumulate at specific topographical levels was analyzed in $2\times2\ \mu m^2$ square regions of interest (ROIs) selected to cover the cell-coverslip contact area over all tested cells (in total 846 CD4 WT ROIs in 21 cells and 1044 CD4 CS1 ROIs in in 18 cells; Supplementary Fig. S6, Table 1). As mentioned above, for quantitative analyses, the distribution of relative z-positions for localizations in ROIs were fitted with a sum of two Gaussians (bi-Gaussian, Fig. 5e). From these fits, three parameters were derived, i.e., the spread of the bi-Gaussian termed z-distribution width (z_w) (Fig. 5f-g), distance of its mean values or peak-to-peak distance (p-p) (Supplementary Fig. S8) and the difference of the widths of the two Gaussians (Δ_{FWHM}) (Supplementary Fig. S8). By compiling the z_w values of all ROIs, a histogram was obtained (Fig. 5f) and further analyzed (**Methods**). For wild-type CD4, we calculated an axial mean value of 120 nm and a standard deviation (s.d.) of 25 nm (cf. Table 1), signifying a strong tendency of wild-type CD4 to accumulate at one specific topographical level in resting T cells (Fig. 5f-g). On the contrary, a lack of palmitoylation in CD4 CS1 variant caused much broader distribution of this receptor on the T-cell surface, with z_W predominantly at 141 nm ± 27 nm (mean ± s.d.) and a smaller, yet broader fraction at 247 ± 83 nm (mean ± s.d.). Furthermore, the axial analysis of localizations revealed a more pronounced mean value of Δ_{FWHM} for CD4 CS1 (88 nm) than for CD4 WT (57 nm) (Supplementary Fig. S8c, Table 1).

The specificity of CD4 receptor clusters was further emphasized by a less constrained lateral and axial distribution of CD45 in T cells imaged using dTRABI (Fig. 5h,i; 13 cells and 305 ROIs were analyzed). Quantitative analyses were performed consistent with the CD4 variants and demonstrated a broader axial distribution of CD45 receptors than CD4 WT (Fig. 5f-g). We found the z_W values to be similarly distributed at 118 ± 20 nm (mean ± s.d.), but in contrast to CD4 WT, CD45 had an additional large fraction of z_W at 263 ± 117 nm (mean ± s.d.). This broad CD45 distribution was further noticeable when analyzing the peak-to-peak distance (p-p) of the fitted bimodal distribution to the relative z-position of the receptor (Supplementary Fig. S8b, see **Methods**). The obtained p-p values were exponentially distributed and the mean values for CD4 WT and CS1 were 23 and 36 nm, respectively, whereas the mean value for CD45 was 121 nm. More examples of three-dimensional dTRABI images and their quantitative analysis for all three receptors are shown in Supplementary Fig. S9 and Supplementary Fig. S6, respectively.

Segregation of CD45 from CD4 clusters in non-stimulated T cells

When analyzing dTRABI images, we noted areas with very few CD45 localizations (Fig. 6a-b; yellow arrowheads). Similarly, CD45 exclusion zones were detectable in two-dimensional SOFI images of antibody-labeled T cells (Fig. 6c). The narrow shape of these exclusion zones was reminiscent of CD4 clusters observed on T cells imaged by the dTRABI approach (Fig. 5a and Supplementary Fig. S9). We thus wondered whether the CD45 exclusion zones represent areas with CD4 accumulation. T cells expressing CD4 WT fused to photo-switchable protein mEos2 (ref.[28]) were labelled with specific anti-CD45 antibodies and analyzed using two-color SMLM. Our data indicate that CD4 and CD45 are essentially segregated into two separate zones on the surface of non-stimulated T cells immobilized on glycine-coated coverslips (Fig. 7a,b). Since CD4 clusters to one topographical level near the T cell-coverslip contact sites (Fig. 5a,b,f), we suspect that CD4 preferentially accumulates at the tips of membrane protrusions (e.g., microvilli) and CD45 to the shaft of these structures and their base at the plasma membrane (Fig. 7c). Indeed, we observed the accumulation of CD4 at the tips of large T-cell membrane protrusions in several cells (Fig. 7d,e). In turn, the shaft of protrusions was extensively covered with CD45 signal. Often, CD45 was essentially segregated from CD4 in these nanoscopic membrane structures (Fig. 7e). These data are in agreement with recently reported observations that CD45 segregates from microvilli tips in resting and activated T cells [82].

DISCUSSION

In this work, we have introduced a new approach for molecular mapping of the membrane receptor topography with nanometer precision. The method combines the use of glycine-coated optical surfaces, which preserve the native membrane morphology of immobilized cells with an advanced and simplified dTRABI algorithm for quantitative, near isotropic three-dimensional SMLM imaging. Using directly labelled antibodies and dTRABI processing of biplane SMLM data, we achieved 10–20 nm localization precision in all spatial directions. This enabled us to reveal the origin of CD4 clusters and the involvement of cell surface morphology in CD45 segregation from signaling receptor clusters.

Our principal task was to preserve fine structures on the surface of T cells and to analyze the distribution of signaling receptors therein. Even though flat in most common illustrations, the plasma membrane of differentiated metazoan cells is a three-dimensional structure densely covered with finger-like protrusions (microvilli, filopodia), ruffles and invaginations (endocytic cavities and podosomes)[40]. Membrane imaging with two-dimensional methods thus leads to simplifications and, potentially, misinterpretations. The availability of SR microscopy capable of resolving nanoscopic three-dimensional structures is currently limited to specialized nanophotonics laboratories. Nevertheless, standard methods of sample preparation for imaging (e.g., on PLL-coated coverslips) rapidly damage the fragile surface morphology of studied cells, as indicated also by our data showing that the T-cell surface complexity is diminished within a few minutes of the first contact with a PLL-coated coverslip. Several materials were previously developed to prevent cell deformation during their immobilization in a three-dimensional space, for example, Matrigel and synthetic hydrogels. Matrigel enables three-dimensional cell cultures, but it is derived from the extracellular matrix of mouse tumors and exhibits autofluorescence. On the contrary, fluorescence properties of synthetic hydrogels (e.g., CyGEL Sustain) can be controlled and the cells prepared in hydrogels display numerous protrusions on their surface, including nanoscopic structures that require SR microscopy for their detection[58]. However, TIRF and HILO sample illumination techniques which can reduce the out-of-focus background signal and, thus, improve the quality of SMLM images, enable fluorescence signal detection solely in the vicinity of the optical surface[76,83]. Hydrogels do not allow efficient positioning of immobilized cells at the optical glass.

Here, we developed and analyzed glycine coating of coverslips, which better preserves cell membrane morphology. The coating of coverslips with a narrow layer of gel-like glycine improves the stability of membrane protrusions and facilitates the positioning of immobilized cells close to the optical surface. Importantly, cells immobilized on glycine exhibit improved viability and reduced non-specific stimulation compared to PLL-immobilized cells. Of note, the preparation of glycine-coated coverslips is straightforward, fast (<30 min) and inexpensive. All these properties qualify glycine-coating of coverslips for the advanced imaging of cells, including high-resolution three-dimensional dTRABI mapping of cell surface molecules.

We have also developed the dTRABI algorithm to allow for faster and computationally more efficient processing of SMLM data, while achieving significantly higher structural resolution, than that found with our original TRABI approach. It is built for a quantitative analysis of the axial distribution of fluorescent molecules. Importantly, dTRABI can be used with any localization software that supports fixed Gaussian fitting in combination with a biplane detection scheme. In contrast to classical biplane imaging that compares the width of spots evaluated by free Gaussian PSF fitting, dTRABI employs fixed-width Gaussian fit which facilitates an improved localization precision. The ability of dTRABI to localize fluorescent molecules on complex, irregular, three-dimensional cellular structures was highlighted on a T cell that was not included in the quantitative analysis of an axial receptor distribution (Supplementary Fig. S10). Complex membrane structures formed by this dying cell were effectively labeled and visualized using the dTRABI approach.

Importantly, dTRABI offers a tool for mapping localization of molecules within ~1 µm of the optical surface. Such working space provides a sufficient axial signal penetration to visualize the eukaryotic plasma membrane with its nanotopography. Under the conditions used in our experiments, the plasma membrane protrusions were positioned 100–400 nm from the optical surface (Fig. 5). Thus, molecules that do not localize to the protrusions can be monitored as well. This was facilitated by the folding of membrane protrusions, the length of which often exceeded the axial depth of our method, under the cell body (Fig. 4 and Supplementary Fig. 11a,b). Evidently, a partial loss of molecular localizations in the areas where the base of the plasma membrane is positioned outside of the optical limit of this method is caused by a diverse positioning of cells and intensive bending of cell-glass contacts (Supplementary Figs. S9 and S11c,d).

The quantitative character of dTRABI data also enabled a detailed analysis of axial receptor distribution, which we modelled by fitting a sum of two Gaussian functions (bi-Gaussian) to the axial localization data. Although CD4 distribution can be modelled by a single Gaussian to a high degree of confidence, a bi-Gaussian is even more accurate and accounts for a slight asymmetric organization of receptors. In contrast, non-palmitoylatable CD4 CS1 mutant does not follow a mono-Gaussian distribution and the bi-Gaussian is essential. The analysis allowed us to derive quantitative parameters describing axial receptor distribution in detail, i.e., z_W, p-p and Δ_{FWHM}. All these analytical approaches emphasized the narrow and symmetrical distribution of CD4 WT, while CD4 CS1 and CD45 show significantly broader distributions.

To highlight the effectiveness of our new imaging approach, we explored two important biological questions: i) what is the origin of receptor microclusters in T cells, and ii) how does membrane morphology affect segregation of signaling receptors into different areas of the plasma membrane? Both questions cannot be studied by previously reported protocols. Using quantitative SOFI analysis, we have previously shown that CD4 accumulates in high-density regions (clusters) in unstimulated T cells by a process that depends on its post-translational lipid modification, palmitoylation[28]. However, as in many other cases, these data represented two-dimensional projections of receptor localizations on the complex T-cell surface. Using dTRABI imaging of unstimulated T cells immobilized on glycine-coated coverslips, we demonstrate that CD4 accumulates on the tips of microvilli. Thus, CD4 clusters, and potentially other clusters, represent receptors (or other molecules) trapped at the tips of membrane protrusions, stressing that intact cell surface morphology is essential for the proper spatial representation of signaling molecules. Our data are in agreement with recently reported clustering of CD4 on the tips of T cell microvilli [84] but provide more detailed and quantitative insight into the CD4 distribution to these structures. Importantly, the mutant CD4 CS1 variant which cannot be palmitoylated distributed more randomly over the complex surface of T cells. Targeting to or stabilizing proteins on membrane protrusions thus may be another, previously unreported role of protein palmitoylation[85].

The best-described function of CD4 is to deliver critical Lck kinase to the proximity of T cell receptor for a rapid response to antigens[60]. TCR was recently reported to accumulate in T cell microvilli by projecting a two-dimensional SMLM image onto the morphological map generated by varying-angle TIRF microscopy (VA-TIRFM) of a membrane dye [84,86]. VA-TIRFM is diffraction-limited and, therefore, does not provide a high-resolution map of cell surface nanotopography. However, the data indicated the accumulation of TCR in domains formed by or dependent on membrane morphology. We thus speculate that CD4 and TCR localize to the protrusions, the tips of which can represent membrane areas with concentrated signaling molecules arranged to rapidly respond to appropriate signals (Fig. 7c). How these molecules accumulate in these structures and whether the tips of protrusions undergo further compartmentalization remains unclear. In future ventures, we will establish a robust workflow consisting of reliable sample preparation, labelling and multi-color dTRABI analysis to investigate the multi-molecular architecture of these structures. Our current approach already provides a good basis for such advancement and is adaptable to multiple avenues of inquiry.

Several molecules, including CD45, were shown to segregate from signaling microclusters (e.g., refs.[63,87]). Using dTRABI and glycine-coated coverslips, we demonstrated that CD45 distributes over a broader axial spectrum than CD4. Since CD45 segregates from CD4 in non-stimulated T cells under the experimental conditions used in this study, we conclude that CD45 segregates from signaling molecules by localizing to the shaft of microvilli and basis of the plasma membrane (Fig. 7c). The molecular mechanism of such segregation remains unknown. Even though listed in a high-throughput study of palmitoylated proteins[88], direct experimental proof of CD45 palmitoylation is missing. Since the non-palmitoylated CD4 CS1 variant exhibits a more random distribution compared to its native variant, we speculate that the lack of CD45 palmitoylation contributes to its preference for the basis of the plasma membrane.

In summary, we provide a new and undemanding workflow to study nanotopography of receptors at the cell surface. We highlight the importance of appropriate sample preparation for the imaging of three-dimensional structures. The improved algorithm of dTRABI exemplifies an easily implemented and high-quality method to generate three-dimensional SMLM data. Finally, we demonstrate the applicability of the workflow by answering two critical questions related to the localization of surface receptors on lymphocytes. Even though the method was used here for human receptors, it can be implemented for molecular characterization of the surface on other organisms (e.g., yeast, plants) but also for complex nanomaterials that do not exceed the current axial penetration of dTRABI (~ 1 µm).

METHODS

Cell culture and transfection

Jurkat T cells (clone E6; ATCC) and their CD4-knock-out variants (Jurkat CD4-KO cells) were grown in RPMI-1640 medium (Gibco) supplemented with 10% fetal bovine serum (Gibco), Non-essential amino-acids (Gibco) and 10mM HEPES under controlled conditions in a humidified incubator at 37°C, and 5 % CO_2 (Eppendorf). Jurkat CD4-KO cells were derived from wild-type Jurkat T cells (clone E6; ATCC) using CRISPR/Cas9 technology as described[89]. Both cell lines were regularly tested for morphology and mycoplasma infection.

For the expression of exogenous proteins, Jurkat T cells and their CD4 KO variant were transiently transfected with plasmid DNA using Neon® transfection system (Thermo Fisher Scientific) according to the manufacturer's instructions. Briefly, 1 µg of vector DNA was used per 200 000 cells in 0.5 ml culture medium. The instrument settings were: 3 pulses, each 1350 V for 10 ms. Transfected cells were used within 36 h since the transfection.

Sample preparation for SR microscopy

Cleaning and handling of coverslips and solutions for microscopy

High precision microscopy coverslips (round, 25 mm in diameter; Marienfeld) in Teflon holders (Wash-N-Dry Coverslip Rack; Diversified Biotech Inc.) were cleaned by incubation at 56°C overnight in 2% Hellmanex III (Hellma Analytics) dissolved in ultrapure Milli-Q® water (Millipore) followed by 30 minutes sonication in a heated sonication bath. Several washes in ultrapure water and one additional sonication step were used to remove all traces of Hellmanex III components. Cleaned coverslips were stored in ultrapure water to avoid drying and contamination with particles of a dust from air.

All other glassware was regularly treated with piranha solution (3 parts of 30% hydrogen peroxide and 7 parts of concentrated sulfuric acid) for 45 minutes followed by several washes with ultrapure water. All solutions were made from concentrated stocks stored in glass containers, diluted with ultrapure water and filtered using syringe filters with 0.22 µm pores (TPP) into piranha-treated glassware.

Glycine coating of coverslips

Ultraclean coverslips were coated by applying 0.5 ml of 2M glycine solution and incubation for 20 min at room temperature in the laminar flow box. Afterwards, the liquid phase was aspirated, and the hydrogel was washed with ultrapure water. Coverslips coated with glycine hydrogel were used immediately for immobilization of cells. The hydrogel-coated coverslips can be stored at 4°C covered with a layer of ultrapure water for several days.

PLL coating of coverslips

Ultraclean coverslips were coated by applying 0.5 ml of 0.01% (w/v) PLL solution in ultrapure water and incubation for 20 min at room temperature in the laminar flow box. Unbound PLL was removed by aspiration of the liquid and a single wash with ultrapure water. Dried, PLL-coated coverslips can be stored for several weeks. For SR imaging, freshly prepared PLL-coated coverslips were used exclusively.

Immobilization and fixation of cells for SR imaging

Jurkat T cells express varying levels of CD4 which are changing when cells are grown in culture. Therefore, we used transiently transfected Jurkat-CD4KO cells with reintroduced CD4-GFP to study CD4 surface distribution with dTRABI. Cells expressing similar levels of CD4-GFP were selected for imaging and data processing.

For SR imaging, after centrifugation for 3 minutes at 500 g (room temperature), cells were resuspended in pre-warmed PBS (made from 10x stock, Gibco) and seeded on glycine-coated coverslips immediately after the aspiration of a coating liquid. Cells were enabled to land on the coated optical surface for 10 minutes at 37°C in the CO_2 incubator. Afterwards, cells were fixed with pre-warmed 4% paraformaldehyde (Electron Microscopy Sciences) containing 2% saccharose in PBS for 45 minutes at room temperature and the process was stopped with 50 mM NH_4Cl (Sigma-Aldrich) in PBS and three rounds of washing with PBS.

Immunofluorescence

For labeling, cells were first incubated with 5% BSA in PBS (Blocking solution) for 1 hour at the ambient temperature to prevent non-specific binding of antibodies. Immunostaining of specific receptors was performed by incubating cells overnight with AlexaFluor 647 conjugated primary antibodies (human CD4: OKT4, dilution: 1:100, source: Biolegend; human CD45: MEM-28, dilution: 1:2000, source: ExBio) diluted in Blocking solution. The process was performed at the ambient temperature in a humid chamber to avoid drying of the solutions. After removing of redundant antibodies and 3 times washing with PBS for 5 minutes, the cells were post-fixed with 4% PFA for 5 minutes and washed 5 times with PBS.

The identical protocol was applied for the staining of CD45 on Jurkat CD4 KO cells transfected with pXJ41-CD4-mEOS2 plasmid for 2-color 2D SMLM analysis.

Single-Molecule Localization Microscopy

Three-dimensional SMLM experiments for dTRABI analysis were performed on a home-built wide-field setup, which is described elsewhere in detail[65]. Raw image stacks were analyzed with rapidSTORM 3.2 (ref.[90]). Herein, the FWHM was set to 300 nm as an invariant parameter. Furthermore, the lower intensity threshold was set to 500 photons and the fit window radius to 1200 nm. All other fit parameters were kept from the default settings in rapidSTORM 3.2. Linear lateral drift correction was applied manually by spatio-temporally aligning distinct structures to themselves. This was facilitated by color-coding of the temporal coordinate with the built-in tool.

Two-color SMLM experiments were performed on a Nikon Eclipse Ti microscope, which is specified elsewhere in detail[44]. Contrary to the case of dTRABI analysis, the FWHM was set as a free fit parameter, but in the limits of 275–750 nm, both for Alexa Fluor 647 antibody and mEOS2 fusion protein localizations. All other parameters were kept consistent to the previous experiments. Prior to imaging, a glass surface with Tetraspeck beads (Thermo Scientific) was imaged with alternating 561 nm and 647 nm excitation to create a nanometer precise map to allow the correction of chromatic shift. The 561 nm excitation channel was then mapped onto the 647 nm after the localization step.

Prior to acquisition, cells were irradiated in epifluorescence illumination mode to turn emitters, which were out-of-focus in the HILO illumination scheme, into the dark state. In all experiments, the length of the acquisition was set to capture the majority of emitters, i.e. imaging was concluded when only a very minor number of active emitters was detectable. Typical acquisition lengths were 60,000–120,000 frames for Alexa Fluor 647 channel and 30,000–60,000 frames for mEos2 channel, where integration times were set to 20 ms and 16 ms in the single- and dual-color cases, respectively. Hereby, mEOS2 was excited at 561 nm and activated with 405 nm. The activation power density was increased over the time to create an almost constant signal density.

Intensity based biplane imaging – dTRABI

The principle of dTRABI

We previously reported TRABI-based biplane (BP-TRABI; ref.[65]), which utilizes the photometric ratios P of the molecules for the image reconstruction. P was calculated as the quotient of the fit intensity (I_{Fit}) and reference intensity (I_R), where I_{Fit} was derived from a PSF fit with fixed width, which was set in rapi*d*STORM software. For BP-TRABI, the photometric ratio of both planes ($P_{1,2}$) was calculated according to

$$P_{1,2}(z) = \frac{P_1 - P_2}{P_1 + P_2} \qquad (1)$$

with P_1 and P_2 being the photometric ratio of the individual planes.

The quality of the resulting axial coordinate depended on the precision of the TRABI intensity measurement. In order to exclude any interference from neighboring emitters as well as temporal overlap with other fluorophores, a set of rigorous exclusion criteria for spots was employed. As a consequence, many localizations given by the localization software were rejected by TRABI. To compensate, significantly longer image stacks had to be recorded to ensure structural consistency in the reconstructed images regarding the Nyquist-criterion. Though this was already an inconvenience for common SMLM organic fluorophores, which exhibit high repetition counts, it can be a significant obstacle for imaging approaches utilizing photo-activatable or -convertible fluorescent proteins. Furthermore, in cases of sub-optimal photo-switching rates that lead to high spot densities, the TRABI approach was computationally expensive or could even fail to produce an image due to a high rejection rate of fluorescent spots.

For a reasonable large TRABI radii I_R converges for both spots in both planes, thus Eq. (1) can be effectively simplified to

$$I_{\text{Fit},1,2}(z) = \frac{I_{\text{Fit},1} - I_{\text{Fit},2}}{I_{\text{Fit},1} + I_{\text{Fit},2}} \qquad (2)$$

As Eq. (2) demonstrates, in order to achieve three-dimensional BP imaging, there is no need for an actual photometric TRABI analysis anymore, since I_R is cancelled out. Therefore, dTRABI allowed for higher emitter densities, was quicker and required less input parameters.

Calibration and allocation

Raw calibration curves were generated by linearly moving the focal plane through the sample plane while imaging a single-molecule surface under dSTORM conditions as previously described[65]. For this, a surface of BSA was doped with BSA molecules, attached to a short DNA sequence, labeled with Cy5. Fitting the raw emission patterns by independent Gaussians with the same fixed FWHM yielded axially dependent single-molecule intensity curves. An axially precise raw calibration function γ was derived according to Eq. (2). The running median (binning width 25 nm) of the raw data was fitted with a high order polynomial to generate the axial lookup table.

After an initial rough alignment between the channels, experimental localizations from both optical channels were assigned by a framewise, linear nearest neighbor analysis. Here, the distance threshold was set to 500 nm, which seemed a reasonable value for the robust allocation between channels in a semi-sparse single-molecule environment. From these sets of localizations, the axially dependent intensity quotient $I_{\mathrm{Fit},1,2}$ (Fig. 2b) was calculated and roughly allocated to the look-up table (LUT). The final axial coordinate was determined by a linear interpolation of $I_{\mathrm{Fit},1,2}$ between its “left” and “right” nearest neighbor coordinate of the LUT. Obtained axial coordinates were corrected for the refractive index mismatch as previously described[65].

Drift and tilt correction

Since the plasma membrane can be seen as flat over the whole-cell scale, we reckoned that it can be used as its own fiducial marker. We traced the spatio-temporal axial footprint of the entire membrane by fitting the raw localizations by a high-order polynomial in time. This is followed by the straightforward temporal linearization of the localization data, leading to a stable axial mean value over time. In order to instantly assess the quality of three-dimensional SMLM data we suggest looking for white regions in the color-coded image. In our experience, the abundance of these features usually suggests significant axial drift. However, even a subtle axial drift, which cannot be easily recognized by eye, will be detected by the approach described above. Additionally, non-linear drift, commonly occurring due to heating and resting of threads, can be accounted for.

Since we regularly observed a subtle axial tilt in the nanoscopic color-coded images due to the usage of a round coverslip in a magnetic holder, we developed a simple correction workflow (Fig. 3). The axial tilt of the sample is extrapolated by fitting a plane to the raw image data (pixel size 100 nm). Afterwards, the data was linearized by simply subtracting the precise local plane-value from the raw localization.

Localization precision calculation

Drift and tilt corrected localizations were tracked in time by determining the three-dimensional nearest neighbor distances of localizations in consecutive frames. Localizations constructing a track with a total inter-localization distance of less than 75 nm were considered to stem from the same fluorophore. For each sample type, we combined the nearest-neighbor tracks from all recorded independent fields of view, calculated the deviation from the mean coordinate of each track for all relevant spatial coordinates and derived a normalized histogram (Supplementary Fig. S6). By fitting these distributions with a Gaussian, we derived the localization precisions as the standard deviation of the mean.

Fourier Ring Correlation (FRC) analysis

Standard TRABI-biplane files were created with a TRABI radius of 8.5 camera pixel, a base-jump of 2 frames, an exclusion zone factor of 2, a highlander-filter of 250 frames and a number of averaged background frames of 5. Three-dimensional data sets were then sorted into groups of localizations apparent in even and odd numbered frames, respectively, which were rendered to high-resolved images in rapi*d*STORM with 10 nm pixel size. FRC was performed on these two respective images, using the NanoJ-Squirrel Fiji plugin[78] with the input of 20 segments per dimension. Since the resulting FRC resolution maps showed a prevalence for extreme outliers, we chose the median FRC resolution over the entire displayed image as resolution criteria (Supplementary Fig. S5).

Axial localization distribution analysis

Localization files obtained from rapi*d*STORM were loaded and processed in Fiji [79] with custom written scripts[80]. First, all localization coordinates in x, y and z were used to generate a quantitative stack of 2D images with 20 nm pixel size using a separation of 20 nm in z (i.e. z-stack). The numeric value in each pixel was equivalent to the number of localizations. Then the z-stack was segmented into defined regions of interest (ROIs). The interior of the cells was manually selected to serve as boundary ROI, in which the edges of the cells were spared. Within this master ROI a set of squared ROIs with 2×2 µm² area was automatically generated. The ROIs were allowed to be confined by the border of the master ROI and only kept when more than 75% of the ROI area, i.e. > 3 µm were preserved (Supplementary Fig. S6).

Afterwards, the localization density of each ROI was analyzed by accumulating the grey values per ROI within the image stack, i.e. stepwise in z every 20 nm, and plotted as a function of z. The plot was then fitted to a bi-Gaussian function of the form

$$y = a_1 \exp\left(-\frac{1}{2}\left(\frac{x-m_1}{s_1}\right)^2\right) + a_2 \exp\left(-\frac{1}{2}\left(\frac{x-m_2}{s_2}\right)^2\right),$$

with $a_{1,2}$ as amplitude, $m_{1,2}$ as mean value and $s_{1,2}$ as standard deviation of each Gaussian.

To characterize the axial distribution of localizations of CD4-WT, CD4-CS1 and CD45, three parameters were derived from this fit. 1) the z-distribution width (Fig. 5e-g) calculated according to

$$z_w = \left(m_2 + \frac{\mathrm{FWHM2}}{2}\right) - \left(m_1 - \frac{\mathrm{FWHM1}}{2}\right)$$, for $m_2 > m_1$ with $\mathrm{FWHM}_{1,2} = s_{1,2} \times 2.355$;

2) the peak-to-peak distance (Supplementary Fig. S10) according to $\text{p-p} = |m_2 - m_1|$;

and 3) the width difference of the two Gaussians (Supplementary Fig. S8) according to $\Delta_{\mathrm{FWHM}} = |\mathrm{FWHM}_1 - \mathrm{FWHM}_2|$.

Quantifying axial receptor distribution

For quantifying the obtained axial receptor distribution in Fig. 5f, we fitted the histogram of z_w for CD4 WT, CD4 CS1 and CD45 with a model of Gaussian functions. CD4 WT was fitted using a mono-Gaussian and yielded the mean value μ and standard deviation σ, the range of z_w in Table 1 was stated as $\mu \pm \mathrm{FWHM}/2$, with FWHM as full width at half maximum of the distribution. CD4 CS1 and CD45 z_w histograms were fitted using a bi-Gaussian yielding μ_1, μ_2 and σ_1, σ_2 as mean and standard deviation, respectively. The range of values in Table 1 was stated as $\mu \pm \mathrm{FWHM}/2$. The p-p distributions (Supplementary Fig. S8) were modeled with a mono-exponential decay, and the inverse of the decay constant of the fit (τ), i.e. the value at which the amplitude is reduced to 36.8%, was stated as mean value. The distribution of Δ_{FWHM} was modeled with a mono-Gaussian, thus obtaining μ and σ as mean and standard deviation, respectively; the range of values in Table 1 was stated as $\mu \pm \mathrm{FWHM}/2$.

SOFI

Sample preparation, coverslip coating and image acquisition were performed as described above for SMLM imaging. The raw data were analyzed using balanced SOFI algorithm as described before[28,91].

Calcium measurements

Calcium sensor

Plasmid DNA with the ultrafast, genetically encoded calcium sensor GCaMP6f_u was a kind gift from Katalin Török and Silke Kerruth (St George's, University of London). The coding sequence was amplified using primers AATAGATCTGCCACCATGGGCTGCGTGTGCTCCTC and AATGGATCCTCACTTCGCTGTCATCATTTGTACAAA and subcloned into pXJ41 vector using *BglII* and *BamHI* restriction sites as described before[92].

Sample preparation

For calcium measurements, the coverslips were coated with 0.01% (w/v) poly-*L*-lysine (Sigma-Aldrich) or 2M glycine as described above. For coating with OKT3 (anti-CD3ε) antibody, clean coverslips were incubated with 0.01 µg/µl OKT3 in PBS for 30 minutes at 37°C. After a brief wash with PBS, the coverslips were used within a day. Prior to acquisition, coated coverslips were mounted into a ChamLide holder (Live Cell Instruments), filled with 500ul of color-free medium, placed on the microscope and focused to the focal plane. The measurements were performed twenty hours after transfection of Jukrat T cells with the calcium sensor. For image analysis, cells were washed with PBS, resuspended in phenol red-free RPMI-1640 media

(Sigma-Aldrich) supplemented with 2mM *L*-glutamine, 10mM HEPES, 1mM CaCl2 and 1mM $MgCl_2$ and dropped onto the prepared coverslip while running the image acquisition.

The microscope setup and image acquisition

Live cell calcium mobilization imaging was performed on a home built TIRF microscope consisting of the IX73 frame (Olympus), UApo N, 100x 1.49 Oil immersion TIRF objective (Olympus) and OptoSplit II image splitter (CAIRN Optics) mounted on the camera port. Samples were illuminated using 200mW 488 nm laser (Sapphire, Coherent) in a TIRF mode and the intensity was regulated by acousto-optic tunable filter (AOTFnC-400.650-TN, AA Optoelectronics). Fluorescence emission was detected by an EMCCD camera (iXon ULTRA DU-897U, Andor) with EM gain set to 200. Images were taken in 500ms intervals with the exposure time set to 50 ms.

Data processing

Calcium mobilization was quantified by calculating mean fluorescence in cells immobilized on coated coverslips over the period of 10 minutes. Fiji/ImageJ software was used for the analysis[79]. Graphs in Supplementary Fig. S3 represent a mean fluorescence changes in cells immobilized on PLL-, glycine- or OKT3-coated coverslips. The peak intensity (I_max) was determined by finding a maximum value using Excel software (Microsoft). To determine the extent of calcium response, we calculated the decrease in intensity after the maximal response. The early phase of the measurement (an increase in intensity) represents a combination of the rise of background fluorescence due to cell spreading on the optical surface and of the specific sensor fluorescence caused by increased calcium in the cytosol. The kinetics of fluorescence decay was calculated as a ratio I_max/I_max+5min and I_max/I_max+10min. Higher values indicate a more rapid decay of the fluorescence, which indicates stronger response. Values of I_max+5min and I_max+10min represent the fluorescence intensity 5 and 10 minutes, respectively, after the maximum calcium response (I_max) was reached. To avoid the impact of the intensity fluctuations, we calculated I_max), I_max+5min and I_max+10min as an average of 10 images (frames).

Characterization of T cell surface in contact with a coated coverslip and cell viability measurements

Microscope setup

For imaging of living T cells forming contact with a coated coverslip and for determining the viability of T cells immobilized on a coated coverslip, a home-build inverted microscope system (IX71, Olympus) equipped with 150 mW 488 nm and 150 mW 561 nm lasers (Sapphire, Coherent) was used. Fluorescence emission for cell surface-contact analysis and viability assay was detected by an EMCCD (iXon DU-897, Andor) and a sCMOS (Zyla-4.2-CL10, Andor) cameras, respectively. Two acousto-optic tunable filters (AOTFnC-400.650-TN, AA Optoelectronics) provided fast switching and synchronization of lasers with a camera. For TIRF imaging, the 488 nm laser beam was focused onto the back focal plane of an objective (UApoN 100x, NA = 1.49, Olympus). TIRF illumination was achieved using a manual micrometer-scale tilting mirror mechanism in the excitation pathway (Thorlabs). For cell viability measurements, the laser light was defocused to achieve a homogenous illumination at the objective sample plane (UPlanSApo 10x, NA = 0.4, Olympus). The system was controlled using the µManager software (version 1.4.22; ref.[93]).

Analysis of the T cell surface in contact with a coated coverslip

For T cell-coverslip contact analysis, Jurkat T CD4-KO cells were transfected with pXJ41-CD4-wt-eGFP plasmid 24-hours prior to the measurement. Cells were then harvested and transferred into color-free RMPI medium (Gibco) supplemented with 2 mM L-glutamine (Lonza) pre-warmed to 37°C. In parallel, cleaned coverslips were mounted for imaging into a ChamLide holder equipped with tubing adaptors (Live Cell Instruments), coated as described above and washed with ultrapure water. Immediately after coating fluid removal through the attached tubing, cells were injected into the ChamLide chamber attached to the microscope stage. Landing cells were selected under transmitted light and the fluorescence was recorded on EMCCD camera using TIRF illumination for 20 minutes. Images were acquired in one second intervals with 50 ms exposure time. The camera EM gain was set to 100. The experiment was performed at 37°C using the environmental chamber (OKO lab) with controlled temperature. Acquired images were processed using standard functions (ROI Manager, Plot Profile) of Fiji/ImageJ software (version 1.52p; ref.[79]).

T cell viability assay

To evaluate the viability of cells in contact with coated coverslips, Jurkat T cells were transfected with mTurquoise-Farnesyl-5 plasmid (#55551, Addgene) 24 hours prior to the assay. This was done to mimic the conditions used for all other experiments in this work but to avoid interference of the protein fluorescence with the dyes used for the assay. For the measurement, cells were washed with PBS, transferred into color-free RPMI (Gibco) medium supplemented with 2 mM *L*-glutamine (Lonza), 10% fetal bovine serum (Gibco), 10 mM HEPES and Non-essential amino-acid mixture (Gibco) containing 25 µg/ml (w/v) calcein-AM dye and incubated for 10 minutes at 37°C in the CO_2 incubator. Cells were then transferred into a fresh, color-free RPMI medium supplemented with 2 mM *L*-glutamine and 7AAD (7-Amino-Actinomycine D; 1:20 dilution) viability stain (eBioscience) and incubated for another 5 minutes at 37°C in the CO_2 incubator. After loading with the dyes, cells were injected onto the coated coverslips in ChamLide chamber using attached tubing. Imaging was performed for 30 minutes (with 10-minute acquisition intervals) from the time of the fist cell-coverslip contact detection. Two randomly selected ROIs were selected for each time point to avoid the effect of the fluorophore photo-destruction. Calcein and 7AAD dyes were excited separately by 488 nm and 561 nm lasers, respectively, using defocused light to achieve homogenous illumination. Cells were also imaged under transmitted light to control their morphology. To avoid the impact of fluorescence fluctuations, five frames were collected for each channel, ROI and time point. The frames were then summed to generate a collate image for further quantitative analysis. Data analysis was performed in Fiji/ImageJ (version 1.52p, ref.[79]). Cells were counted by determining local maxima for each channel. The final result was calculated as a percentage of 7AAD positive (dying) cells in all detected cells (calcein positive). The experiment was performed at 37°C using the environmental chamber (OKO lab) with controlled temperature.

Atomic force microscopy

Atomic Force Microscopy (AFM) topography images were collected with Dimension Icon AFM (Bruker Instruments). All images were measured in the Peak Force Tapping mode for fluids, using a probe holder for fluid operation and Scanasyst-Fluid probes (Bruker) with a tip radius of 20 nm and a spring constant of 0.7 N/m.

12 mm diameter coverslips were coated with PLL and glycine as described above. A bare coverslip was prepared as a reference. The AFM probe was submerged in the solution in order to land on the coverslip surface. Due to a delicate nature of the samples and to avoid long measurement times, setpoint and number of lines were set to 400 pN and 256 x 256 lines respectively, with a scan rate of 1 Hz. Images with scan sizes of 1, 2 and 10 μm were collected.

Acknowledgements

We would like to thank Peter Kapusta, Silke Kerruth and Harsha Mavila for technical assistance and professional advice. We are grateful to Markus Sauer (University of Würzburg) for support of the project. C.F. would like to thank Laure Plantard and Jan Peychl from the MPI-CBG LMF for technical support. M.C. acknowledges funding from Czech Science Foundation (19-0704S), S.vdL. acknowledges funding from Academy of Medical Sciences/the British Heart Foundation/the Government Department of Business, Energy and Industrial Strategy/the Wellcome Trust Springboard Award (SBF003\1163). The measurements at the Imaging Methods Core Facility in BIOCEV, Vestec, Czech Republic were supported by MEYS CR grant Z.02.1.01/0.0/0.0/16_013/0001775.

Contributions

C.F., S.vdL. and M.C. conceived the study. C.F., T.C., Z.K., D.G. and D.A.H. performed the experiments, C.F., T.C., D.G., S.vdL. and M.C. analyzed the data. A.R. measured and analyzed the AFM data. O.F. and T.B. provided research advice. C.F., S.vdL. and M.C. wrote the paper. All authors reviewed and approved the manuscript.

Corresponding authors

Correspondence to Christian Franke, Sebastian van de Linde and Marek Cebecauer

Additional information

Supplementary Information accompanies this paper at …

Competing interests

The authors declare no competing financial interests.

REFERENCES

1. Cebecauer, M., Spitaler, M., Serge, A. & Magee, A.I. Signalling complexes and clusters: functional advantages and methodological hurdles. *J Cell Science* **123**, 309-320 (2010).
2. Pak, A.J. et al. Immature HIV-1 lattice assembly dynamics are regulated by scaffolding from nucleic acid and the plasma membrane. *Proc Natl Acad Sci U S A* **114**, E10056-E10065 (2017).
3. Rossier, O. et al. Integrins beta1 and beta3 exhibit distinct dynamic nanoscale organizations inside focal adhesions. *Nat Cell Biol* **14**, 1057-67 (2012).
4. Barreiro, O. et al. Endothelial adhesion receptors are recruited to adherent leukocytes by inclusion in preformed tetraspanin nanoplatforms. *J Cell Biol* **183**, 527-42 (2008).
5. Kellermayer, B. et al. Differential Nanoscale Topography and Functional Role of GluN2-NMDA Receptor Subtypes at Glutamatergic Synapses. *Neuron* **100**, 106-119 e7 (2018).
6. Sevcsik, E. & Schutz, G.J. With or without rafts? Alternative views on cell membranes. *Bioessays* **38**, 129-139 (2015).
7. Dustin, M.L. & Davis, S.J. TCR signaling: the barrier within. *Nat Immunol* **15**, 136-7 (2014).
8. Bernardino de la Serna, J., Schutz, G.J., Eggeling, C. & Cebecauer, M. There Is No Simple Model of the Plasma Membrane Organization. *Front Cell Dev Biol* **4**, 106 (2016).
9. Brameshuber, M. et al. Monomeric TCRs drive T cell antigen recognition. *Nat Immunol* **19**, 487-496 (2018).
10. James, J.R. et al. The T Cell Receptor Triggering Apparatus Is Composed of Monovalent or Monomeric Proteins. *J Biol Chem* **286**, 31993-32001 (2011).
11. Gomes de Castro, M.A. et al. Differential organization of tonic and chronic B cell antigen receptors in the plasma membrane. *Nat Commun* **10**, 820 (2019).
12. Campi, G., Varma, R. & Dustin, M.L. Actin and agonist MHC-peptide complex-dependent T cell receptor microclusters as scaffolds for signaling. *J Exp Med* **202**, 1031-6 (2005).
13. Tolar, P., Hanna, J., Krueger, P.D. & Pierce, S.K. The constant region of the membrane immunoglobulin mediates B cell-receptor clustering and signaling in response to membrane antigens. *Immunity* **30**, 44-55 (2009).
14. Saka, S.K. et al. Multi-protein assemblies underlie the mesoscale organization of the plasma membrane. *Nat Commun* **5**, 4509 (2014).
15. Letschert, S. et al. Super-resolution imaging of plasma membrane glycans. *Angew Chem Int Ed Engl* **53**, 10921-4 (2014).
16. Mateos-Gil, P., Letschert, S., Doose, S. & Sauer, M. Super-Resolution Imaging of Plasma Membrane Proteins with Click Chemistry. *Front Cell Dev Biol* **4**, 98 (2016).
17. Puchner, E.M., Walter, J.M., Kasper, R., Huang, B. & Lim, W.A. Counting molecules in single organelles with superresolution microscopy allows tracking of the endosome maturation trajectory. *Proc Natl Acad Sci U S A* **110**, 16015-20 (2013).
18. Loschberger, A., Franke, C., Krohne, G., van de Linde, S. & Sauer, M. Correlative super-resolution fluorescence and electron microscopy of the nuclear pore complex with molecular resolution. *J Cell Sci* **127**, 4351-5 (2014).
19. Ehmann, N. et al. Quantitative super-resolution imaging of Bruchpilot distinguishes active zone states. *Nat Commun* **5**, 4650 (2014).
20. Jungmann, R. et al. Quantitative super-resolution imaging with qPAINT. *Nat Methods* **13**, 439-42 (2016).
21. Lillemeier, B.F. et al. TCR and Lat are expressed on separate protein islands on T cell membranes and concatenate during activation. *Nat Immunol* **11**, 90-6 (2010).
22. Rossy, J., Owen, D.M., Williamson, D.J., Yang, Z. & Gaus, K. Conformational states of the kinase Lck regulate clustering in early T cell signaling. *Nat Immunol* **14**, 82-9 (2013).
23. Rossboth, B. et al. TCRs are randomly distributed on the plasma membrane of resting antigen-experienced T cells. *Nat Immunol* **19**, 821-827 (2018).

24. Mattila, P.K. et al. The actin and tetraspanin networks organize receptor nanoclusters to regulate B cell receptor-mediated signaling. *Immunity* **38**, 461-74 (2013).
25. Balint, S., Lopes, F.B. & Davis, D.M. A nanoscale reorganization of the IL-15 receptor is triggered by NKG2D in a ligand-dependent manner. *Sci Signal* **11**, eaal3606 (2018).
26. Annibale, P., Vanni, S., Scarselli, M., Rothlisberger, U. & Radenovic, A. Identification of clustering artifacts in photoactivated localization microscopy. *Nat Methods* **8**, 527-528 (2011).
27. Burgert, A., Letschert, S., Doose, S. & Sauer, M. Artifacts in single-molecule localization microscopy. *Histochem Cell Biol* **144**, 123-31 (2015).
28. Lukes, T. et al. Quantifying protein densities on cell membranes using super-resolution optical fluctuation imaging. *Nat Commun* **8**, 1731 (2017).
29. Levet, F. et al. SR-Tesseler: a method to segment and quantify localization-based super-resolution microscopy data. *Nat Methods* **12**, 1065-71 (2015).
30. Baumgart, F. et al. Varying label density allows artifact-free analysis of membrane-protein nanoclusters. *Nat Methods* **13**, 661-4 (2016).
31. Spahn, C., Herrmannsdorfer, F., Kuner, T. & Heilemann, M. Temporal accumulation analysis provides simplified artifact-free analysis of membrane-protein nanoclusters. *Nat Methods* **13**, 963-964 (2016).
32. Vangindertael, J. et al. An introduction to optical super-resolution microscopy for the adventurous biologist. *Methods Appl Fluoresc* **6**, 022003 (2018).
33. Raghunathan, K. & Kenworthy, A.K. Dynamic pattern generation in cell membranes: Current insights into membrane organization. *Biochim Biophys Acta Biomembr* **1860**, 2018-2031 (2018).
34. Sezgin, E., Levental, I., Mayor, S. & Eggeling, C. The mystery of membrane organization: composition, regulation and roles of lipid rafts. *Nat Rev Mol Cell Biol* **18**, 361-374 (2017).
35. Jarsch, I.K., Daste, F. & Gallop, J.L. Membrane curvature in cell biology: An integration of molecular mechanisms. *J Cell Biol* **214**, 375-87 (2016).
36. Fisher, P.J., Bulur, P.A., Vuk-Pavlovic, S., Prendergast, F.G. & Dietz, A.B. Dendritic cell microvilli: a novel membrane structure associated with the multifocal synapse and T-cell clustering. *Blood* **112**, 5037-45 (2008).
37. Kim, H.R. et al. T cell microvilli constitute immunological synaptosomes that carry messages to antigen-presenting cells. *Nat Commun* **9**, 3630 (2018).
38. Shalek, A.K. et al. Nanowire-mediated delivery enables functional interrogation of primary immune cells: application to the analysis of chronic lymphocytic leukemia. *Nano Lett* **12**, 6498-504 (2012).
39. Gorelik, J. et al. Dynamic assembly of surface structures in living cells. *Proc Natl Acad Sci U S A* **100**, 5819-22 (2003).
40. Lange, K. Fundamental role of microvilli in the main functions of differentiated cells: Outline of an universal regulating and signaling system at the cell periphery. *J Cell Physiol* **226**, 896-927 (2011).
41. Millington, P.F., Critchley, D.R., Tovell, P.W. & Pearson, R. Scanning electron microscopy of intestinal microvilli. *J Microsc* **89**, 339-44 (1969).
42. Griffiths, G. & Lucocq, J.M. Antibodies for immunolabeling by light and electron microscopy: not for the faint hearted. *Histochem Cell Biol* **142**, 347-60 (2014).
43. Schwarz, H. & Humbel, B.M. Correlative light and electron microscopy using immunolabeled sections. *Methods Mol Biol* **1117**, 559-92 (2014).
44. Franke, C. et al. Correlative single-molecule localization microscopy and electron tomography reveals endosome nanoscale domains. *Traffic* **20**, 601-617 (2019).
45. Li, D. et al. ADVANCED IMAGING. Extended-resolution structured illumination imaging of endocytic and cytoskeletal dynamics. *Science* **349**, aab3500 (2015).

69. Schermelleh, L. et al. Super-resolution microscopy demystified. *Nat Cell Biol* **21**, 72-84 (2019).
70. de Kruijff, B. & Cullis, P.R. The influence of poly(L-lysine) on phospholipid polymorphism. Evidence that electrostatic polypeptide-phospholipid interactions can modulate bilayer/non-bilayer transitions. *Biochim Biophys Acta* **601**, 235-40 (1980).
71. Pachmann, K. & Leibold, W. Insolubilization of protein antigens on polyacrylic plastic beads using poly-L-lysine. *J Immunol Methods* **12**, 81-9 (1976).
72. van de Linde, S. et al. Direct stochastic optical reconstruction microscopy with standard fluorescent probes. *Nat Protoc* **6**, 991-1009 (2011).
73. Klein, T. et al. Live-cell dSTORM with SNAP-tag fusion proteins. *Nat Methods* **8**, 7-9 (2011).
74. Santos, A.M. et al. Capturing resting T cells: the perils of PLL. *Nat Immunol* **19**, 203-205 (2018).
75. Helassa, N., Podor, B., Fine, A. & Torok, K. Design and mechanistic insight into ultrafast calcium indicators for monitoring intracellular calcium dynamics. *Sci Rep* **6**, 38276 (2016).
76. Tokunaga, M., Imamoto, N. & Sakata-Sogawa, K. Highly inclined thin illumination enables clear single-molecule imaging in cells. *Nat Methods* **5**, 159-61 (2008).
77. Franke, C. & van de Linde, S. Reply to 'Impact of optical aberrations on axial position determination by photometry'. *Nat Methods* **15**, 990-992 (2018).
78. Culley, S. et al. Quantitative mapping and minimization of super-resolution optical imaging artifacts. *Nat Methods* **15**, 263-266 (2018).
79. Schindelin, J. et al. Fiji: an open-source platform for biological-image analysis. *Nat Methods* **9**, 676-82 (2012).
80. van de Linde, S. Single-molecule localization microscopy analysis with ImageJ. *J Phys D* **52**(2019).
81. Hermiston, M.L., Xu, Z. & Weiss, A. CD45: a critical regulator of signaling thresholds in immune cells. *Annu Rev Immunol* **21**, 107-37 (2003).
82. Jung, Y., Wen, L., Altman, A. & Ley, K. CD45 pre-exclusion from the tips of microvilli establishes a phosphatase-free zone for early TCR triggering. *bioRxiv* (2020).
83. Axelrod, D. Cell-substrate contacts illuminated by total internal reflection fluorescence. *J Cell Biol* **89**, 141-5 (1981).
84. Ghosh, S. et al. ERM-Dependent Assembly of T Cell Receptor Signaling and Co-stimulatory Molecules on Microvilli prior to Activation. *Cell Rep* **30**, 3434-3447 e6 (2020).
85. Blaskovic, S., Blanc, M. & van der Goot, F.G. What does S-palmitoylation do to membrane proteins? *FEBS J* **280**, 2766-74 (2013).
86. Jung, Y. et al. Three-dimensional localization of T-cell receptors in relation to microvilli using a combination of superresolution microscopies. *Proc Natl Acad Sci U S A* **113**, E5916-E5924 (2016).
87. Hashimoto-Tane, A. et al. Micro-adhesion rings surrounding TCR microclusters are essential for T cell activation. *J Exp Med* **213**, 1609-25 (2016).
88. Martin, B.R. & Cravatt, B.F. Large-scale profiling of protein palmitoylation in mammalian cells. *Nat Methods* **6**, 135-8 (2009).
89. Kornete, M., Marone, R. & Jeker, L.T. Highly Efficient and Versatile Plasmid-Based Gene Editing in Primary T Cells. *J Immunol* **200**, 2489-2501 (2018).
90. Wolter, S. et al. rapidSTORM: accurate, fast open-source software for localization microscopy. *Nat Methods* **9**, 1040-1041 (2012).
91. Geissbuehler, S. et al. Mapping molecular statistics with balanced super-resolution optical fluctuation imaging (bSOFI). *Optical Nanoscopy* 1, 4 (2012).
92. Chum, T. et al. The role of palmitoylation and transmembrane domain in sorting of transmembrane adaptor proteins. *J Cell Science* **129**, 95-107 (2016).
93. Edelstein, A.D. et al. Advanced methods of microscope control using muManager software. *J Biol Methods* **1**(2014).

69. Schermelleh, L. et al. Super-resolution microscopy demystified. *Nat Cell Biol* **21**, 72-84 (2019).
70. de Kruijff, B. & Cullis, P.R. The influence of poly(L-lysine) on phospholipid polymorphism. Evidence that electrostatic polypeptide-phospholipid interactions can modulate bilayer/non-bilayer transitions. *Biochim Biophys Acta* **601**, 235-40 (1980).
71. Pachmann, K. & Leibold, W. Insolubilization of protein antigens on polyacrylic plastic beads using poly-L-lysine. *J Immunol Methods* **12**, 81-9 (1976).
72. van de Linde, S. et al. Direct stochastic optical reconstruction microscopy with standard fluorescent probes. *Nat Protoc* **6**, 991-1009 (2011).
73. Klein, T. et al. Live-cell dSTORM with SNAP-tag fusion proteins. *Nat Methods* **8**, 7-9 (2011).
74. Santos, A.M. et al. Capturing resting T cells: the perils of PLL. *Nat Immunol* **19**, 203-205 (2018).
75. Helassa, N., Podor, B., Fine, A. & Torok, K. Design and mechanistic insight into ultrafast calcium indicators for monitoring intracellular calcium dynamics. *Sci Rep* **6**, 38276 (2016).
76. Tokunaga, M., Imamoto, N. & Sakata-Sogawa, K. Highly inclined thin illumination enables clear single-molecule imaging in cells. *Nat Methods* **5**, 159-61 (2008).
77. Franke, C. & van de Linde, S. Reply to 'Impact of optical aberrations on axial position determination by photometry'. *Nat Methods* **15**, 990-992 (2018).
78. Culley, S. et al. Quantitative mapping and minimization of super-resolution optical imaging artifacts. *Nat Methods* **15**, 263-266 (2018).
79. Schindelin, J. et al. Fiji: an open-source platform for biological-image analysis. *Nat Methods* **9**, 676-82 (2012).
80. van de Linde, S. Single-molecule localization microscopy analysis with ImageJ. *J Phys D* **52**(2019).
81. Hermiston, M.L., Xu, Z. & Weiss, A. CD45: a critical regulator of signaling thresholds in immune cells. *Annu Rev Immunol* **21**, 107-37 (2003).
82. Jung, Y., Wen, L., Altman, A. & Ley, K. CD45 pre-exclusion from the tips of microvilli establishes a phosphatase-free zone for early TCR triggering. *bioRxiv* (2020).
83. Axelrod, D. Cell-substrate contacts illuminated by total internal reflection fluorescence. *J Cell Biol* **89**, 141-5 (1981).
84. Ghosh, S. et al. ERM-Dependent Assembly of T Cell Receptor Signaling and Co-stimulatory Molecules on Microvilli prior to Activation. *Cell Rep* **30**, 3434-3447 e6 (2020).
85. Blaskovic, S., Blanc, M. & van der Goot, F.G. What does S-palmitoylation do to membrane proteins? *FEBS J* **280**, 2766-74 (2013).
86. Jung, Y. et al. Three-dimensional localization of T-cell receptors in relation to microvilli using a combination of superresolution microscopies. *Proc Natl Acad Sci U S A* **113**, E5916-E5924 (2016).
87. Hashimoto-Tane, A. et al. Micro-adhesion rings surrounding TCR microclusters are essential for T cell activation. *J Exp Med* **213**, 1609-25 (2016).
88. Martin, B.R. & Cravatt, B.F. Large-scale profiling of protein palmitoylation in mammalian cells. *Nat Methods* **6**, 135-8 (2009).
89. Kornete, M., Marone, R. & Jeker, L.T. Highly Efficient and Versatile Plasmid-Based Gene Editing in Primary T Cells. *J Immunol* **200**, 2489-2501 (2018).
90. Wolter, S. et al. rapidSTORM: accurate, fast open-source software for localization microscopy. *Nat Methods* **9**, 1040-1041 (2012).
91. Geissbuehler, S. et al. Mapping molecular statistics with balanced super-resolution optical fluctuation imaging (bSOFI). *Optical Nanoscopy* 1, 4 (2012).
92. Chum, T. et al. The role of palmitoylation and transmembrane domain in sorting of transmembrane adaptor proteins. *J Cell Science* **129**, 95-107 (2016).
93. Edelstein, A.D. et al. Advanced methods of microscope control using muManager software. *J Biol Methods* 1(2014).

Table 1. Overview of distribution parameters derived from axial receptor analysis. *N* is the number of cells or ROIs. z_w = z-distribution width, p-p = peak-to-peak distance, Δ_{FWHM} = width difference; μ is the mean and σ is the standard deviation of the histogram, range = $\mu \pm$ FWHM/2 with FWHM = 2.355σ; τ is the mean of the exponential distribution. The raw data are shown in Fig. 5 and Supplementary Fig. 8.

		WT	**CS1**	**CD45**
N cells		24	18	13
N ROIs		846	1044	305
z_w	μ_1 (nm)	120	141	118
	σ_1 (nm)	25	27	20
	range$_1$ (nm)	90-150	110-173	94-145
	μ_2 (nm)	-	247	263
	σ_2 (nm)	-	83	117
	range$_2$ (nm)	-	149-345	126-400
p-p	τ (nm)	23	36	121
Δ_{FWHM}	μ (nm)	57	88	63
	σ (nm)	15	28	22
	range (nm)	40-75	55-120	37-89

FIGURE CAPTIONS

Figure 1. Coating of coverslips with glycine better preserves cell surface morphology and resting state of immobilized T cells. a-b) Schematic illustration of T cell landing on PLL- (left panels) and glycine-coated coverslips (right panels). The arrows indicate forces influencing the cell on the coated coverslip. The g-force is the sole force affecting T cells on glycine. T cells on PLL are further stretched due to electrostatic interactions of the surface molecules with PLL. The blue stripes represent glass coverslip, the light blue stripes above represent the glycine layer (not to scale). **c-d)** Live-cell TIRF microscopy of CD4-GFP in T cells landing on PLL-coated (c) or glycine-coated coverslips (d) measured at 37°C (see also Supplementary Movies 1 and 2). Blue arrowheads indicate areas of rapid flattening of the cell surface and random distribution of CD4, as indicated by line-profiles in Supplementary Fig. S1. Red arrowheads indicate areas with heterogeneous distribution of CD4 on the cell surface as indicated by line-profiles in Supplementary Fig. S1. Selected time points for the representative cells are shown. In total, 14 cells on glycine-coated and 10 cells on PLL-coated coverslips were analyzed. **e)** Calcium response induced by the interaction of Jurkat T cells with coverslips coated with stimulating antibody (anti-CD3ε; OKT3), PLL or glycine as indicated by the changes in ultrafast genetically encoded calcium sensor GCaMP6f_u fluorescence over 5 min (black bars) and 10 min (grey bars) from the maximal stimulation of cells. Relative calcium response equal 1 indicates no stimulation. Higher values indicate stimulation of cells (see **Methods** and Supplementary Fig. S3 for more details). **f)** Viability of Jurkat T cells interacting with coverslips coated with PLL- (black bars) or glycine-coated (grey bars) coverslips. Dying cells were defined as a fraction of 7-aminoactinomycin-positive cells within the imaged area using wide-field microscopy (see **Methods** for more details). Values at 1 min represent the starting point for the analysis – a minimal period required for cells to land at the optical surface.

Figure 2. Principle of 3D super-resolution biplane imaging using dTRABI. a) Overview of the experimental setup applied to perform 3D dTRABI imaging of T cells. HILO illumination of the sample (blue beam; only shown in enlarged box) triggers fluorescence emission (orange), which is split by a 50/50 non-polarizing beamsplitter (50/50 BS) to acquire biplane images on two separate EM-CCD cameras. The respective imaging lenses are shifted along the optical axis to induce a relative defocus of the image detection on synchronized cameras. Spots, apparent in both detection planes, are fitted by a Gaussian with identically set FWHM. **b)** Using a piezo stage, the focal plane was linearly moved through the sample plane while imaging a single-molecule surface under dSTORM conditions. Hereby, both cameras were synchronized. Fitting the raw PSFs by independent Gaussians with invariable FWHM yielded axially dependent single-molecule intensity curves (upper panel). The relative change of position of the imaging lens in the reflection path is mirrored by the relative shift of the respective intensity curve (indicated by circles). Data points were spline interpolated to guide the eye (solid lines). An axially precise calibration function γ is derived directly from the raw intensities ($I_{Camera1}$, $I_{Camera2}$) of corresponding localizations from both cameras as $\gamma(z) = (I_{Camera2} - I_{Camera1})(I_{Camera2} + I_{Camera1})^{-1}$. The running median of the raw data

image of non-palmitoylatable CD4 CS1 mutant at the surface of T cell immobilized on a glycine-coated coverslip. **d**) The axial distribution of CD4 CS1 localizations of the 4 µm^2 ROI of the cell in c). **e-g)** Quantitative analysis of the receptor axial (z-axis) distribution on the surface of T cells. Receptors were analyzed by using a bi-Gaussian fit to the axial distribution of localizations for each ROI as in b, d and i (see Supplementary Fig. S6 for more examples) and the FWHM range of the two Gaussian functions represent the z-distribution width (z_W) as depicted in **e**. Black circles in **e** represent the axial distribution of receptor localizations for a selected ROI, black line the bi-Gaussian fit, which is the sum of two Gaussians as depicted in red and blue, dashed lines in gray depict z_W and lines in light grey depict mean values of the Gaussian distributions. The graphs in **f** and **g** represent histograms of z_W obtained from 21 CD4 WT cells with 846 ROIs (black), 18 CD4 CS1 cells with 1044 ROIs (green) and 13 CD45 WT cells with 305 ROIs (magenta). The histograms in f) and g) show relative and absolute occurrence, respectively. Data points in b), d), f) and i) were spline interpolated to guide the eye. **h**) Representative 3D dTRABI image of CD45 at the surface of T cell immobilized on a glycine-coated coverslip. Color-bars in the upper right corner a), c) and h) indicate the axial position of the localizations in the image. **i**) The axial distribution of CD45 localizations of the 4 µm^2 ROI of the cell in h). Scale bars in a) and c) and h), 5 µm.

Figure 6. Areas on the surface of resting T cells lacking CD45. **a**) Three-dimensional dTRABI image of CD45 on T cell. **b**) Magnified ROI as in a) with indicated areas lacking CD45 localizations (yellow arrowheads). **c)** 2D SOFI image of CD45 on T cell immobilized on a glycine-coated coverslip. CD45 was labelled using Alexa Fluor-647 conjugated MEM-28 antibody. Yellow arrowheads indicate cell surface areas lacking CD45 signal. Scale bars, a) 5 µm, b) 1 µm and c) 5 µm.

Figure 7. Nanoscopic segregation of CD4 WT and CD45 on the surface of resting T cells. a) Representative two-dimensional image of T cell surface sequentially analyzed for CD4 WT (green) and CD45 (magenta) by SMLM. CD4 was visualized as mEos2 fusion protein (PALM) after transient transfection of cells, and the surface CD45 was labelled using Alexa Fluor-647 conjugated MEM-28 antibody (dSTORM). ROIs 1-2 were zoomed to indicate details of proteins' distribution (right side). **b**) Intensity line-profiles were measured along the transparent grey regions indicated in ROIs 1-2 (as in a). Green line represents CD4 WT and magenta CD45 signals. **c**) Schematic illustration of microvillus with indicated structural segments: tip, shaft and the basis. The two panels below indicate the organization of CD4 and CD45 on the protrusions in cells expressing native CD4 (WT; middle panel) or its non-palmitoylatable variant (CS1; lower panel) CD4 as indicated by the nanoscopy. **d)** Two-dimensional SMLM image of a selected T cell captured during its association with the optical surface which was sequentially analyzed for CD4 WT and CD45 (as in a). The accumulation of CD4 WT on the tips of large membrane protrusions was observed in 10 out of 32 imaged T cells. ROIs 3-4 were zoomed to show the details of membrane protrusions with accumulated CD4 WT on their tips (right side). **e**) Intensity line-profiles were measured along the

transparent grey regions indicated in ROIs 3-4. The arrows indicate the onset of line-profiles. Scale bars, 5 µm. Images from three independent experiments are shown (n=32).

transparent grey regions indicated in ROIs 3-4. The arrows indicate the onset of line-profiles. Scale bars, 5 μm. Images from three independent experiments are shown (n=32).

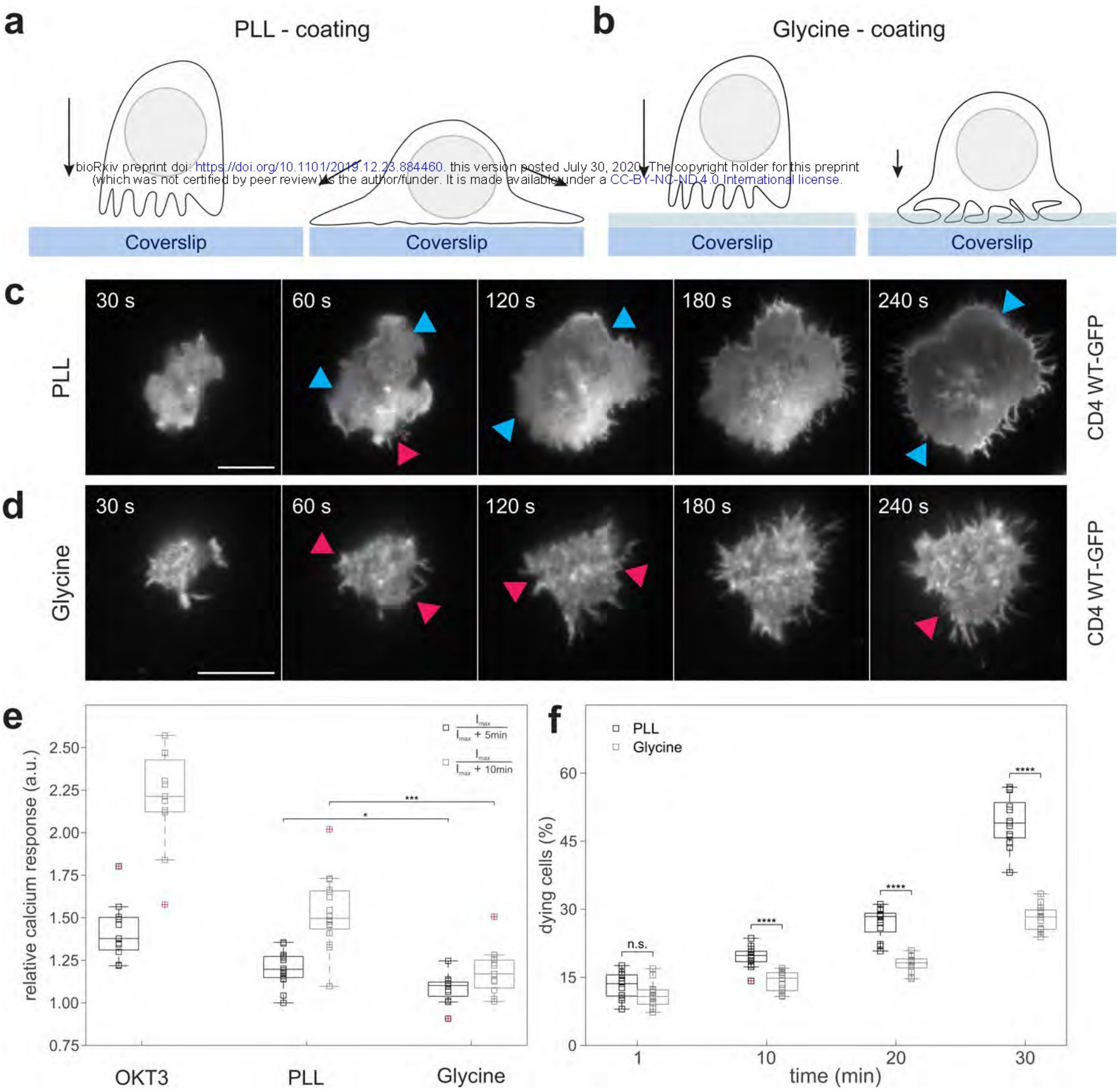

Franke et al. 2020, Fig. 1

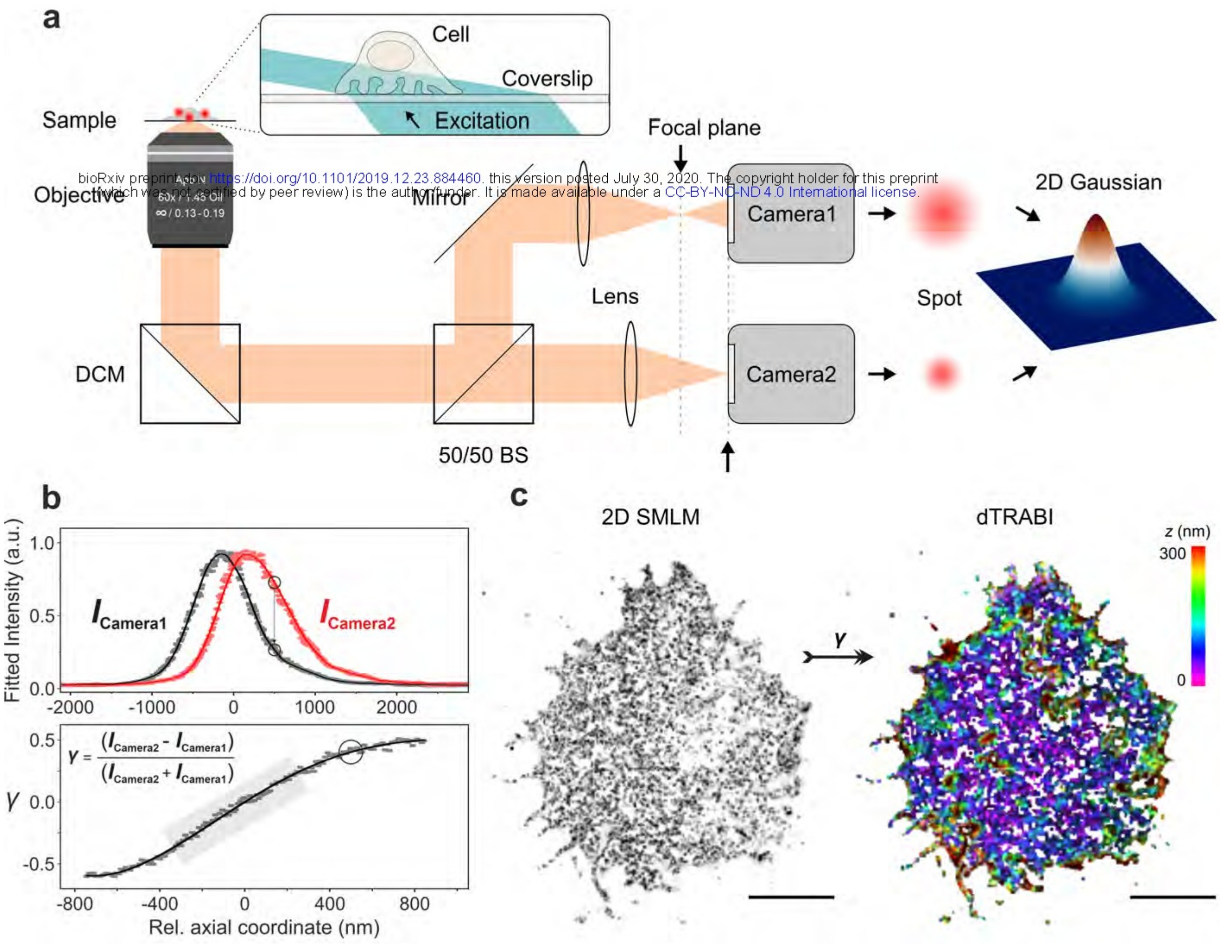

Franke et al. 2020, Fig. 2

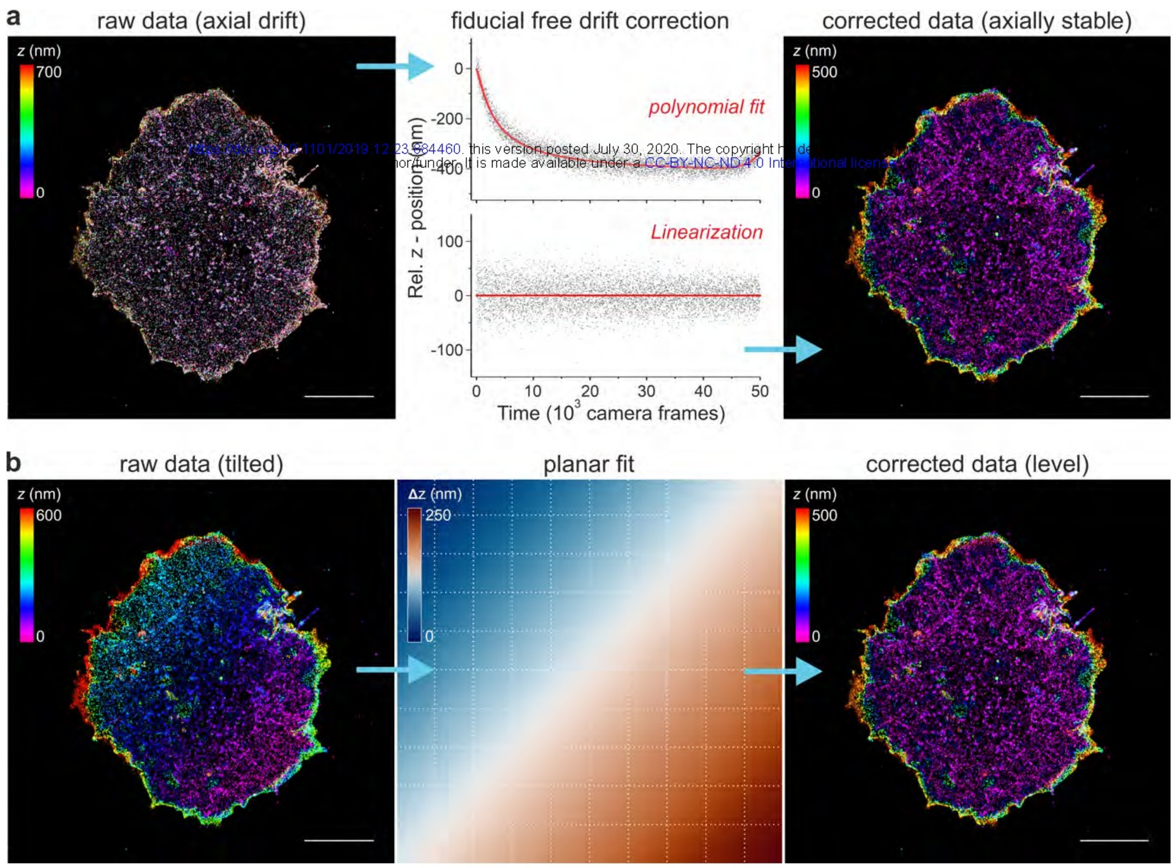

Franke et al. 2020, Fig. 3

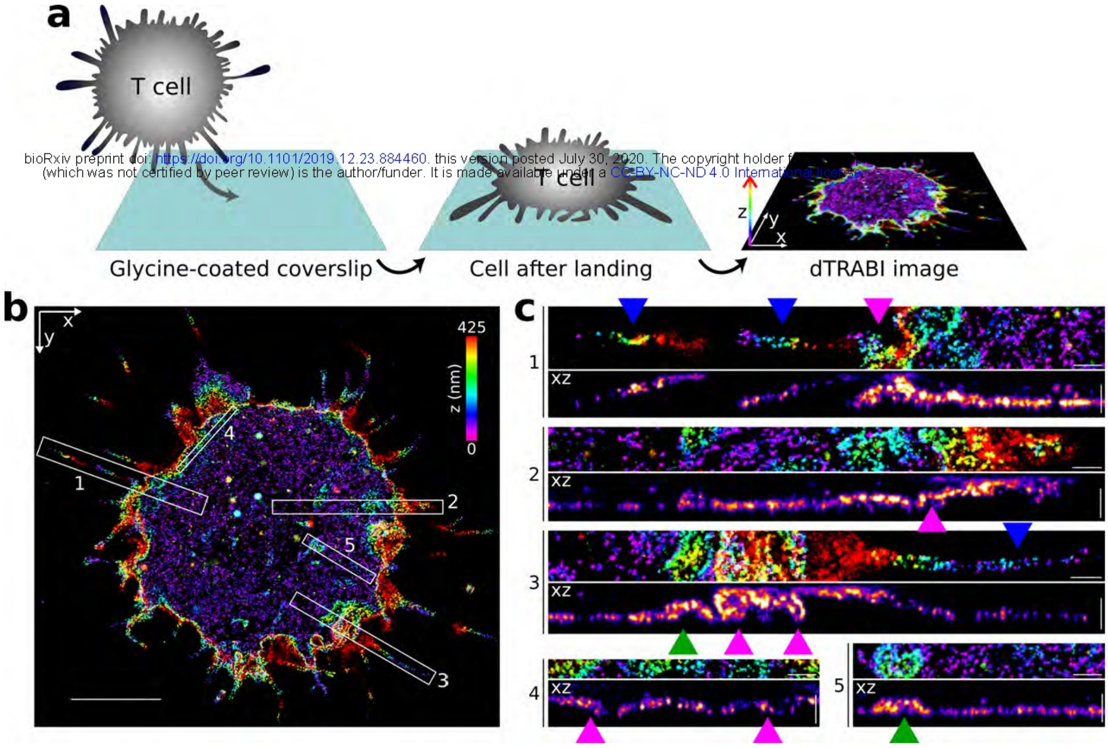

Franke et al. 2020, Fig. 4

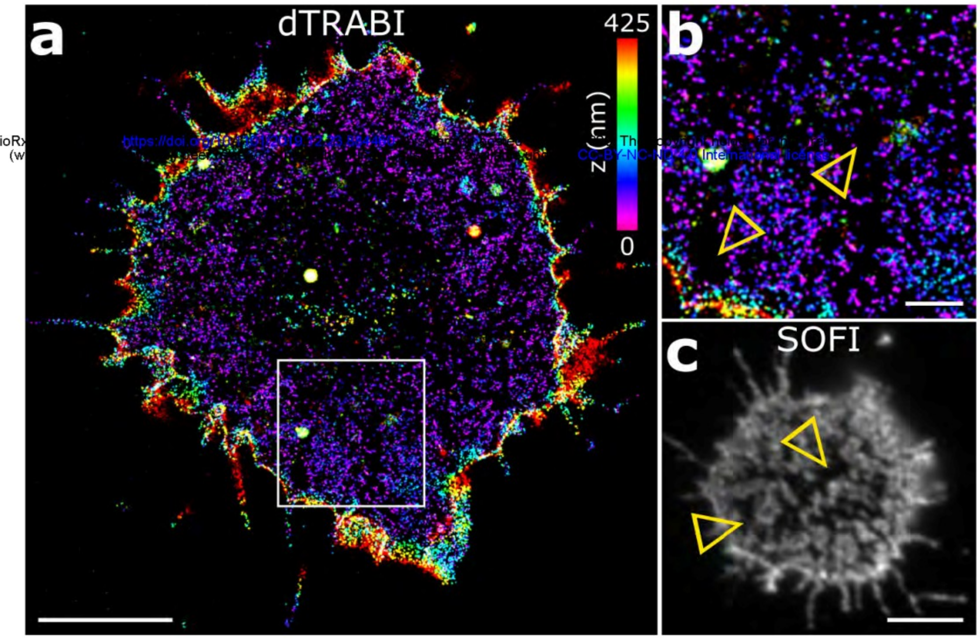

Franke et al. 2020, Fig. 6

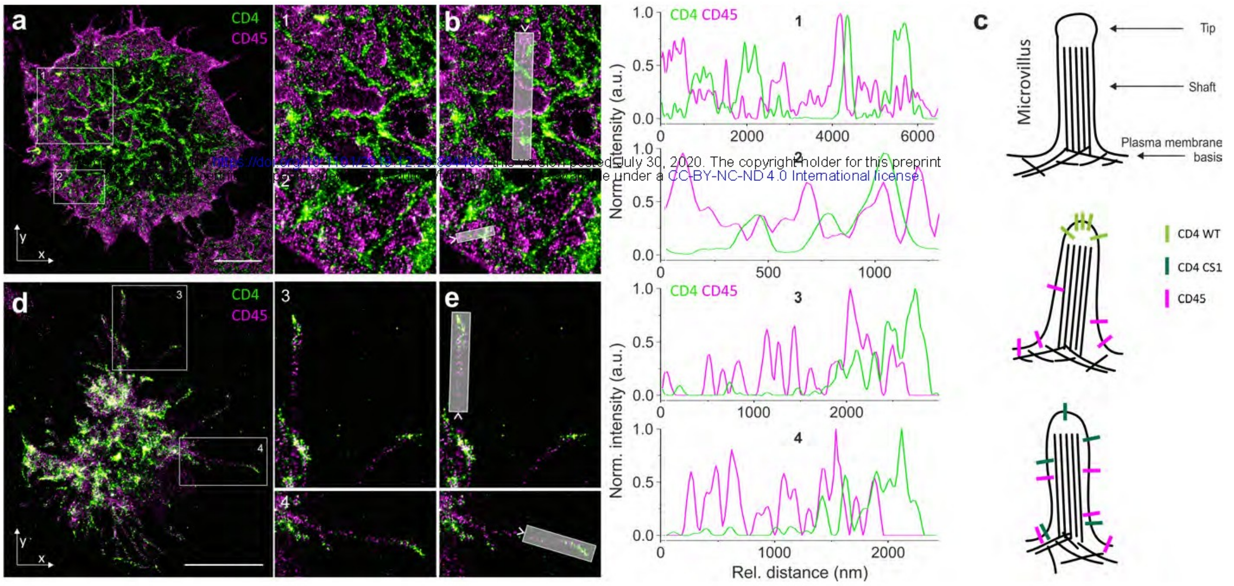

Franke et al. 2020, Fig. 7

Supplementary Information

For the manuscript: Franke et al. Unraveling nanotopography of cell surface receptors

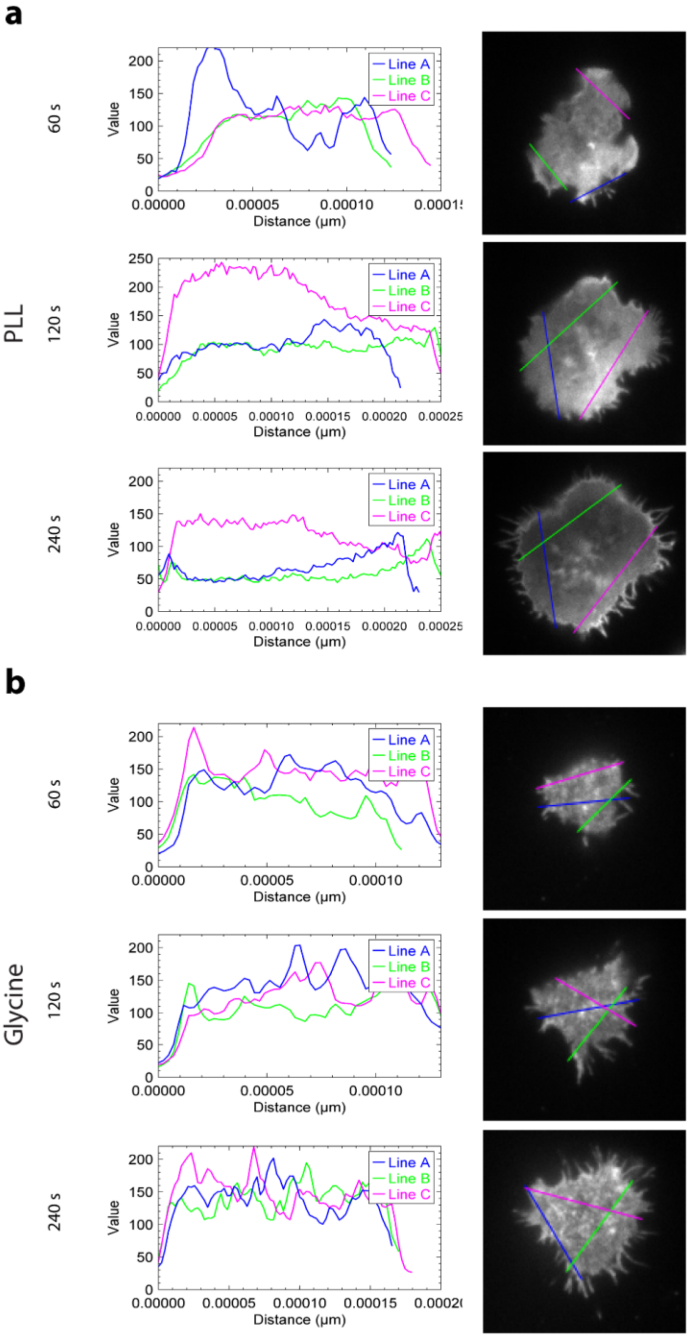

Supplementary Figure S1. The impact of coverslip coating on cell surface morphology. Two-dimensional images of T cell-coverslip contact sections with indicated line selections (right panels) and the corresponding intensity line profiles (left panels). Cells were transfected with CD4-GFP, transferred to the chambers with PLL- (**a**) or glycine-coated (**b**) coverslips and living cells were imaged using TIRF microscopy at 1 fps. Snapshots acquired 60, 120 and 240 s after the first contact of the cell with the coverslip are presented.

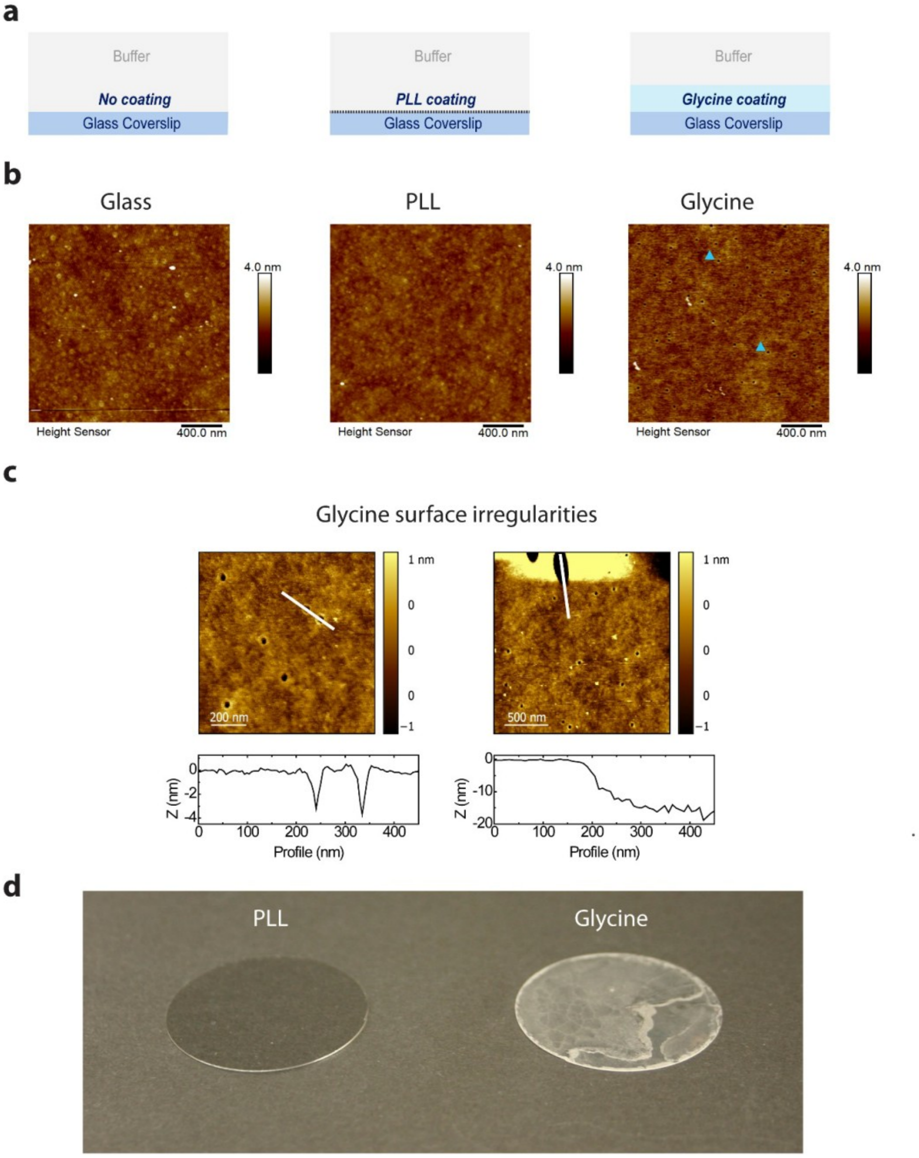

Supplementary Figure S2. Glycine forms a narrow, gel-like structure on glass coverslips. a) Schematic illustration of the coverslip coatings tested using atomic force microscopy (AFM). **b)** Comparison of the AFM topography images of the coverslip surface without further coating (left panel) and after coating with poly-*L*-Lysine (PLL; middle panel) or glycine (right panel). Blue arrowheads in the right-hand panel indicate two examples of small topography features (holes), which populate the surface of glycine-coated coverslip. **c)** Magnified AFM topography images on a glycine-coated coverslip (upper panels) with respective height profiles (lower panels) taken in the area with the smaller, almost perfectly circular holes (diameter ~30 nm, depth ~3–4 nm on the average; left panels), and in the area with a larger hole with the diameter >200 nm and depth >20 nm (right panels). **d)** Glycine coating of glass coverslips (right) forms a white precipitate after a brief drying, indicating a hydrogel formation. No such precipitate can be observed on the PLL-coated coverslips (left), which do not differ from the uncoated coverslips (not shown).

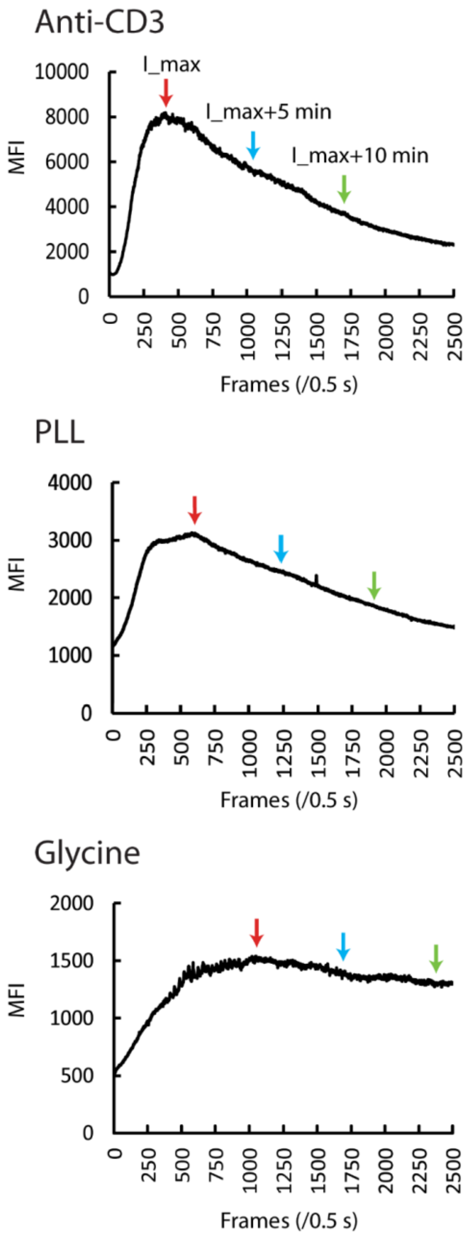

Supplementary Figure S3. Calcium response measurements on coverslips functionalized to stimulate (OKT3 antibody) or immobilize T cells (PLL and glycine). Representative time profiles of mean fluorescence intensity measured in T cells transfected with calcium sensor (GCaMP6f_u) using TIRF microscopy (2 fps) and illumination with 488 nm laser line. 11 cells were imaged on OKT3-antibody (upper panel), 16 cells on PLL- (middle panel) and 12 cells on glycine-coated (lower panel) coverslips. Cell footprints were manually selected at the time of maximum signal detection. Red arrows indicate maximum mean intensity (I_max), blue the signal detected 5 minutes later (I_max+5 min) and green the signal detected after another 5 minutes (I_max+10 min). The calcium response of cells interacting with the functionalized surface was calculated as I_max/I_max+5min and I_max/I_max+10min as summarized in Fig.1e.

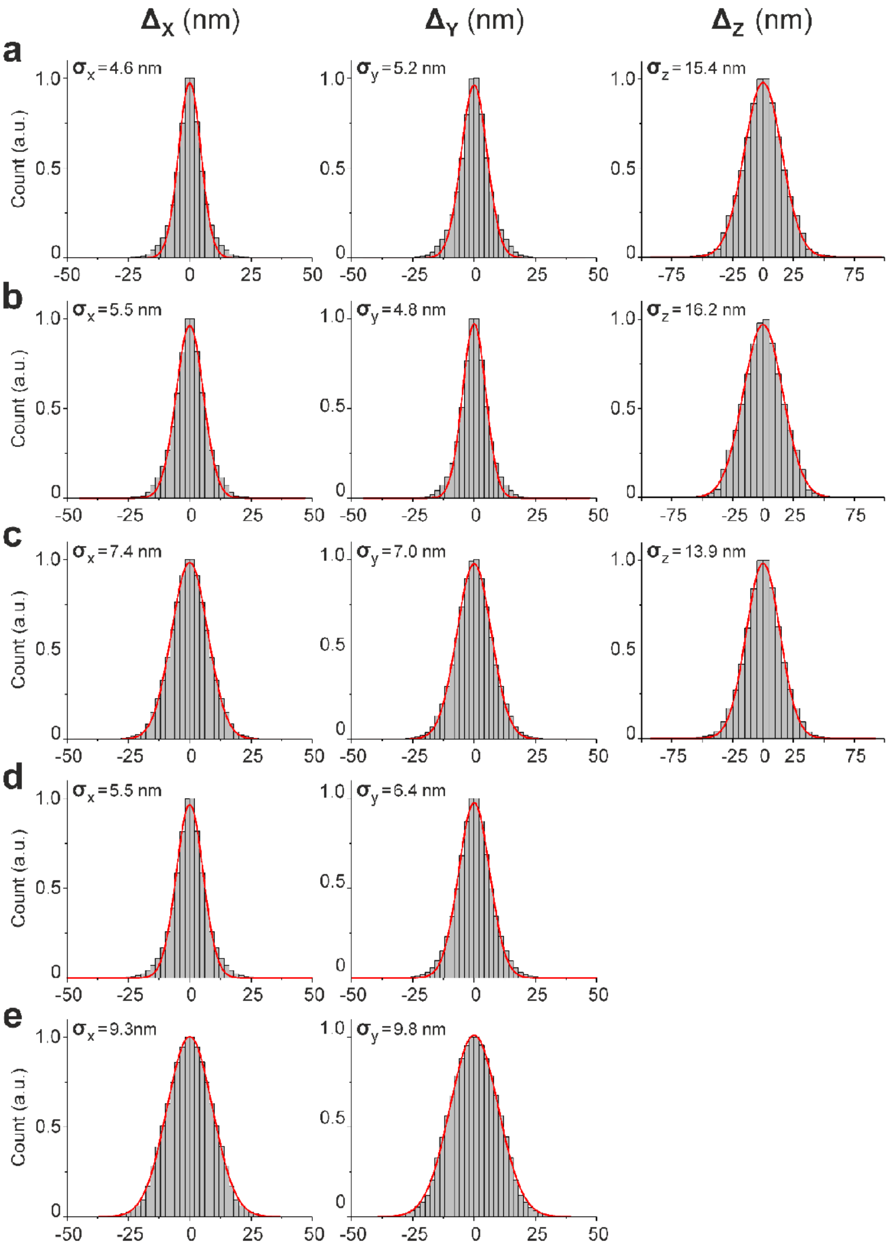

Supplementary Figure S4. Localization precision. Normalized histograms of spatio-temporal nearest neighbour tracks, constituting the three-dimensional localization precision of the dTRABI and two-color SMLM measurements (see **Methods**). x-, y- and z- were individually determined and are stated as the standard deviation of the respective distribution as numerical value **σ**. Sample and imaging modalities: **a)** dTRABI of CD4 WT (Alexa Fluor 647) **b)** dTRABI of CD4 CS1 (Alexa Fluor 647) **c)** dTRABI of CD45 (Alexa Fluor 647) **d)** two-dimensional *d*STORM of CD45 (Alexa Fluor 647) **e)** two-dimensional PALM of CD45 (mEos2).

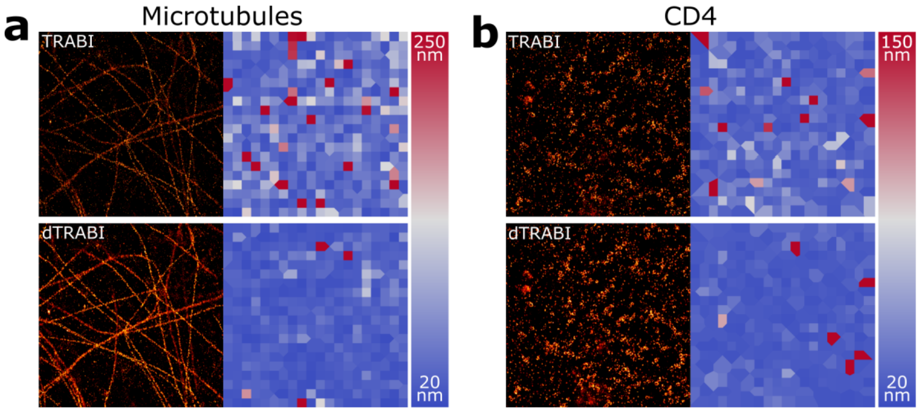

c

FRC resolution (nm)	**Microtubules**		**CD4**	
	TRABI	**dTRABI**	**TRABI**	**dTRABI**
Median	**49.1**	**33.7**	**30.9**	**26.9**
MAD	15.0	5.5	5.3	2.2
Mean	78.6	40.1	42.4	32.4
SD	117.5	35.5	50.0	30.6
Max	1139.5	430.3	490.3	340.9
Min	21.4	21.3	22.9	22.9

Supplementary Figure S5. Resolution improvement of dTRABI compared to TRABI determined by Fourier Ring Correlation (FRC). **a**) Representative three-dimensional dSTORM images of microtubules (data from ref.[1]). The three-dimensional localization sets were derived according to either the standard TRABI-Biplane algorithm (TRABI, *top*) or the new dTRABI approach (*bottom*). The according FRC maps, visualizing the local FRC-resolution, are depicted on the right. We selected the median FRC resolution of the images as the most robust resolution metric, which was derived to 49 nm (TRABI) and 34 nm (dTRABI). dTRABi improves the structural resolution in a medium density sample by 30 percent. **b**) Representative three-dimensional dSTORM images of CD4 (data reanalyzed from **Fig. 5a**). The three-dimensional localization sets were derived according to either the standard TRABI-Biplane algorithm (TRABI, *top*) or the dTRABI approach (*bottom*). The according FRC maps are depicted on the right. The median FRC resolution of the images was derived to 31 nm (TRABI) and 27 nm (dTRABI). dTRABI improves the structural resolution in a low-density sample by 13 percent. FRC analysis was performed with NanoJ-Squirrel[2], additional relevant FRC metrics are listed in **c**). Scale bars, 1 µm.

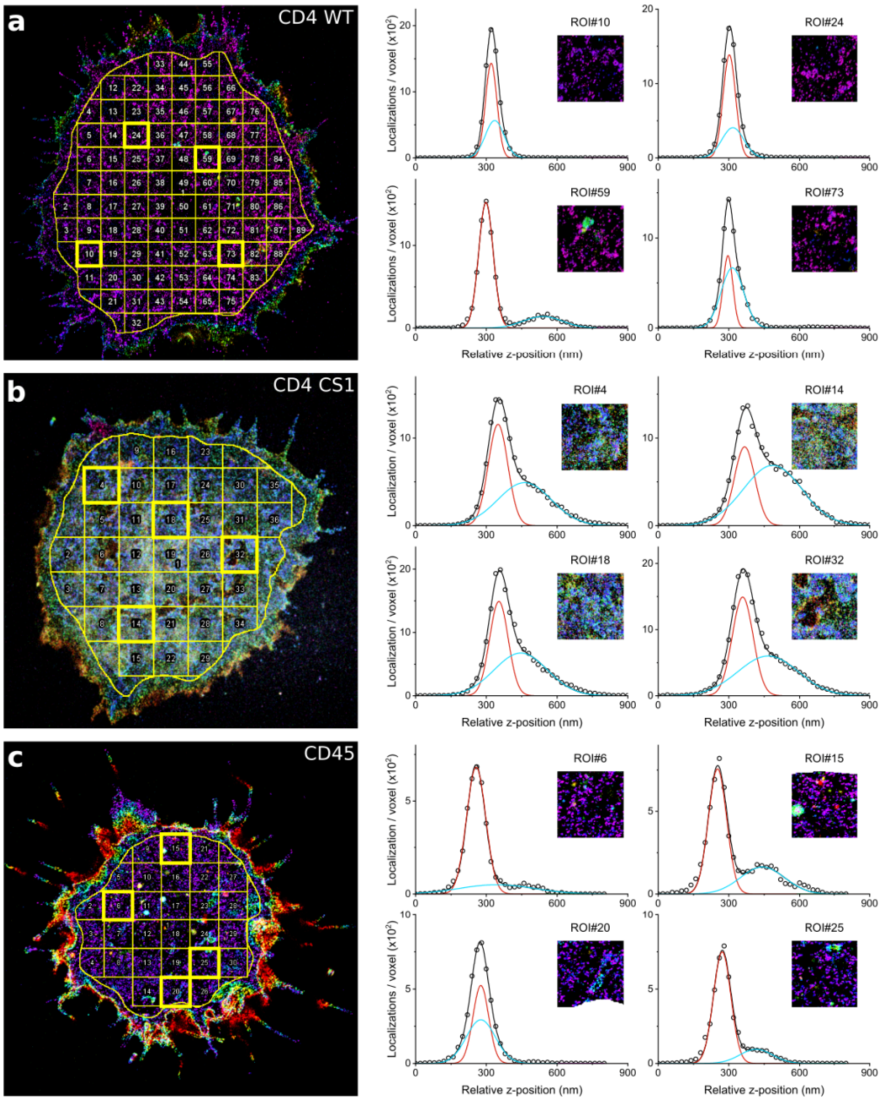

Supplementary Figure S6. Segmentation of cells. For quantitative axial analysis of surface receptors, the interior of each cell footprint was first manually selected (ROI#1) to avoid the impact of cell edges. Afterwards, the area was further segmented into squared 2 µm × 2 µm ROIs. In border areas, ROIs were kept if the area was ≥75% of 4 µm² (see **Methods**). **a**) Segmentation and quantitative axial analysis for CD4 WT. *Left*: The cell as shown in Fig. 5a segmented, *right*: example ROIs and Gaussian fitting for quantitative analysis of receptor z-distribution as in Fig.5e-g. **b**) Segmentation and quantitative axial analysis for CD4 CS1. *Left*: The cell as shown in Fig. 5c segmented, *right*: example ROIs and Gaussian fitting for quantitative analysis of receptor z-distribution. **c**) Segmentation and quantitative axial analysis for CD45. *Left*: The cell as shown in Fig. 4b segmented, *right*: example ROIs and Gaussian fitting for quantitative analysis of receptor z-distribution. Selected ROIs are depicted with a bold frame in the whole-cell images on the left-hand side. In graphs with the axial receptor distribution, black circles represent raw data, black line the bi-Gaussian fit, which is the sum of two Gaussians as depicted in red and blue.

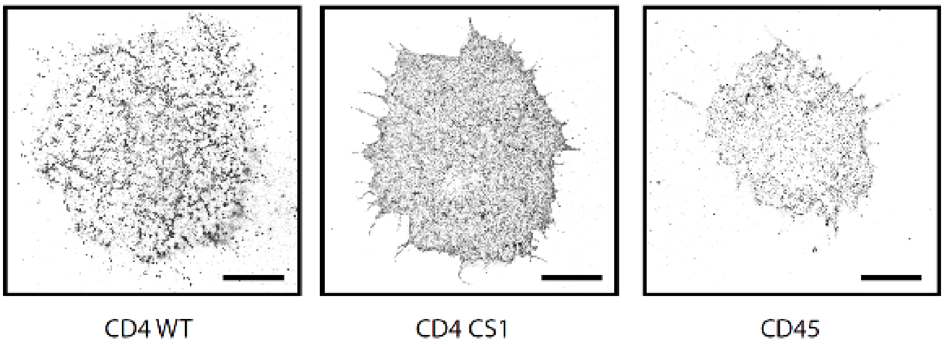

Supplementary Figure S7. Two-dimensional SMLM of tested T cell receptors immobilized on glycine-coated coverslips. dSTORM images of CD4 WT (left), CD4 CS1 (middle) and CD45 (right) on the surface of unstimulated T cells. The two-dimensional images indicate different nanoscopic organization of the receptors but cannot be analyzed quantitatively due to a three-dimensional character of the T cell surface. Scale bars, 5 µm.

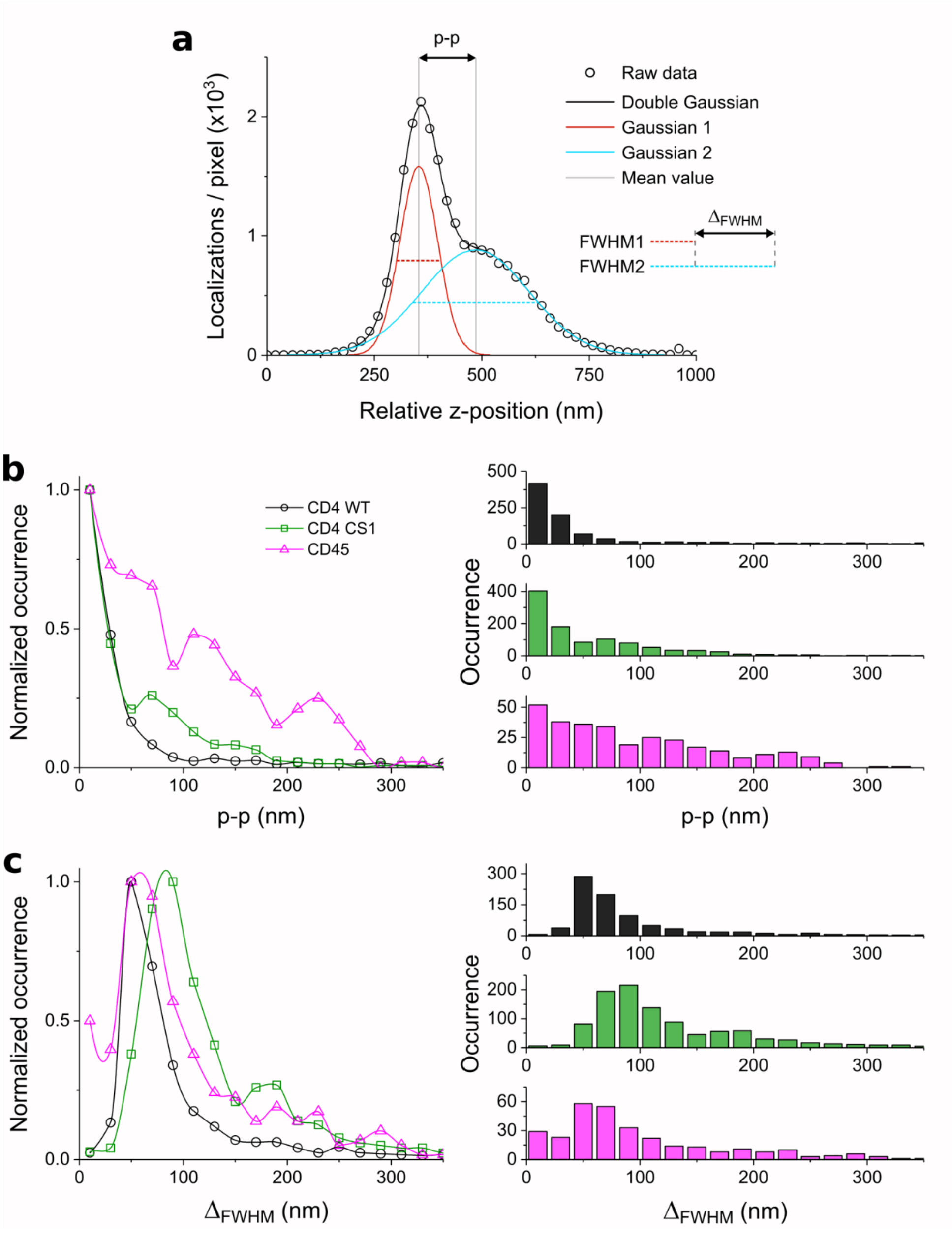

Supplementary Figure S8. Quantitative analysis of axial receptor distribution. a) The principle of data analysis using a bi-Gaussian fit to derive the quantitative parameters peak-to-peak distance (p-p) and width difference (Δ_{FWHM}). **b**) p-p, which represents the absolute value of the difference the mean values as indicated in a) (p-p = mean2-mean1). **c**) Δ_{FWHM}, which represents the absolute value of the difference between the FWHM values of the two Gaussians as indicated in a) (Δ_{FWHM} = FWHM2-FWHM1). The normalized distributions are plotted on the left and histograms with absolute values on the right-hand side. In b and c, black represents data for CD4 WT, green for CD4 CS and magenta for CD45. All data points were spline interpolated to guide the eye. For CD4 WT 21 cells, CD4 CS1 18 cells and CD45 13 cells were analyzed.

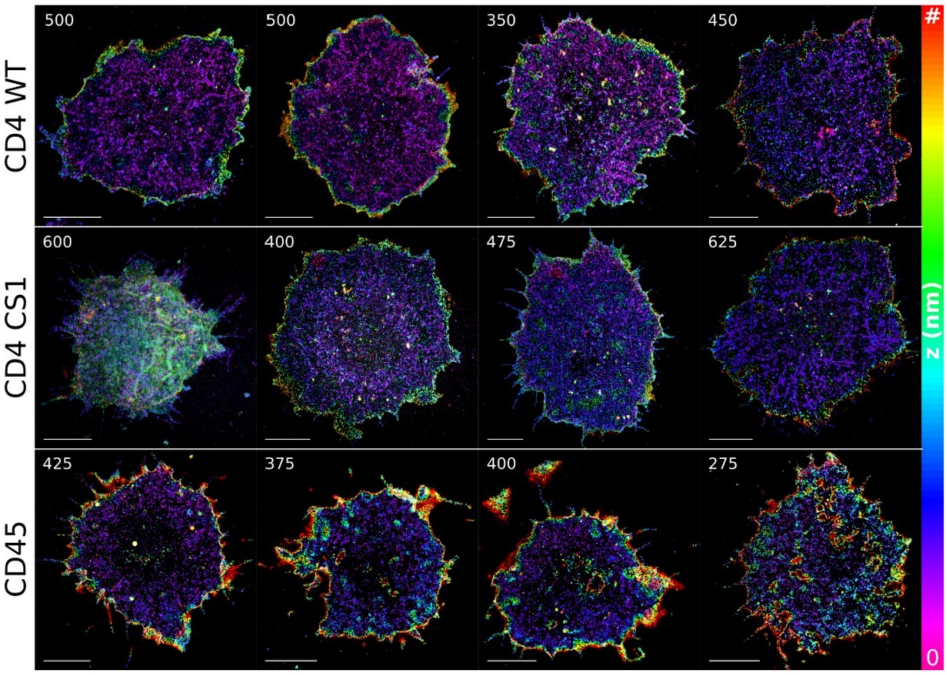

Supplementary Figure S9. Exemplary selection of dTRABI images for CD4 WT, CD4 CS1 and CD45. The maximum z-value is depicted for each cell (top left corner), e.g. for the cell in the upper right corner the z-range is from 0 to 450 nm. Marker '#' in the color-bar means the maximum z-value for each cell. In total, 21, 18 and 13 cells were analyzed for CD4 WT, CD4 CS1 and CD45, respectively. Scale bars, 5 µm.

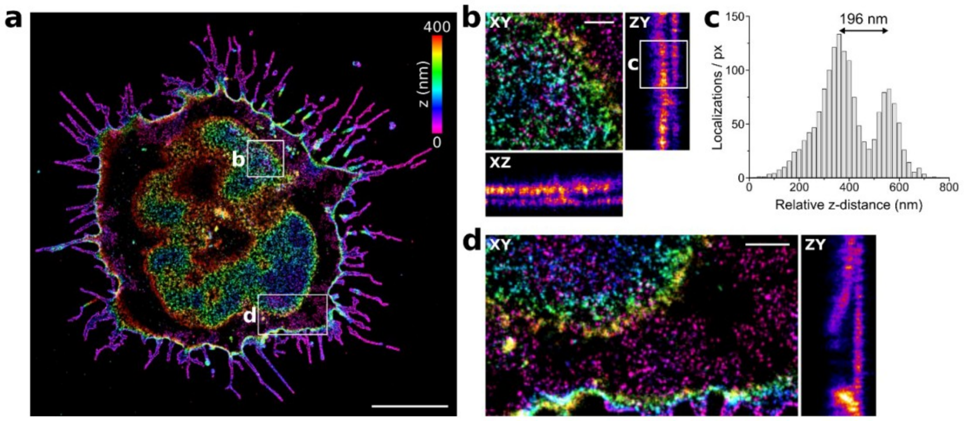

Supplementary Figure S10. Cell surface receptor nanotopography on a dying cell with extensive three-dimensional deformations visualized by three-dimensional dTRABI imaging. a) Three-dimensional dTRABI image of CD4 with selected ROIs exhibiting broad z-distribution of receptor localizations. **b)** Magnified x-y, x-z and z-y projections of the ROI indicated in a). **c)** The axial distribution of localizations as depicted in the y-z plot in b). **d)** Magnified x-y and z-y projections of the ROI indicated in a). Scale bars, a) 5 µm (x, y), b, d) 500 nm (x, y, z).

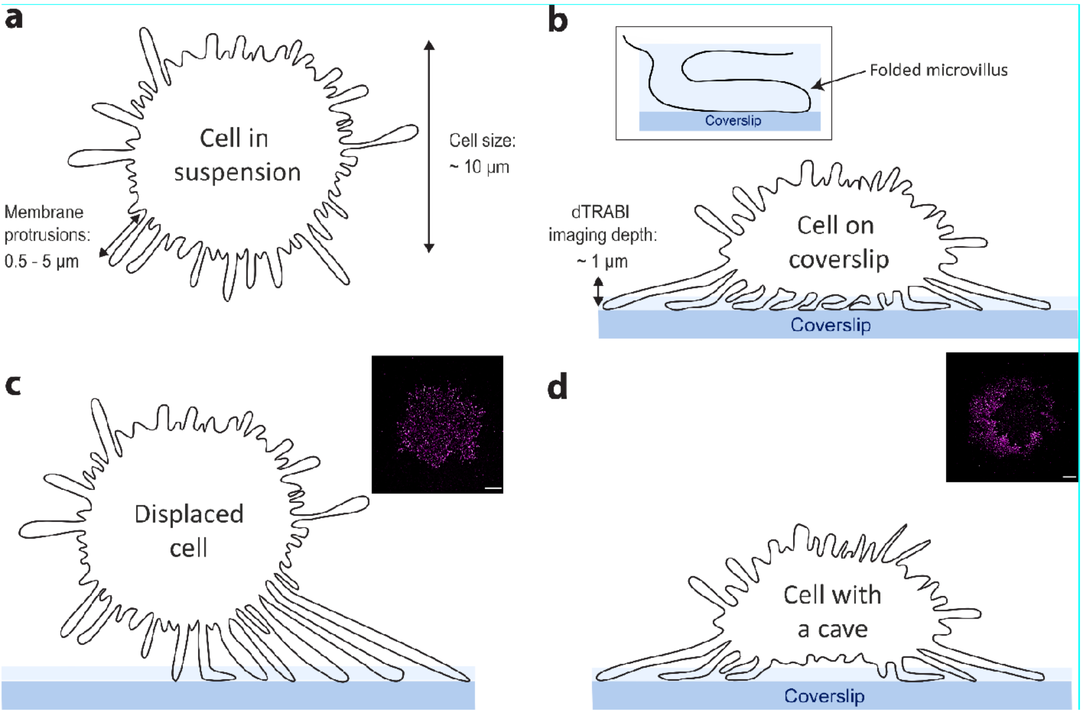

Supplementary Figure S11. T-cell surface morphology on glycine-coated coverslips. a) Schematic illustration of a T cell in suspension. The cell is covered with numerous membrane protrusions of different sizes. The size of Jurkat T cells is, on average, 10 µm in diameter, the protrusions, even though a majority are small (0.5–2 µm length), can extend up to 5 µm from the cell body. **b)** After landing on a glycine-coated coverslip, membrane protrusions of T cells fold under the cell body but are not rapidly removed as on PLL. **c-d)** With the axial penetration depth of dTRABI being ~1 µm, we were unable to detect receptors at the plasma membrane basis of T cells exhibiting displacement of the cell body from the contact site (c) or those with the cavity formed between the cell body and the coated coverslip. The footprints of such cells show discontinuous labeling or a hole in the middle of the image (see the inserts). The blue stripes represent glass coverslip, the light blue stripes above, the glycine layer (not to scale).

Supplementary Movies

Supplementary Movie 1 **Live cell TIRF microscopy of CD4-GFP in T cells landing on PLL**-coated measured at 37°C. Representative cell as in Fig. 1c shown. Acquisition rate: 1 fps; video fame rate: 15 fps; scale bar: 5 µm. The image sequence was corrected for the photobleaching; the brightness and contrast were leveled using plugins of Fiji software.

Supplementary Movie 2. Live cell TIRF microscopy of CD4-GFP in T cells landing on glycine-coated coverslips measured at 37°C. Representative cell as in Fig. 1d shown. Acquisition rate: 1 fps; video fame rate: 15 fps; scale bar: 5 µm. The image sequence was corrected for the photobleaching; the brightness and contrast were leveled using plugins of ImageJ/Fiji software.

References

1. Franke, C., Sauer, M. & van de Linde, S. Photometry unlocks 3D information from 2D localization microscopy data. *Nat Methods* **14**, 41-44 (2017).

2. Culley, S. *et al.* Quantitative mapping and minimization of super-resolution optical imaging artifacts. *Nat Methods* **15**, 263-266 (2018).

Publication 3:

Daniela Glatzová, Harsha Mavila, Maria Chiara Saija, **Tomáš Chum**, Lukasz Cwiklik,
Tomáš Brdička and Marek Cebecauer

The role of prolines and glycine in transmembrane domain of LAT

(preprint). bioRxiv, Cell Biology, 2020

https://doi.org/10.1101/2020.08.10.244251

The role of prolines and glycine in transmembrane domain of LAT

Daniela Glatzová[1,2,3], Harsha Mavila[1], Maria Chiara Saija[1], Tomáš Chum[1], Lukasz Cwiklik[1], Tomáš Brdička[2] and Marek Cebecauer[1]

[1]Department of Biophysical Chemistry, J. Heyrovsky Institute of Physical Chemistry, Czech Academy of Sciences, Dolejskova 3, 18223 Prague, Czech Republic.
[2]Laboratory of Leukocyte Signaling, Institute of Molecule Genetics, Czech Academy of Sciences, Videnska 1083, Prague, Czech Republic.
[3]Faculty of Science, Charles University, Czech Republic

ABSTRACT

LAT is a critical regulator of T cell development and function. It organises signalling events at the plasma membrane. However, the mechanism, which controls LAT localisation at the plasma membrane is not fully understood. Here, we studied the impact of helix-breaking amino acids, two prolines and one glycine, in the transmembrane segment on localisation and function of LAT. Using *in silico* analysis, confocal and superresolution imaging and flow cytometry we demonstrate that central proline residue destabilises transmembrane helix by inducing a kink. The helical structure and dynamics is further regulated by glycine and another proline residue in the luminal part of LAT transmembrane domain. Replacement of these residues with aliphatic amino acids reduces LAT dependence on palmitoylation for sorting to the plasma membrane. Surface expression of these mutants is not sufficient to recover full function of non-palmitoylated LAT in stimulated T cells. These data indicate that geometry and dynamics of LAT transmembrane segment regulate its localisation and function in immune cells.

INTRODUCTION

Function of proteins (e.g., enzymes or signal transducers) is defined by their structure, but also localisation within a cell or an organism. Amino acid sequence, small molecule co-factors and interacting partners are primary determinants of the structure. However, features defining protein localisation are less well understood. The process defining protein localisation is called sorting. Short motifs within a primary sequence were found to firmly control sorting of proteins to some organelles, e.g., the ER retainment (KDEL motif), the ER exit (DxE and YxxΦ coupled motifs) or nucleus (NES/NLS motifs) [1, 2, 3]. Trafficking of proteins to the plasma membrane appears to be controlled by several unrelated determinants. Post-translational modifications, such as glycosylation and palmitoylation facilitate anterograde membrane transport of proteins to the cell surface [4, 5, 6]. On the contrary, ubiquitination regulates retrograde protein transport from the surface towards the cell interior [7]. However, the primary determinant of the plasma membrane sorting, at least for single-spanning membrane proteins, is the length and amino acid composition of the transmembrane domain (TMD) [6, 8]. A comprehensive study demonstrated that, in vertebrates, proteins with TMDs of 22 residues or longer localise to the plasma membrane [9]. Those with shorter TMDs remain in the Golgi apparatus or the ER. The voluminous amino acids (Phe, Tyr, Trp) were found to accumulate in the cytosolic part of the TMD of the plasma membrane proteins. The position of other amino acids is also non-random [9, 10]. These data indicate that physico-chemical properties of TMDs strongly influence trafficking of proteins in cells.

In vertebrates, the structure of TMD is almost exclusively formed by an α-helix. The hydrophobic core is largely composed of aliphatic (Leu, Val, Ala, Ile) and aromatic amino acids (Phe, Tyr, Trp). Weakly polar amino acids (Ser, Thr, Met, Cys) are also common components of TMDs [10]. Cysteine residues due to their propensity to form disulphide bridges in the oxidative environment, can force the protein to dimerise. Their presence is thus reduced in the exoplasmic part of the TMDs. Moreover, cysteine residues at the cytosolic end of the TMD reveal palmitoylation sites [11]. Positively charged amino acids (Lys, Arg, His) often define the cytosolic end of TMDs (*positive-inside rule*; ref. [12]). In addition, these residues can form electrostatic bridges between the TMDs of multi-spanning or multi-component membrane assemblies [13]. Interestingly, negatively charged amino acids (Asp, Glu) and their amido-derivatives (Asn, Gln) are almost absent from TMDs of vertebrate membrane proteins [10]. A weak preference for the membrane proximal part at the luminal end of the TMD was found for Asp and Glu [9, 10]. Finally, proline and glycine are the two amino acids with physico-chemical properties, which can affect the stability of TMDs.

Proline and glycine were defined as typical 'helix-breakers' in soluble globular proteins. Indeed, they are virtually absent from the helical structures of such proteins [14]. However, proline is often present in the TMDs of integral proteins, exhibiting the highest occupancy to the ends but, with a lower frequency, also to the central parts of the α-helices [10, 15, 16]. The cyclic structure of proline makes it unique among the 20 natural amino acids because its amide group lacks the proton necessary for the hydrogen bond stabilising the α-helix or the β-sheet structure [17]. Therefore, prolines in transmembrane (TM) helices are predicted to induce regions of helix distortions and/or dynamic flexibility (i.e., kinks, hinges, swivels; refs. [15, 18]). Such structural distortions may play a role in the transmission of conformational changes along the helix, establish crucial helix-helix packing interactions or geometries, but can also help the helix to adapt the optimal position [15, 19]. Proline was found in the TM helix of many membrane proteins, especially with a polytopic structure [20]. There, the presence of central proline can lead to the change in the orientation of helix [16]. Moreover, such prolines in TMDs are critical for the function of several proteins [19, 21, 22].

Glycine is also rather frequent in the TMDs of integral membrane proteins [10]. In analogy to proline, glycine helix-affecting properties depend on the local environment [23, 24]. No strong effect of a single glycine residue on basic structure of transmembrane α-helices was found experimentally [23, 24]. It functions primarily as an interface between individual helices of the polytopic membrane proteins and is involved in protein dimerisation [25, 26]. However, when positioned close to the proline, it enhances local dynamics of the helix and, thus, can affect the function of transmembrane peptides or proteins [27, 28]. The complexity of proline and glycine environment-sensitive properties suggests that it is important to characterise their role in the TMD of individual proteins separately.

LAT, linker for activation in T cells, is 36-kDa protein belonging to the family of transmembrane adaptor proteins (TRAPs). It plays an important role in membrane immuno-receptor signalling pathways of T cells, NK cells, mast cells and platelets [29, 30]. LAT is indispensable for the T-cell function and development [31]. It plays an essential role in T-cell activation by providing a platform for signal transmission initiated by the T-cell receptor (TCR) at the plasma membrane [30, 32]. T cells lacking LAT, i.e. the Jurkat mutants J.CaM2.5, fail to mobilise calcium and promote other downstream effector events upon TCR stimulation (e.g., ERK phosphorylation or IL-2 production). Human LAT is a type III transmembrane protein, i.e. it is missing a signal peptide and, thus, uses its unique TMD for its membrane insertion. Its extracellular part has only 3 amino acids, the TMD is 24 residues long and the cytoplasmic tail (235 amino acids) contains nine conserved tyrosine residues involved in T-cell signalling. The cytoplasmic tail of LAT also possesses conserved juxtamembrane cysteines required for its palmitoylation (residues 26 and 29). Palmitoylation is mainly responsible for sorting of LAT to the plasma membrane [6, 33, 34].

In this study, we have investigated the impact of highly conserved proline and glycine residues of the LAT TMD on its plasma membrane localisation and function. We demonstrate that replacement of prolines and glycine with aliphatic amino acid (alanine or leucine) partially recovers the surface localisation of LAT. However, such effect is not sufficient for LAT function. We also tested whether nanoscopic surface organisation of LAT mutants is altered and, thus, leads to their malfunction in T cells.

RESULTS

Atypical transmembrane domain of LAT with highly conserved helix-breakers at the positions 8, 12 and 17

We have previously shown that TMD controls sorting of LAT to the plasma membrane [6]. General plasma membrane sorting rules determined for other proteins are not obeyed by LAT: i) 23-residues long TMD should provide sufficient sorting signal but LAT, which lacks cysteines at the positions 26 and 29 and, therefore, cannot be palmitoylated, remains trapped in the Golgi apparatus [6, 9, 33], and ii) there are no voluminous amino acids in the exoplasmic portion of the LAT TMD (Fig. 1A). It was previously reported that prolongation of the TMD leads to the plasma membrane localisation of the proteins, which normally reside in the Golgi apparatus [8]. Nevertheless, prolongation of LAT TMD by 6 amino acids (six leucine residues or PILAML sequence) did not overcome dependence of LAT surface expression on its palmitoylation (Supplementary Fig. S1). We observed the accumulation of LAT with prolonged TMD in lysosomes and some unspecified intracellular vesicles (Supplementary Fig. S1). These data indicate that LAT TMD contains residues, which control its geometry or stability with respect to the lipid membranes of the secretory pathway.

The amino acid sequence of the LAT TMD exhibits high level of conservation with 48% identity in mammals (Fig. 1A). Among the conserved residues are two prolines, which were reported to introduce distortions into the helical structure of TMDs in several proteins [15]. One proline is positioned centrally (Pro17) and one close to the lumenal end of the LAT TMD (Pro8). Moreover, the lumenal part of LAT TMD contains glycine (Gly12) in the position i+4 with respect to Pro8 and i-5 with respect to Pro17. The motif (PxxxG) was described to control the dynamics of pore-forming peptides and proteins [27]. Importantly, helix-breaking residues were shown to exhibit cumulative effect on TM helices [24]. We, therefore, hypothesised that Pro8, Gly12 and Pro17 residues play a role in membrane stability and sorting of LAT to the plasma membrane.

All-atom MD simulations indicate kink formation in the helical structure of LAT TMD

We have first characterised the role of Pro8, Gly12 and Pro17 residues in LAT TMD structure using all-atom MD simulations. Residues 2-33, EEAILVPCVLGLLLLPILAMLMALCVHCHRLP, which form the hydrophobic core and membrane proximal parts, were used to simulate human LAT TMD in a lipid membrane composed of 128 palmitoyl-oleoyl phosphatidylcholine (POPC) molecules for 1 µs. The peptide was first enforced to adapt α-helical structure and inserted into the membrane in a transbilayer orientation. Afterwards, the system was left to adjust its optimal conformation for 500 ns. The following 500 ns of the trajectory were used for the analysis of peptide behaviour in a model membrane. The structure of LAT WT peptide exhibited high level of helicity. However, a kink could be observed in the central part of the peptide at around the position of Leu14 (Fig. 1B,C). This non-helical segment involving residues 13-15 is downstream of Gly12 (i+2 for Leu14) and upstream of Pro17 (i-3 for Leu14). Such deviation within the α-helix is in agreement with previously observed kinks induced by proline and glycine residues in the TMDs of several membrane proteins (e.g., bacteriorhodopsins, ref. [28]). The maximal impact was reported for positions i-3 or i-4 with respect to the proline residue [35]. Maximal effect of glycine was observed for residues i+1 and i+2 [24]. Another deviation from the α-helical structure, even though much smaller compared to the central non-helical segment, could be observed near Pro8 residue (Fig. 1C).

We have further used MD simulations to characterise behaviour of LAT TMD mutants, in which helix-breaking residues were replaced with alanine or leucine. Mutation of proline to alanine in the position 17 (P17A) led to complete disappearance of the kink for the full period of the simulation (Fig. 1B,C). A minor helix deviation near Pro8 was preserved in P17A mutant (Fig. 1C). On the contrary, no effect on the central kink was observed in the mutant P8A. Nevertheless, the mutant exhibited shortening of the helical TM segment (Fig. 1C) and higher dynamics of the kink, as represented by the analysis of the kink angles (Supplementary Fig. S2). The helix was 2 residues shorter compared to LAT WT peptide. No such shortening was observed for P17A mutant (Fig. 1C). MD simulations of G12L mutant of LAT TMD peptide provided similar results as for LAT WT peptide (Fig. 1C and Supplementary Fig. S2). However, the helical TM segment was 3 residues shorter than in the LAT WT peptide. The overall tilt angle of the peptides in the bilayer was similar for all variants except for the G12L mutant, probably caused by shortening of its helical fragment (Supplementary Fig. S3). The *in silico* data indicate that Pro17 is critical for the kink formation in the LAT TMD but Pro8 and Gly12 fine-tune the overall TMD structure and dynamics of the kink.

Mutation of helix-breaking amino acids in the TMD does not impact LAT sorting to the plasma membrane and its function

We have therefore investigated the impact of Pro8, Gly12 and Pro17 on LAT sorting to the plasma membrane. The coding DNA sequence was individually modified to replace Pro8 and Pro17 residues with alanine (Fig. 2A) and expressed as mutant LAT-GFP fusion proteins in LAT-deficient Jurkat T-cell line, J.CaM2.5. Gly12 residue was mutated to leucine to prevent the disruption of leucine-rich segment of the LAT TMD (Figs. 1A and 2A). The cells were transiently transfected with the plasmid DNA and the expression was analysed 16-24h later using confocal scanning microscopy. All mutant proteins exhibited a distribution, which was comparable to the native LAT protein. The proteins prevalently localised to the plasma membrane of transfected J.CaM2.5 cells (Fig. 2B). A partial trapping of the proteins in the Golgi apparatus could be observed. This observation is in agreement with previous findings that T cells express two pools of LAT, one localized in the plasma membrane and the other in the Golgi apparatus [36]. However, no extensive accumulation of the mutant LAT proteins in intracellular membranes, e.g. the ER, was visible. These results indicate that mutating individual 'helix-breaking residues' of the LAT TMD to alanine (or leucine) does not substantially destabilise LAT protein.

We further verified whether Pro->Ala or Gly->Leu mutations influence function of LAT in T cells. It was shown previously that antigen response of T cells is LAT-dependent process [37]. High level of cytosolic calcium was rapidly mobilised in J.CaM2.5 cells transiently transfected with LAT WT stimulated with anti-TCR as measured by flow cytometry (Fig. 3A; see also **Methods**). A three-fold signal increase was observed less than a minute after stimulation, as detected by changes in fluorescence properties of the calcium-sensitive probe Fura Red (Fig. 3B). Similarly, stimulation of cells expressing LAT-P8A, LAT-G12L or LAT-P17A variants was associated with a rapid, strong, and sustained calcium response (Fig. 3B). Together, these data indicate that mutation of helix-breaking residues does not affect localisation and function of LAT in T cells.

Mutation of helix-breaking amino acids promotes sorting of non-palmitoylated LAT to the plasma membrane

As mentioned above, LAT requires palmitoylation of its membrane proximal cysteines 26 and 29 for its localization to the plasma membrane and function. We were, thus, interested whether a kink in the helix of the TMD determined using MD simulations can influence plasma membrane sorting of LAT in the absence of its palmitoylation. We prepared LAT-GFP variants (Fig. 4A), which combined alanine mutants of Pro8 and Pro17 (or leucine mutant of Gly12) with cysteines 26 and 29 replaced for serines as described before [6]. The mutant proteins were transiently expressed in J.CaM2.5 cells and analysed by confocal microscopy 16-24h post transfection. The images shown in Fig. 4B demonstrate that mutation of helix breaking amino acids in the TMD to alanine or leucine partially restores the plasma membrane localisation of non-palmitoylatable LAT in 30-50% of cells. Compared to LAT-P8A-CS, slightly stronger surface signal was observed on the plasma membrane in cells expressing LAT-G12L-CS and LAT-P17A-CS (Fig. 4B and Supplementary Figs. S5-7). Nevertheless, LAT-P8A-CS, LAT-P17A-CS and LAT-G12L-CS were found in the intracellular membranes, mainly Golgi apparatus and the ER. Such intracellular trapping is similar to LAT-CS mutant with preserved kink-forming amino acids (Fig. 4B and Supplementary Fig. S4).

When analysing response to antibody stimulation, no calcium mobilisation was observed in J.CaM2.5 cells expressing any of the non-palmitoylated LAT-CS variants (Fig. 3B). Surface expression is thus not sufficient for LAT function in antigen-induced T cell signalling. Previously, we demonstrated that addition of the CD4 extracellular domain to LAT-CS rescued plasma membrane sorting of CD4ex-LAT-CS variant ([6] and Supplementary Fig. S8). Importantly, robust calcium mobilisation is induced by antibody stimulation in J.CaM2.5 cells expressing CD4ex-LAT or its non-palmitoylatable variant - CD4ex-LAT-CS (Fig. 3B). CD4ex-LAT and CD4ex-LAT-CS contain intact LAT TMD (apart from cysteine residues 26 and 29 in the CS variant). These data indicate that replacement of helix-breaking amino acids in the TMD with helix supporting ones partially rescues LAT sorting to the plasma membrane, but such surface LAT molecules remain inaccessible for early T cell signalling molecules (e.g. Lck and ZAP-70; ref. [32]).

Nanoscopic organisation of LAT mutants on the surface of T cells

We were thus interested whether this is due to the different nanoscopic organisation of LAT-WT and the mutants, which cannot be visualized by standard confocal microscopy. We employed super-resolution (SR) microscopy called photoactivation localization microscopy (PALM) to image nanoscopic organization of the variants LAT-WT, LAT-P17A and LAT-P17A-CS at the surface of transiently transfected J.CaM2.5 cells. For this purpose, GFP tag was replaced with mEos2, which exhibits photoconvertible behaviour essential for PALM imaging [38]. Transfected cells were immobilized on glycine-coated coverslips to avoid artificial stretching of T cells caused by poly-L-lysine coated surfaces [39]. As shown in Fig. 5, LAT-WT exhibits a random distribution over the surface of unstimulated T cells. LAT-P17A variant, which generates similar calcium response in antibody-stimulated T cells, is also randomly distributed (Fig.5, upper middle panel). For J.CaM2.5 cells expressing the LAT-P17A-CS variant (Fig. 4), which do not respond to antibody stimulation, irregular distribution of molecules was observed using PALM (Fig. 5, upper right panel). This is probably caused by reduced spreading of LAT-P17A-CS-transfected cells on glycine-coated coverslips as represented by a cell footprint on the optical surface analysed using interference reflection microscopy (IRM; Fig. 5, lower right panel). The IRM images of these cells are highly non-homogenous indicating an extensive three-dimensional surface structure probably caused by the accumulation of microvilli or membrane ruffles at the contact site. Intensive spreading was observed for cells expressing LAT-WT and LAT-P17A (Fig. 5, lower panel). Similar protein distributions were detected for palmitoylated and non-palmitoylated LAT-P8A variants, respectively (Supplementary Fig. S9). These data indicate that Pro8 and Pro17 of the TMD are not directly involved in the nanoscopic organisation of LAT at the T-cell surface. However, the ability of T cells to spread on non-stimulating surface is affected by the palmitoylation state of LAT.

DISCUSSION

In this work, we demonstrate the impact of helix-breaking residues on dynamic geometry of LAT TMD and localisation of LAT in T-cell membranes. Using MD simulations, we uncovered the presence of a kink in the TMD of human LAT. The *in silico* and live cell imaging data indicate that the kink is primarily caused by the presence of proline residue in the central segment of the TMD. Replacement of this residue with alanine (P17A mutant) completely removed the kink in the LAT TMD structure. Moreover, non-palmitoylated LAT-P17A mutant localised to the plasma membrane in approximately half of the cells. No such localisation was observed for non-palmitoylated LAT with native TMD sequence, thus, indicating that Pro17 is critical for the dependence of LAT surface expression on palmitoylation. This is probably caused by a highly dynamic central region of native TMD, which is destabilised by the presence of the kink. Indeed, similar helix destabilisation was observed in TM peptides with centrally positioned proline residue [18]. In oligomeric and multispanning (polytopic) proteins, central prolines were found to facilitate tight packing of TMDs and to function as transmission elements of conformational changes required for a rapid response to external stimuli (e.g., ligands, photons or electrochemical fluctuations; refs. [19, 21, 22, 40]). Potentially, such kinked TMD can affect the stability of single-spanning protein such as LAT in membranes. We did not observe any cytosolic expression of native and mutant LAT protein, independent of its palmitoylation state. Therefore, dynamic geometry of LAT TMD must form the basis of the protein adaptability for the specific areas of cell membranes (see below).

Neighbouring amino acids were found to regulate function of prolines in TMDs [21, 22]. Indeed, our live cell imaging data indicate such role for glycine, positioned five residues upstream of the central proline, in LAT localisation in T cells. But no effect on the kink and its dynamics was observed in MD simulations. This may be caused by a subtle effect of glycine residue on TMD dynamics, which is more pronounced in the complex lipid mixture of cell membranes. Glycine was found to enhance the helix-destabilising effect of proline in channel-forming peptide alamethicin [27]. On its own, it destabilises helical structure of downstream residues, especially in the presence of additional helix-breaking residues in the TM segment [24]. The observed kink of LAT TMD spreads over 3 residues downstream of Gly12 and positions i-2 to i-4 with respect to Pro17. This is in agreement with reported destabilising effect of glycine and proline downstream and upstream, respectively, of their position in the helix [24, 35].

Interestingly, as demonstrated by MD simulations, replacement of Pro8 in the lumenal part of LAT TMD for alanine increased dynamics of the kink in the central part. Moreover, non-palmitoylated LAT-P8A mutant localised to the T-cell surface in a similar proportion of cells as observed for the LAT-P17A mutant. A minor reduction of the helicity of native LAT TMD was observed around Pro8 residue. However, similar instability was detected for all tested peptides, including P8A variant. This minor helical instability is probably not caused by Pro8. Von Heijne and Deber groups reported significant impact of prolines localised at the TMD ends on protein (peptide) function and structure [41, 42]. No effect of central proline was found using protein topology-sensitive glycosylation assay [41]. We have observed a strong effect of central proline and only a minor, if any, effect of proline present in the first loop of the helix. We speculate that local lipid environment and overall structure of the TM segment modulate the influence of TM prolines on membrane proteins.

Cellular membranes can have diverse lipid composition, which, among other things, determines their thickness [43]. Hydrophobic segment of human LAT TMD is rather long (24 residues) but the protein requires palmitoylation for its sorting to the thinker bilayer of the plasma membrane [6, 33, 34]. This contradicts previous observation that, in vertebrates, TMDs with >22 residues are sufficient for protein sorting to the plasma membrane [8, 9]. The presence of kink may thus affect the apparent 'length' of LAT TMD. Localization of membrane proteins is also affected by the presence of specific amino acids along the oriented structure of TMDs [9, 10, 44]. For example, acidic amino acids accumulate at the luminal end of the plasma membrane TMDs [10]. Moreover, we have shown that voluminous amino acids form a rough surface of TM segments, which locally rigidifies membranes and may interfere with membrane properties [45]. In this biophysical study, a poly-leucine TM peptide and simple lipid membrane composition was used. In cell membranes, exact geometry, and dynamic structure of TMD can define protein stability and orientation in these complex structures. LAT, with its flexible TM helix, can probably adapt to membranes with diverse lipid composition [6].

Recently, Levental and colleagues reported the role of TMD asymmetry in protein sorting to the plasma membrane [44]. Using bioinformatic approach, they found that proteins at the plasma membrane have smaller surface area in the lumenal (exoplasmic) half of their TMD compared to the cytosolic half. This is in agreement with previously reported accumulation of voluminous amino acids in the cytosolic part of the TMD of the plasma membrane proteins [9, 10]. These amino acids are rather absent in the luminal part of the TMD of these proteins. Levental and colleagues argue that chemical asymmetry of the plasma membrane, which exhibit higher rigidity in its outer leaflet compared to the inner leaflet, selects proteins with asymmetric TMD in terms of surface area [44]. However, this is a static view and cellular membranes exhibit high local dynamics. LAT with evenly distributed voluminous amino acids throughout its TMD (leucine and isoleucine) does not fulfil this criterion. Phenylalanine, tryptophan, and tyrosine are absent from human LAT TMD, but could be found in other species (e.g., mouse or rat). Therefore, it must be the highly dynamic character of LAT TMD, which facilitates LAT localisation to the plasma membrane.

Additionally, LAT is one of very few integral proteins, which segregate into more ordered parts of the membrane, at least in giant plasma membrane vesicles [46]. Even though, membrane domains with similar properties have not been indisputably proven in cells yet, their existence is supported by a lot of indirect evidence [43, 47]. The ability of LAT TMD to change geometry rapidly (intrahelically) may again represent an advantage for segregation into membrane areas with more rigid organisation. Stabilisation of such structures is predicted to involve curvature [48]. The kink in LAT TMD can provide an advantage for localisation into domains with complex geometry. Indeed, our data indicate that elimination of the kink or modification of its properties in P8A, G12L and P17A mutants removes the sorting block for non-palmitoylated LAT trapped in the Golgi apparatus, but cannot recover its function. This is probably due to the sorting of native and palmitoylated LAT into membrane areas with complex chemical composition and geometry.

In summary, we demonstrate the existence of kink in LAT TMD, which controls LAT sorting to the plasma membrane. The kink is induced by centrally positioned proline but is further modulated by neighbouring glycine. Replacement of these residues with helix-stabilising amino acids partially recovers LAT sorting to the plasma membrane but not the function of this adapter. These data indicate complex control of LAT function by highly dynamic structure of its TMD.

ACKNOWLEDGEMENT

The work was supported by Charles University Grant Agency (GAUK; project number 298216) and Czech Science Foundation (19-26854X). We acknowledge Light Microscopy Core Facility, IMG CAS, Prague, Czech Republic, supported by MEYS (LM2015062, CZ.02.1.01/0.0/0.0/16_013/0001775), OPPK (CZ.2.16/3.1.00/21547) and MEYS (LO1419).

CONTRIBUTIONS

L.C., T.B. and M.C. conceived the study. D.G., H.M., M.C.H. and T.Ch. performed the experiments, D.G., H.M., M.C.H., T.Ch. and L.C. analyzed the data. D.G and M.C. wrote the paper. All authors reviewed and approved the manuscript.

Corresponding authors

Correspondence to Marek Cebecauer: marek.cebecauer@jh-inst.cas.cz

Additional information

Supplementary Information accompanies this paper at ...

Competing interests

The authors declare no competing financial interests.

METHODS

Cell culture and transfection

LAT-negative Jurkat T cell variant (J.CaM2.5) was cultured in RPMI-1640 media (Sigma-Aldrich), complemented with 10% fetal calf serum (FCS; Life Technologies) in a humidified incubator (Eppendorf) under controlled conditions of 37°C and 5% CO2. The cells were transiently transfected using the Neon® transfection system (Life Technologies) according to the manufacturer's instructions. One µg of vector DNA was used per shot (3 pulses of 1325 V lasting for 10 ms) per 500 000 cells, which were then incubated in 0.5 ml of media. Cells were analysed 16-20 hours post transfection.

DNA cloning

To generate LAT mutants P8A and G12L, LAT TMD coding sequence was modified using polymerase chain reaction (PCR) and the primers with the appropriate mutations (Supplementary Table S1), and cloned into pXJ41-LAT-EGFP plasmid (or its non-palmitoylatable CS mutant; ref. [6]) using EcoRI and BamHI restriction sites. The variants without the CD148 leader, c-Myc and 5′ UTR were used. LAT-P17A variants were prepared by annealing the appropriate oligonucleotides (Supplementary Table S1) and subcloning as above. LAT-P8,17A mutants were generated from LAT-P17A variant using P8A forward and reverse primers. For super-resolution microscopy, the EGFP coding sequence was changed to mEos2 using BamHI and XhoI restriction sites.

Live-cell confocal microscopy

Cells transiently transfected with GFP variants of LAT in pre-heated, colour-free RPMI-1640 medium supplemented with 10% FCS were placed on 1% gelatine-coated Ibidi µ-Slide 8-well chambers (Ibidi, Germany) and imaged using a Leica TCS SP8 laser scanning confocal microscope equipped with sensitive hybrid detectors (HyD), 488 nm (20mW) and 638 nm (30 mW) lasers and a 63×1.4 NA oil-immersion objective. Five to ten percent laser power and 10% gain were used for image acquisition. Acquired images were manually thresholded to remove signal noise detected outside of the cell using ImageJ software package [49].

Two-colour confocal microscopy of fixed cells

Cells were immobilized on poly-L-lysine-coated Ibidi µ-Slide 8 well chambers for 5 minutes, fixed with 4% paraformaldehyde in PBS for 20 minutes at room temperature and subsequently washed with PBS. Cells were permeabilized for 40min using 10x Permeabilisation Buffer (eBioscience) diluted in water, washed with PBS, and subsequently blocked with 5% BSA. Plasma membrane and Golgi apparatus of transfected cells were stained with 0.5µg/ml lectin-HPA conjugated to Alexa Fluor 647 in PBS supplemented with 1% BSA (Life Technologies) and washed twice with PBS prior imaging. Images were taken using a Leica TCS SP8 laser scanning confocal microscope equipped with a 63× 1.4 NA oil-immersion objective. Minor contrast and/or brightness level adjustments were applied, and images were processed for publishing by ImageJ software.

Single Molecule Localization Microscopy (SMLM)

Sample preparation. Round 25 mm coverslips (No 1.5H, High precision; Marienfeld) cleaned with Helmanex III solution, were coated with 500 µl of 2M glycine solution in ultrapure water for 30 minutes at room temperature. Prior adding the cells, coated coverslips were once washed with Mili Q® water (Merck Millipore). Transfected cells were harvested (3 min at 300 rcf) and transferred into PBS prewarmed to 37°C. After 10 minutes incubation at 37°C cells were fixed for 1 hour at room temperature with 4% paraformaldehyde (Electron Microscopy Sciences) and 2% sucrose (Sigma-Aldrich) solution in PBS. Fixation was stopped with 50mM NH_4Cl in PBS followed by three rounds of washing with PBS. Coverslips were transferred into ChamLide holder (LiveCell Instruments). 200 nm gold beads (BBI) fiducial markers were loaded to the sample in 0,9% NaCl for 5 minutes. Imaging was performed in PBS.

Microscope setup and measurements. SMLM measurements were performed on a home built microscope (IX71 body; Olympus) equipped with 150mW 405nm (Cube; Coherent) and 150mW 561nm (Sapphire; Coherent) lasers, 100x 1.49 NA objective (UApoN; Olympus), EMCCD camera (iXon DU-897, Andor) and manual TIRF tilting mechanism (Thorlabs). Synchronisation of laser switching, and camera recording was performed with two acousto-optic tuneable filters (AOTF; AOTFnC-400.650-TN, AA Optoelectronics) and a home written acquisition software (LabView). To turn the fluorophores into the dark state, fast epifluorescence irradiation with 561nm laser in was applied. Data were acquired using the highly inclined and laminated optical sheet (HILO) illumination mode with 50 ms/frame collection time. The power of activation laser (405 nm) was increased gradually to collect 10 000 – 15 000 frames with a uniform emitter signal.

Data analysis. To generate super-resolution maps of LAT localisations, data were analysed using ThunderSTORM plugin of the ImageJ/Fiji software package [49].

Interference Reflection Microscopy (IRM)

IRM on living cells was recorded on modified Olympus Fluoview 1000 setup equipped with 60x 1.2 NA water immersion objective (UPlanSApo; Olympus). GFP signal was excited with 20mW 488nm laser (Sapphire; Coherent) and recorded on a single-channel PMT detector equipped with a selective dichroic mirror (DM488/543/633; Olympus). For acquisition and system control the FluoView 1000 software package (Olympus) was used. The images were processed using ImageJ/Fiji software package.

Calcium measurements by flow cytometry

Cells resuspended at 10^6 cells/ml in pre-warmed PBS containing 1 µM Fura Red AM (Invitrogen) were incubated at 37°C under 5% CO_2 in a humidified incubator for 30 minutes. Cells were then washed twice with PBS, resuspended in RPMI-1640 (Sigma-Aldrich) supplemented with 10% FCS (Life Technologies) and kept on ice. Prior measurement, cells were equilibrated to 37°C for 4 minutes in a water bath.

All experiments were performed on an LSRII flow cytometer (BD Bioscience). A steady-state (background) signal was recorded for 20 seconds. Afterwards, the cells were stimulated with an antibody: pre-warmed RPMI (Sigma-Aldrich) supplemented with 10% foetal calf serum (Life Technologies) containing anti-TCR antibody C305 (home-produced supernatant, 10 µg/ml) was added in 1:1 ratio. Changes in calcium level were recorded continuously for over 200 seconds. Transfected cells were gated for EGFP positivity. The relative calcium concentration was measured as a ratio of the Fura Red fluorescence intensity elicited by the excitation at 405 nm (emission measured at 635–720 nm) and 488 nm (emission measured at 655–695 nm). The calcium values were calculated as the increasing signal stimulated by the 405 nm laser over the decreasing signal stimulated by the 488 nm laser using the Kinetics tool in FlowJo software version 10.6.1 (Tree Star Inc., OR, USA). The fold increase in signal was calculated as a ratio between maximum peak response and a mean of the steady-state signal recorded without stimulation.

All-atom MD simulations

For atomistic MD simulations, the amino acid sequence of wild type LAT (EEAILVPCVLGLLLLPILAMLMALCVHCHRLP) was used to construct a fully helical model of the peptide employing the Protein Builder of the Molefacture plugin in the VMD software [50]. The standard GROMACS tool (pdb2gmx) was used to apply the fully atomistic AMBER99SB-ILDN force field for the peptide [51, 52]. A lipid membrane consisting of 128 POPC molecules (64 in each leaflet) was hydrated with ~5000 water molecules and pre-equilibrated. The Slipid force field was used for phospholipids and TIP3P model was employed for water [53, 54, 55]. Then, the method of Javanainen was employed to insert the LAT peptide into the membrane in a transmembrane orientation. [56]. The overall -1 charge of LAT was neutralized by inserting one Na+ cation into the water phase. The standard Dang's force field parameters were used for the sodium cation [57]. The membrane with LAT was then simulated using GROMACS software [51]. The same protocol of system preparation and simulations was used for the three LAT mutants considered in MD.

In simulations, fully periodic boundary conditions were used. The simulations were performed at the temperature of 310 K controlled by Nose-Hoover thermostat with the time constant 1.0 ps [58]. Pressure of 1 bar was controlled employing the semi-isotropic Parrinello-Rahman barostat with the time constant of 5 ps and compressibility of 4.5×10^{-5} bar^{-1} [59]. The Particle Mesh Ewald algorithm was used for accounting for long-range electrostatic interactions with the real-space cut-off set to 1.2 nm [60]. For long-range non-bonded interactions, 1.2 nm cut-off was used, switched at the distance of 1.0 nm. All covalent bonds were constrained by LINCS algorithm, and water molecules were constrained by SETTLE method [61, 62]. The equations of motion were integrated with 2 fs time step. All simulations were performed for 1000 ns. Stabilization of the root mean square displacement and peptide-lipid contacts was used as an equilibration criterion. The initial 500 ns were treated as equilibration period while the final 500 ns were used for the analysis.

The analysis of the simulated trajectories was performed using standard GROMACS tools combined with in house Python scripts. In the case of the helix tilt angle and bending, the method of Bansal et al. implemented in the HELANAL Python library was applied [63]. The numerical data were presented using Matplotlib Python library and MATLAB [64]. Molecular visualization was performed with the VMD software [50].

REFERENCES

1. Munro S, Pelham HR. A C-terminal signal prevents secretion of luminal ER proteins. *Cell* **48**, 899-907 (1987).

2. Nishimura N, Balch WE. A di-acidic signal required for selective export from the endoplasmic reticulum. *Science* **277**, 556-558 (1997).

3. Sandoval IV, Bakke O. Targeting of membrane proteins to endosomes and lysosomes. *Trends Cell Biol* **4**, 292-297 (1994).

4. Xiang Y, *et al.* Regulation of protein glycosylation and sorting by the Golgi matrix proteins GRASP55/65. *Nat Commun* **4**, 1659 (2013).

5. Diaz-Rohrer BB, Levental KR, Simons K, Levental I. Membrane raft association is a determinant of plasma membrane localization. *Proc Natl Acad Sci U S A* **111**, 8500-8505 (2014).

6. Chum T, Glatzova D, Kvicalova Z, Malinsky J, Brdicka T, Cebecauer M. The role of palmitoylation and transmembrane domain in sorting of transmembrane adaptor proteins. *J Cell Science* **129**, 95-107 (2016).

7. Smith CJ, McGlade CJ. The ubiquitin ligase RNF126 regulates the retrograde sorting of the cation-independent mannose 6-phosphate receptor. *Exp Cell Res* **320**, 219-232 (2014).

8. Munro S. Sequences within and adjacent to the transmembrane segment of alpha-2,6-sialyltransferase specify Golgi retention. *EMBO J* **10**, 3577-3588 (1991).

9. Sharpe HJ, Stevens TJ, Munro S. A comprehensive comparison of transmembrane domains reveals organelle-specific properties. *Cell* **142**, 158-169 (2010).

10. Baker JA, Wong WC, Eisenhaber B, Warwicker J, Eisenhaber F. Charged residues next to transmembrane regions revisited: "Positive-inside rule" is complemented by the "negative inside depletion/outside enrichment rule". *BMC Biol* **15**, 66 (2017).

11. Blaskovic S, Blanc M, van der Goot FG. What does S-palmitoylation do to membrane proteins? *FEBS J* **280**, 2766-2774 (2013).

12. von Heijne G. Control of Topology and Mode of Assembly of a Polytopic Membrane-Protein by Positively Charged Residues. *Nature* **341**, 456-458 (1989).

13. Fink A, Sal-Man N, Gerber D, Shai Y. Transmembrane domains interactions within the membrane milieu: principles, advances and challenges. *Biochim Biophys Acta* **1818**, 974-983 (2012).

14. Levitt M. Conformational preferences of amino acids in globular proteins. *Biochemistry* **17**, 4277-4285 (1978).

15. Sansom MS, Weinstein H. Hinges, swivels and switches: the role of prolines in signalling via transmembrane alpha-helices. *Trends Pharmacol Sci* **21**, 445-451 (2000).

16. Cordes FS, Bright JN, Sansom MS. Proline-induced distortions of transmembrane helices. *J Mol Biol* **323**, 951-960 (2002).

17. Bywater RP, Thomas D, Vriend G. A sequence and structural study of transmembrane helices. *J Comput Aided Mol Des* **15**, 533-552 (2001).

18. Thomas R, Vostrikov VV, Greathouse DV, Koeppe RE, 2nd. Influence of proline upon the folding and geometry of the WALP19 transmembrane peptide. *Biochemistry* **48**, 11883-11891 (2009).

19. Peralvarez-Marin A, Bourdelande JL, Querol E, Padros E. The role of proline residues in the dynamics of transmembrane helices: the case of bacteriorhodopsin. *Mol Membr Biol* **23**, 127-135 (2006).

20. Wilman HR, Shi J, Deane CM. Helix kinks are equally prevalent in soluble and membrane proteins. *Proteins* **82**, 1960-1970 (2014).

21. Konopka JB, Margarit SM, Dube P. Mutation of Pro-258 in transmembrane domain 6 constitutively activates the G protein-coupled alpha-factor receptor. *Proc Natl Acad Sci U S A* **93**, 6764-6769 (1996).

22. Weber M, Tome L, Otzen D, Schneider D. A Ser residue influences the structure and stability of a Pro-kinked transmembrane helix dimer. *Biochim Biophys Acta* **1818**, 2103-2107 (2012).

23. Li SC, Deber CM. Glycine and beta-branched residues support and modulate peptide helicity in membrane environments. *FEBS Lett* **311**, 217-220 (1992).

24. Hogel P, *et al.* Glycine Perturbs Local and Global Conformational Flexibility of a Transmembrane Helix. *Biochemistry* **57**, 1326-1337 (2018).

25. Lemmon MA, Treutlein HR, Adams PD, Brunger AT, Engelman DM. A dimerization motif for transmembrane alpha-helices. *Nat Struct Biol* **1**, 157-163 (1994).

26. Javadpour MM, Eilers M, Groesbeek M, Smith SO. Helix packing in polytopic membrane proteins: role of glycine in transmembrane helix association. *Biophys J* **77**, 1609-1618 (1999).

27. Jacob J, Duclohier H, Cafiso DS. The role of proline and glycine in determining the backbone flexibility of a channel-forming peptide. *Biophys J* **76**, 1367-1376 (1999).

28. Kumar S, Bansal M. Geometrical and sequence characteristics of alpha-helices in globular proteins. *Biophys J* **75**, 1935-1944 (1998).

29. Horejsi V, Zhang W, Schraven B. Transmembrane adaptor proteins: organizers of immunoreceptor signalling. *Nat Rev Immunol* **4**, 603-616 (2004).

30. Zhang W, Trible RP, Samelson LE. LAT palmitoylation: its essential role in membrane microdomain targeting and tyrosine phosphorylation during T cell activation. *Immunity* **9**, 239-246 (1998).

31. Zhang W*, et al.* Essential role of LAT in T cell development. *Immunity* **10**, 323-332 (1999).

32. Lin J, Weiss A. Identification of the minimal tyrosine residues required for linker for activation of T cell function. *J Biol Chem* **276**, 29588-29595 (2001).

33. Tanimura N, Saitoh S, Kawano S, Kosugi A, Miyake K. Palmitoylation of LAT contributes to its subcellular localization and stability. *Biochem Biophys Res Commun* **341**, 1177-1183 (2006).

34. Hundt M, Harada Y, De Giorgio L, Tanimura N, Zhang W, Altman A. Palmitoylation-dependent plasma membrane transport but lipid raft-independent signaling by linker for activation of T cells. *J Immunol* **183**, 1685-1694 (2009).

35. Richardson JS. The anatomy and taxonomy of protein structure. *Adv Protein Chem* **34**, 167-339 (1981).

36. Bonello G*, et al.* Dynamic recruitment of the adaptor protein LAT: LAT exists in two distinct intracellular pools and controls its own recruitment. *J Cell Sci* **117**, 1009-1016 (2004).

37. Zhang W, Sloan-Lancaster J, Kitchen J, Trible RP, Samelson LE. LAT: the ZAP-70 tyrosine kinase substrate that links T cell receptor to cellular activation. *Cell* **92**, 83-92 (1998).

38. McKinney SA, Murphy CS, Hazelwood KL, Davidson MW, Looger LL. A bright and photostable photoconvertible fluorescent protein. *Nat Methods* **6**, 131-133 (2009).

39. Franke C*, et al.* Unraveling nanotopography of cell surface receptors. *bioRxiv*, 2019.2012.2023.884460 (2020).

40. Senes A, Engel DE, DeGrado WF. Folding of helical membrane proteins: the role of polar, GxxxG-like and proline motifs. *Curr Opin Struct Biol* **14**, 465-479 (2004).

41. Nilsson I, Saaf A, Whitley P, Gafvelin G, Waller C, von Heijne G. Proline-induced disruption of a transmembrane alpha-helix in its natural environment. *J Mol Biol* **284**, 1165-1175 (1998).

42. Li SC, Goto NK, Williams KA, Deber CM. Alpha-helical, but not beta-sheet, propensity of proline is determined by peptide environment. *Proc Natl Acad Sci U S A* **93**, 6676-6681 (1996).

43. Bernardino de la Serna J, Schutz GJ, Eggeling C, Cebecauer M. There Is No Simple Model of the Plasma Membrane Organization. *Front Cell Dev Biol* **4**, 106 (2016).

44. Lorent JH*, et al.* Plasma membranes are asymmetric in lipid unsaturation, packing and protein shape. *Nat Chem Biol* **16**, 644-652 (2020).

45. Olsinova M*, et al.* Roughness of Transmembrane Helices Reduces Lipid Membrane Dynamics. *iScience* **10**, 87-97 (2018).

46. Levental I, Lingwood D, Grzybek M, Coskun U, Simons K. Palmitoylation regulates raft affinity for the majority of integral raft proteins. *Proc Natl Acad Sci U S A* **107**, 22050-22054 (2010).

47. Sezgin E, Levental I, Mayor S, Eggeling C. The mystery of membrane organization: composition, regulation and roles of lipid rafts. *Nat Rev Mol Cell Biol* **18**, 361-374 (2017).

48. Cebecauer M*, et al.* Membrane Lipid Nanodomains. *Chem Rev* **118**, 11259-11297 (2018).

49. Schindelin J*, et al.* Fiji: an open-source platform for biological-image analysis. *Nat Methods* **9**, 676-682 (2012).

50. Humphrey W, Dalke A, Schulten K. VMD: Visual molecular dynamics. *Journal of Molecular Graphics* **14**, 33-38 (1996).

51. Abraham MJ*, et al.* GROMACS: High performance molecular simulations through multi-level parallelism from laptops to supercomputers. *SoftwareX* **1**, 19-25 (2015).

52. Lindorff-Larsen K*, et al.* Improved side-chain torsion potentials for the Amber ff99SB protein force field. *Proteins: Structure, Function, and Bioinformatics* **78**, 1950-1958 (2010).

53. Jambeck JP, Lyubartsev AP. Derivation and systematic validation of a refined all-atom force field for phosphatidylcholine lipids. *The journal of physical chemistry B* **116**, 3164-3179 (2012).

54. Jämbeck JPM, Lyubartsev AP. An Extension and Further Validation of an All-Atomistic Force Field for Biological Membranes. *Journal of Chemical Theory and Computation* **8**, 2938-2948 (2012).

55. Chen F, Smith PE. Simulated surface tensions of common water models. *J Chem Phys* **126**, (2007).

56. Javanainen M, Martinez-Seara H. Efficient preparation and analysis of membrane and membrane protein systems. *Biochimica et Biophysica Acta (BBA)-Biomembranes*, (2016).

57. Dang LX, Schenter GK, Glezakou V-A, Fulton JL. Molecular simulation analysis and X-ray absorption measurement of Ca2+, K+ and Cl-ions in solution.). ACS Publications (2006).

58. Nose S. A molecular dynamics method for simulations in the canonical ensemble. *Mol Phys* **52**, 255-268 (1984).

59. Bussi G, Donadio D, Parrinello M. Canonical sampling through velocity rescaling. *The Journal of chemical physics* **126**, 014101 (2007).

60. Essmann U, Perera L, Berkowitz ML, Darden T, Lee H, Pedersen LG. A smooth particle mesh Ewald method. *J Chem Phys* **103**, 8577-8593 (1995).

61. Hess B, Bekker H, Berendsen HJC, Fraaije JGEM. LINCS: A linear constraint solver for molecular simulations. *J Comput Chem* **18**, 1463-1472 (1997).

62. Hockney RW, Goel SP, Eastwood JW. Quiet High-Resolution Computer Models of a Plasma. *J Comput Phys* **14**, 148-158 (1974).

63. Bansal M, Kumar S, Velavan R. HELANAL: a program to characterize helix geometry in proteins. *J Biomol Struct Dyn* **17**, 811-819 (2000).

64. Hunter JD. Matplotlib: A 2D graphics environment. *Computing in Science & Engineering* **9**, 90-95 (2007).

FIGURE LEGENDS

Figure 1. Helix-breaking amino acids in the transmembrane domain of LAT. (A) Sequence alignment of LAT transmembrane segment and the proximal parts (hydrophobic region in bold) showing conservation of amino acids among twelve mammalian species. **(B)** Representative snapshot from MD simulations of LAT TMD peptide and its variants in POPC bilayer. Transmembrane helix is shown in magenta, phospholipid headgroups are indicated with light blue spheres. **(C)** Helicity plot showing the propensity of individual amino acids in the LAT TMD peptide and its variants to accommodate helical geometry. Standard error is indicated as shadowing of the curves.

Figure 2. Localisation of palmitoylated LAT variants in J.Cam2.5 T cell line. (A) Schematic representation of human LAT construct with attached EGFP and indicated TMD region with accompanied primary sequence. Amino acids mutated in tested LAT variants are highlighted in red. **(B)** Confocal microscopy of J.CaM2.5 T cells expressing LAT-WT-EGFP, LAT-P8A-EGFP, LAT-G12L-EGFP and LAT-P17A-EGFP stained with the plasma membrane (PM) and Golgi apparatus (GA) marker lectin-HPA AF647. Single-channel (EGFP and GA + PM marker) or two-channel overlay images (merge; EGFP – green, GA + PM – red, overlay – yellow) are shown together with brightfield image (BF). Scale bars, 10 µm. More examples in Supplementary Figs. S4-S7. Representative images of 3 measurement days are shown.

Figure 3. Calcium response of J.CaM2.5 T cells expressing LAT variants to stimulation. (A) A representative plot of calcium mobilisation (FuraRed ratio Ex405/Ex488) recorded between 0 and 200 s in transiently transfected J.CaM2.5 T cells by flow cytometry. Transfected cells were stained with Fura-Red and stimulated by the addition of c305 antibody 25 seconds after the beginning of the measurement (indicated by red arrow; y – maximum peak response, x - mean of the non-specific calcium flux without stimulation). For the analysis, transfected cells were selected using gating of GFP signal. **(B)** A bar graph showing increased intracellular calcium levels by c305 antibody in J.CaM2.5 T cells expressing indicated LAT variants (palmitoylatable LAT variants – dark grey bars; non-palmitoylatable LAT variants – light grey bars). Error bars indicate standard deviation of the mean, black puncta represent individual experiments. The data show measurements for 6 independent measurement days.

Figure 4. Localisation of non-palmitoylated LAT variants in J.CaM2.5 T cell line. (A) Schematic representation of human non-palmitoylated LAT construct with attached EGFP and indicated TMD region with accompanied primary sequence. Amino acids mutated in tested LAT-CS variants are highlighted in red. **(B)** Confocal microscopy of J.CaM2.5 T cells expressing LAT-CS-EGFP, LAT-P8A-CS-EGFP, LAT-G12L-CS-EGFP and LAT-P17A-CS-EGFP stained with the plasma membrane (PM) and Golgi apparatus (GA) marker lectin-HPA AF647. Single-channel (EGFP and GA + PM marker) or two-channel overlay images (merge; EGFP – green, GA + PM – red, overlay – yellow) are shown together with brightfield image (BF). Scale bars, 10 µm. More examples in Supplementary Figs. S4-S7. Representative images of 3 measurement days are shown.

Figure 5. Super-resolution (SR) imaging of LAT variants on the surface of T cells. (A) SR images of LAT-WT, LAT-P17A and LAT-P17A-CS in transiently transfected J.CaM2.5 T cells imaged by photoactivation localisation microscopy (PALM) of mEos2 fusion proteins. The images represent a footprint of fixed cells on glycine-coated coverslips. **(B)** IRM images of living J.CaM2.5 T cells transiently transfected with LAT-WT, LAT-P17A and LAT-P17A-CS. Dark areas represent a contact with the optical surface.

Diffraction rings (blue arrowheads) indicate complex surface morphology of an imaged cell. Scale bars, 5 µm. Representative images from 2 measurement days. At least 7 cells were analysed for each LAT variant.

Supplementary Information

For the manuscript: Glatzova et al. The role of intramembrane prolines and glycine in T cell homeostasis and function of LAT

SUPPLEMENTARY FIGURE LEGENDS

Supplementary Figure S1. Localisation of LAT variants with prolonged TMD in J.CaM2.5 T cell line. Confocal microscopy of J.CaM2.5 T cells expressing LAT-6Leu-EGFP **(A)**, LAT-6Leu-CS-EGFP **(B)**, LAT-PILAML-EGFP **(C)** and LAT-PILAML-CS-EGFP **(D)** stained with the marker of lysosomes (Lysotracker-Red). Single-channel (EGFP and Lysosome marker) or two-channel overlay images (Merge; EGFP – green, Lysosome – red, overlay – yellow) are shown together with a brightfield image (BF). Scale bars, 10 μm.

Supplementary Figure S2. Angles formed by kinked helix of LAT peptides in POPC membrane – MD simulation data. (A) Plots representing mean angle between individual amino acids of the LAT WT peptide and indicated mutant variants. Angles were calculated by HELANAL Python library with the geometry of the α-helix characterized by computing local helix axes and local helix origins for four contiguous carbon-α atoms. Angles larger than 20° indicate non-helical structure [63]. **(B)** Plots representing standard deviation of mean angles between individual amino acids (as in A) of the LAT WT peptide and indicated mutant variants. Higher values of standard deviation indicate larger flexibility of the TMD peptide within kinked region.

Supplementary Figure S3. Tilt angles of LAT peptides in POPC membrane – MD simulation data. (A) A plot of tilt angles with respect to the membrane normal accommodated by the LAT WT peptide and indicated mutant variants. The data represent a distribution of tilt angles from the trajectories of the peptides in POPC membranes acquired in all-atom MD simulations. Tilt angles were calculated by HELANAL Python library [63]. The tilt angle value of zero represents a helix orientation parallel to membrane normal, and the tilt angle of 90 degree – perpendicular to the membrane normal.

Supplementary Figure S4. Localisation of LAT-WT-EGFP (A) and its non-palmitoylatable variant LAT-CS-EGFP (B). Nine examples of J.CaM2.5 cell expressing LAT variants imaged by confocal microscopy. EGFP channel is shown along the brightfield image. In total 74 cells were analysed for LAT-WT and 51 cells for LAT-WT-CS variant. Scale bars, 10 μm.

Supplementary Figure S5. Localisation of LAT-P8A-EGFP (A) and its non-palmitoylatable variant LAT-P8A-CS-EGFP (B). Nine examples of J.CaM2.5 cell expressing LAT variants imaged by confocal microscopy. EGFP channel is shown along the brightfield image. In total 80 cells were analysed for LAT-P8A and 76 cells for LAT-P8A-CS variant. Scale bars, 10 μm.

Supplementary Figure S6. Localisation of LAT-G12L-EGFP (A) and its non-palmitoyable variant LAT-G12L-CS-EGFP (B). Nine examples of J.CaM2.5 cell expressing LAT variants imaged by confocal microscopy. EGFP channel is shown along the brightfield image. In total 90 cells were analysed for LAT-G12L and 55 cells for LAT-G12L-CS variant. Scale bars, 10 μm.

Supplementary Figure S7. Localisation of LAT-P17A-EGFP (A) and its non-palmitoylatable variant LAT-P17A-CS-EGFP (B). Nine examples of J.CaM2.5 cell expressing LAT variants imaged by confocal microscopy. EGFP channel is shown along the brightfield image. In total 118 cells were analysed for LAT-P17A and 56 cells for LAT-P17A-CS variant. Scale bars, 10 μm.

Supplementary Figure S8. Localisation of LAT variants containing the extracellular domain of CD4 in J.CaM2.5 T cell line. Confocal microscopy of J.CaM2.5 T cells expressing CD4ex-LAT-EGFP **(A)** and CD4ex-LAT-CS-EGFP **(B)** stained with the plasma membrane (PM) and Golgi apparatus (GA) marker lectin-HPA AF647. Single-channel (EGFP and GA + PM marker) or two-channel overlay images (Merge; EGFP – green, GA + PM – red, overlay – yellow) are shown together with brightfield image (BF). Scale bars, 10 µm.

Supplementary Figure S9. Super-resolution (SR) imaging of LAT variants on the surface of T cells. (A) SR images of LAT-WT, LAT-P8A and LAT-P8A-CS in transiently transfected J.CaM2.5 T cells imaged by photoactivation localisation microscopy (PALM) of mEos2 fusion proteins. The images represent a footprint of fixed cells on glycine-coated coverslips. **(B)** IRM images of living J.CaM2.5 T cells transiently transfected with LAT-WT, LAT-P8A and LAT-P8A-CS. Dark areas represent a contact with the optical surface. Diffraction rings (blue arrowheads) indicate complex surface morphology of an imaged cell. Scale bars, 5 µm. Representative images from 2 measurement days. At least 7 cells were analysed for each LAT variant.

Supplementary Table S1. List of PCR primers

Primer	Sequence	Company
P8A forward	GAATTCGCCACCATGGAGGAGGCCATCCTGGTCGCCTGC	Merck
P8A reverse	GGATCCGTTCAGCTCCTGCAG	Merck
G12L forward	TCCTGGTCCCCTGCGTGCTGCTGCTCCTG	Merck
G12L reverse	TCCTGGTCCCCTGCGTGCTGCTGCTCCTG	Merck
P17A forward	AATAATGAATTCGCCACCATGGAGGAGGCCATCCTGGTCCCCTGCGTGCTGGGGCTCCTGCTGCTGGCCATCCTGGCCATGTTGATGGCACTGTGTGTGCACTGCCACAGACTGCCAGGATCCAATAAT	Merck
P17A reverse	ATTATTGGATCCTGGCAGTCTGTGGCAGTGCACACACAGTGCCATCAACATGGCCAGGATGGCCAGCAGCAGGAGCCCCAGCACGCAGGGGACCAGGATGGCCTCCTCCATGGTGGCGAATTCATTATT	Merck
P17A-CS forward	AATAATGAATTCGCCACCATGGAGGAGGCCATCCTGGTCCCCTGCGTGCTGGGGCTCCTGCTGCTGGCCATCCTGGCCATGTTGATGGCACTGAGTGTGCACAGCCACAGACTGCCAGGATCCAATAAT	Merck
P17A-CS reverse	ATTATTGGATCCTGGCAGTCTGTGGCTGTGCACACTCAGTGCCATCAACATGGCCAGGATGGCCAGCAGCAGGAGCCCCAGCACGCAGGGGACCAGGATGGCCTCCTCCATGGTGGCGAATTCATTATT	Merck

SUPPLEMENTARY MOVIE LEGENDS

Supplementary Movie 1. The last 500 ns of the 1 µs-long MD simulation of the LAT WT peptide in POPC bilayer, related to Figure 1b. Side view (parallel to the bilayer midplane) of the simulation box is shown. The video was created based on the trajectory sampled each 500 ps. The trajectory was centered with respect to the peptide center of geometry. Phosphorous atoms of POPC are shown as cyan balls, and the peptide is depicted using NewCartoon representation (purple). The remaining atoms and molecules, including water, are not shown for clarity. The video was prepared employing MovieMaker plugin of VMD. H264-MPEG-4 encoding was used.

Supplementary Movie 2. The last 500 ns of the 1 µs-long MD simulation of the LAT P8A peptide in POPC bilayer, related to Figure 1b. Side view (parallel to the bilayer midplane) of the simulation box is shown. The video was created as described for Movie 1.

Supplementary Movie 3. The last 500 ns of the 1 µs-long MD simulation of the LAT G12L peptide in POPC bilayer, related to Figure 1b. Side view (parallel to the bilayer midplane) of the simulation box is shown. The video was created as described for Movie 1.

Supplementary Movie 4. The last 500 ns of the 1 µs-long MD simulation of the LAT P17A peptide in POPC bilayer, related to Figure 1b. Side view (parallel to the bilayer midplane) of the simulation box is shown. The video was created as described for Movie 1.

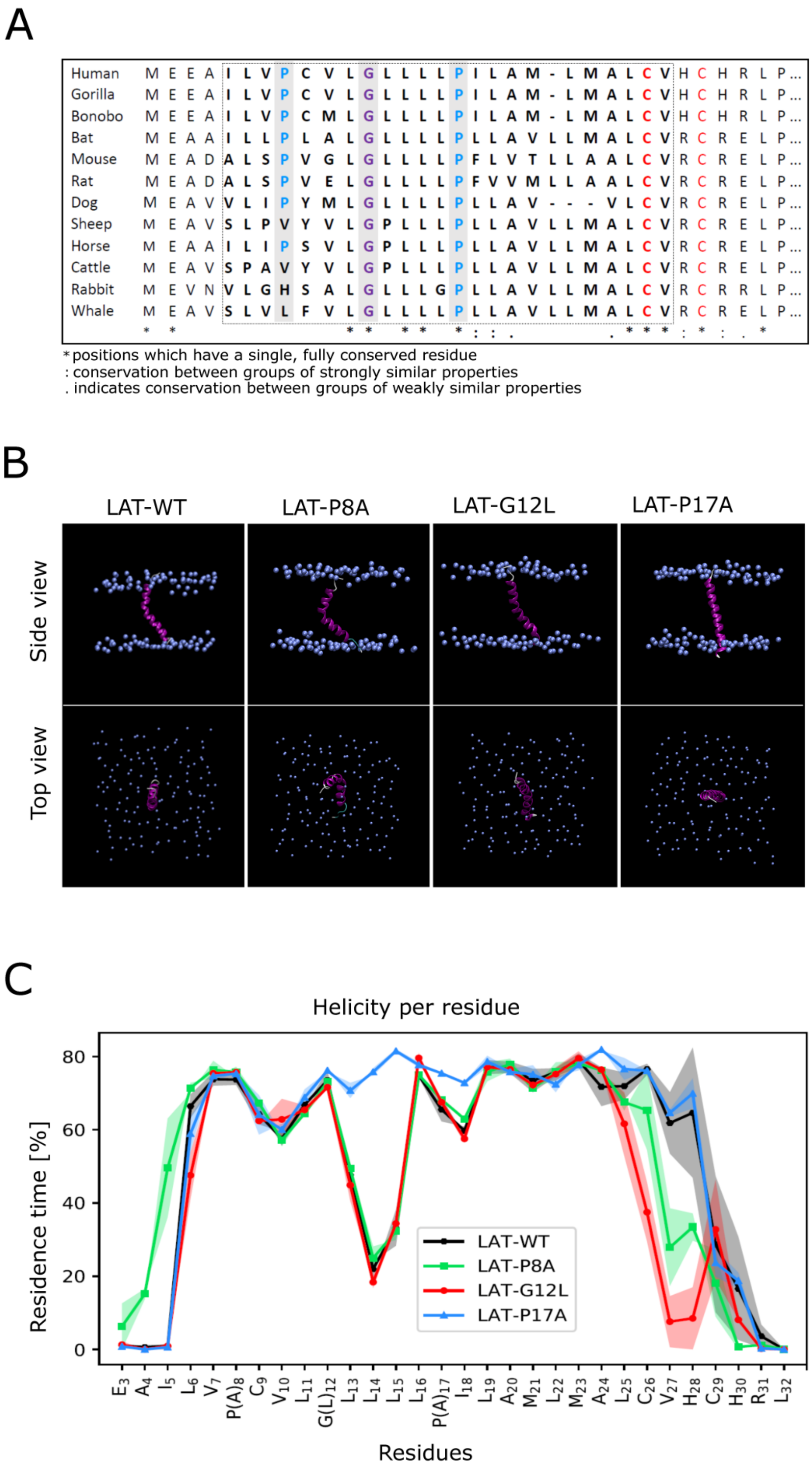

Human	M	E	E	A	I	L	V	P	C	V	L	G	L	L	L	L	P	I	L	A	M	-	L	M	A	L	C	V	H	C	H	R	L	P...
Gorilla	M	E	E	A	I	L	V	P	C	V	L	G	L	L	L	L	P	I	L	A	M	-	L	M	A	L	C	V	H	C	H	R	L	P...
Bonobo	M	E	E	A	I	L	V	P	C	M	L	G	L	L	L	L	P	I	L	A	M	-	L	M	A	L	C	V	H	C	H	R	L	P...
Bat	M	E	A	A	I	L	L	P	L	A	L	G	L	L	L	L	P	L	L	A	V	L	L	M	A	L	C	V	R	C	R	E	L	P...
Mouse	M	E	A	D	A	L	S	P	V	G	L	G	L	L	L	L	P	F	L	V	T	L	L	A	A	L	C	V	R	C	R	E	L	P...
Rat	M	E	A	D	A	L	S	P	V	E	L	G	L	L	L	L	P	F	V	V	M	L	L	A	A	L	C	V	R	C	R	E	L	P...
Dog	M	E	A	V	V	L	I	P	Y	M	L	G	L	L	L	L	P	L	L	A	V	-	-	-	V	L	C	V	R	C	R	E	L	P...
Sheep	M	E	A	V	S	L	P	V	Y	V	L	G	P	L	L	L	P	L	L	A	V	L	L	M	A	L	C	V	R	C	R	E	L	P...
Horse	M	E	A	A	I	L	I	P	S	V	L	G	P	L	L	L	P	L	L	A	V	L	L	M	A	L	C	V	R	C	R	E	L	P...
Cattle	M	E	A	V	S	P	A	V	Y	V	L	G	P	L	L	L	P	L	L	A	V	L	L	M	A	L	C	V	R	C	R	E	L	P...
Rabbit	M	E	V	N	V	L	G	H	S	A	L	G	L	L	L	G	P	L	L	A	V	L	L	M	A	L	C	V	R	C	R	R	L	P...
Whale	M	E	A	V	S	L	V	L	F	V	L	G	L	L	L	L	P	L	L	A	V	L	L	M	A	L	C	V	R	C	R	E	L	P...
	*	*									*	*		*	*		*	:	:	.					.	*	*	*	:	*	:	.	*	

*positions which have a single, fully conserved residue
: conservation between groups of strongly similar properties
. indicates conservation between groups of weakly similar properties

Glatzova 2020 Figure 1

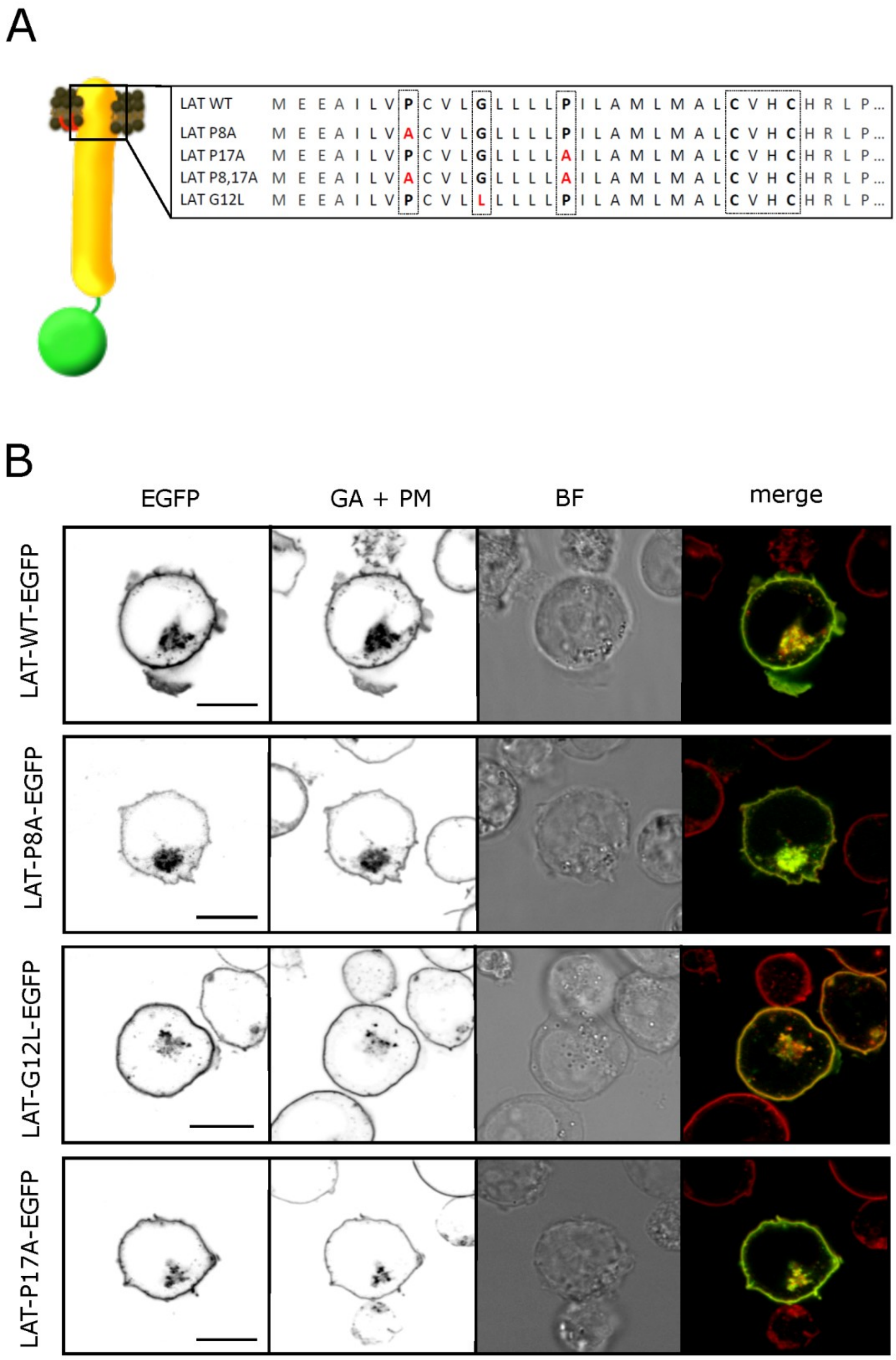

Glatzova 2020 Figure 2

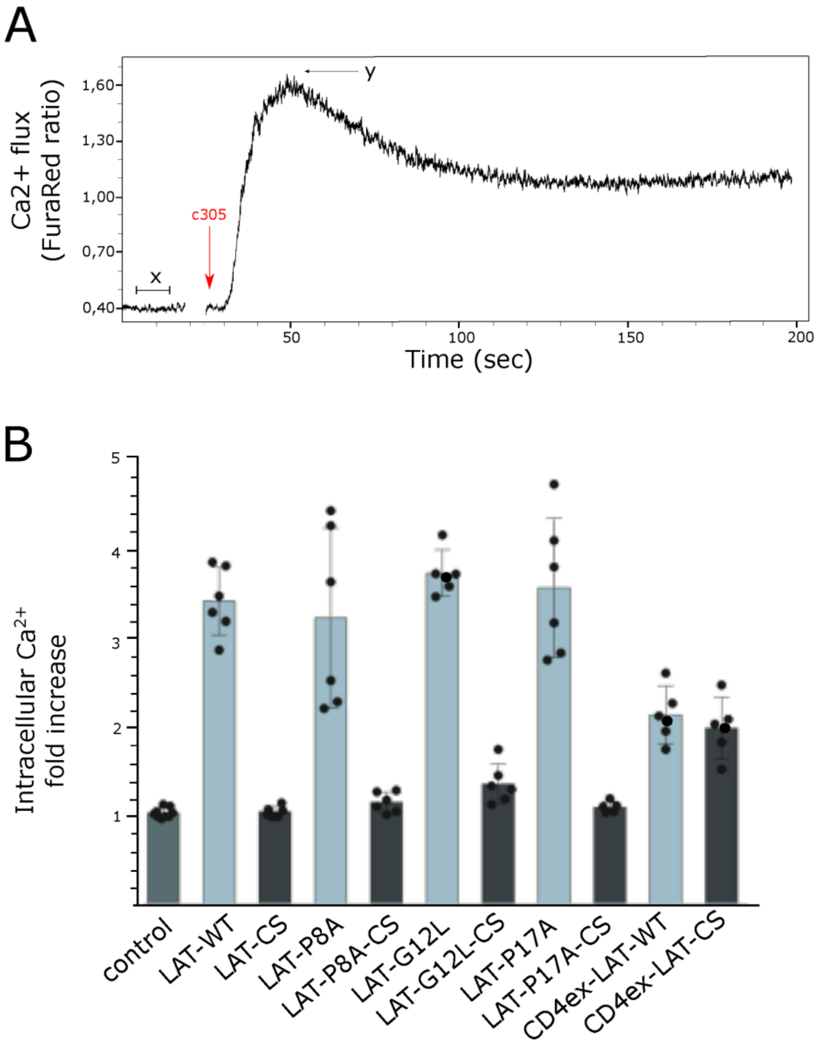

Glatzova 2020 Figure 3

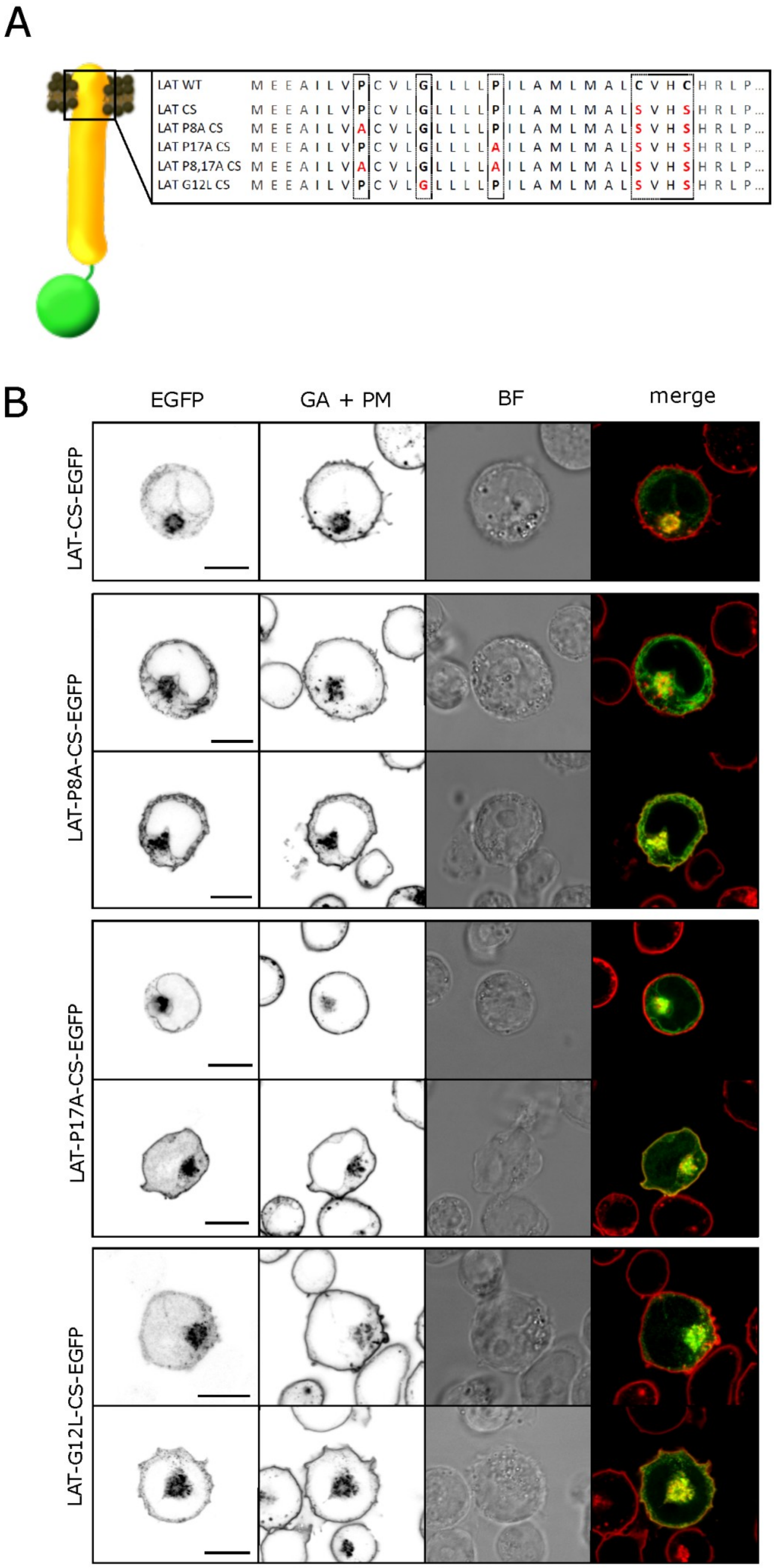

Glatzova 2020 Figure 4

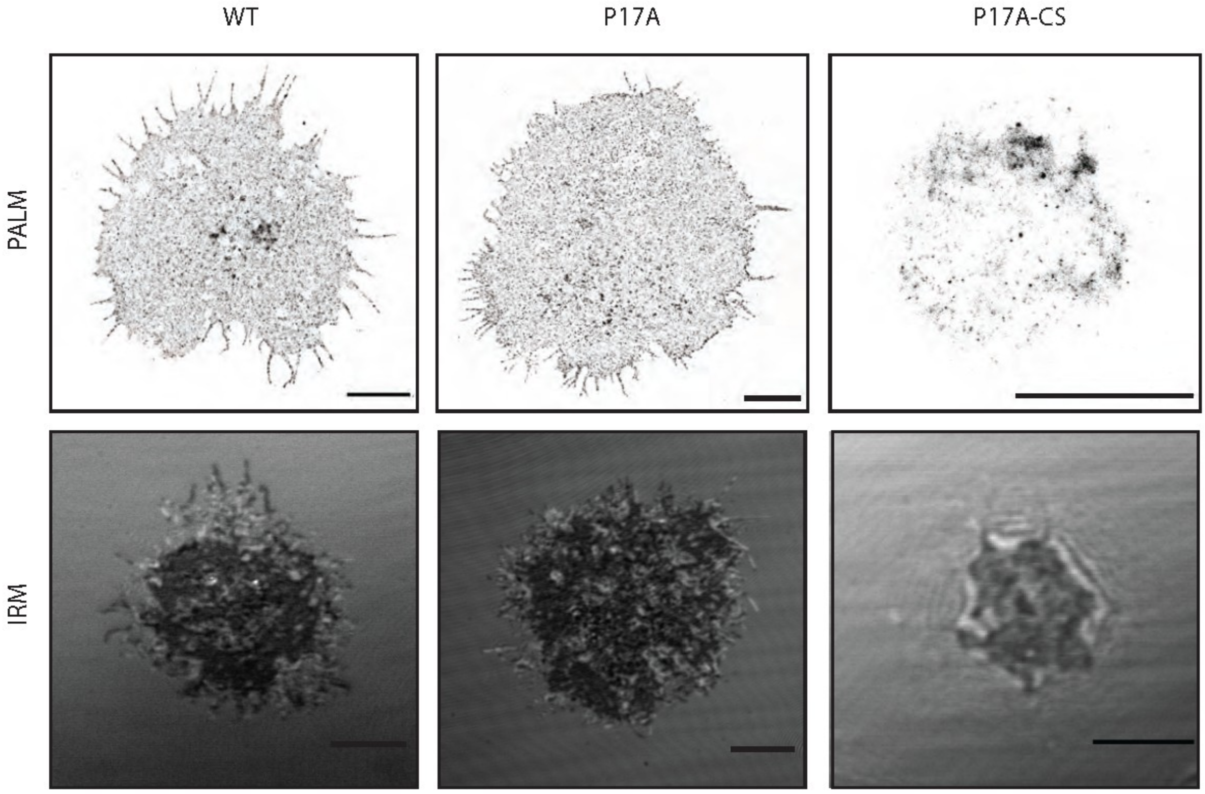

Glatzova 2020, Figure 5

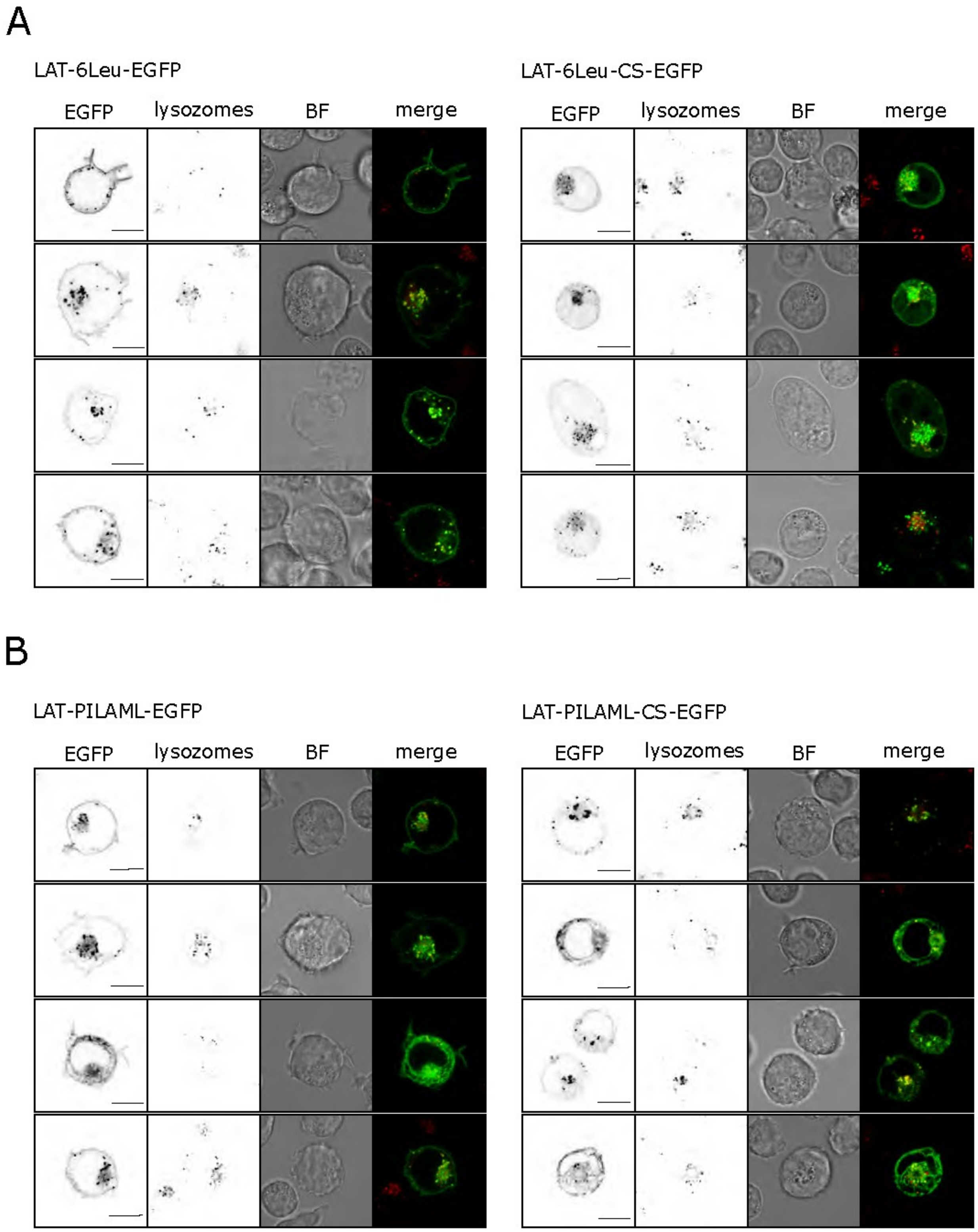

Glatzova 2020 Supplementary figure S1

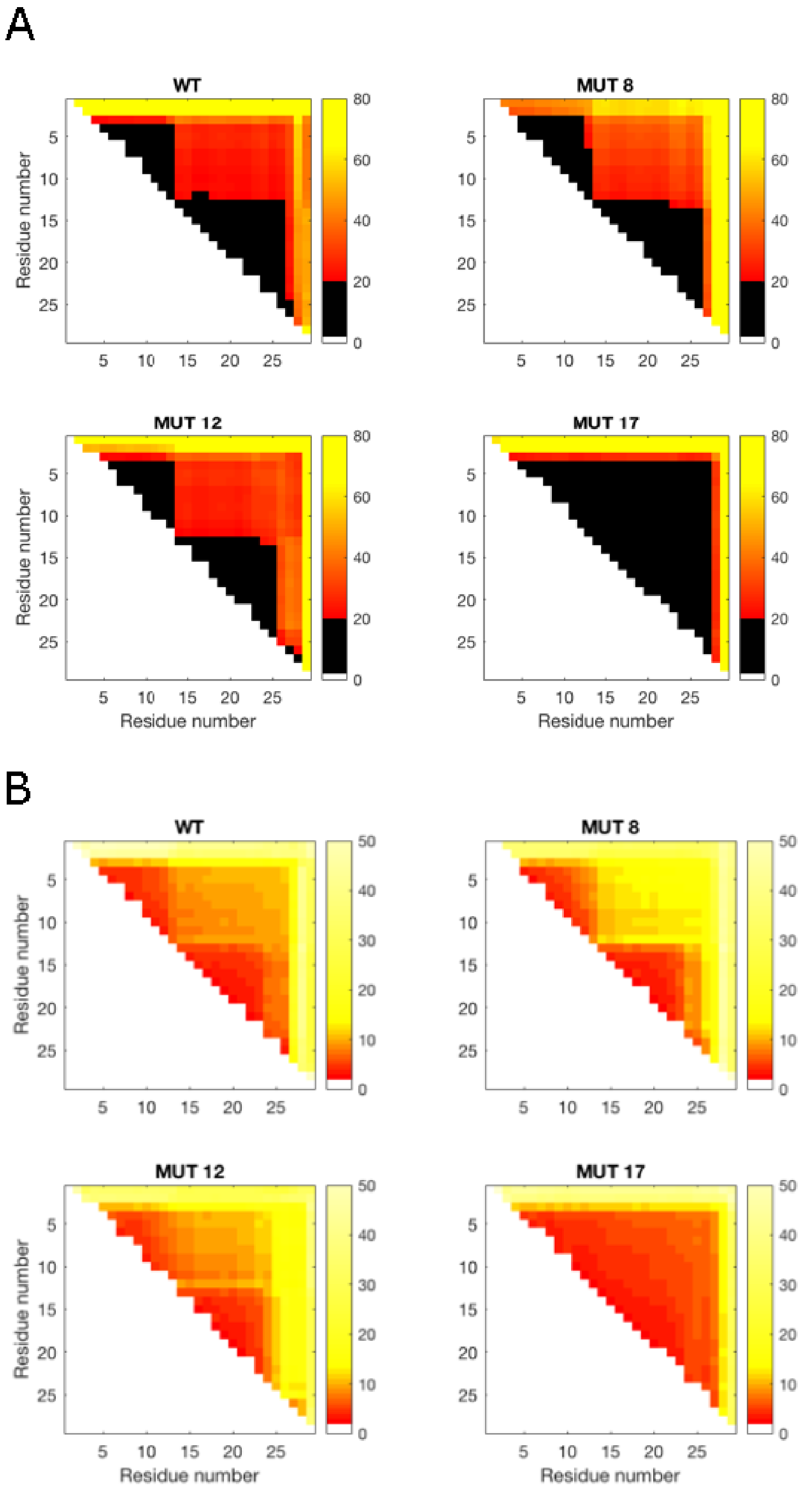

Glatzova 2020 Supplementary figure S2

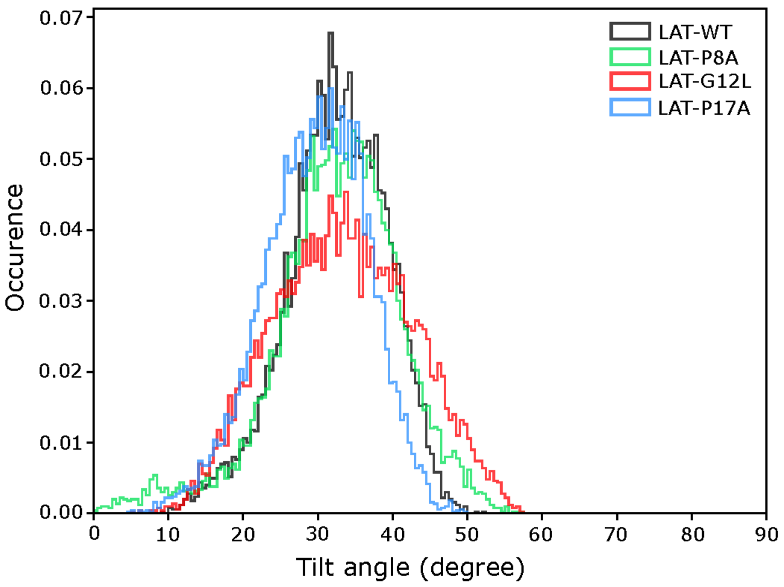

Glatzova 2020 Supplementary figure S3

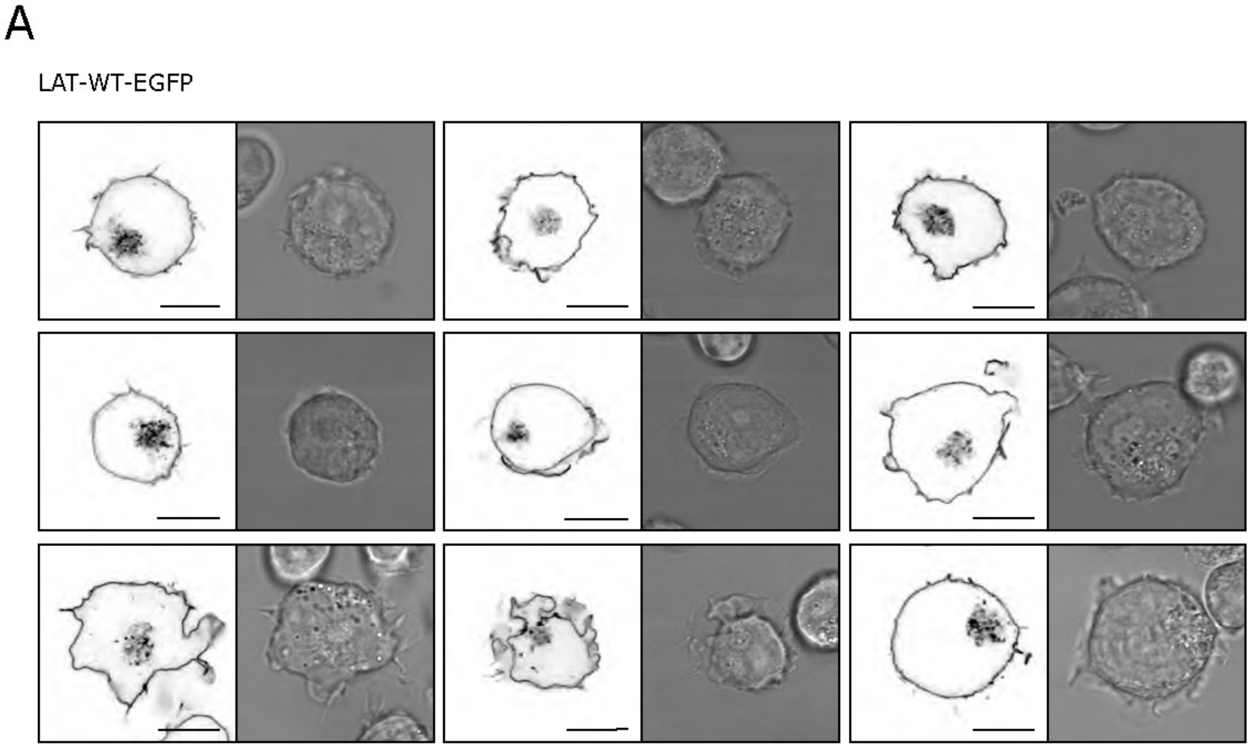

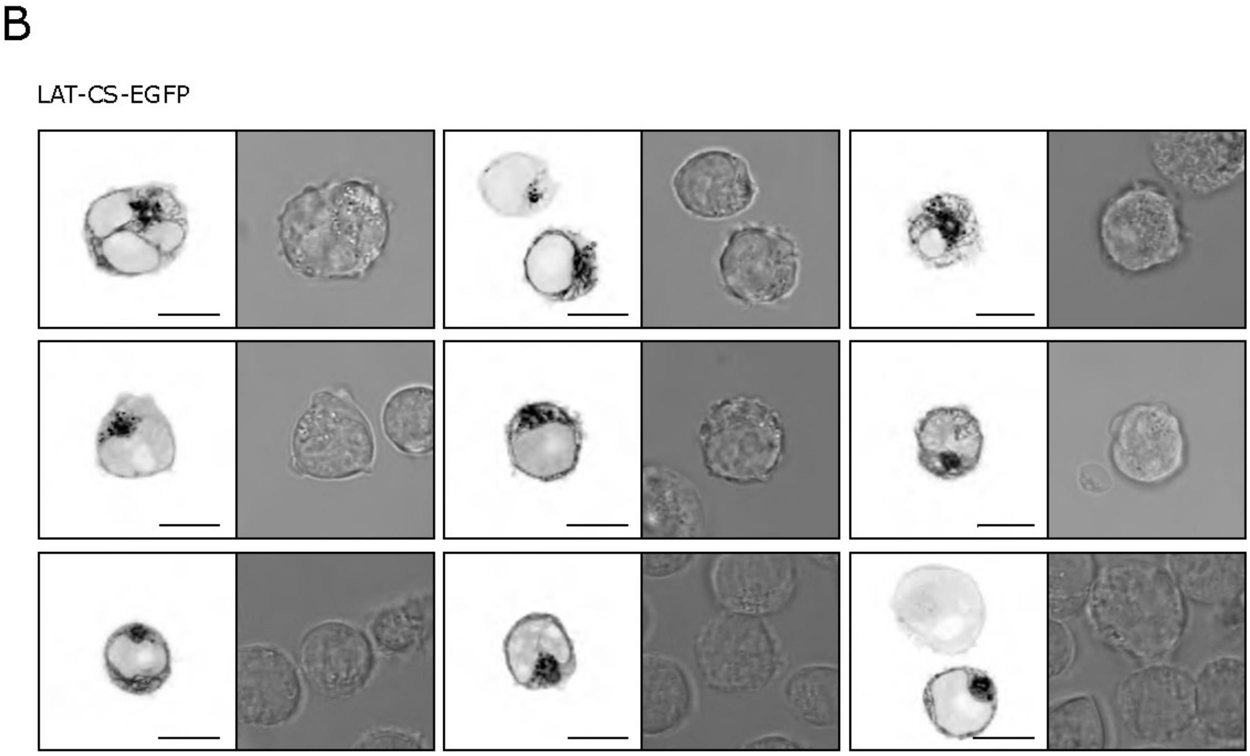

Glatzova 2020 Supplementary S4

A

LAT-P8A-EGFP

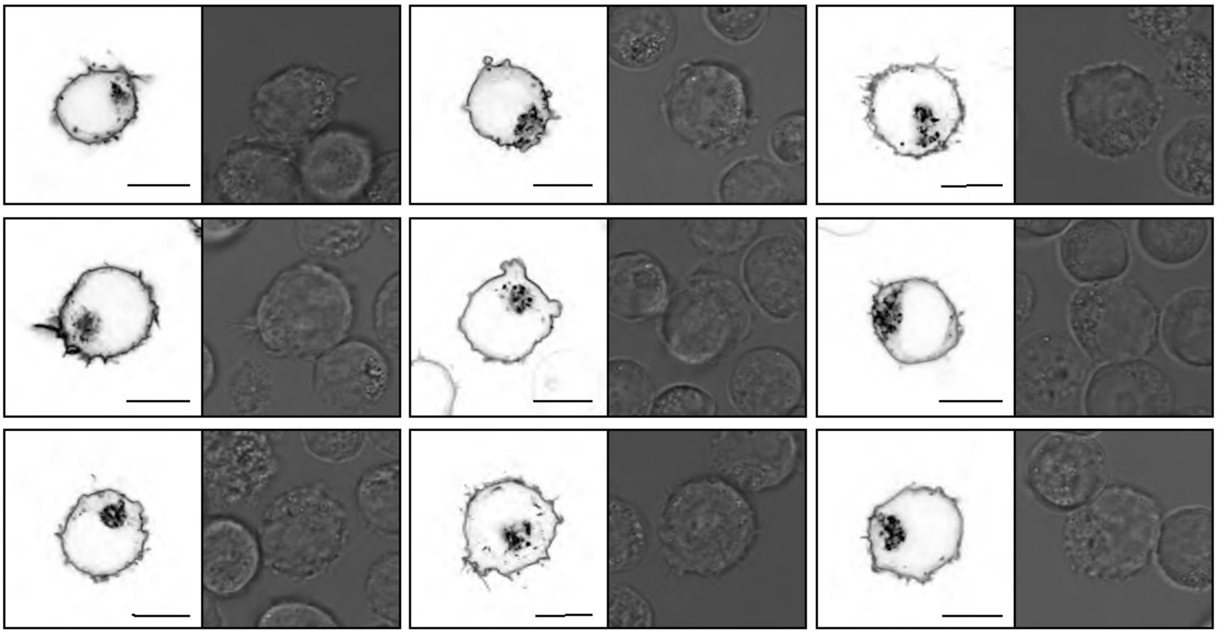

B

LAT-P8A-CS-EGFP

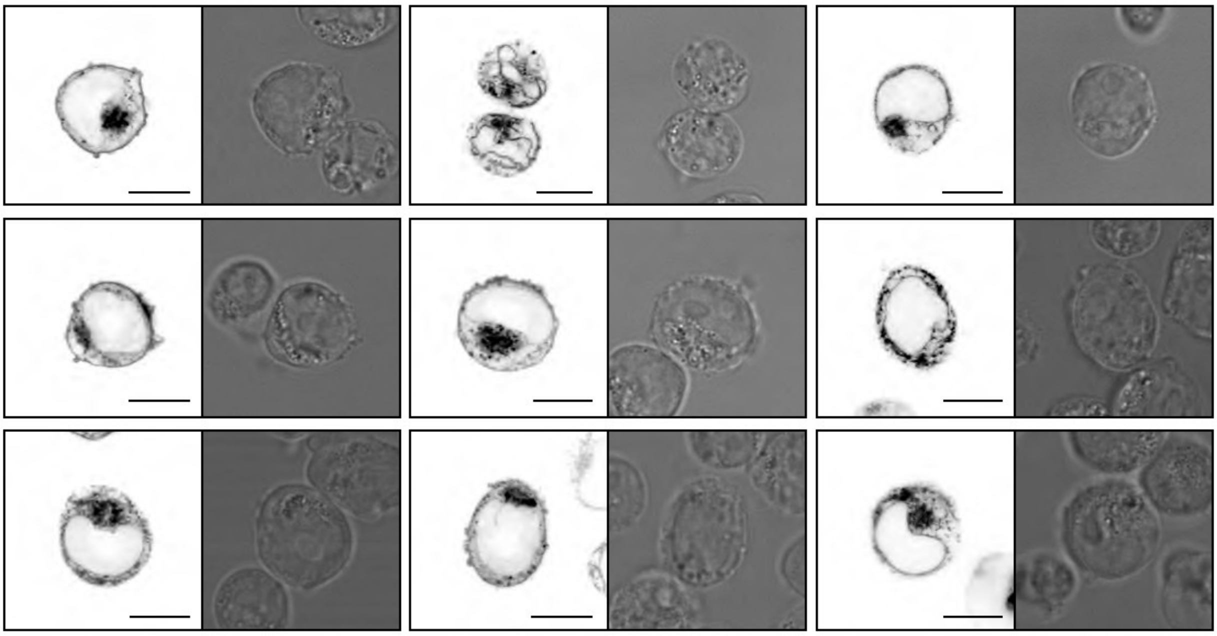

Glatzova 2020 Supplementary S5

A

LAT-G12L-EGFP

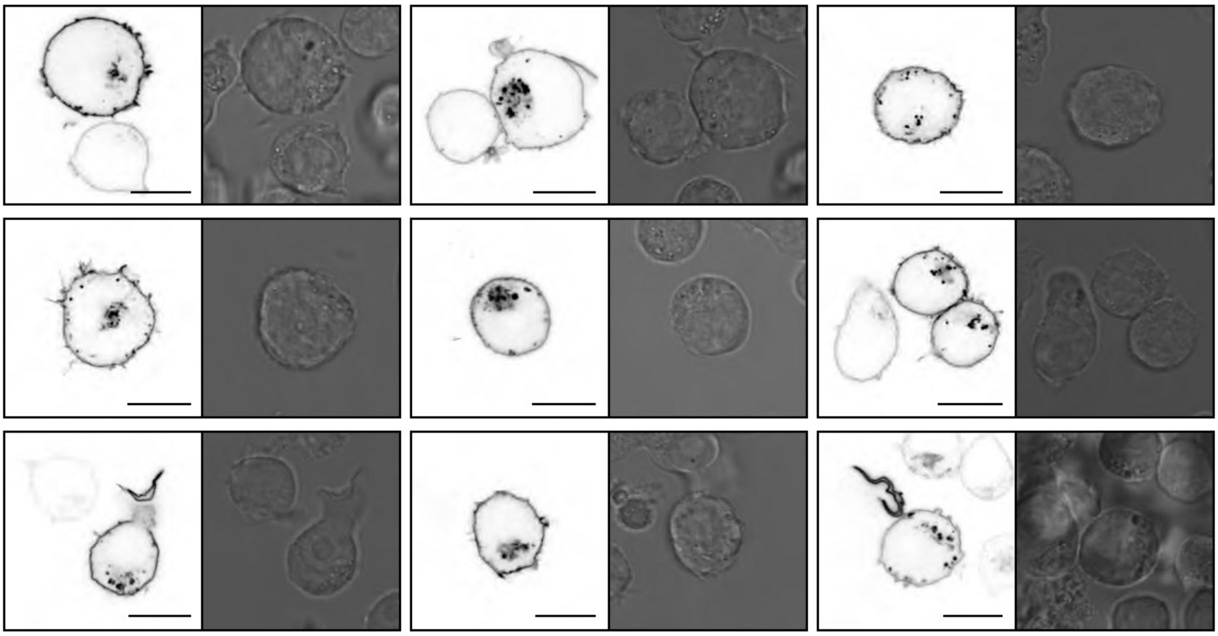

B

LAT-G12L-CS-EGFP

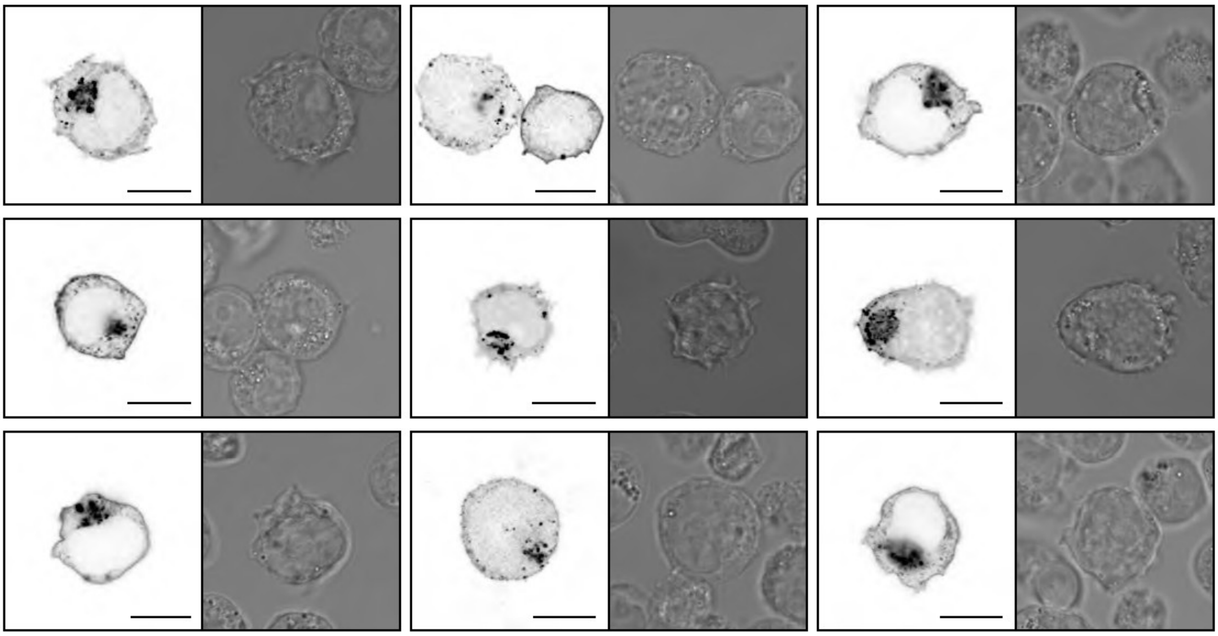

Glatzova 2020 Supplementary S6

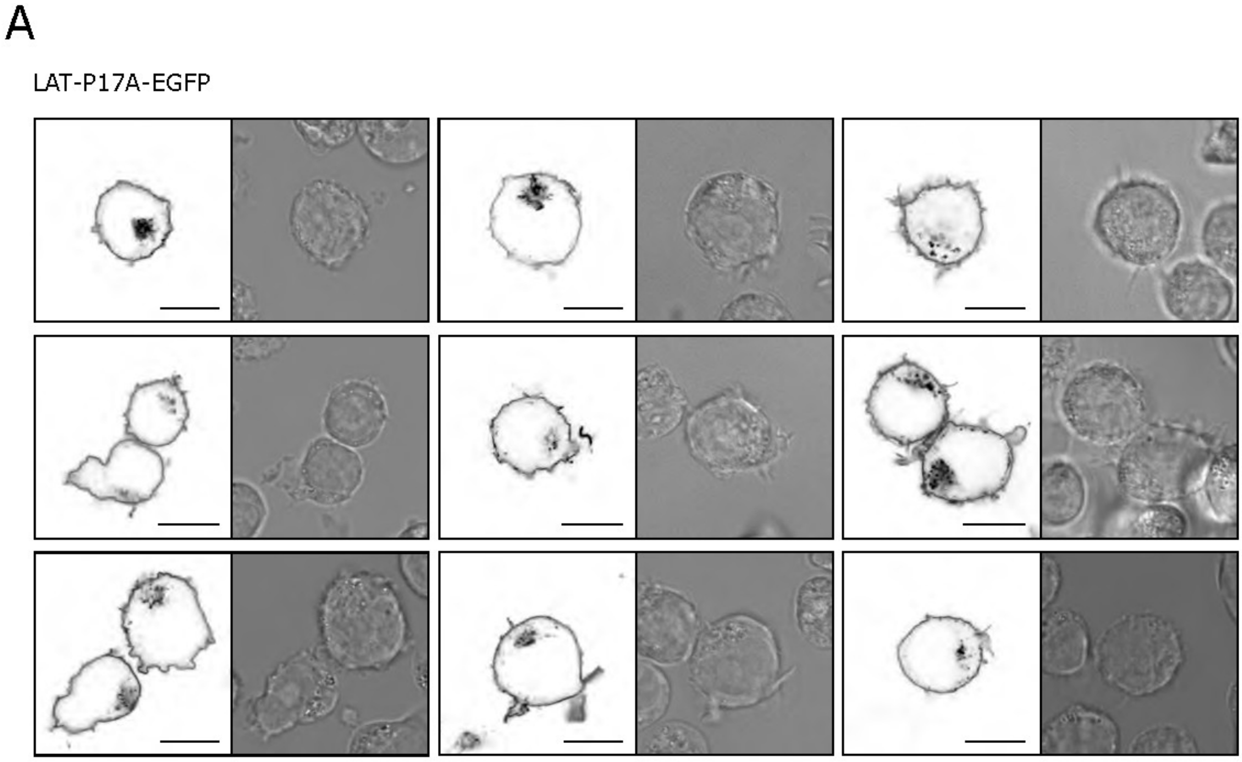

LAT-P17A-EGFP

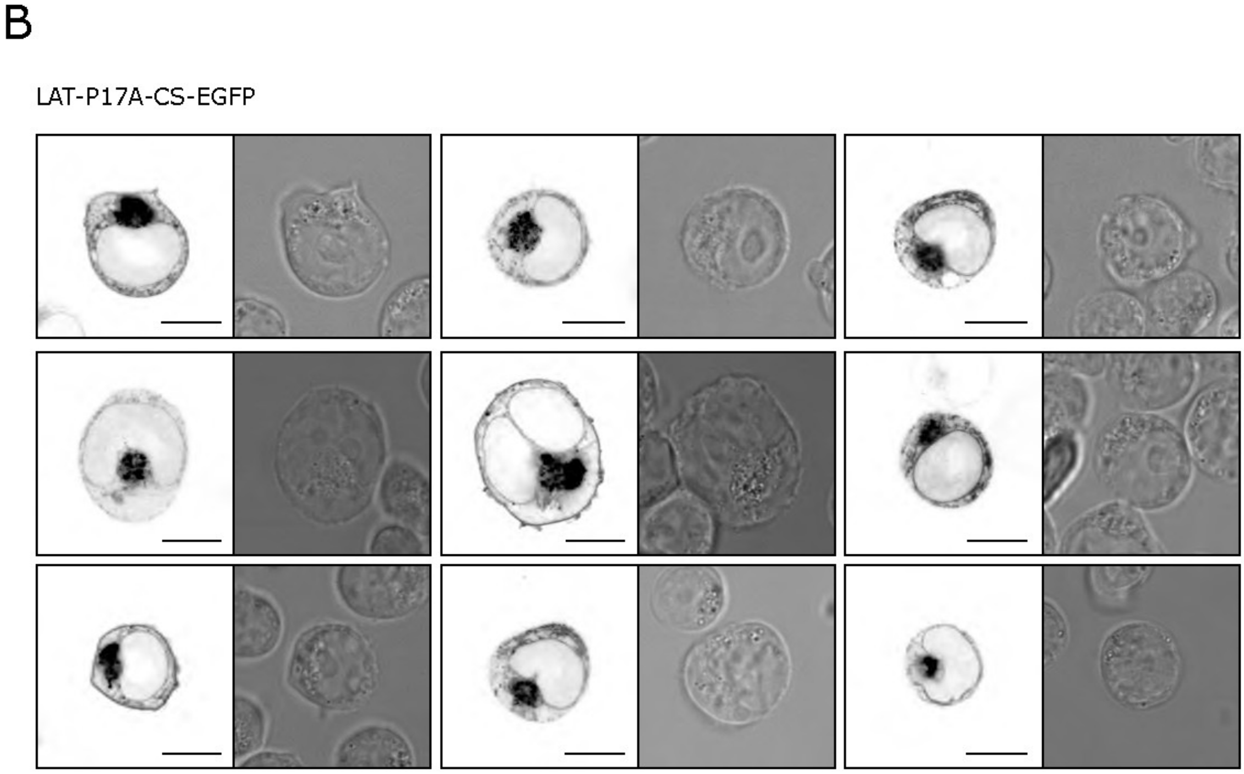

LAT-P17A-CS-EGFP

Glatzova 2020 Supplementary S7

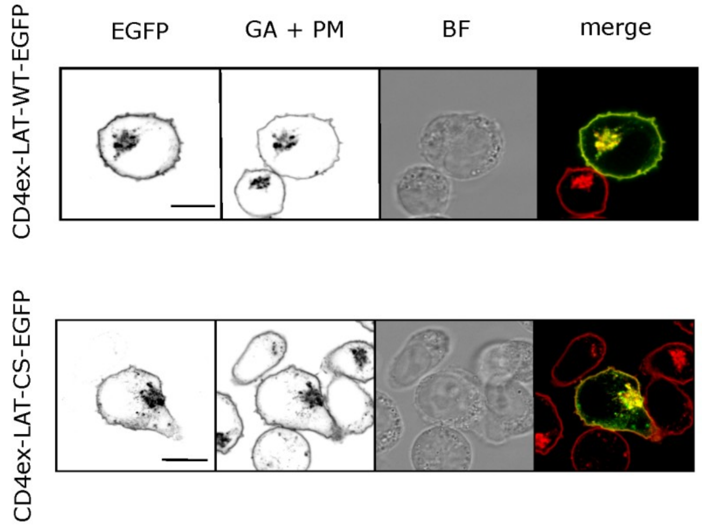

Glatzova 2020 Supplementary figure S8

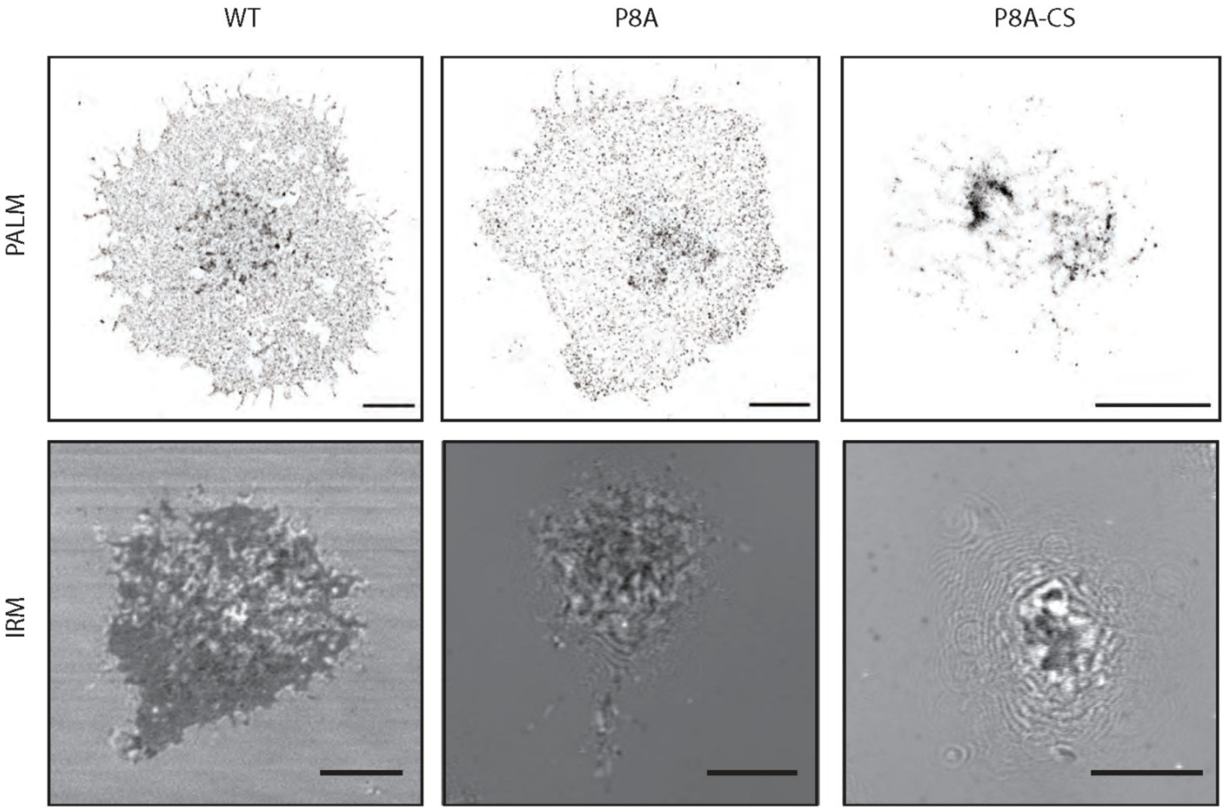

Glatzova 2020, Supplementary Figure S9